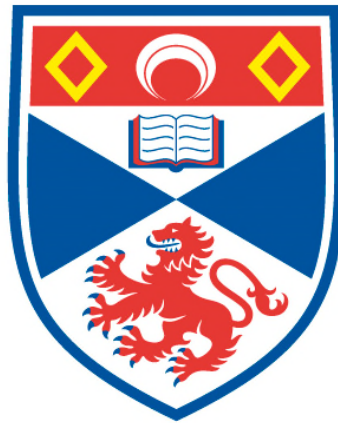


**INVESTIGATION OF CORRELATED  
ELECTRON SYSTEMS UNDER UNI-AXIAL STRAIN**

**Daniel Owen Brodsky**

**A Thesis Submitted for the Degree of PhD  
at the  
University of St Andrews**



**2015**

**Full metadata for this item is available in  
St Andrews Research Repository  
at:**

**<http://research-repository.st-andrews.ac.uk/>**

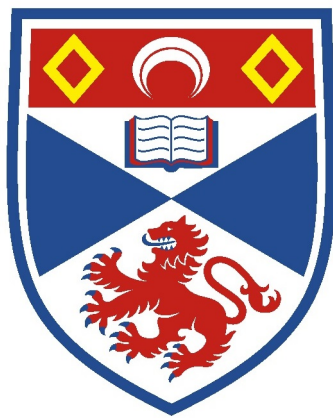
**Please use this identifier to cite or link to this item:**

**<http://hdl.handle.net/10023/9622>**

**This item is protected by original copyright**

# Investigation of Correlated Electron Systems under Uni-axial Strain

Daniel Owen Brodsky



University of  
St Andrews

This thesis is submitted in partial fulfilment for  
the degree of Doctor of Philosophy at the  
University of St Andrews

August 2015



# Declarations

## Candidate's declarations

I, Daniel Owen Brodsky, hereby certify that this thesis, which is approximately 52,000 words in length, has been written by me, and that it is the record of work carried out by me, or principally by myself in collaboration with others as acknowledged, and that it has not been submitted in any previous application for a higher degree.

I was admitted as a research student in August 2011 and as a candidate for the degree of Doctor of Philosophy in August 2011; the higher study for which this is a record was carried out in the University of St Andrews between 2011 and 2015.

*Date:* *signature of candidate:*

## Supervisor's declaration

I hereby certify that the candidate has fulfilled the conditions of the Resolution and Regulations appropriate for the degree of Doctor of Philosophy in the University of St Andrews and that the candidate is qualified to submit this thesis in application for that degree.

*Date:* *signature of supervisor:*

## Permission for publication

In submitting this thesis to the University of St Andrews I understand that I am giving permission for it to be made available for use in accordance with the regulations of the University Library for the time being in force, subject to any copyright vested in the work not being affected thereby. I also understand that the title and the abstract will be published, and that a copy of the work may be made and supplied to any bona fide library or research worker, that my thesis will be electronically

accessible for personal or research use unless exempt by award of an embargo as requested below, and that the library has the right to migrate my thesis into new electronic forms as required to ensure continued access to the thesis. I have obtained any third-party copyright permissions that may be required in order to allow such access and migration, or have requested the appropriate embargo below.

The following is an agreed request by candidate and supervisor regarding the publication of this thesis:

Embargo on all of both printed and electronic copies for a period of one year on the following ground: publication would preclude future publication in the research literature.

*Date:* *signature of candidate:*

*Date:* *signature of supervisor:*

# Abstract

A central paradigm for classifying the phases of correlated electron systems is their symmetry. Having the ability to controllably tune symmetry-related properties of the system is therefore a powerful probe.

In this thesis experiments on quasi-two-dimensional metals  $\text{Sr}_3\text{Ru}_2\text{O}_7$  and  $\text{Sr}_2\text{RuO}_4$  are reported, where uni-axial strain was used as a means of lifting the native tetragonal symmetry. Uni-axial strain was applied to the samples using a piezo-electric based device which can apply both positive and negative strains to the sample, to study the symmetry of the response about zero strain.

$\text{Sr}_3\text{Ru}_2\text{O}_7$  exhibits a magnetic-field-tuned quantum critical point, in the vicinity of which a novel phase is stabilized. The transport properties of the phase were previously shown to be highly susceptible to in-plane magnetic fields. We show that resistivity inside the phase responds strongly to strain applied along one of the in-plane crystal axes, with the responses parallel and perpendicular to that of the applied strain mirroring each other about zero strain. Our results suggest that the underlying symmetry of the phase is  $C_4$  rather than  $C_2$  symmetric.

$\text{Sr}_2\text{RuO}_4$  is an unconventional superconductor which was predicted to have an order parameter of the form  $p_x \pm ip_y$ . This should result in a splitting of the transitions of the two components as a function of strain, with a cusp in  $T_c$  versus strain at zero strain, where  $T_c$  is the upper of the two transitions. We find that the response of  $T_c$  to strain along  $[100]$  is large and symmetric about zero strain, whilst the response to  $[110]$  strain is weak and mostly anti-symmetric. No cusp is observed for either strain direction. We argue that although our results are in contradiction with the simplest  $p_x \pm ip_y$  models, they may still be consistent with certain scenarios where the cusp would have been too small to be observed.



# Acknowledgements

The work presented in this thesis is the culmination of nearly four years of study and experimental research. The experiments on  $\text{Sr}_2\text{RuO}_4$  were carried out in St Andrews, whilst those on  $\text{Sr}_3\text{Ru}_2\text{O}_7$  took place mainly at the Max Planck Institute for Chemical Physics of Solids (MPICPfs) in Dresden. As a student of the Scottish Centre for Doctoral Training in Condensed Matter Physics (CM-CDT), my research was complemented by a broad range of taught courses from which I benefited greatly. None of this work would have been possible without the help and support from a great many collaborators and friends.

I would first like to thank my supervisor Andy Mackenzie, who welcomed me into his research group. The group is characterized by inquisitiveness and the open sharing of ideas, which makes for a stimulating working environment. Andy has given me the freedom to explore new ideas, whilst always being available to give advice and point me in the right direction. I am also grateful to have been given the opportunity to work at the exceptional facilities at the MPICPfs, where I spent the second half of my PhD.

I would like to extend my warm thanks to Clifford Hicks, with whom I have worked very closely over the past four years. Cliff taught me many of the experimental skills necessary to carry out my work, and his encouragement through tough times was invaluable. Cliff's creativity and inventiveness are what got this project off the ground: he fully designed the uni-axial strain probes which were used for the  $\text{Sr}_3\text{Ru}_2\text{O}_7$  and  $\text{Sr}_2\text{RuO}_4$  experiments.

I thank Ed Yelland, my second supervisor, for the helpful discussions and several tricks of the trade which he taught me. The electronic structure calculations which he performed on  $\text{Sr}_2\text{RuO}_4$  were instrumental in helping us interpret our data.

Of course, none of the experiments would have been possible without the excellent samples which were available. All of the  $\text{Sr}_3\text{Ru}_2\text{O}_7$  crystals used were grown by Robin Perry and characterized by Robin and J.-F. Mercure. Two batches of  $\text{Sr}_2\text{RuO}_4$  crystals were used: one grown by Alex Gibbs, and the other by Keigo Nishimura in Prof. Y. Maeno's group at Kyoto University.

I was fortunate to overlap with Jan Bruin in the final year of his PhD, who taught me the ins and outs of the adiabatic demagnetization refrigerator (ADR), with which I spent much of my time.

I give my thanks to Mark Barber, a fellow student and group member, who

contributed to much of the work presented in this thesis. Mark performed the finite element calculations which were used to estimate the sample strain for the  $\text{Sr}_3\text{Ru}_2\text{O}_7$  and  $\text{Sr}_2\text{RuO}_4$  measurements. He also wrote an excellent piece of software to control the ADR, and helped to set up and run the measurements on the first  $\text{Sr}_3\text{Ru}_2\text{O}_7$  sample.

My time as a PhD student was greatly enhanced by my fellow students both in St Andrews and Dresden. Many interesting and thought-provoking discussions were had with Lishan Zhao, who worked on a similar topic and was always a good person to bounce ideas off. I would like to take this chance to thank Justyna Cwik, Stephen Edkins, Calum Lithgow, Edmund Bennett, Steven Thomson and Sam Ridgway from the CM-CDT in St Andrews, for their insights and help along the way. I thank Veronika Sunko for her help with running the last  $\text{Sr}_3\text{Ru}_2\text{O}_7$  measurements, and the other new members of the group in Dresden: Nabhanila Nandi, Maja Bachmann and Jack Bartlett. I also want to thank group members Alexander Steppke, Markus König and Pallavi Kushwaha.

Countless scientific discussions over the past four years stimulated my research and enhanced my understanding of correlated electron systems. Among the many who imparted their wisdom to me, I wish to highlight Chris Hooley, J.-P. Reid, Andreas Rost, Rodolfo Borzi, Manuel Brando and Thomas Scaffidi.

The technical staff at St Andrews and Dresden in the mechanical and electronics workshops, as well as the cryogenics services, were instrumental in the running of our experiments, and so I am grateful for their hard work. I would also like to give a special thanks to the administrative staff of the CM-CDT, Christine Edwards and Julie Massey, who provided excellent support for me during my time as a student, and who made sure that my transition between St Andrews and Dresden went smoothly. Claudia Strohbach on the Dresden side made sure that I was given a warm welcome upon my arrival.

I am eternally grateful to my family for their love and encouragement over the years, and for having provided me with the opportunities and support to achieve my goals.

Last but not least, I wish to thank Suzannah for her love and dedication, and helping me make it through this whole affair in one piece.

I gratefully acknowledge financial support from the Engineering and Physical Sciences Research Council (EPSRC), the Scottish Universities Physics Alliance (SUPA), the Scottish Centre for Doctoral Training in Condensed Matter Physics (CM-CDT) and the Max Planck Society.

# Contents

<b>1</b>	<b>Introduction</b>	<b>1</b>
<b>2</b>	<b>Quantum Criticality in <math>\text{Sr}_3\text{Ru}_2\text{O}_7</math></b>	<b>5</b>
2.1	Non-interacting electrons . . . . .	6
2.2	Fermi liquid theory . . . . .	8
2.3	Magnetism in an itinerant electron system . . . . .	10
2.3.1	Pauli paramagnetism . . . . .	10
2.3.2	Itinerant metamagnetism . . . . .	11
2.3.3	Spin-density wave . . . . .	13
2.4	Quantum criticality . . . . .	13
2.4.1	Quantum critical end-point . . . . .	15
2.5	The physics of $\text{Sr}_3\text{Ru}_2\text{O}_7$ . . . . .	17
2.5.1	Electronic structure . . . . .	18
2.5.2	Metamagnetism & quantum criticality . . . . .	20
2.5.3	Properties of the novel phase . . . . .	23
2.5.4	Theoretical work on the phase . . . . .	29
2.6	Summary and motivation . . . . .	30
<b>3</b>	<b>Spin-triplet Superconductivity in <math>\text{Sr}_2\text{RuO}_4</math></b>	<b>33</b>
3.1	Conventional superconductivity and BCS theory . . . . .	34
3.2	Introduction to unconventional superconductivity . . . . .	36
3.3	$d$ -vector notation . . . . .	38
3.4	Chiral $p$ -wave pairing . . . . .	40
3.5	The physics of $\text{Sr}_2\text{RuO}_4$ . . . . .	42
3.5.1	Electronic structure . . . . .	44
3.5.2	Evidence for spin-triplet superconductivity in $\text{Sr}_2\text{RuO}_4$ . . . . .	45
3.5.3	Evidence for chiral $p$ -wave superconductivity . . . . .	47
3.5.4	Uni-axial strain as a probe of the superconducting order parameter . . . . .	52
3.6	Summary . . . . .	55

<b>4</b>	<b>Experimental Techniques</b>	<b>57</b>
4.1	Uni-axial strain . . . . .	57
4.1.1	Introduction . . . . .	57
4.1.2	Strain and stress tensors . . . . .	58
4.1.3	Uni-axial techniques . . . . .	62
4.1.4	Uni-axial strain probe . . . . .	64
4.1.5	Sample mounting . . . . .	68
4.1.6	Strain calculation . . . . .	68
4.2	Sample preparation . . . . .	70
4.3	Resistivity measurements . . . . .	72
4.4	AC magnetic susceptibility measurements . . . . .	74
4.5	Adiabatic demagnetization refrigerator . . . . .	76
4.5.1	Stray field cancellation (for $\text{Sr}_2\text{RuO}_4$ experiment) . . . . .	80
4.5.2	Sample temperature (for $\text{Sr}_2\text{RuO}_4$ experiment) . . . . .	80
4.5.3	Note on temperature for the $\text{Sr}_3\text{Ru}_2\text{O}_7$ experiment . . . . .	81
<b>5</b>	<b>Effect of Uni-axial Strain on <math>T_c</math> of <math>\text{Sr}_2\text{RuO}_4</math>: Results and Discussion</b>	<b>83</b>
5.1	Strong dependence of $T_c$ of $\text{Sr}_2\text{RuO}_4$ on uni-axial strain . . . . .	84
5.1.1	Effect of cut-angle on $T_c(\varepsilon)$ . . . . .	87
5.2	Experimental details . . . . .	89
5.2.1	Strain measurement and determination of zero strain . . . . .	90
5.2.2	Excitation current and frequency . . . . .	93
5.3	Discussion . . . . .	96
5.3.1	Strain inhomogeneity . . . . .	97
5.3.2	$T_c(\varepsilon)$ and chiral $p$ -wave superconductivity in $\text{Sr}_2\text{RuO}_4$ . . . . .	99
5.3.2.1	Electronic structure calculations . . . . .	99
5.4	Summary and outlook . . . . .	103
<b>6</b>	<b><math>\text{Sr}_3\text{Ru}_2\text{O}_7</math> Under Uni-axial Strain: Results and Discussion</b>	<b>105</b>
6.1	Effect of uni-axial strain on novel phase of $\text{Sr}_3\text{Ru}_2\text{O}_7$ . . . . .	106
6.1.1	Longitudinal and transverse measurements . . . . .	110
6.2	Experimental details . . . . .	116
6.2.1	Frequency dependence and subtraction of background for samples #2 and #3 . . . . .	116
6.2.2	Measurement current . . . . .	119
6.2.3	Strain measurement and determination of zero strain . . . . .	120
6.2.4	Sample comparison . . . . .	121
6.2.5	Strain inhomogeneity . . . . .	123
6.2.6	Transverse signal and $\rho_{bb}$ . . . . .	125
6.3	Discussion . . . . .	126
6.3.1	Symmetry of the phase . . . . .	127
6.3.2	Resistivity enhancement and the SDW . . . . .	129
6.3.3	Resistivity enhancement and metamagnetism . . . . .	130

6.4 Summary and outlook . . . . .	131
<b>7 Conclusions and Outlook</b>	<b>133</b>



# Chapter 1

## Introduction

The rapid development of quantum theories of electrons in solids over the past century, in conjunction with advances in material growth, has radically changed the world in which we live. Indeed, these are at the heart of all silicon-based technologies in use today. In condensed matter physics one is able to write down the Schrödinger equation which governs the motion of the electrons and nuclei in a solid, containing only a small number of constants, all of which can be experimentally determined to high accuracy [1]. These are Planck's constant, the charge and mass of the electron, and the charges and masses of the atomic nuclei. The equation itself contains several terms, describing the kinetic energy of the electrons and nuclei, and their Coulomb interactions with each other.

This has been described as the “theory of everything” for solids [1], and from the reductionist point of view, one should in principle be able to calculate all of a system's properties from it. In practice however, this is far from being the case. The difficulty stems from the interaction terms, which correlate the motions of each single electron with all of the others, making Schrödinger's equation accurately solvable only for small numbers of particles. The success of quantum theories of electrons in silicon and other so-called *weakly correlated* materials is due to the weakness of the interaction energy compared to the kinetic energy in these materials. In this limit, interactions can be treated by a mean-field approximation, thus removing the issue of electron correlation.

There is however a large class of materials in which the electrons are strongly interacting and where this approximation breaks down. Many exotic behaviours are found in these materials, such as unconventional superconductivity, magnetism, or quantum criticality. These materials hold considerable scientific and technological potential, and understanding the physics behind them represents one of the great challenges of the twenty-first century. Applications of strongly correlated materials are varied, ranging from quantum computation to energy storage and transmission, explaining the large effort devoted to the field worldwide.

The many-body interacting problem, as noted previously, cannot be solved directly by “brute force” for realistic numbers of particles. This failure of the reduc-

tionist approach means that progress in the field relies instead on the development of theories which describe the collective behaviours of electrons in solids. The most notable examples of this are the Fermi liquid theory, which describes elementary excitations in a correlated system in terms of *quasiparticles*, and the Bardeen, Cooper and Schrieffer (BCS) theory of superconductivity which describes the superconducting state using a single wavefunction.

The complexity and variety of correlated electron systems means that they must often be studied on a case-by-case basis, there being no unified theory for these systems to date. Theoretical and experimental research are for this reason intimately linked, with theoretical advances prompting new experiments and vice-versa. The focus of this thesis is the ruthenates  $\text{Sr}_3\text{Ru}_2\text{O}_7$  and  $\text{Sr}_2\text{RuO}_4$ , which have been the subject of a broad body of research. Both are quasi-two-dimensional metals which exhibit Fermi liquid behaviour, and develop a highly unusual phase at low temperature.

In the case of  $\text{Sr}_3\text{Ru}_2\text{O}_7$ , the system can be tuned by magnetic field through a quantum critical point, in the vicinity of which a novel phase forms [2]. The study of quantum criticality is one of the central themes of correlated electron research, as Fermi liquid theory breaks down near a quantum critical point and new phases are often found to form there [3].  $\text{Sr}_3\text{Ru}_2\text{O}_7$  is an ideal system in which to study quantum criticality and phase formation as magnetic field-tuning, in contrast to chemical doping, introduces no defects into the crystal, thus enabling one to observe the underlying physics in the clean limit. The novel phase in  $\text{Sr}_3\text{Ru}_2\text{O}_7$  itself presents many interesting and unexplained properties, such as a large anisotropy in the resistivity in the presence of a small in-plane field, leading to the suggestion that the electronic state breaks the symmetry of the lattice [4].

$\text{Sr}_2\text{RuO}_4$  on the other hand is a superconductor below 1.5 K. Its superconducting state is unconventional [5], i.e. its symmetry is different from the simple *s*-wave described by the original BCS theory, with suggestions that it is chiral *p*-wave, analogous to the  $^3\text{He}$  A-phase [6]. Evidence for time-reversal symmetry breaking [7] and spin-triplet pairing [8] support this proposal, however there are many discrepancies between theory and experiment, casting much controversy over the nature of the superconductivity in  $\text{Sr}_2\text{RuO}_4$ . Should a chiral *p*-wave state be realized in  $\text{Sr}_2\text{RuO}_4$ , it would be host to properties such as topologically protected edge states and half-quantum vortices, which may be applicable for example in quantum computing [9].

$\text{Sr}_3\text{Ru}_2\text{O}_7$  and  $\text{Sr}_2\text{RuO}_4$  are excellent candidates in which to study the physics of correlated systems. From a materials point of view, large single crystals of both compounds are available, with ultra-pure samples having mean-free paths of the order of 3000 Å. The normal state from which the new phase condenses is well characterized for each compound, with their electronic structures known in detail thanks to extensive angle-resolved photo-emission and quantum oscillation measurements. This has facilitated the development of theoretical models describing the physics of  $\text{Sr}_3\text{Ru}_2\text{O}_7$  and  $\text{Sr}_2\text{RuO}_4$ , a more tractable task than in other strongly correlated systems such as the cuprate family of high-temperature superconductors whose normal

state is still not well understood.

States of correlated matter are generally classified in terms of their symmetries, and controllably altering the symmetry properties of the system can be a powerful probe. This can be achieved for instance by distorting the lattice by applying pressure, or applying a magnetic field along a chosen direction, to break translational or rotational symmetries which may have existed in the crystal lattice. In this thesis I describe experiments performed on  $\text{Sr}_3\text{Ru}_2\text{O}_7$  and  $\text{Sr}_2\text{RuO}_4$  using uni-axial strain as a means of lifting their tetragonal crystal symmetry. A specially designed probe incorporating piezo-electric stacks was used, which allows tensile and compressive strains to be applied to the sample, so that the symmetry of the system's response about zero strain can be studied.

The novel phase of  $\text{Sr}_3\text{Ru}_2\text{O}_7$  has already been shown to be sensitive to symmetry-breaking magnetic fields [4], so we expect symmetry-breaking strain to yield similarly large effects. For this experiment we applied strain along one of the in-plane axes, and measured the in-plane transport both parallel and perpendicular to the strain direction. In the case of  $\text{Sr}_2\text{RuO}_4$ , uni-axial strain provides a means for testing its superconducting order parameter, as symmetry-based predictions have been made for how a chiral  $p$ -wave state should be affected by strain [10]. We observed the evolution of the sample's superconducting transition temperature as a function of strain, by measuring its AC magnetic susceptibility. Through both of these experiments we show that the new strain technique used enables fine-tuning, with directional resolution, of the electronic properties of correlated electron materials.

This thesis is organized into seven chapters. Chapters 2 and 3 introduce the background physics relating to  $\text{Sr}_3\text{Ru}_2\text{O}_7$  and  $\text{Sr}_2\text{RuO}_4$  respectively. These chapters are structured such that they begin with a discussion of relatively general concepts, before gradually leading the reader towards more specialized topics relating to the compound studied, and finishing with a literature review of said compound. Next is Chapter 4, which describes the experimental techniques used for all of the measurements. This chapter begins with an introduction to the framework for describing deformations in a solid, namely the stress and strain tensors, followed by a description of the uni-axial strain probe which was designed and built for our experiments. Details of sample preparation and measurement methods, as well as the cryogenic platform used are also given. Chapters 5 and 6 present the results of our measurements on  $\text{Sr}_3\text{Ru}_2\text{O}_7$  and  $\text{Sr}_2\text{RuO}_4$  respectively, followed by a discussion of the data. Whereas the background chapter of  $\text{Sr}_3\text{Ru}_2\text{O}_7$  is before that of  $\text{Sr}_2\text{RuO}_4$  because it contains material which is relevant to the latter, the results chapter for  $\text{Sr}_2\text{RuO}_4$  is placed before that of  $\text{Sr}_3\text{Ru}_2\text{O}_7$  as this is the chronological order in which the experiments were carried out. The thesis ends with a chapter which summarizes the work carried out and results obtained, followed by an outlook towards possible future research directions.



## Chapter 2

# Quantum Criticality in $\text{Sr}_3\text{Ru}_2\text{O}_7$

The field of condensed matter physics is continuously evolving as a result of the discovery and prediction of new phenomena in solid state systems. This may seem surprising, as the basic ingredients which constitute the materials in question have been known for a long time: atomic nuclei, electrons, and the interactions between them. The existence of behaviours as exotic as heavy fermions or high-temperature superconductivity in the cuprates, suggests however that one cannot apply the reductionist approach and simply break such a system down into its constituent parts to understand it as a whole. Ever since Drude's model of electrical conduction in 1900, more and more sophisticated theories have had to be put forward to account for the collective phenomena of electrons in solids. Nevertheless despite this apparent complexity, a single-electron picture gives surprisingly good predictions for the properties of a wide range of metals. The reason for this was explained by Landau's Fermi liquid theory in a series of papers from 1956 to 1958 ([11–13]), where he showed that the elementary excitations of a system of interacting electrons are electron-like quasiparticles which obey Fermi statistics. The electron-electron interactions thus do not affect the functional form of most of the predictions from the single-electron model, and instead take the form of a renormalization factor. In fact, the results of Fermi liquid theory apply to such a variety of systems, that cases where it appears to break down are of particular interest. Systems where the predictions from Fermi liquid theory no longer hold include for example the normal state of the high-temperature cuprate superconductors and materials close to a quantum critical point [3].

I will begin this chapter by briefly reviewing the physics of non-interacting electron systems, before moving on to an overview of Fermi liquid theory and some of its main predictions. I will then discuss a selection of magnetic phenomena which can occur in a Fermi liquid, which are believed to be relevant for the material  $\text{Sr}_3\text{Ru}_2\text{O}_7$ . After introducing the concept of quantum criticality I will give a review of  $\text{Sr}_3\text{Ru}_2\text{O}_7$ , which is the subject of much of the experimental work described in Chapter 6. This

compound appears to host a magnetic-field-tuned quantum critical point, in the vicinity of which a phase with anomalous electronic properties forms. In the final part of this chapter, I will argue why uni-axial strain could yield important new insight on  $\text{Sr}_3\text{Ru}_2\text{O}_7$ 's novel phase.

## 2.1 Non-interacting electrons

Drude's model, published in 1900 [14], was one of the first to describe electron conduction in metals. It is a classical theory which considers a gas of electrons scattering elastically off of immobile ion cores. The velocity distribution of the electrons is assumed to be given by the Maxwell-Boltzmann distribution for an ideal gas. This however leads to a prediction of a contribution of  $\frac{3}{2}k_B$  per electron to the specific heat, which is not observed in experiment. This apparent paradox was resolved by the Sommerfeld model, which essentially replaced Maxwell-Boltzmann statistics by the Fermi-Dirac statistics required by quantum mechanics.

As a part of the development of quantum theory, it was realized that the energy states of electrons are quantized, and that electrons must obey the Pauli exclusion principle, meaning that two electrons cannot simultaneously occupy the same state. This causes them to "stack up" in energy, so that we can define a Fermi energy  $\varepsilon_F$  which marks the boundary between the occupied and unoccupied states at zero temperature. This stacking of the electrons is described by the Fermi distribution function:

$$f(\varepsilon_k) = \frac{1}{e^{(\varepsilon_k - \mu(T))/k_B T} + 1}. \quad (2.1.1)$$

$\mu(T)$  is the temperature-dependent chemical potential, which is equal to  $\varepsilon_F$  at  $T = 0$  K. The Fermi function is broadened for  $T > 0$  by a width  $\sim k_B T$ , which is small for most metals even at room temperature. The energy  $\varepsilon_k$  of a free electron with wave-vector  $k$  is given by the quadratic dispersion:

$$\varepsilon_k = \frac{\hbar^2 k^2}{2m}, \quad (2.1.2)$$

where  $m$  is the mass of the electron [15]. By solving the simple problem of a particle in a box of volume  $L^3$ , we find that the allowed  $k$ -states are quantized in units of  $(\frac{2\pi}{L})$ . Each  $k$ -state can be doubly occupied, accounting for the two possible spin states of the electron. From the dispersion relation (2.1.2), several properties can be defined, such as an effective mass of the electron:

$$m_{band} = \left( \frac{1}{\hbar^2 k} \frac{d\varepsilon_k}{dk} \Big|_{k_F} \right)^{-1} \quad (2.1.3)$$

and the so-called *Fermi velocity*:

$$v_F = \frac{1}{\hbar} \frac{d\varepsilon_k}{dk} \Big|_{k_F}. \quad (2.1.4)$$

$k_F$  is the Fermi wave-vector. For a gas of free non-interacting electrons, the effective mass  $m_{band}$  is simply the bare electron mass, and the momentum is given by  $p = m_{band}v = \hbar k$ . Using this simple model of a gas of electrons confined to a box and interacting only via the exclusion principle already allows one to resolve the specific heat paradox mentioned above, and calculate other properties such as the thermal conductivity which are in good agreement with experiment for many of the elements [15]. However such a simple model fails to describe several important phenomena observed in nature, such as why some materials are insulators. For this, one must introduce a crystal lattice and consider its effects on the electronic dispersion (2.1.2).

The presence of a lattice destroys the translational invariance of the system, meaning that the electron momentum  $p$  is no longer a good quantum number. Instead,  $p = \hbar k$  is referred to as the *crystal momentum*, to reflect the fact that this quantity does not in general represent the electron's momentum. The Fourier transform of the real-space lattice unit cell is the  $k$ -space<sup>1</sup> unit cell known as the *Brillouin zone*. In one limit, the crystal lattice is modelled by a periodic potential which is added as a weak perturbation to the single-electron Schrödinger equation. Calculating the electron energies perturbatively, one finds that gaps in the spectrum open up at the Brillouin zone boundaries. Hence the electronic dispersion is split up into a series of energy bands, and the behaviour of the system strongly depends on the filling of the bands and where the Fermi level lies in relation to the gaps. According to Bloch's theorem, the eigenstates of the single-electron Hamiltonian with a periodic potential have the form of a plane wave multiplied by a function with the same periodicity as the potential. A consequence of this is that all  $k$ -states can be mapped to the first Brillouin zone by reciprocal lattice vectors, meaning that a complete set of the system's electronic states is contained within it.

Alternatively, one could analyse the effect of the lattice by considering electrons which are tightly bound to an atomic nucleus, and calculating the shift in the atomic orbitals due to the presence of neighbouring atoms. This approach is, rather unsurprisingly, called the *tight-binding* method, and is, for example, useful for describing transition metals with partially filled  $d$ -orbitals. Whereas before we were treating the lattice as a small perturbation on the electron gas, here we are treating the overlap of the single atomic orbitals with neighbouring orbitals as a small perturbation. In both cases the system is excited by promoting an electron from just below the Fermi level to just above it. The excited electron leaves an empty state behind (*hole*), so we call this a particle-hole excitation.

It turns out that, using both the free electron model and the tight-binding model, we are able to describe quite a wide range of materials. This is a striking result, as throughout this section we have completely neglected electron-electron interactions, which one would naively assume should play an important role. To understand why the results derived from these non-interacting theories hold even in the presence of non-negligible interactions, we must turn to Landau's Fermi liquid theory.

---

<sup>1</sup> $k$ -space is also sometimes known as reciprocal space.

## 2.2 Fermi liquid theory

A central concept to Landau's Fermi liquid theory is that of *adiabatic continuity*. The basic assumption is that there is a one-to-one correspondence between the eigenstates in the non-interacting system and those in the interacting system. To picture this, one can imagine starting with a non-interacting gas of electrons, and slowly turning on an interaction potential. This will change the shape of the eigenstates by mixing of the original eigenstates, however the new eigenstates can still be mapped back to the original ones. This is important because it allows us to retain the framework developed in the single-particle picture where there is a Fermi surface and particle-hole excitations. In the interacting picture, the eigenstates do not correspond to single electrons, but rather to *quasiparticles* which are a collective excitation of the whole Fermi sea. Even though in the presence of interactions the electron distribution changes from that shown in Figure 2.1a to that in Figure 2.1b, the quasiparticle distribution function resembles that of Figure 2.1a, as the quasiparticles are labelled in terms of the non-interacting eigenstates. The fact that a discontinuity at  $\varepsilon_F$  in the electron distribution remains after interactions have been turned on is a direct consequence of adiabatic continuity.

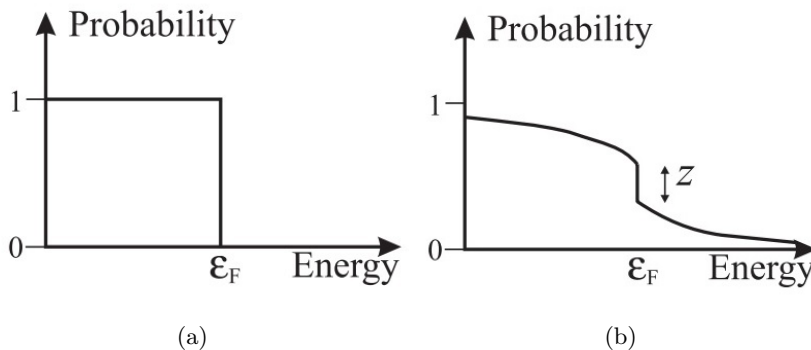


Figure 2.1: (a) The electron distribution as a function of energy in the case of a Fermi gas at  $T = 0$  K, described by equation (2.1.1). (b) The electron distribution changes when electron-electron interactions are slowly turned on. A discontinuity at  $\varepsilon_F$  remains, the height of which is called the quasiparticle weight  $Z$ . The smaller  $Z$  the stronger the electron-electron interactions. Taken from [3].

Quasiparticle excitations are not independent of one another, as when a quasiparticle is excited above the Fermi level, the rest of the Fermi liquid is displaced as a result of quasiparticle-quasiparticle interactions. The strength of the interaction is related to the quasiparticle's effective mass  $m^*$ , which can be many times larger than  $m_{band}$  calculated from the non-interacting electron dispersion (2.1.3):

$$m^* = \left(1 + \frac{F_1^s}{3}\right) m_{band}. \quad (2.2.1)$$

Thus the stronger the interactions, the greater  $m^*$ , and the more slowly a quasiparticle moves through the Fermi liquid. The so-called *Landau parameters*  $F_l^{s/a}$  characterize the quasiparticle interactions, and are related to thermodynamic quantities, meaning that they can be deduced from experiment. The presence of these interactions means that quasiparticles are not infinitely long-lived and that they must decay. Therefore to show that Fermi liquid theory provides a useful particle-like description of the system, we must consider the decay rate of the quasiparticles. Given a quasiparticle with energy  $\varepsilon$  above the Fermi surface, it can be shown via consideration of the Pauli principle and conservation of energy, that the number of final states which it can scatter into is proportional to  $\varepsilon^2$ . According to Fermi's golden rule, the scattering rate  $\Gamma$  is proportional to the number of final states, so we have the result:

$$\Gamma \sim \varepsilon^2. \quad (2.2.2)$$

Therefore quasiparticles are increasingly long-lived the closer they are to the Fermi level, meaning that Fermi liquid theory is an asymptotically correct approximation. In other words, because the quasiparticle energy goes as  $\sim \varepsilon$  and the scattering rate as  $\sim \varepsilon^2$ , we will always be able to find a temperature below which quasiparticles will be sufficiently long-lived to accurately describe the excitations of the interacting electron fluid. This is why Fermi liquid theory is particularly effective at low temperatures. A consequence of the  $\varepsilon^2$  scattering rate is a term of the form  $AT^2$ , where  $A$  is a constant, in the Fermi liquid's low-temperature resistivity [64].

Using the quasiparticle picture, one can derive various thermodynamic quantities, for example the specific heat  $C_v$  or the spin susceptibility  $\chi$  of an isotropic Fermi liquid [65]:

$$C_v = \frac{m^* k_F}{3\hbar^2} k_B^2 T, \quad (2.2.3)$$

$$\chi = \frac{m^*}{m_{band}(1 + F_0^a)} \chi_{band}. \quad (2.2.4)$$

The result for  $C_v$  is modified from that for non-interacting electrons by a renormalization factor of  $m^*/m_{band}$ , however the functional form is identical in both cases [15]. The spin susceptibility of a Fermi liquid is further enhanced by the Wilson ratio  $1/(1 + F_0^a)$ . More generally, Fermi liquid theory shows that a consequence of interactions is to renormalize most of the properties calculated in the non-interacting picture. This explains why the single-particle approximation works for such a variety of systems. Equation (2.2.3) shows that a Fermi liquid has a specific heat which is linear in temperature, allowing one to define the Sommerfeld coefficient  $\gamma = C_v/T$  which is proportional to the effective mass. In the case of a real material where more than one band crosses the Fermi surface, each band may be renormalized in a different way via its own set of Landau parameters. This however only leads to a quantitative change in the predictions, rather than a change in the functional form.

The power of Fermi liquid theory resides in its ability to describe the behaviour of a broad range of systems, using only a small number of parameters which characterize the quasiparticle interactions. The robustness of Fermi liquid theory can

be illustrated for example by heavy fermion compounds, which exhibit very strong correlations. In these materials the effective mass can be more than one hundred times the bare electron mass, such as in UPt<sub>3</sub> [16]. Even in this extreme case, predictions from Fermi liquid theory hold and quasiparticles are an accurate description of the system's eigenstates. Systems in which Fermi liquid theory breaks down are therefore particularly interesting, as a new framework for describing excitations is required.

## 2.3 Magnetism in an itinerant electron system

In this section, we will give a brief overview of a selection of magnetic phenomena which can occur in a system of itinerant electrons. We will begin by a study of the paramagnetic state, before moving on to describe metamagnetism and finally the spin-density wave state, each of which is believed to be relevant for the compound Sr<sub>3</sub>Ru<sub>2</sub>O<sub>7</sub>.

### 2.3.1 Pauli paramagnetism

Let us consider the magnetic moments of the delocalized conduction electrons in a metal in an applied field. In the paramagnetic state we can calculate the contribution of the conduction electrons to the sample's magnetization using a simple non-interacting model, the results of which can later be extended to the interacting case using Fermi liquid theory. For simplicity let us neglect the coupling between the electron's orbital motion and the magnetic field. The total magnetization  $M$  of the sample is proportional to the difference between the number of electrons with spin aligned with the applied field ( $\uparrow$ ) and those anti-aligned with it ( $\downarrow$ ):

$$M = \mu_B(n_\uparrow - n_\downarrow), \quad (2.3.1)$$

where  $\mu_B$  is the Bohr magneton. The energy of spin-up electrons is shifted by  $-\mu_B H$  and that of the spin-down electrons by  $+\mu_B H$  for an applied field  $H$ . However, in thermal equilibrium the chemical potential must remain constant, meaning that the spin-down electrons with energy between  $\varepsilon_F$  and  $(\varepsilon_F - 2\mu_B H)$  are spin-flipped. This leads to a net magnetization of the sample. In the limit where the shift in energy  $\mu_B H$  is small compared to  $\varepsilon_F$ , we can approximate the number of spin-flipped electrons as  $\Delta n = \mu_B g(\varepsilon_F) H$ , where  $g(\varepsilon_F)$  is the density of states at the Fermi level (see for example [15]). Hence from (2.3.1) we obtain  $M = \mu_B^2 g(\varepsilon_F) H$  which allows us to define the Pauli susceptibility:

$$\chi_s = \mu_B^2 g(\varepsilon_F). \quad (2.3.2)$$

Even in the absence of an external magnetic field, the paramagnetic state can be unstable to the formation of a state with non-zero magnetization. If we imagine exciting electrons within  $\delta\varepsilon$  of  $\varepsilon_F$  by spin-flipping them, the Fermi level of the spin-up electrons will increase due to the exclusion principle. The number of excited

electrons is  $\frac{1}{2}g(\varepsilon_F)\delta\varepsilon$ , meaning that the increase in kinetic energy of the system is [17]:

$$\Delta F_{kin} = \frac{1}{2}g(\varepsilon_F)(\delta\varepsilon)^2. \quad (2.3.3)$$

However the increase in kinetic energy is offset by a gain in potential energy. Indeed, due to the net magnetization  $M$  of the system, the electron spins experience a molecular field  $\lambda M$  which reduces the total energy by an amount  $\frac{1}{2}\mu_0\lambda M^2$ . Using equation (2.3.1), we can rewrite the gain in potential energy as:

$$\Delta F_{exc} = -\frac{1}{2}I(g(\varepsilon_F)\delta\varepsilon)^2, \quad (2.3.4)$$

where  $I = \mu_0\mu_B^2\lambda$  is a constant describing the strength of the interaction, corresponding to the potential energy in the Hubbard Hamiltonian. The condition for ferromagnetic ordering to be stable is therefore that the total change in the magnetic part of the free energy be negative:

$$\Delta F_M = \Delta F_{kin} + \Delta F_{exc} = \frac{1}{2}g(\varepsilon_F)\delta\varepsilon^2(1 - Ig(\varepsilon_F)) \leq 0. \quad (2.3.5)$$

This condition leads to what is known as the *Stoner criterion* for ferromagnetism [17]:

$$Ig(\varepsilon_F) \geq 1. \quad (2.3.6)$$

In other words, an itinerant paramagnet will be unstable towards a state with net magnetization if it has a high density of states at the Fermi level, and/or a strong interaction term  $I$ .

### 2.3.2 Itinerant metamagnetism

A metamagnetic transition is an abrupt first order transition in magnetic field to a state of higher magnetization. Let us consider a simple model which illustrates how such a phenomenon can occur, in analogy to the discussion in Section 2.3.1. If an itinerant electron system has a peak in its density of states just below the Fermi energy, this peak can be made to move through the Fermi level by the application of a magnetic field  $H$ . Indeed, a magnetic field will split the Fermi surface into two spin-polarized Fermi surfaces, with an energy splitting  $2\mu_B H$ . The energy of the spin-up Fermi surface is lowered, whilst that of the spin-down Fermi surface is increased. Therefore by increasing the field, the peak in the spin-down density of states will cross the Fermi energy, causing an increase in  $g(\varepsilon_F)$  and satisfying the Stoner criterion (2.3.6) within a narrow field range. As we will see in Section 2.5, this kind of scenario may turn out to be particularly relevant for the compound  $\text{Sr}_3\text{Ru}_2\text{O}_7$ , as it is believed to have a peak in the density of states just below the Fermi level.

A more general approach for describing metamagnetism is to consider the free energy expansion of an itinerant system in powers of its magnetization  $M$  [18]:

$$F(M) = \frac{\alpha(T)}{2}M^2 + \frac{\beta(T)}{4}M^4 + \frac{\gamma(T)}{6}M^6 - HM. \quad (2.3.7)$$

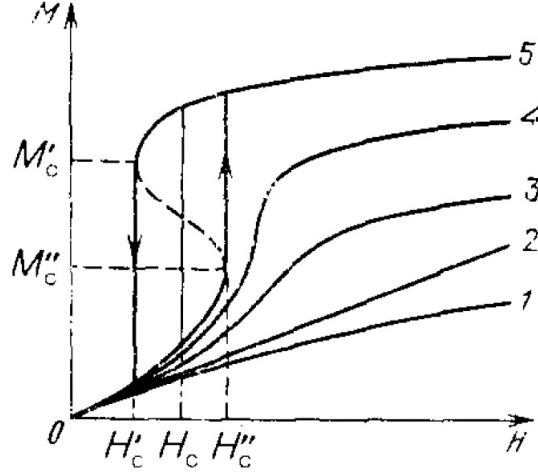


Figure 2.2: Plot of magnetization isotherms for different values of  $\beta(T)$  and  $\gamma(T)$  from equation (2.3.8). Curve 1 shows  $M(H)$  for  $\beta(T) > 0$  and  $\gamma(T) > 0$ , corresponding to the normal paramagnetic state. Curve 2 is for  $\beta(T) = \gamma(T) = 0$ . Curves 3-5 are for different values of  $\beta(T)$  and  $\gamma(T)$  with  $\beta(T) < 0$  and  $\gamma(T) > 0$ . Metamagnetism is illustrated by curve 5, where there is a first order jump in the magnetization with field, the arrows illustrating how the magnetization depends on the direction of the field sweep. Taken from ref. [18].

The coefficients  $\alpha(T)$ ,  $\beta(T)$  and  $\gamma(T)$  are related to the density of states  $g(\varepsilon)$  near the Fermi level. If  $\alpha(T) < 0$ , there is a minimum in the free energy for a non-zero  $M$  and the system is ferromagnetic. The Stoner criterion can therefore be rewritten as  $\alpha(T) \leq 0$ . The sign of  $\beta(T)$  determines whether the transition is first or second order. If it is negative, the transition is first order, and we require the sixth order term to ensure that the free energy does not diverge. Let us consider the paramagnetic state, i.e.  $\alpha(T) > 0$ . Minimizing the free energy in (2.3.7) gives us:

$$H = \alpha(T)M + \beta(T)M^3 + \gamma(T)M^5. \quad (2.3.8)$$

From this result we can see that, depending on the values of coefficients  $\beta(T)$  and  $\gamma(T)$ ,  $M(H)$  may not always be single valued, which is un-physical. This is illustrated in Figure 2.2 where magnetization isotherms for different values of  $\beta(T)$  and  $\gamma(T)$  are shown. Curve number 5 shows  $M(H)$  for  $\beta(T) < 0$  and  $\gamma(T) > 0$ , where between the fields  $H_c'$  and  $H_c''$   $M(H)$  has three possible values. In this situation, the system's magnetization depends on the direction in which the field is being swept, as illustrated by the arrows. As the field is swept up, the magnetization increases smoothly before making a first order jump at  $H_c''$  to a state of enhanced magnetization. When sweeping down in field, the system drops sharply at  $H_c' < H_c''$  back into the paramagnetic state. The dependence of the transition field on the direction of the field sweep results in a measurable hysteresis of width  $H_c'' - H_c'$ .

### 2.3.3 Spin-density wave

We saw in Section 2.3.1 how a system of itinerant electrons can be tipped into the ferromagnetic state when the Stoner criterion (2.3.6) is satisfied. In the ferromagnetic state, the electron spin density is constant in space, so the spin modulation wave-vector is  $q = 0$ . The Stoner criterion can be generalized to the  $q \neq 0$  case, so that it also describes antiferromagnetic instabilities [17]:

$$\chi(\mathbf{q})I \geq 1, \quad (2.3.9)$$

where  $\chi(\mathbf{q})$  is the wave-vector-dependent susceptibility. The Stoner criterion for ferromagnetism is given by setting  $q = 0$ , in which case conditions (2.3.6) and (2.3.9) become equivalent. Therefore according to the generalized Stoner criterion (2.3.9), antiferromagnetism can occur even with a small  $I$ , if the susceptibility is large enough for a particular wave-vector.

The susceptibility  $\chi(\mathbf{q})$  depends on the geometry of the Fermi surface. In particular  $\chi(\mathbf{q})$  diverges at a particular wave-vector  $\mathbf{Q}$  if two or more sections of the Fermi surface are connected by  $\mathbf{Q}$ , in other words if  $\varepsilon_{\mathbf{k}+\mathbf{Q}} = \varepsilon_{\mathbf{k}}$ . This is known as *nesting* of the Fermi surface. The new periodicity of wave-vector  $\mathbf{Q}$  enables the system to lower its energy by opening up an energy gap on the nested portions of the Fermi surface. The nested portions of the Fermi surface are therefore “removed” from the Fermi sea, causing a reduction in the conduction due to the loss of charge carriers. The magnetization of the system oscillates in space, as described by the following:

$$\mathbf{M}(\mathbf{r}) = \mathbf{M}_0 e^{i\mathbf{Q}\cdot\mathbf{r}}. \quad (2.3.10)$$

$\mathbf{r}$  is the position of the spin, and  $\mathbf{M}_0$  a constant giving the magnitude of the ordered moment. Such a state is known as a *spin-density wave* (SDW) state.

Spin-density waves were first predicted by Overhauser in 1962 [19], who showed that the paramagnetic state of a system of interacting electrons is unstable to the formation of a spin-density wave at  $\mathbf{Q} = 2\mathbf{k}_F$ . A famous example of an experimentally observed SDW state is in chromium [20], where the SDW appears below a Néel temperature of 311 K. The SDW state can be studied using a variety of different experimental probes, such as resistivity, specific heat or neutron diffraction. The last is particularly useful in determining the spatial structure of the density wave, as neutrons are sensitive to the magnetic moments of the electrons.

## 2.4 Quantum criticality

In section 2.2 we described how Fermi liquid theory could be used to describe a wide range of interacting electron systems. Even in extreme cases such the heavy fermion compounds where the effective quasiparticle mass can be more than 100 times greater than that of the bare electron, Fermi liquid theory holds. Understanding cases in which Fermi liquid theory breaks down has therefore become a central problem in condensed matter research. In particular, quantum critical systems are

a strong focus of experimental and theoretical investigation, as exotic phases such as unconventional superconductivity are often stabilized in the vicinity of a quantum critical point (QCP). An understanding of the physics of quantum criticality could therefore provide a unified framework for describing a diverse range of strongly correlated electron phenomena.

The usual way of reaching a QCP is by suppressing a second order phase transition down to zero temperature, using some external tuning parameter. A second order phase transition will occur at a critical temperature  $T_c$ , generally between a high-temperature disordered state and a low-temperature ordered state. The ordered state is defined by some order parameter which grows continuously from zero at  $T_c$  up to its low temperature value, such as magnetization in the case of a ferromagnetic transition. A second order phase transition corresponds to the breaking of some symmetry between the high- and low-temperature phases. As  $T_c$  is approached from either above or below, spatial fluctuations of the order parameter slow down, as their correlation length  $\xi$  and time  $\tau$  diverge. By considering the uncertainty principle  $\Delta E \Delta t \geq \hbar$ , we can show that quantum fluctuations will occur on a time-scale  $\tau_{quant} \approx \hbar/k_B T$  at temperature  $T$ ; for the spatial fluctuations  $\tau \propto \xi^z = (|T - T_c|/T_c)^{-z\nu}$ , where  $\nu$  and  $z$  are critical exponents. As the frequency of spatial fluctuations  $\omega = 1/\tau$  goes to zero as  $T \rightarrow T_c$ , we will always be able to satisfy  $k_B T \gg \hbar \omega$  for  $T$  close enough to  $T_c$ ; in other words the system appears to be static and the phase transition can be treated classically using Landau theory. In fact, as long as  $T_c > 0$  the second order phase transition can be treated classically sufficiently close to  $T_c$ .

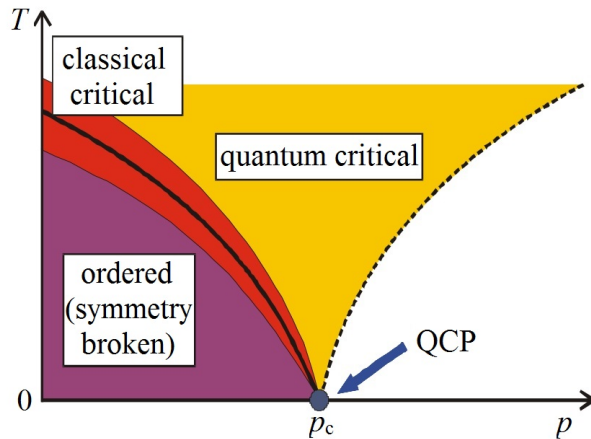


Figure 2.3: Sketch of the phase diagram around a generic quantum critical point (QCP). A second order phase transition, shown by the thick black line, is suppressed via some tuning parameter  $p$ . The region in which the classical theory of second order phase transitions is valid is shown in red. At a critical value  $p_c$ ,  $T_c$  is driven to zero giving rise to a QCP. Taken from ref. [21].

From the simple arguments given above, we can see that if  $T_c$  is suppressed to zero,  $\tau_{quant}$  diverges meaning that the region in which the classical treatment is valid shrinks to zero. In this case the fluctuations associated with the phase transition are purely quantum mechanical, hence the name quantum critical point. A phase diagram is shown in Figure 2.3, where a second order phase transition is suppressed to zero temperature using the tuning parameter  $p$ . In practice,  $p$  is often pressure or chemical doping. In the region above the QCP, shown in yellow in Figure 2.3, fluctuations which are governed by the QCP are thermally activated, explaining why the region broadens with temperature. It is in this part of the phase diagram where Fermi liquid theory is observed to break down and quasiparticles are no longer thought to be an accurate description of the system's excitations.

General predictions can be made for the properties of systems in the vicinity of a QCP [3]. For instance the specific heat is expected to diverge as  $C_v/T \sim -\ln T$  at the critical tuning  $p_c$ , corresponding to a diverging effective mass. The scattering rate is modified from the  $\varepsilon^2$  dependence of Fermi liquid theory, resulting in a resistivity that no longer has a  $T^2$  dependence. These signatures are observed in many different quantum critical systems, such as  $\text{YbRh}_2\text{Si}_2$  [22] or  $\text{CePd}_2\text{Si}_2$  [23], both of which display a temperature exponent in the resistivity close to unity at critical tuning. In both cases an antiferromagnetic phase transition is tuned to zero, the tuning parameter being magnetic field and pressure for  $\text{YbRh}_2\text{Si}_2$  and  $\text{CePd}_2\text{Si}_2$  respectively. At low temperatures, a superconducting phase appears around where  $\text{CePd}_2\text{Si}_2$ 's QCP is believed to exist, thus “masking” the QCP.

### 2.4.1 Quantum critical end-point

In the previous discussion of quantum criticality, a key ingredient for producing a QCP was a second order phase transition which gives rise to a diverging susceptibility of the order parameter as  $T_c$  is approached. First order phase transitions on the other hand, which correspond to a discontinuous jump in the order parameter but do not break any symmetry, are not a source of order parameter fluctuations and diverging susceptibilities. Hence one would expect that first order phase transitions cannot lead to quantum criticality.

However, because a first order transition does not have to break any symmetry, the low-temperature discontinuous jump in the order parameter can become a continuous crossover at higher temperatures. This allows us to define a critical end-point at the end of the line of first order phase transitions. A well known example of this is the liquid-gas transition in water, where density plays the role of the order parameter. At low pressures and temperatures there is a first order phase transition as the density abruptly changes between the liquid and gas phases, up until a critical point beyond which there is no longer a phase transition between the two. At the critical point the transition becomes second order, meaning that the susceptibility diverges, and the system is governed by fluctuations. Hence a critical point possesses the key ingredient for leading to quantum criticality, the difference being that it is not associated with a broken symmetry.

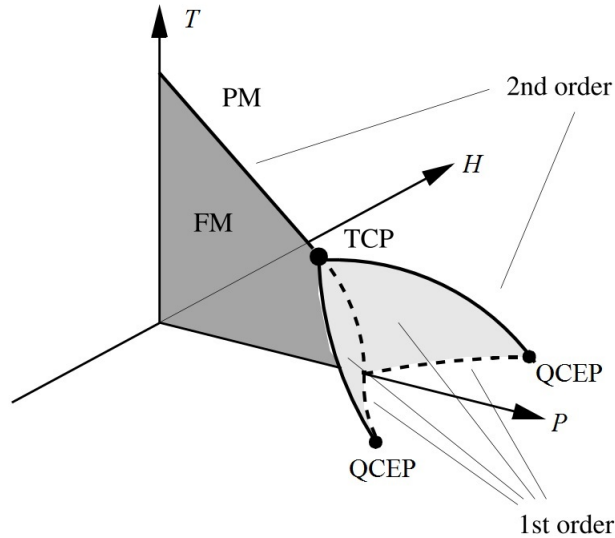


Figure 2.4: Phase diagram of an itinerant ferromagnet near a tricritical point (TCP). The second order paramagnetic (PM) to ferromagnetic (FM) phase transition is suppressed with pressure  $P$  and becomes first order beyond the TCP. The application of a magnetic field  $H$  causes “wings” of first order metamagnetic transitions to extend outwards from the TCP, bounded by lines of critical points. The lines of critical points intersect with the  $T = 0$  K plane to form quantum critical end-points (QCEP). Adapted from ref. [24].

One can therefore imagine a scenario where a critical point is suppressed to zero temperature via some tuning parameter, leading to a quantum critical end-point (QCEP). Such a phenomenon is believed occur in itinerant ferromagnets such as  $\text{UGe}_2$  or  $\text{MnSi}$  [24]. At zero applied field  $H$ , a second order phase transition is observed between the paramagnetic and ferromagnetic states at the Curie temperature  $T_c$ . This second order transition is suppressed by the application of pressure  $P$ , until a tricritical point is reached beyond which the transition becomes first order. The application of a magnetic field induces a net magnetization in the system, thus breaking the symmetry associated with the second order transition so that it can no longer take place. However, as there is no symmetry related to the first order transition, lines of critical points extend outwards in field from the tricritical point, bounding surfaces of first order transitions. These surfaces correspond to jumps in the magnetization, i.e. metamagnetic transitions (as described in Section 2.3.2). At particular  $(P, H)$  points, the lines of critical points cross the  $T = 0$  K surface, giving rise to a QCEP. The generic phase diagram of these itinerant ferromagnets is illustrated in Figure 2.4. As we shall see in section 2.5, there is significant experimental evidence that quantum criticality in the compound  $\text{Sr}_3\text{Ru}_2\text{O}_7$  is associated with the suppression of the critical end-point of a metamagnetic transition, however in its

case the tuning parameter is the magnetic field angle.

## 2.5 The physics of $\text{Sr}_3\text{Ru}_2\text{O}_7$

Now that we have covered some of the general concepts relating to interacting electron systems, let us turn our attention to  $\text{Sr}_3\text{Ru}_2\text{O}_7$ .  $\text{Sr}_3\text{Ru}_2\text{O}_7$  is the  $n = 2$  member of the Ruddlesden-Popper series  $\text{Sr}_{n+1}\text{Ru}_n\text{O}_{3n+1}$ , of which  $\text{Sr}_2\text{RuO}_4$  (described in Section 3.5) is the  $n = 1$  member. Whereas  $\text{Sr}_2\text{RuO}_4$  undergoes a superconducting transition at 1.5 K,  $\text{Sr}_3\text{Ru}_2\text{O}_7$  remains an enhanced paramagnet down to low temperatures, with a large Wilson ratio of  $\sim 10$  [25]. Below 10 K,  $\text{Sr}_3\text{Ru}_2\text{O}_7$  exhibits conventional Fermi liquid behaviour, with a  $T^2$  dependent resistivity. It also appears to be close to a ferromagnetic instability, as evidenced by a transition to ferromagnetism with an applied pressure of around 1 GPa [25].  $\text{Sr}_3\text{Ru}_2\text{O}_7$  has attracted much attention since its discovery, as it provides an example of a magnetic field-tuned QCP, in the vicinity of which a phase with anomalous electronic properties is found.

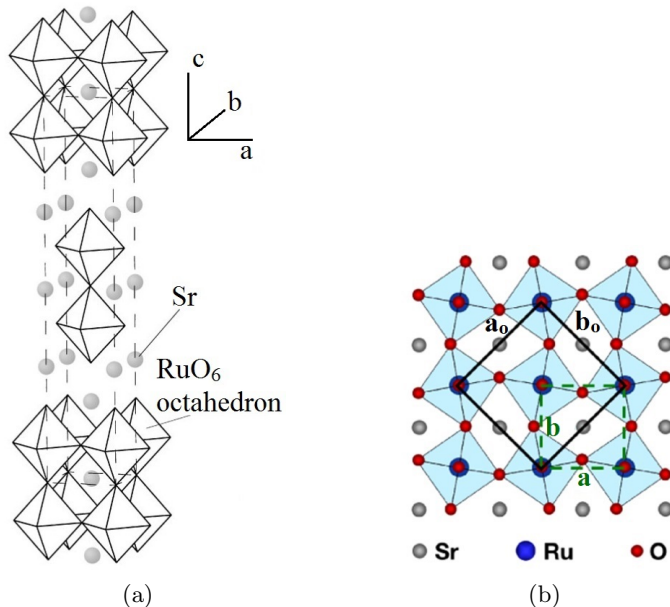


Figure 2.5: (a) Crystal structure of  $\text{Sr}_3\text{Ru}_2\text{O}_7$ , showing the bi-layers of  $\text{RuO}_6$  octahedra spaced by Sr atoms. Adapted from ref. [27]. (b) Sketch of a plane formed by a single layer of  $\text{RuO}_6$  octahedra. The counter-rotation of adjacent octahedra leading to the doubling of the unit cell is illustrated.  $a_o$  and  $b_o$  denote the orthorhombic lattice constants.  $a$  and  $b$  represent the Ru-Ru nearest-neighbour distances, in analogy to  $\text{Sr}_2\text{RuO}_4$ 's lattice vectors. Adapted from ref. [28].

Like  $\text{Sr}_2\text{RuO}_4$ ,  $\text{Sr}_3\text{Ru}_2\text{O}_7$  is a highly two dimensional material. It is formed of bi-layers of corner-sharing  $\text{RuO}_6$  octahedra, which are spaced by Sr atoms, as shown

in Figure 2.5a. The anisotropy of the crystal structure is reflected by the resistive anisotropy, which is  $\rho_c/\rho_{ab} \approx 300$  at 0.3 K [25]. However, unlike  $\text{Sr}_2\text{RuO}_4$ ,  $\text{Sr}_3\text{Ru}_2\text{O}_7$  is orthorhombic with Bbcb symmetry, rather than tetragonal. This is caused by a counter-rotation of adjacent  $\text{RuO}_6$  octahedra about the  $c$ -axis by an angle of  $7.85^\circ$  [26], which results in a  $\sqrt{2} \times \sqrt{2}$  reconstruction of the unit-cell in the  $ab$ -plane, as illustrated by Figure 2.5b. The direction of the rotation alternates between the two planes within a single bi-layer. The lattice parameters, as measured by neutron scattering, are  $a_o = 5.4979 \text{ \AA}$ ,  $b_o = 5.5008 \text{ \AA}$  and  $c = 20.7327 \text{ \AA}$  [26]. Even though the rotation of the octahedra, which gives rise to the difference between the in-plane lattice parameters of 5 parts in  $10^4$ , cannot be detected by X-ray diffraction, it has a significant effect on the material’s electronic structure as discussed in Section 2.5.1. For simplicity, for the remainder of this thesis we will use the same convention for the in-plane crystal axes as with  $\text{Sr}_2\text{RuO}_4$ : the direction of the nearest-neighbour Ru-Ru bonds shown by  $a$  and  $b$  in Figure 2.5b. Hence the [100] and [010] labels each refer to one of the two orthogonal in-plane nearest-neighbour Ru-Ru directions, for both  $\text{Sr}_2\text{RuO}_4$  and  $\text{Sr}_3\text{Ru}_2\text{O}_7$ . For the experimental work described in Section 6, we will treat the [100] and [010] directions as equivalent. Indeed, the small difference in lattice constant between the two directions cannot be detected by X-ray diffraction or resistivity, which are the two probes which we use to study the  $\text{Sr}_3\text{Ru}_2\text{O}_7$  crystals. Moreover, the physics studied is not believed to be a consequence of  $\text{Sr}_3\text{Ru}_2\text{O}_7$ ’s slight orthorhombicity, as will be discussed further on.

### 2.5.1 Electronic structure

The Fermi surface of  $\text{Sr}_3\text{Ru}_2\text{O}_7$  can be derived using that of  $\text{Sr}_2\text{RuO}_4$ , which is described in detail in Section 3.5.1, as a starting point [29]. As for  $\text{Sr}_2\text{RuO}_4$ , we assume that the Fermi surface arises predominantly from the Ru  $4d$  bands crossing the Fermi level. Following the arguments given in Section 3.5.1, this gives rise to pairs of nearly flat sheets with  $d_{xz}$  and  $d_{yz}$  character and a circular sheet with  $d_{xy}$  character, as shown in Figure 2.6a. These sheets hybridize to give the  $\alpha$ ,  $\beta$  and  $\gamma$  bands which make up  $\text{Sr}_2\text{RuO}_4$ ’s Fermi surface, as shown in Figure 2.6b. Our next assumption is that the bi-layer in  $\text{Sr}_3\text{Ru}_2\text{O}_7$  causes a splitting of the bands, in other words the number of bands doubles without affecting the two-dimensional coupling between the bi-layers (Figure 2.6c). At the points where the sheets originating from the  $d_{xz}$  and  $d_{yz}$  orbitals cross, hybridization gaps open up causing the sheets to reconnect. The resulting Fermi surface, shown in Figure 2.6d, is what that of  $\text{Sr}_3\text{Ru}_2\text{O}_7$  would look like without the unit-cell reconstruction. However, due to the  $\sqrt{2} \times \sqrt{2}$  reconstruction, the area of the Brillouin zone is halved and rotated by  $45^\circ$ , as indicated by the dashed line in Figure 2.6e. The portions of the Fermi surface lying outside of the reconstructed Brillouin zone must therefore be “backfolded” into the zone, leading to the complex Fermi surface depicted in Figure 2.6e. This Fermi surface contains many band crossings, therefore in order to predict the manner in which the bands will reconnect it is necessary to turn to experiment or calculations.

Both ARPES [28] and quantum oscillation [30] measurements find six closed

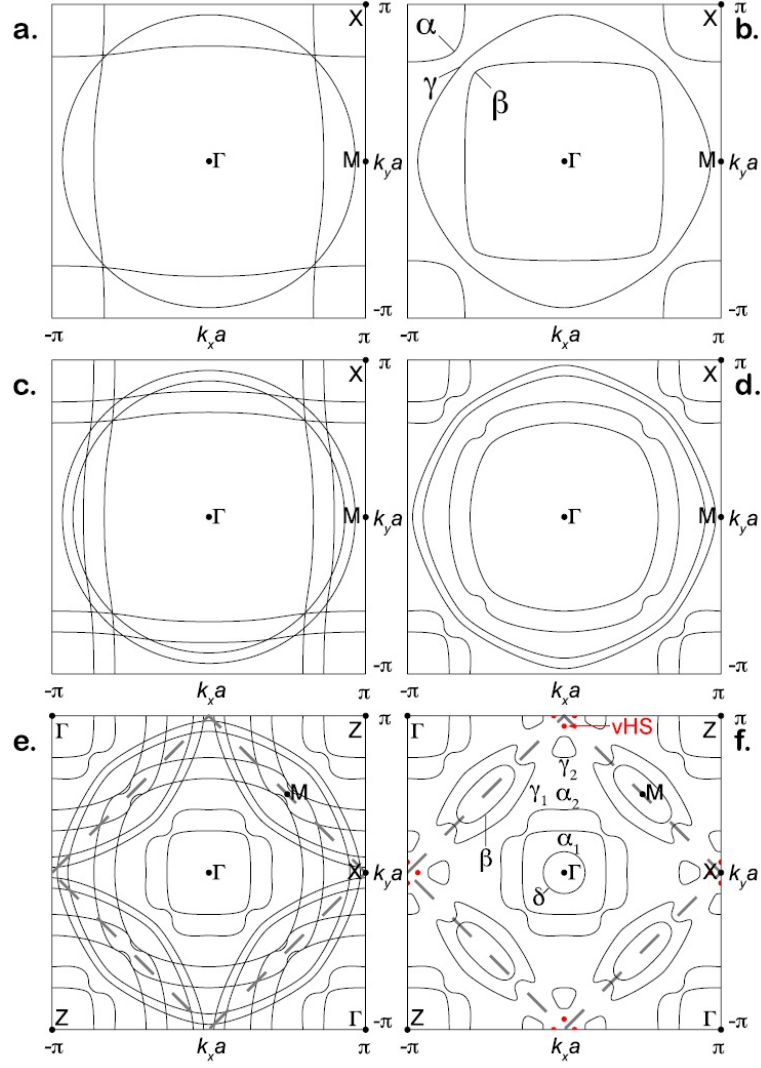


Figure 2.6: (a)(b) Sketch of how Sr<sub>2</sub>RuO<sub>4</sub>'s Fermi surface is derived from the  $d_{xy}$ ,  $d_{xz}$  and  $d_{yz}$  orbitals, as discussed in Section 3.5.1. (c) The bi-layer splitting of the bands, (d) and how they reconnect. (e)  $\sqrt{2} \times \sqrt{2}$  reconstruction of the Brillouin zone causes a backfolding of the Fermi surface. (f) The Fermi surface of Sr<sub>3</sub>Ru<sub>2</sub>O<sub>7</sub>, as measured by ARPES and dHvA. The red dots indicate the presence of van Hove singularities. For each figure the full size of the panel corresponds to the size of Sr<sub>2</sub>RuO<sub>4</sub>'s Brillouin zone. Figures taken from ref. [29].

orbits, which are shown in Figure 2.6f. Each of the Fermi surface sheets is labelled to indicate which of the Sr<sub>2</sub>RuO<sub>4</sub> sheets it derives from. In the centre of the Brillouin zone are square- and cross-shaped hole pockets,  $\alpha_1$  and  $\alpha_2$  respectively, each with  $d_{xz}$  and  $d_{yz}$  character. At the M-point, two elongated electron pockets  $\gamma_1$  and  $\beta$  result

from hybridization between the  $d_{xy}$  and  $d_{xz}$ ,  $d_{yz}$  orbitals. A fifth pocket,  $\delta$ , which is centred at the  $\Gamma$  point, has no analogue in  $\text{Sr}_2\text{RuO}_4$ , as it derives from the  $d_{x^2-y^2}$  orbital (as indicated by LDA calculations [28]) which is unoccupied in  $\text{Sr}_2\text{RuO}_4$ . The sixth pocket is a small hole-type pocket labelled  $\gamma_2$  with predominantly  $d_{xy}$  character, and located near the X-point. The resolution of the ARPES measurement is not high enough to distinguish unambiguously whether the  $\gamma_2$  pocket crosses the Fermi level or lies just below it. The measurement is made difficult because of the small area of the pocket (which also makes it hard to detect using dHvA), and the very weak band dispersion in that part of the Brillouin zone. From the experimental data, the  $\gamma_2$  pocket is expected to lie within 1 meV of the Fermi level.

Despite their small size, the  $\gamma_2$  pockets appear to play an important role in the physics of  $\text{Sr}_3\text{Ru}_2\text{O}_7$ . Indeed, ARPES measurements have shown that there are a pair of peaks (referred to as van Hove singularities) in  $\gamma_2$ 's density of states, which are believed to lie 1 meV and 4 meV respectively below the Fermi level [28]. As we will see in Section 2.5.2,  $\text{Sr}_3\text{Ru}_2\text{O}_7$  undergoes a metamagnetic transition in an applied magnetic field corresponding to an energy scale of  $\sim 1$  meV, which has led to the speculation that the metamagnetism is driven by the  $\gamma_2$  pockets. Moreover, the  $\gamma_2$  pocket appears essential in explaining the compound's thermodynamic properties. Indeed, according to estimates of the band masses from quantum oscillation measurements,  $\gamma_2$  would account for  $\sim 45\%$  of the total low temperature specific heat [29].

### 2.5.2 Metamagnetism & quantum criticality

As mentioned previously,  $\text{Sr}_3\text{Ru}_2\text{O}_7$  is a strongly enhanced paramagnet close to a ferromagnetic instability, so it is no large surprise that the application of a magnetic field induces a metamagnetic transition. It was shown experimentally that a metamagnetic transition occurs at a field of approximately 5 T when the field lies in the  $ab$ -plane [31]. The magnetization of  $\text{Sr}_3\text{Ru}_2\text{O}_7$  is plotted against field for a series of different temperatures in Figure 2.7a. The jump in the magnetization is well defined at low temperatures, and becomes broadened at higher temperatures. It was later found that sample purity plays a large role in the observed physics, as illustrated in Figure 2.7b, where two separate metamagnetic jumps can be resolved at 5 T and 5.8 T for a high-purity sample with a residual resistivity  $\rho_{res} = 0.5 \mu\Omega\text{cm}$  [32].

Interestingly, it was demonstrated that the field at which the metamagnetic transition takes place depends on the orientation of the applied field. This was shown by Grigera et al. who performed a systematic study of the angular dependence of the AC magnetic susceptibility in  $\text{Sr}_3\text{Ru}_2\text{O}_7$  [33]. The AC magnetic susceptibility, which is defined as  $\chi_{ac} = dM/dH_{ac}$  in a small oscillating excitation field  $H_{ac}$ , exhibits a peak in its real part when there is a sudden increase of the magnetization. In the case of a first order transition, such as a metamagnetism, there is also a peak in the imaginary part of  $\chi_{ac}$  which is related to dissipation due to the transition's hysteresis. In this way, by measuring the temperature  $T^*$  at which the imaginary component of  $\chi_{ac}$  vanishes, Grigera et al. were able to determine the critical end-

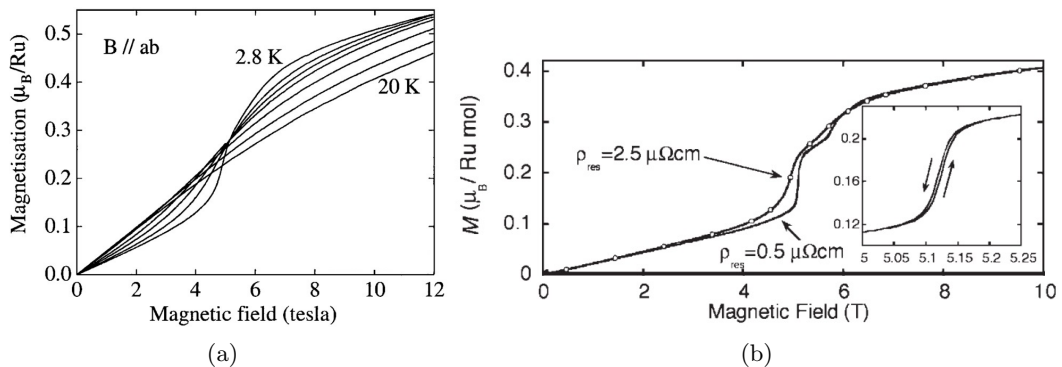


Figure 2.7: (a) Plot of the sample magnetization against magnetic field for temperatures ranging between 2.8 K and 20 K. From ref. [31]. (b) When the sample purity is increased so that  $\rho_{res} = 0.5 \mu\Omega\text{cm}$ , two metamagnetic transitions are resolved: one at 5 T and one at 5.8 T. The inset shows the hysteresis of the lower transition, confirming the first order nature of the transition. Taken from ref. [32].

point of the metamagnetic transition as a function of applied field and field angle. Rotating the field from the  $ab$ -plane towards the  $c$ -axis,  $T^*$  is suppressed from 1.2 K to below the lowest measured temperature (50 mK in this experiment). Moreover, the critical field increases smoothly from  $\sim 5$  T to  $\sim 8$  T during this rotation. This tuning of the critical end-point is illustrated in Figure 2.8a, where the thick black line represents the locii of the end-points, and the green surface the metamagnetic transitions. As argued in Section 2.4.1, one expects the suppression of a critical end-point to zero temperature to lead to a QCEP, and indeed many signatures of quantum criticality have been observed in  $\text{Sr}_3\text{Ru}_2\text{O}_7$ . In the present case, the tuning parameter would be the field angle, with critical tuning being when the field is aligned along the  $c$ -axis.

One of the earliest signatures of quantum criticality observed in  $\text{Sr}_3\text{Ru}_2\text{O}_7$  was seen in the magneto-resistivity [34]. Sample resistivity was measured as a function of temperature at a series of different fields (applied along the  $c$ -axis), and analyzed using the following formula:

$$\rho(T, H) = \rho_{res}(H) + A(H)T^\alpha. \quad (2.5.1)$$

The assumption is that the sample resistivity is a combination of a temperature-independent term  $\rho_{res}$  due to impurity scattering, and a term with a power law dependence on temperature. As mentioned in Section 2.2, a Fermi liquid typically has  $\alpha = 2$ , whilst in the proximity of a quantum critical point this is no longer expected to be the case. The data are shown in Figure 2.8b, where the temperature exponent  $\alpha$  is plotted in the (field, temperature) plane. The temperature below which Fermi liquid-like behaviour is observed (shown in blue) decreases with field and shrinks below the lowest measured temperature in the vicinity of the putative quantum critical end-point at  $H_c \approx 8$  T. Extending to high temperature above the

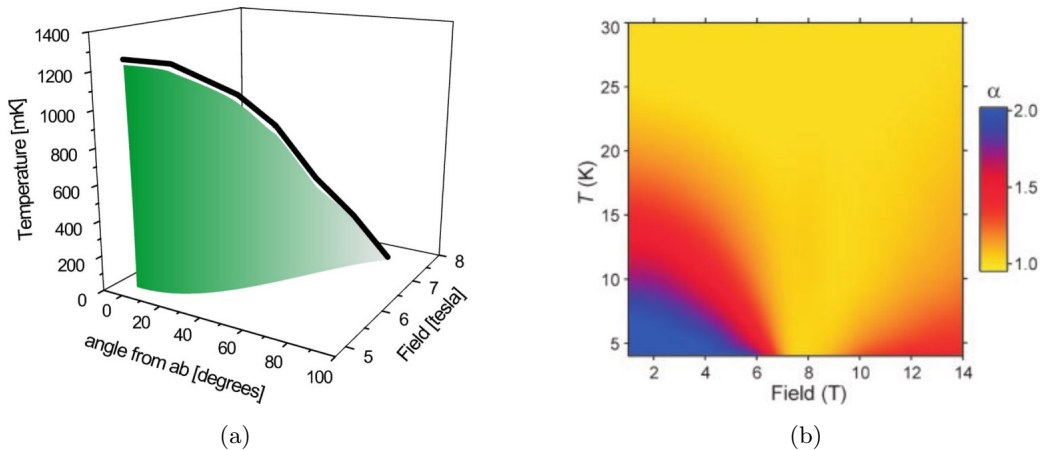


Figure 2.8: (a) Phase diagram deduced from measurements of the angular dependence of the magnetic susceptibility. The green surface depicts the location of the metamagnetic transitions, separating a low-field paramagnetic state from a high-field state with enhanced magnetization. The surface of first order transitions is bounded by a line of critical end-points, drawn in black. When the applied field is parallel to the  $c$ -axis, the critical end-point is suppressed to zero or near-zero temperature at a field  $H_c \approx 8$  T. Taken from [33]. (b) Plot of the temperature exponent in the resistivity  $\alpha$  from equation (2.5.1), as a function of field applied along the  $c$ -axis and temperature. Non-Fermi liquid behaviour extends out from the point  $(H_c, 0)$ , suggestive of an underlying QCEP. Taken from [34].

QCEP is a large region with non-Fermi liquid transport properties, which suggests that quantum critical fluctuations are responsible for this anomalous behaviour. Low-temperature measurements show that  $\alpha = 2$  is recovered again at high fields [34]. Another result of this experiment is the divergence of the  $A$  coefficient of equation (2.5.1) on approaching  $H_c$ . The  $A$  coefficient can be shown to be proportional to the square of the quasiparticle effective mass for a single band metal [15], so such a divergence can be indicative of a diverging effective mass. The relationship between  $A$  and  $m^*$  however does not hold in general for a multi-band material in a magnetic field such as  $\text{Sr}_3\text{Ru}_2\text{O}_7$ , so further thermodynamic evidence is needed.

Measurements of the specific heat against temperature [31, 35] show that as  $H_c$  is approached, the Sommerfeld coefficient  $\gamma = C_v/T$  exhibits a divergence of the form  $-\ln T$ , consistent with predictions of quantum critical behaviour [3]. This logarithmic divergence is shown in Figure 2.9a. One notices that the divergence is cut off at some temperature marked by the gray dashed line. This is believed to be caused by the appearance of a new phase surrounding the QCEP, the properties of which are described in Section 2.5.3. The low-temperature evolution of the specific heat with field also provides evidence for quantum criticality, as a divergence on approach of  $H_c$  is seen (Figure 2.9b). Again, the divergence appears to be cut off,

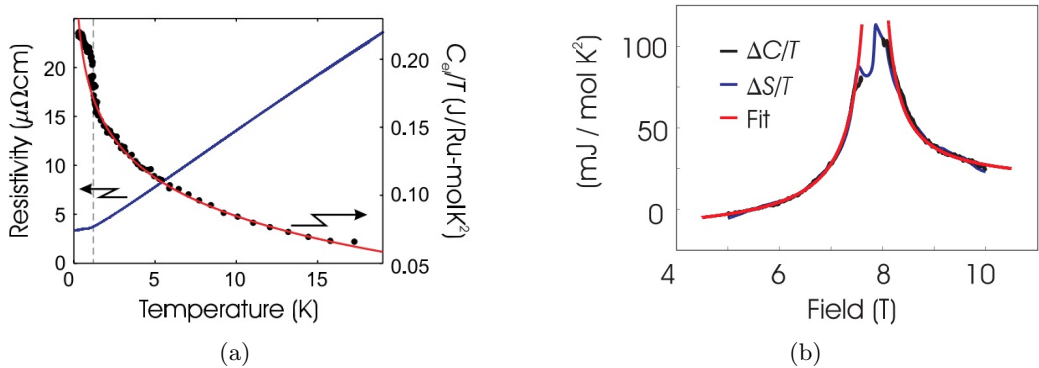


Figure 2.9: (a) Electronic part of the specific heat (black dots) and resistivity (blue line) against temperature in an applied field of 7.95 T parallel to  $c$ . The red line shows a fit to the data of the form  $-a \ln T$ , and the dashed gray line signals the temperature at which a novel low-temperature phase appears. The resistivity’s linear temperature dependence is a typical signature of quantum criticality. Taken from [35]. (b) Evolution of the change in specific heat  $\Delta C/T$  and the entropy  $\Delta S/T$  in a magnetic field at  $T = 250$  mK. The red line corresponds to a fit of the form  $A[(H - H_c)/H_c]^{-1} + B$ . The value of  $B$  is different on the low- and high-field sides, whereas  $A$  is the same on both. Taken from [36].

which could be a consequence of the intervening phase. The entropy  $S/T$ , obtained by integration of the magnetocaloric data, is also plotted on the same graph.

To summarize, we have seen that  $\text{Sr}_3\text{Ru}_2\text{O}_7$  exhibits a metamagnetic transition, the critical end-point of which can be tuned to near-zero temperature by aligning the magnetic field along the  $c$ -axis. This leads to a novel kind of quantum critical point, namely the quantum critical end-point, as evidenced by the observation of quantum critical behaviour in resistivity and thermodynamic measurements. We mentioned that there is evidence of a new phase which exists around the QCEP, which cuts off the divergence of the specific heat and the entropy. In the next section we will discuss in some detail the exotic phenomena exhibited by this phase.

### 2.5.3 Properties of the novel phase

Following the discussion in the previous section, there appears to be a good body of evidence showing that  $\text{Sr}_3\text{Ru}_2\text{O}_7$  is host to a magnetic-field-tuned quantum critical point. This has generated much interest, especially since  $\text{Sr}_3\text{Ru}_2\text{O}_7$  was one of the first examples of a new class of quantum criticality: unlike in the case of a conventional QCP which is reached by suppressing a second order phase transition to zero temperature, that in  $\text{Sr}_3\text{Ru}_2\text{O}_7$  is reached by suppressing a critical end-point. From an experimental point of view, magnetic-field-tuning presents significant advantages compared to tuning via pressure or chemical doping, as it does not introduce defects

into the crystal and the sample size is not limited by that of a pressure cell. It also allows one to explore the phase diagram with a single sample during a single cool-down, making it a very convenient tuning-parameter.  $\text{Sr}_3\text{Ru}_2\text{O}_7$  is therefore an ideal candidate for studying the physics of quantum criticality in a clean system. This prompted a large effort to increase sample purity by systematically optimizing the growth conditions, leading to single crystals with mean-free paths of the order of 3000 Å [37]. A consequence of the production of higher purity samples was the discovery of a novel phase in the vicinity of the QCEP, which had hitherto only been hinted at in the experimental data. The electronic properties of this phase appear to be highly unusual, and have been the subject of much experimental and theoretical work.

In high-purity samples with  $\rho_{res} < 1 \mu\Omega\text{cm}$ , instead of the metamagnetic transition being suppressed to zero when the field is along  $c$ , it bifurcates into two metamagnetic transitions when the field is  $\sim 30^\circ$  from  $c$  [38]. These two metamagnetic transitions were found to bound a novel phase, which is highly sensitive to disorder [39]. The resulting phase diagram is shown in Figure 2.10a, in contrast to that for less pure samples shown in Figure 2.8a. With the field along  $c$ , the metamagnetic transitions occur at  $\sim 7.85$  T and  $\sim 8.1$  T, and above the critical points of these transitions the phase is bounded by a second order “roof” (Figure 2.10b). One of the most striking signatures of the phase is seen in the in-plane transport (Figure 2.10c). In between the two metamagnetic transitions, the resistivity is strongly enhanced, with the jumps in resistivity coinciding with those in magnetization. Additionally, the resistivity inside the phase appears to have little or no temperature dependence. The small dip in resistivity before the phase at  $\sim 7.5$  T is associated with an increase in the magnetization, however this not a first order transition as the imaginary part of the AC susceptibility is zero at that field (Figure 2.10d). The boundaries of the phase were mapped out using a variety of different probes, including AC magnetic susceptibility, magnetization, resistivity and magnetostriction, all of which are in good agreement with each other. It is interesting to note in Figure 2.10a that there is a second region of enhanced resistivity, where the field is applied close to the  $ab$ -plane [32]. In contrast to the region of high resistivity described above, this second region does not appear to mask a QCEP. The work described in this thesis pertains to the novel phase appearing for  $H$  parallel to  $c$ , so we will focus on this region of the phase diagram for the rest of the discussion.

Specific heat and entropy measurements shown in Figures 2.9a and 2.9b also provide evidence for phase formation for  $H$  parallel to  $c$ , as mentioned in the previous section. The divergence of the entropy as the critical field  $H_c$  is approached is cut off at the crossover at  $\sim 7.5$  T, before jumping up as the novel phase is entered. The entropy then drops back down where the phase is exited at  $\sim 8.1$  T. The observation that the entropy inside the phase is higher than outside may seem surprising, as at the first metamagnetic transition sample magnetization increases with magnetic field, so one would intuitively expect a decrease in entropy associated with the increased magnetic ordering. This observation is however consistent with

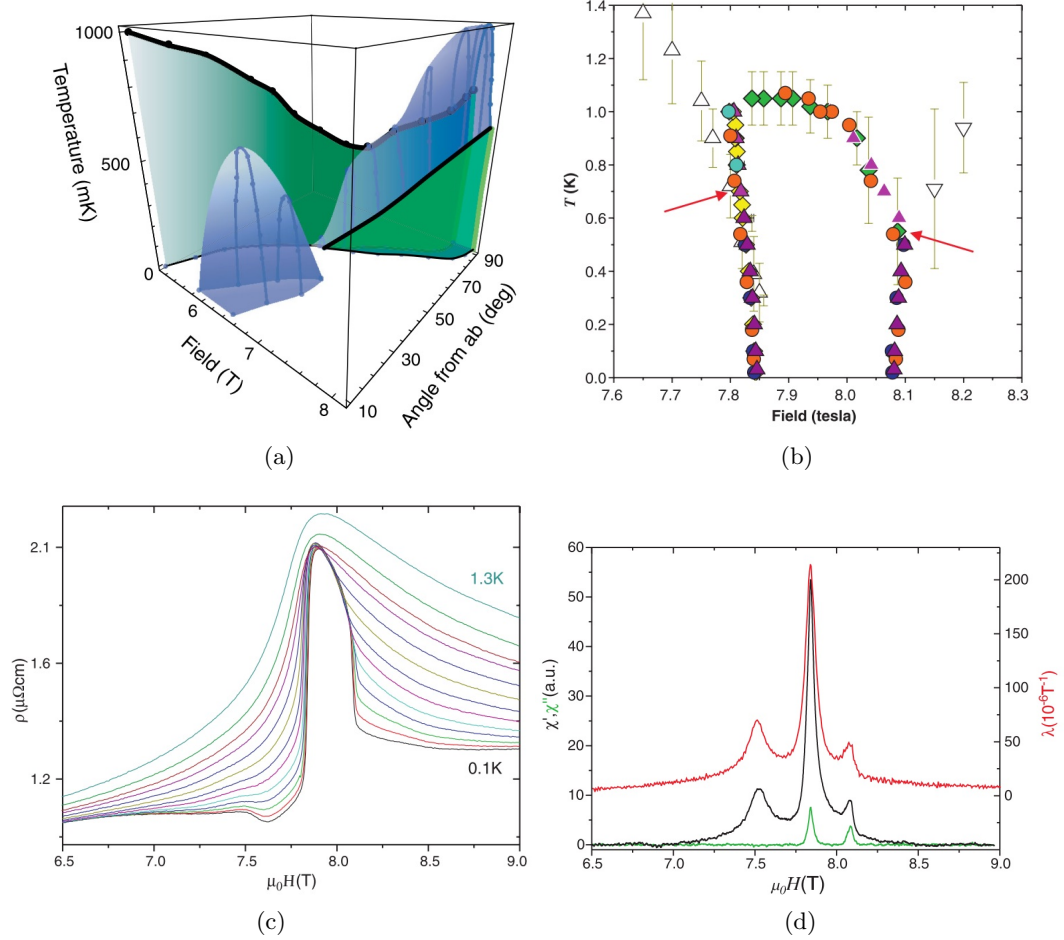


Figure 2.10: (a) Phase diagram for high-purity  $\text{Sr}_3\text{Ru}_2\text{O}_7$  samples, deduced from transport measurements. As in Figure 2.8a, the green sheets represent metamagnetic transitions, and the black lines the critical end-points. The blue sheets define regions where the in-plane resistivity is anomalously large. Taken from ref. [40]. (b) Boundaries of the novel phase for field aligned along the  $c$ -axis. The phase boundaries shown were constructed with data from AC magnetic susceptibility, magnetization, resistivity and magnetostriction. The red arrows indicate the critical points, above which the phase is entered via a second order phase transition. (c) In-plane resistivity against magnetic field applied parallel to  $c$ , for a series of temperatures between 0.1 K and 1.3 K in 100 mK steps. The onset of a high-resistivity state inside the phase coincides with the metamagnetic transitions. (d) The real and imaginary parts of the AC magnetic susceptibility  $\chi'$  and  $\chi''$  at 100 mK, showing that the transitions bounding the phase are first order. The red curve represents the linear magnetostriction  $\lambda = d(\Delta c/c)/dH$ . The strong correlation between  $\chi'$  and  $\lambda$  indicate a strong magnetostructural coupling. (b), (c) and (d) taken from [39].

the Clausius-Clapeyron relation  $\mu_0 dH_c/dT_c = -\Delta S/\Delta M$ , due to the inward-sloping transition lines below the red arrows in Figure 2.10b<sup>2</sup>. One interpretation that has been put forward for the entropy data is that phase formation occurs to prevent a divergence of the entropy at low temperature, which would otherwise occur at the QCEP [36]. This suggests that phase formation in  $\text{Sr}_3\text{Ru}_2\text{O}_7$  is strongly linked with quantum criticality.

Having shown that there is a well-defined phase which emerges in the vicinity of  $\text{Sr}_3\text{Ru}_2\text{O}_7$ 's QCEP, the next question is that of the phase's order parameter. This is still an unresolved question, although several clues are given by transport and neutron scattering measurements, the main results of which are described here.

In-plane transport in the novel phase is found to be highly sensitive to an in-plane component of the magnetic field. This was shown by measuring resistivity along different in-plane directions for a series of tilt angles  $\theta$  between the  $ab$ -plane and magnetic field [4] (Figure 2.11b). The magnetic field in this case is the sum of an in-plane component  $H_{ab}$ , made to lie parallel to  $a$  or  $b$  (equivalently), and an out-of-plane component  $H_c$ . The case for  $\theta = 77^\circ$  is illustrated in Figure 2.11a, where a large resistive anisotropy between the two in-plane axes is observed. If the current is run parallel to  $H_{ab}$ , a strongly enhanced resistivity is measured, whilst for a current perpendicular to  $H_{ab}$  a lower resistivity is measured. One can thus define “easy” and “hard” directions, the hard direction being that parallel to  $H_{ab}$ . In contrast, if there is no in-plane component (left panel of Figure 2.11a), no resistive anisotropy is measured. This experiment was accompanied by a neutron scattering measurement to see if a lattice distortion could be the cause of the observed anisotropy, however no difference between the  $a$  and  $b$  lattice parameters could be detected within experimental resolution [4]. A subsequent measurement of the in-plane thermal expansion found a relative change in lattice parameters upon entering the phase of  $10^{-7}$  at small tilt angles, increasing to  $10^{-6}$  for  $\theta > 80^\circ$  [41]. This difference in the lattice parameters, which is only seen in the presence of an in-plane field, is on its own not large enough to account for the factor of  $\sim 1.5$  between the resistivity along the easy and hard directions. Moreover, even though an in-plane component is applied over the whole field range, resistive anisotropy is only observed within a narrow field range.

Subsequent resistivity measurements performed by Bruin et al. using a vector magnet revealed that the anisotropy is not confined to the region between the metamagnetic transitions, but extends up to  $\sim 8.5$  T [42]. This prompted the suggestion that a second phase may exist between 8.1 T and 8.5 T, which is distinct from the main phase but which also has a strongly field-dependent resistive anisotropy. Another interesting feature of their data is that a small anisotropy also extends in temperature outside the phase, with the field range over which it is observed decreasing at low temperatures. This behaviour is reminiscent of quantum critical

---

<sup>2</sup>The Clausius-Clapeyron relation is valid for first order transitions between two thermal equilibrium phases, suggesting that the phases on either side of the metamagnetic transitions are in thermodynamic equilibrium.

fluctuations which are thermally activated, and which extend over a wider range at higher temperatures as they become increasingly populated.

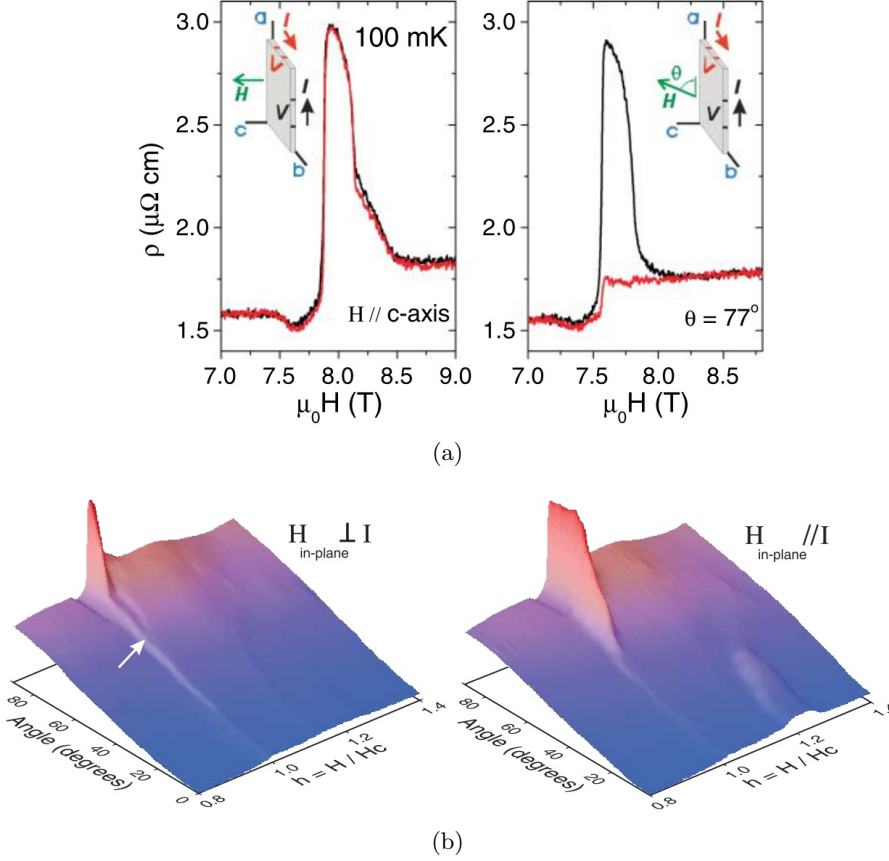


Figure 2.11: (a) *Left panel*: Resistivity along  $a$  and  $b$  against magnetic field, with the field applied parallel to  $c$ . No resistive anisotropy is seen. *Right panel*: Same measurement, but with the field tilted so that it has a component parallel to  $a$ . Resistivities along  $a$  and  $b$  display the “hard” and “easy” responses respectively. The measurement configurations are illustrated in the insets. (b) Sample resistivity for the easy and hard directions as a function of field and field angle. In-plane field suppresses high resistivity inside the phase more rapidly along the easy axis than the hard axis, giving rise to a large resistive anisotropy. The field scale is normalized by  $H_c(\theta)$ , the field at which the metamagnetic transition on the low-field side of the phase occurs. The white arrow marks where the metamagnetic transitions bounding the anomalous phase join into a single transition. Figures from [4].

The experiments described above led to the suggestion that the anisotropy is an intrinsic property of  $\text{Sr}_3\text{Ru}_2\text{O}_7$ 's novel phase. An interpretation of the data is that the phase is host to an electron nematic state, in other words that the symmetry of the system is lowered from four-fold symmetric to two-fold symmetric. An in-plane

field would then be necessary to align domains of the symmetry broken phase, which would otherwise average out when the field is along  $c$  to give the same response along  $a$  and  $b$  (as is the case in the left panel of Figure 2.11a). A discussion of nematic electron fluids and  $\text{Sr}_3\text{Ru}_2\text{O}_7$  is given for example in a 2010 review article [43].

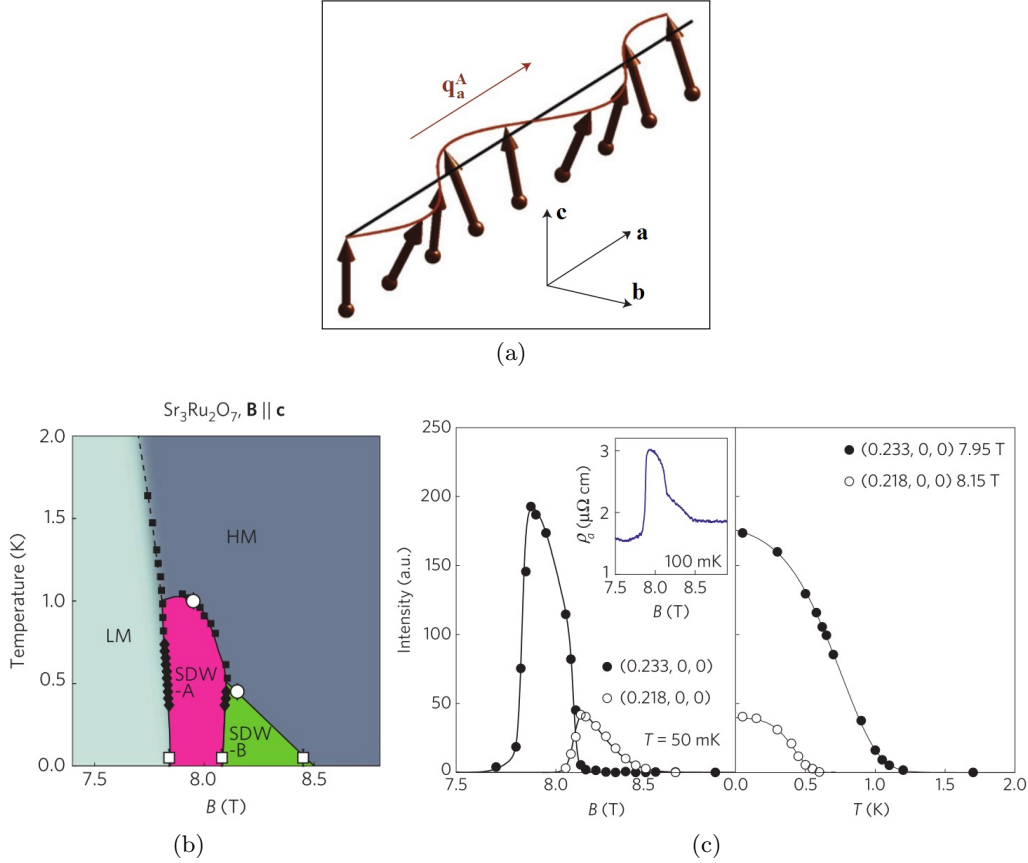


Figure 2.12: (a) Proposed structure of a single SDW in the A-phase, with its propagation vector running along  $a$ . (b)  $\text{Sr}_3\text{Ru}_2\text{O}_7$ 's phase diagram based on neutron scattering data (open squares and circles) and the data from Figure 2.10b (black diamonds and squares). The dotted line represents the crossover between a low-magnetization (LM) and a high-magnetization (HM) state. (c) Measured intensities of the Bragg peaks at  $\mathbf{q}_a^A = (0.233, 0, 0)$  (black circles), and at  $\mathbf{q}_a^B = (0.218, 0, 0)$  (white open circles) as a function of magnetic field (left panel) and temperature (right panel). The inset of the left panel shows the in-plane resistivity versus field, revealing the similarity between the profiles of the peak intensities and the resistivity against field. The phase boundaries extracted from field sweeps are shown as open squares in (b), whilst those from temperature sweeps are shown as open circles. Figures from [44].

Recent data from neutron scattering experiments show however that  $\text{Sr}_3\text{Ru}_2\text{O}_7$ 's

novel phase is not truly nematic, as evidence of translational symmetry breaking in the form of a spin-density wave is seen<sup>3</sup> [44]. C. Lester et al. performed a series of magnetic neutron scattering measurements at different fields and temperatures, to study the magnetic structure of the phase. They found that they could tune the system through two distinct SDW states with a magnetic field applied along  $c$ . They named the first SDW state the A-phase, and this corresponds to the novel phase described above, bounded on either side by metamagnetic transitions. The B-phase lies on the high-field side of the A-phase, and matches the region seen in resistivity by Bruin et al. [42] between 8.1 T and 8.5 T. The B-phase corresponds to the “shoulder” in the in-plane resistivity, which can be seen in the left panel of Figure 2.11a. The phase diagram from Figure 2.10b can be modified to include the B-phase, as shown in Figure 2.12b. In the A-phase, two pairs of Bragg peaks were found with  $\mathbf{q}_a^A = (\pm 0.233, 0, 0)$  and  $\mathbf{q}_b^A = (0, \pm 0.233, 0)$ , corresponding to SDWs with propagation vectors running along  $a$  and  $b$  respectively. The proposed form of a single SDW is illustrated in Figure 2.12a. By tilting the magnetic field along one of the in-plane axes, they showed that one pair of Bragg peaks could be “selected”, so that the SDW running along the easy direction disappears. This effect mirrors that seen in resistivity (Figure 2.11a), where in-plane field suppresses the resistivity inside the phase along the easy direction. In the B-phase an SDW with a slightly different wavevector of  $\mathbf{q}_a^B = (\pm 0.218, 0, 0)$  was observed. The SDWs in both the A- and B-phases are incommensurate with the lattice. The intensity of the Bragg peaks, which is directly related to the magnitude squared of the SDW’s ordered moment, is shown as a function of magnetic field and temperature in Figure 2.12c, illustrating how the phase boundaries can be defined using the neutron data. A striking feature of the peak intensities against field is how closely the profile of the in-plane resistivity tracks the sum of the two intensities. This, in combination with the effect of in-plane field on the SDWs, suggests that the anomalous resistivity inside the phase is closely linked to SDW formation.

#### 2.5.4 Theoretical work on the phase

Prior to the discovery of the SDW, the order parameter of the novel phase was believed to be nematic, in other words the electron fluid breaks the four-fold symmetry of the underlying lattice. This motivated a large body of theoretical work which attempts to explain the phase’s exotic properties, as well as the overall phase diagram. Theories relating to  $\text{Sr}_3\text{Ru}_2\text{O}_7$ ’s novel phase can be roughly divided into two categories.

In the first, purely microscopic models are considered, with the metamagnetic transitions and nematicity being explained by the band structure and effect of magnetic field, without making any reference to fluctuations associated with quantum criticality. Several of these models consider the presence of van Hove singularities in the density of states located near the  $\gamma_2$  pockets, which can be made to cross the

---

<sup>3</sup>A nematic state has an orientational order, but no translational order.

Fermi level by Zeeman splitting the Fermi surface in a  $\sim 10$  T field [45, 46]. A high density of states at the Fermi level can lead to metamagnetism and the stabilization of ordered states, as illustrated by the Stoner criterion. In these models, the van Hove singularities cause a nematic distortion of the Fermi surface which gives rise to anisotropic transport. The distortions of the Fermi surface are however expected to be small, and cannot on their own explain the large resistivity inside the phase or the anisotropy which is observed in an in-plane field. Scattering from domain walls was proposed as a mechanism to explain these effects [4, 47], with the domains containing a locally nematic order. In zero in-plane field, domains of different nematicity would coexist in the sample, the populations of which could be controlled by an in-plane field thus giving rise to the observed anisotropy. With the recent discovery of the SDW, the question becomes whether the resulting gapping of sections of the Fermi surface is sufficient to explain the magnitude of the anomalous transport properties, and whether there are domains containing *a*- or *b*-oriented SDWs as opposed to coexistence of the two SDWs in a single domain.

Another family of microscopic models considers a van Hove singularity in the density of states of the quasi-one-dimensional  $d_{xz}$  and  $d_{yz}$  bands [48, 49]. It is suggested that these bands may be of particular relevance to the physics of  $\text{Sr}_3\text{Ru}_2\text{O}_7$ , as they are the most strongly affected by the bi-layer splitting. Indeed,  $\text{Sr}_2\text{RuO}_4$ , whose band structure is derived from the same orbitals as  $\text{Sr}_3\text{Ru}_2\text{O}_7$  but does not have any bi-layer splitting, does not exhibit metamagnetism or in-plane transport anisotropy.

The second category into which models of  $\text{Sr}_3\text{Ru}_2\text{O}_7$ 's novel phase fall is that where it is postulated that phase formation is closely linked to quantum criticality. Phase formation was shown to cause the bifurcation of the metamagnetic transition as the field is tilted towards *c*, by studying a Landau free energy expansion around a metamagnetic critical point and highlighting the importance of the van Hove singularities [38, 40]. The so-called *order-by-disorder* theory provides a scenario explaining how new phases can be stabilized in the vicinity of ferromagnetic quantum critical points [50], the idea being that Fermi surface distortions associated with the new phase can enhance the phase space available for quantum fluctuations, and thus lower the free energy. Ferromagnetic quantum critical fluctuations, which could lead to a divergence of the residual resistivity, have also been put forward as an explanation for the enhanced resistivity in the phase [51, 52]. Perhaps the most compelling evidence that there is a link between phase formation and quantum criticality comes from the thermodynamic data illustrated in Figures 2.9a and 2.9b. The appearance of the phase in the vicinity of the QCEP appears to cut off a divergence in the specific heat, suggesting that phase formation is driven by criticality [36]. However, all of the theories mentioned fail to account for the  $[(H - H_c)/H_c]^{-1}$  form of the divergence as well as the behaviour of the entropy within the phase.

## 2.6 Summary and motivation

Starting from the non-interacting electron problem, we argued how electronic correlations can be taken into account to describe a wide range of electronic behaviour using Landau's Fermi liquid theory. In the vicinity of a QCP however, the quasiparticle description from Fermi liquid theory of the system's excitations breaks down and a wealth of new physics emerges. We showed that  $\text{Sr}_3\text{Ru}_2\text{O}_7$  is an ideal material in which to study quantum criticality, as large crystals with extremely long mean-free paths are available, and its electronic states are well characterised by ARPES and dHvA. In addition, the tuning parameter is magnetic field, meaning that one can tune continuously through the critical region to acquire a high density of data points without introducing any defects into the sample. The novel phase which appears in the vicinity of  $\text{Sr}_3\text{Ru}_2\text{O}_7$ 's QCEP has highly unusual in-plane transport properties, which are very susceptible to a symmetry breaking in-plane magnetic field. Neither the link between phase formation and criticality or a microscopic model for the phase itself have yet been firmly established from a theoretical point of view, and many experimental questions remain to be answered. The sensitivity of the phase's properties to a symmetry breaking field suggests that it is very likely to be sensitive to in-plane uni-axial strain. Studying  $\text{Sr}_3\text{Ru}_2\text{O}_7$  under uni-axial strain would provide information about how the SDWs are affected by anisotropic lattice distortions, and will yield an interesting comparison with in-plane magnetic field. As will be described in Section 4.1.4, a uni-axial strain probe enabling the fine-tuning of the strain applied to the sample was developed, allowing us to map out in great detail the behaviour of  $\text{Sr}_3\text{Ru}_2\text{O}_7$  in (field, strain) space. The results and a discussion of the data obtained on  $\text{Sr}_3\text{Ru}_2\text{O}_7$  under uni-axial strain are presented in Chapter 6.



## Chapter 3

# Spin-triplet Superconductivity in $\text{Sr}_2\text{RuO}_4$

Since its discovery over a century ago, superconductivity has been one of the most active fields of research in condensed matter physics. The most successful microscopic theory of superconductivity to date, which completely revolutionized our way of thinking about the phenomenon, was published by Bardeen, Cooper and Schrieffer (BCS) in 1957 [53]. In this theory, a mechanism for superconductivity is proposed whereby electrons at the Fermi surface pair up below the transition temperature  $T_c$  through a virtual exchange of phonons to lower their energy, thus opening up a gap. The theory was extremely successful in describing the superconducting properties of many materials, and the observation of the isotope effect was seen as proof for electron pairing via the electron-phonon interaction in these materials [54]. However, with the discovery of new types of superconductors such as the heavy fermion superconductors [55] and high- $T_c$  cuprates [56], it became clear that more exotic superconducting states were possible, with different symmetries and pairing mechanisms to those described in BCS theory. Additionally, with spin-triplet pairing being explored in the context of  $^3\text{He}$ , similar pairing states were searched for in solid state systems.

In this chapter we will begin by summarizing some of the main concepts behind BCS theory, before moving on to the notion of unconventional superconductivity and a framework for describing such a state. In the final part of this section we focus on the material  $\text{Sr}_2\text{RuO}_4$ , which is the subject of the research described in Chapter 5. A review of some of the main experimental results from the literature is presented, many of which indicate that it may have a chiral  $p$ -wave superconducting state analogous to the  $^3\text{He}$  A-phase. It is then argued how uni-axial strain can be used as a probe of the superconducting order parameter, to provide a motivation for the experimental work undertaken.

### 3.1 Conventional superconductivity and BCS theory

Superconductivity is a striking illustration of the principle of emergence [1]: from the extremely complex many-body system made up of correlated electrons and an ionic lattice emerges a coherent superconducting state which can be described by a single simple wavefunction. This wavefunction was first proposed by Bardeen, Cooper and Schrieffer, and forms a central part of their theory of superconductivity [53].

The first building block of BCS theory is Cooper pairing. The idea is that the filled Fermi sea is unstable to the formation of bound pairs of electrons (so-called “Cooper pairs”), should there exist an attractive interaction, no matter how small, between electrons at the Fermi surface. To prove this, Cooper considered a model of two electrons added to a Fermi sea at  $T = 0$  [57]. Assuming the two electrons only interact with those in the Fermi sea via the exclusion principle, the system can be described by the two-particle wavefunction:

$$\psi(\mathbf{r}_1, \mathbf{r}_2) = \sum_k g(k) e^{i\mathbf{k}\cdot\mathbf{r}_1} e^{-i\mathbf{k}\cdot\mathbf{r}_2} \quad (3.1.1)$$

where  $\mathbf{r}_1$  and  $\mathbf{r}_2$  are the coordinates of the two electrons. Electrons with opposite momenta are chosen, as a state with a total momentum of zero is expected to have the lowest energy. The next step is to plug this wavefunction into the two-particle Schrödinger equation to compute the overall energy of the system. For his calculation, Cooper chose an interaction potential  $V_{kk'}$  between the electrons which was attractive within a narrow energy band of width  $\hbar\omega_c$  around the Fermi surface. He found that the energy of the system was lowered below that of the bare Fermi sea by an amount  $\Delta$  proportional to  $\hbar\omega_c$ , corresponding to the binding energy of the Cooper pair.

The mechanism put forward by BCS to explain the attractive interaction is electron-phonon coupling. As an electron travels through a lattice of ionic cores it polarizes the lattice due to the Coulomb attraction, creating a region with excess positive charge. This positive charge in turn attracts a second electron. If the attractive force is large enough to overcome the repulsive Coulomb interaction between the electrons, then there is an effective attraction between them. This interaction is said to be retarded, as the lattice deformation caused by the passing electron exists on a much longer time-scale than that on which the Coulomb force is felt by the electron. In this picture, the cut-off energy  $\hbar\omega_c$  mentioned earlier can be equated to the Debye energy  $\hbar\omega_D$ , which represents the cut-off of the phonon spectrum. It turns out that the simple form of the interaction potential  $V_{kk'}$  used in BCS theory is a good approximation, as only electrons very close to the Fermi surface, i.e. with an energy  $E \ll \hbar\omega_c$ , participate in the formation of Cooper pairs. Hence the behaviour of  $V_{kk'}$  out towards  $\hbar\omega_c$  has little effect on the calculated results.

Experimentally, the electron-phonon interaction was shown to be the origin of the pairing attraction in several materials by the isotope effect. A material’s  $T_c$  is proportional to  $\Delta$ , which in the case of electron-phonon interaction is proportional

to  $\hbar\omega_D$ . The Debye energy has a  $1/\sqrt{M}$  dependence, where  $M$  is the atomic mass. Therefore  $T_c$  should be proportional to  $1/\sqrt{M}$  and different isotopes of the same element should have different  $T_c$ 's.

Calculation of the weighting coefficient  $g(k)$  in (3.1.1) shows that it does not depend on the direction of  $k$ , so the Cooper pair has  $s$ -wave symmetry. Moreover the Cooper pair must be spin-singlet due to the overall requirement that its wavefunction be anti-symmetric under particle exchange.

To describe a superconducting state in a real material with many Cooper pairs, one can no longer simply consider the two-particle wavefunction of equation (3.1.1). Instead we use the following pairing Hamiltonian written in second quantized notation:

$$H = \sum_{k,\sigma} (\epsilon_k - E_F) \hat{c}_{k,\sigma}^\dagger \hat{c}_{k,\sigma} + \sum_{k,k'} V_{k,k'} \hat{c}_{k,\uparrow}^\dagger \hat{c}_{-k,\downarrow}^\dagger \hat{c}_{k',\uparrow} \hat{c}_{-k',\downarrow} \quad (3.1.2)$$

where  $\hat{c}^\dagger$  and  $\hat{c}$  are electron creation and annihilation operators respectively, with the momentum and spin of the electron given by the operator's subscript. The first term corresponds to the electrons' kinetic energy measured relative to the Fermi energy  $E_F$ , and the second to the pairing of electrons via the potential  $V_{kk'}$ . Terms where electrons are not paired in a singlet state with a total momentum of zero are omitted, as they do not contribute to superconductivity in BCS theory. The ground state wavefunction chosen by BCS is a product of pair states:

$$|\psi_0\rangle = \prod_k (u_k + v_k \hat{c}_{k,\uparrow}^\dagger \hat{c}_{-k,\downarrow}^\dagger) |0\rangle. \quad (3.1.3)$$

$|u_k|^2 + |v_k|^2 = 1$  to preserve commutation relations. The probability of the Cooper pair ( $k \uparrow, -k \downarrow$ ) being occupied is given by  $|v_k|^2$ , and that of it being unoccupied by  $|u_k|^2 = 1 - |v_k|^2$ .

The superconducting transition in zero field is of second order, and so as  $T_c$  is crossed one or more symmetries are broken. For instance the superconducting state locally breaks *gauge symmetry*, corresponding to the fact that below  $T_c$  the Cooper pairs form a phase coherent condensate. The "choice" of one of the degenerate states with phase  $\phi$  as the superconducting state is entered is analogous to the choice of direction for the magnetic moment in an isotropic ferromagnet.

Starting from the model Hamiltonian (3.1.2), many properties of the BCS superconducting state can be calculated. For example, by performing a mean-field analysis one can diagonalise the Hamiltonian and obtain the energy spectrum for excitations in the system [54]. The excitations have the form:

$$E_k = \sqrt{\Delta^2 + (\epsilon_k - E_F)^2}. \quad (3.1.4)$$

The minimum excitation energy is therefore equal to the energy gap  $\Delta$ , and the density of states for excitations smaller than  $\Delta$  is zero. Importantly, the magnitude and phase of the gap around the Fermi surface are constant, which is not the case for

unconventional superconductors, as we will see further on. Using the Fermi function, the temperature dependence of the gap  $\Delta(T)$  can be calculated, and the well-known relation  $\Delta(0) \approx 1.764.k_B T_c$  derived. One finds that the gap grows continuously from zero at  $T_c$  to its zero temperature value  $\Delta(0)$ , the number of Cooper pairs increasing as temperature is lowered. In this picture, an excitation corresponds to the destruction of a Cooper pair.

Knowing the temperature dependence of the fermionic excitations, a whole range of quantities can be calculated, such as the entropy, specific heat, critical field, ultrasound attenuation and nuclear relaxation rate. A famous result from BCS theory, for example, is that there is a jump in the specific heat at  $T_c$  proportional to the density of states and the transition temperature. At low temperatures the specific heat decreases exponentially, as opposed to linearly like in the normal state, meaning that superconductors become very good thermal insulators.

The BCS theory of superconductivity is a mean-field theory which is valid for interactions within a small energy band around the Fermi surface. One can justify the mean-field approach by considering the number of electrons contained within a single coherence volume<sup>1</sup>. In a conventional superconductor the coherence length is of the order of 1000 Å, so a large number of electrons will be contained within a coherence volume, meaning that fluctuations in the superconducting state will be small. However in the case of the high- $T_c$  cuprates where the coherence volume is several orders of magnitude smaller, fluctuations can have a significant effect and the mean-field approach breaks down [58]. The results derived from BCS theory are valid within the *weak-coupling* limit, i.e. for  $\lambda = N(0)V \ll 1$  where  $\lambda$  is the coupling constant,  $N(0)$  the density of states at the Fermi level and  $V$  the interaction potential which depends on the separation of the electrons<sup>2</sup>. For example, in most classical superconductors  $\lambda < 0.3$ . Because the derivation of BCS theory does not depend on the details of the attractive interaction, its main results are applicable to all superconductors within the weak-coupling limit.

## 3.2 Introduction to unconventional superconductivity

We have seen that a spin-singlet superconducting state with s-wave symmetry arises naturally when we consider phonon-mediated pairing. This kind of superconductivity typically occurs in simple metals, where the conduction electrons can move nearly freely through the lattice. In the case of strongly correlated electron systems however, where the electrons may be more strongly localized, or have a largely enhanced effective mass, the retardation of the electron-phonon interaction is no longer sufficient to overcome the Coulomb repulsion between the electrons. Nevertheless

---

<sup>1</sup>The superconducting coherence volume is defined as  $\xi_a \xi_b \xi_c$  where  $\xi_a$ ,  $\xi_b$  and  $\xi_c$  are the coherence lengths along the crystallographic axes. These correspond to the spatial extent of the Cooper pair along the respective axis.

<sup>2</sup>The interaction potential is of the form  $V_{kk'} = \Omega^{-1} \int V(\mathbf{r}) e^{i(\mathbf{k}'-\mathbf{k})\cdot\mathbf{r}} d\mathbf{r}$ , where  $\Omega$  is the normalization volume [54].

superconductivity does occur in some strongly correlated materials, for example in the case of the heavy fermion superconductors or high- $T_c$  cuprates. In these cases the superconductivity still results from the pairing up of electrons, as the flux quantisation is shown to correspond to charge carriers of charge  $2e$  [59], however the pairing mechanism is different.

Before moving on to discuss alternative possible pairing mechanisms, let us first consider the form of the Cooper pair wavefunction:

$$\Psi(\mathbf{r}_1, s_1; \mathbf{r}_2, s_2) = f(\mathbf{r}_1 - \mathbf{r}_2)\chi(s_1, s_2) \quad (3.2.1)$$

which we have here written as a product of the pair's orbital and spin wavefunctions,  $f$  and  $\chi$  respectively [60]. As a Cooper pair is made up of two indistinguishable spin-half particles, its wavefunction must be antisymmetric under particle exchange, i.e.  $\Psi(\mathbf{r}_1, s_1; \mathbf{r}_2, s_2) = -\Psi(\mathbf{r}_2, s_2; \mathbf{r}_1, s_1)$ . The spin part can either have total spin  $S = 0$  (singlet) or  $S = 1$  (triplet). The orbital part can be written in terms of spherical harmonics  $Y_l^m$ , where its parity is given by  $(-1)^l$ . The names  $s$ -,  $p$ -,  $d$ -,  $f$ -wave are given to the states with angular momentum  $l = 0, 1, 2, 3$ , as per convention<sup>3</sup>.

The requirement that the overall Cooper pair wavefunction pick up a minus sign under particle exchange therefore leads to the following possible combinations of spin and spatial parts:

$$S = 0 \implies \chi(s_1, s_2) = \frac{1}{\sqrt{2}}(|\uparrow\downarrow\rangle - |\downarrow\uparrow\rangle), \quad l = 0, 2, 4, \dots$$

$$S = 1 \implies \chi(s_1, s_2) = \left\{ \begin{array}{l} |\uparrow\uparrow\rangle \\ \frac{1}{\sqrt{2}}(|\uparrow\downarrow\rangle + |\downarrow\uparrow\rangle), \quad l = 1, 3, 5, \dots \\ |\downarrow\downarrow\rangle \end{array} \right\}$$

We call all pairing states with  $l > 0$  unconventional. In general, angular momentum states with  $l > 0$  are favored when the pairing mechanism is other than the electron-phonon interaction, as for such states there is a vanishing probability of the electrons encountering each other at the origin (as  $f(r) \propto r^l$ ,  $r \rightarrow 0$ ), which reduces the Coulomb repulsion felt by the electrons. The spatial overlap of the electrons in the  $s$ -wave state is only possible because of the retarded nature of phonon-mediated pairing. A key difference between conventional and unconventional superconductivity is that whereas the phase of the gap remains constant around the Fermi surface

---

<sup>3</sup>In the presence of a crystal lattice,  $S$  and  $l$  are no longer good quantum numbers. Therefore technically the ‘‘lattice-free’’  $s$ -,  $p$ -,  $d$ -,  $f$ -wave nomenclature is no longer accurate. However in the case of the materials studied in this thesis, spin-orbit coupling and lattice effects are weak enough that this treatment should provide a good approximation.

in the conventional case, it depends on  $\mathbf{k}$  in the unconventional case such that:

$$\sum_{\mathbf{k}} \Delta(\mathbf{k}) = 0, \quad (3.2.2)$$

where the sum is around the Fermi surface.

$\Delta(\mathbf{k})$ , which is directly related to the Cooper pair wavefunction, is often referred to as the superconducting order parameter, in reference to Ginzburg Landau theory (which is discussed further in section 3.5.4). Indeed, it is a quantity which grows continuously from zero at a second order phase transition, in which all of the information relating to the symmetries and spin configuration of the superconducting state are encoded.

Pairing in unconventional superconductors does not generally arise from interactions with the crystal lattice, but instead from electron-electron interactions. In their 1965 paper, Kohn and Luttinger showed that Cooper pairing could occur based solely on the repulsive Coulomb interaction [61], and that no weakly interacting electronic system would remain normal down to absolute zero temperature. However this model leads to extremely low transition temperatures. Other types of pairing interactions, mainly based on spin-fluctuation exchanges, were later predicted. In these models the spins, which can either be localized or those of itinerant electrons, form a polarizable medium that can provide an attractive interaction between electrons, in a manner analogous to the polarizable crystal lattice for the electron-phonon interaction. These types of interactions are expected to occur in materials close to a magnetic instability. For example, in a 1986 paper which looks at the three-dimensional Hubbard model, it is shown that spin-fluctuation exchange occurring near a spin-density wave instability leads to *d*-wave pairing of electrons [62]. In general however there is no over-arching model which describes pairing in unconventional superconductors. Instead these are often studied on a case by case basis, and proving what the pairing mechanism is in each material is a very active field of research.

### 3.3 *d*-vector notation

In the case of an unconventional superconductor, the superconducting order parameter is no longer isotropic (i.e. it depends on the momentum  $\mathbf{k}$ ), and must be written as a matrix in order to take into account the different possible spin configurations of the Cooper pairs:

$$\Delta(\mathbf{k}) = \begin{pmatrix} \Delta_{\mathbf{k},\uparrow\uparrow} & \Delta_{\mathbf{k},\uparrow\downarrow} \\ \Delta_{\mathbf{k},\downarrow\uparrow} & \Delta_{\mathbf{k},\downarrow\downarrow} \end{pmatrix} \quad (3.3.1)$$

Using this  $2 \times 2$  matrix notation, we can represent a spin-singlet state by setting  $\Delta_{\mathbf{k},\uparrow\uparrow} = \Delta_{\mathbf{k},\downarrow\downarrow} = 0$  and  $\Delta_{\mathbf{k},\uparrow\downarrow} = -\Delta_{\mathbf{k},\downarrow\uparrow} = \Delta_s$ , and a spin-triplet state with  $\Delta_{\mathbf{k},\uparrow\downarrow} = \Delta_{\mathbf{k},\downarrow\uparrow} = \Delta_0$  and arbitrary values for  $\Delta_{\mathbf{k},\uparrow\uparrow}$  and  $\Delta_{\mathbf{k},\downarrow\downarrow}$ . To represent a spin-triplet state, we therefore need a three-component vector. A convenient notation

was introduced by Balian and Werthamer in 1963 [63], with the so called  $d$ -vector. We define the three components of the vector  $\mathbf{d}(\mathbf{k})$  such that:

$$\Delta(\mathbf{k}) = \begin{pmatrix} -d_x(\mathbf{k}) + id_y(\mathbf{k}) & d_z(\mathbf{k}) \\ d_z(\mathbf{k}) & d_x(\mathbf{k}) + id_y(\mathbf{k}) \end{pmatrix} = i(\mathbf{d}(\mathbf{k}) \cdot \boldsymbol{\sigma})\sigma_y, \quad (3.3.2)$$

where  $\boldsymbol{\sigma} = (\sigma_x, \sigma_y, \sigma_z)$  is the Pauli matrix vector. The spin and orbital states of the Cooper pairs, as well as the structure of the energy gap are all described by the  $d$ -vector, which is the order parameter of the triplet state. To see how this is the case, let us first consider how to write the wavefunction of a spin-triplet state. As the order parameter matrix (3.3.1) has the same symmetry properties as the pair wavefunction, we can write the triplet state down as a linear combination:

$$\Psi(\mathbf{k}) = \Delta_{\mathbf{k},\uparrow\uparrow}|\uparrow\uparrow\rangle + \Delta_{\mathbf{k},\downarrow\downarrow}|\downarrow\downarrow\rangle + \Delta_0(|\uparrow\downarrow\rangle + |\downarrow\uparrow\rangle) \quad (3.3.3)$$

where the spin quantization axis is taken along the  $z$ -direction. The three basis states  $|\uparrow\uparrow\rangle$ ,  $|\downarrow\downarrow\rangle$  and  $1/\sqrt{2}(|\uparrow\downarrow\rangle + |\downarrow\uparrow\rangle)$  then represent pairs with spin projections  $S_z = 1$ ,  $-1$  and  $0$  respectively. By plugging the definition of the  $d$ -vector (3.3.2) into (3.3.3), we can move to a new set of basis vectors [5]:

$$\begin{aligned} |x\rangle &= \frac{1}{\sqrt{2}}(|\downarrow\downarrow\rangle - |\uparrow\uparrow\rangle), \\ |y\rangle &= \frac{i}{\sqrt{2}}(|\uparrow\uparrow\rangle + |\downarrow\downarrow\rangle), \\ |z\rangle &= \frac{1}{\sqrt{2}}(|\uparrow\downarrow\rangle + |\downarrow\uparrow\rangle). \end{aligned}$$

The basis vectors  $|x\rangle$ ,  $|y\rangle$  and  $|z\rangle$  each have  $S_x = 0$ ,  $S_y = 0$ ,  $S_z = 0$  respectively. The triplet wavefunction (3.3.3) can now be re-written in terms of the  $d$ -vector:

$$\Psi(\mathbf{k}) = \sqrt{2}(d_x(\mathbf{k})|x\rangle + d_y(\mathbf{k})|y\rangle + d_z(\mathbf{k})|z\rangle). \quad (3.3.4)$$

The direction of the  $d$ -vector is orthogonal to that of the total spin vector  $\mathbf{S}$  of the Cooper pair. For example if we consider the simple case of  $\mathbf{d}(\mathbf{k}) = (0, 0, d_z)$ , we see immediately that  $\Delta_{\mathbf{k},\uparrow\uparrow} = \Delta_{\mathbf{k},\downarrow\downarrow} = 0$ , so  $S_z = 0$  and therefore  $\mathbf{d}(\mathbf{k})$  is perpendicular to  $\mathbf{S}$ , which lies in the  $xy$ -plane. The excitation spectrum, given by (3.1.4) in the case of an  $s$ -wave singlet superconductor, is modified to take into account the multiple gap components of the triplet state and is expressed in terms of the  $d$ -vector:

$$E_k = \sqrt{(\epsilon_k - E_F)^2 + \mathbf{d} \cdot \mathbf{d}^* \pm |\mathbf{d} \times \mathbf{d}^*|}. \quad (3.3.5)$$

Here we can make the distinction between unitary and non-unitary states. A unitary state has  $|\mathbf{d} \times \mathbf{d}^*| = 0$ , meaning that its gap is given simply by the modulus of  $\mathbf{d}$ . In the case of a non-unitary state  $|\mathbf{d} \times \mathbf{d}^*| \neq 0$ , meaning that there are two distinct energy gaps, leading to a double transition. It can happen that one of the gaps is

equal to zero, so that at  $T = 0$  not all of the electrons are in the condensate, thus reducing the condensation energy and making such a state harder to stabilise.

A common use of the  $d$ -vector is for the description of the different superfluid phases of  $^3\text{He}$  [65]. That of the A-phase, which is realised under pressure, is  $\mathbf{d}(\mathbf{k}) = \Delta_0 \hat{z}(k_x \pm ik_y)$ , whilst that of the B-phase is  $\mathbf{d}(\mathbf{k}) = \Delta_0(\hat{x}k_x + \hat{y}k_y + \hat{z}k_z)$ . Both of these are unitary states, whereas the A1-phase, which arises only with the application of a magnetic field, is a non-unitary state with  $\mathbf{d}(\mathbf{k}) = \Delta_0(\hat{x} + i\hat{y})(k_x + ik_y)$ . In the notation used here,  $\hat{x}$ ,  $\hat{y}$  and  $\hat{z}$  are unit vectors denoting a direction in spin-space, and  $k_x$  and  $k_y$  are the  $x$ - and  $y$ -components of the momentum at a point on the Fermi surface. To see how details of the pairing state can be extracted from the  $d$ -vector, let us look in more detail at the A-phase, an analogue of which is predicted to occur in  $\text{Sr}_2\text{RuO}_4$ .

### 3.4 Chiral $p$ -wave pairing

The pairing state described by  $\mathbf{d}(\mathbf{k}) = \Delta_0 \hat{z}(k_x \pm ik_y)$  is a state where the electron spins are confined to the  $xy$ -plane, as  $\mathbf{d}$  is parallel to  $\hat{z}$ . Additionally, both spins within a Cooper pair are aligned, in what is known as an *equal-spin pairing* state<sup>4</sup>. The orbital part has angular momentum  $l = 1$ , with  $m = \pm 1$ , as can be seen by looking at the corresponding spherical harmonic  $Y_l^m$ :

$$Y_1^{\pm 1} = \left(\frac{3}{8}\pi\right)^{1/2} \sin\theta \exp(\pm i\phi) \propto \left(\frac{3}{8}\pi\right)^{1/2} (k_x \pm ik_y) \quad (3.4.1)$$

This state is therefore a  $p$ -wave state, with the Cooper pairs' angular momentum pointing along  $\hat{z}$ , i.e.  $L_z = \pm\hbar$ . Both possible orientations of  $L_z$  are degenerate, so as  $T_c$  is crossed domains with different orientations can form within the sample. However, within a single domain all Cooper pairs possess the same angular momentum, leading to a macroscopic angular momentum of the condensate, and hence why the state is termed *chiral*. An illustration of a chiral  $p$ -wave Cooper pair is shown in Figure 3.1a.

As this state is unitary, its gap is given by  $|\Delta(\mathbf{k})|^2 = \mathbf{d} \cdot \mathbf{d}^* = k_x^2 + k_y^2$ . In the case of  $^3\text{He}$  where there is no crystal lattice, the Fermi surface is a sphere, and the gap has point nodes for  $\mathbf{k}$  along  $(0, 0, \pm 1)$ . For a two-dimensional electron gas with a cylindrical Fermi surface, the gap is completely isotropic in the plane and has no nodes, as shown in Figure 3.1b. The key difference to a state with an isotropic  $s$ -wave gap is that here the order parameter's phase changes continuously around the Fermi surface, reflecting the odd parity of the  $p$ -wave state. In the case of  $\text{Sr}_2\text{RuO}_4$ , which is a highly two-dimensional material, weak spin-orbit coupling is postulated

---

<sup>4</sup>To show that this is the case, one must rotate the coordinate system, for example, so that the basis vectors  $\hat{x}$ ,  $\hat{y}$  and  $\hat{z}$  become  $\hat{z}$ ,  $\hat{x}$  and  $\hat{y}$ . The spin quantization axis is then along the  $y$ -direction, and the paired spins are in an equal superposition of  $|\uparrow\uparrow\rangle_y$  and  $|\downarrow\downarrow\rangle_y$ . More generally, if a coordinate system can be chosen where  $d_z(\mathbf{k}) = 0$  for all  $\mathbf{k}$ , then the spins are in an *equal-spin pairing* state [65].

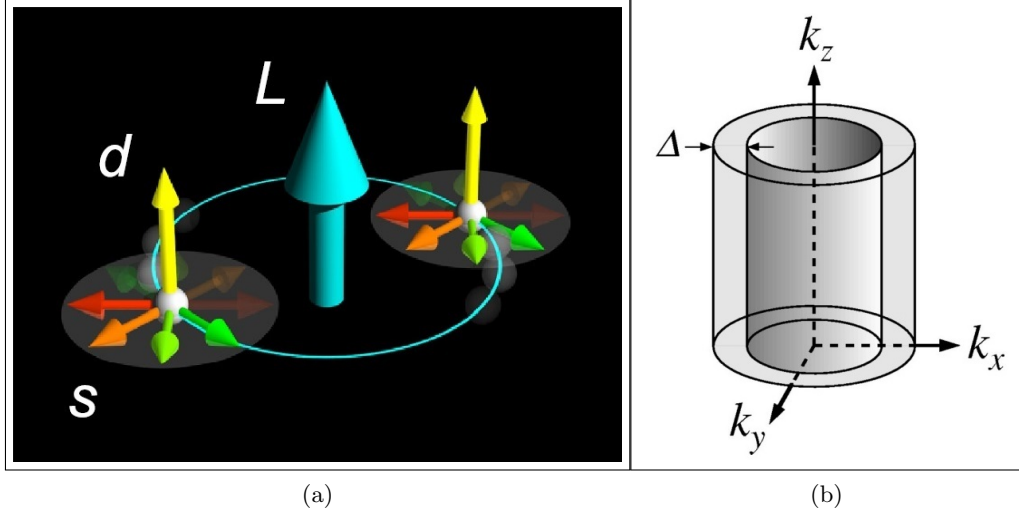


Figure 3.1: (a) A sketch of a Cooper pair with  $\mathbf{d}(\mathbf{k}) = \Delta_0 \hat{z}(k_x \pm ik_y)$ . The spins of both electrons are parallel, and confined to the plane perpendicular to the pair's angular momentum  $\mathbf{L}$ , illustrated by the blue arrow. The direction of the  $d$ -vector is shown by the yellow arrows. Image taken from ref. [69]. (b) The superconducting gap of the pairing state shown in Fig. 3.1a on a two-dimensional cylindrical Fermi surface, from ref. [5].

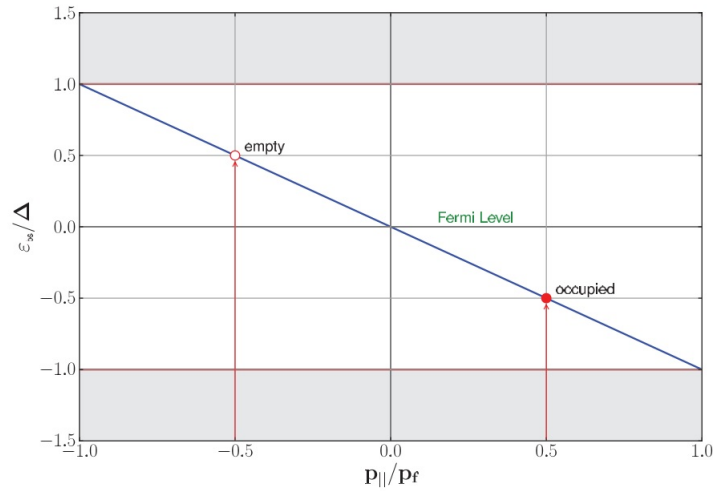


Figure 3.2: At a domain edge, the chiral  $p$ -wave state has mid-gap states which disperse linearly across the gap. The direction in which this occurs depends on the chirality of the order parameter. Here  $\mathbf{p}_{||}$  is the momentum component parallel to the edge. In the case illustrated only states with positive  $\mathbf{p}_{||}$  are occupied, resulting in a net flow of charge. From ref. [67].

to pin  $\hat{z}$  along the crystal  $c$ -axis, meaning that the electron spins are confined to the  $ab$ -plane and  $\mathbf{d}$  is along  $c$  [5].

An important feature of the chiral  $p$ -wave state is that it breaks time-reversal symmetry (TRS). Indeed, aside from gauge symmetry which has already been mentioned, others can in principle also be broken upon entering the superconducting state. For example in the case of the chiral  $p$ -wave state illustrated in Figure 3.1a, the rotational symmetry in spin-space is also broken [65]. The time-reversal operator is defined as  $\hat{K} = -i\hat{\sigma}^y\hat{C}$  where  $\hat{\sigma}^y$  is the  $y$  Pauli matrix and  $\hat{C}$  is the complex conjugation operator. Physically the time-reversal operation corresponds to reversing the momentum and flipping the spin of the electron. Applying this operator to the chiral  $p$ -wave state, we find that it is not invariant upon time-reversal and so breaks TRS. This broken TRS is associated with the spontaneous appearance of the macroscopic angular momentum of the condensate below  $T_c$  mentioned earlier.

It was predicted by Stone and Roy [66], and later by Sauls [67], that this broken TRS should result in the appearance of edge currents at domain walls and along the sample edge. In both papers, the total angular momentum of the condensate is shown to be  $L = N\hbar/2$ , where  $N$  is the number of paired electrons. This can intuitively be thought of as an angular momentum  $\hbar$  per Cooper pair. Other authors have however suggested that the condensate's angular momentum should be reduced by a factor of  $(\Delta/\varepsilon_F)^\alpha$ , where  $\alpha = 1$  or  $2$  [68], resulting in predictions for the angular momentum which range over several orders of magnitude. Although the energy spectrum is fully gapped in the bulk of the sample, at domain or sample edges a branch of chiral states appears. These states disperse linearly across the gap, as shown in Figure 3.2. The direction in which the branch crosses the gap (from negative to positive momentum or vice-versa) depends on the chirality of the condensate, and there is no branch crossing the gap in the other direction. In the case of Figure 3.2, mid-gap states with a positive momentum which lie below the Fermi level are occupied, whilst those with negative momentum are unoccupied. This results in a net charge current along the edge of the domain. The presence of these edge currents is a direct consequence of the topology of the order parameter, and so their existence is said to be *topologically protected*, although their magnitude is not.

### 3.5 The physics of $\text{Sr}_2\text{RuO}_4$

Having introduced some of the main concepts behind BCS theory and expanded those to unconventional superconductivity, let us now turn our attention towards  $\text{Sr}_2\text{RuO}_4$ .

After the discovery of the first high- $T_c$  cuprates in 1986 [56], superconductivity was searched for in many other compounds with similar crystal structures. This led to the discovery in 1994 of superconductivity in  $\text{Sr}_2\text{RuO}_4$ , the first known layered perovskite superconductor without copper [70]. Despite the similarity of its crystal structure to that of the high- $T_c$  cuprates,  $\text{Sr}_2\text{RuO}_4$  has a low transition temperature

of 1.5 K.  $\text{Sr}_2\text{RuO}_4$  is the  $n = 1$  member of the so-called Ruddlesden-Popper series  $\text{Sr}_{n+1}\text{Ru}_n\text{O}_{3n+1}$ , which also includes the paramagnetic metal  $\text{Sr}_3\text{Ru}_2\text{O}_7$  (discussed in detail in Section 2.5) and ferromagnets  $\text{Sr}_4\text{Ru}_3\text{O}_{10}$  and  $\text{SrRuO}_3$  as its  $n = 2, 3$  and  $\infty$  members respectively.

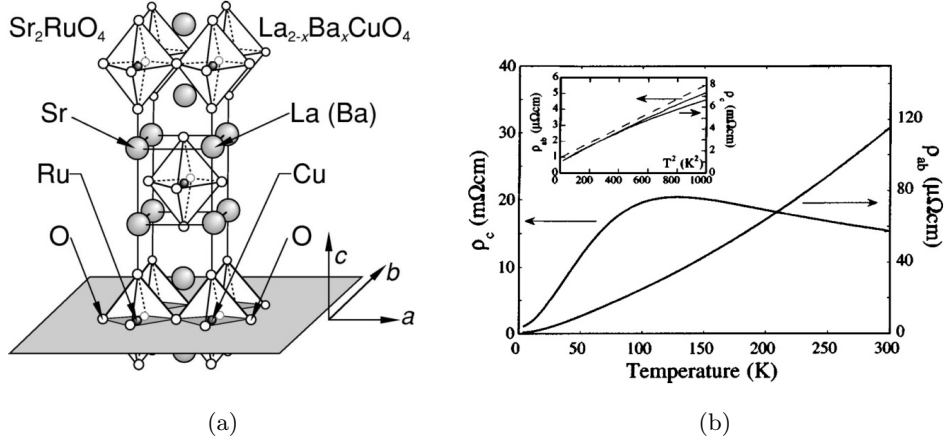


Figure 3.3: (a) Highly two-dimensional crystal structure of  $\text{Sr}_2\text{RuO}_4$ , which is identical to that of the parent cuprate compound  $\text{La}_2\text{CuO}_4$ . Illustration taken from [5]. (b) The temperature dependence of the resistivity within the  $ab$ -plane and along the  $c$ -axis shows that conduction in  $\text{Sr}_2\text{RuO}_4$  is very anisotropic [71].

$\text{Sr}_2\text{RuO}_4$  shares the same crystal structure as the parent compound  $\text{La}_2\text{CuO}_4$  of the La-Ba-Cu-O cuprate family, as shown in Figure 3.3a. Corner-sharing  $\text{RuO}_6$  octahedra with a Ru atom in their centres are arranged in a square lattice, forming two-dimensional planes. The spaces between the octahedra are occupied by Sr atoms, which act as spacers between the planes.  $\text{Sr}_2\text{RuO}_4$ 's space group symmetry is  $I4/mmm$  body-centred tetragonal, and its lattice parameters are  $a = 3.86 \text{ \AA}$  and  $c = 12.72 \text{ \AA}$ , as measured by neutron powder diffraction [72]. Therefore like the cuprates,  $\text{Sr}_2\text{RuO}_4$  is a highly two-dimensional material, with a large anisotropy between in-plane and out-of-plane conduction (Figure 3.3b). The anisotropy is temperature dependent, and its low temperature value is  $\rho_c/\rho_{ab} \approx 1000$ . However, unlike in the case of the cuprates where superconductivity emerges from a doped Mott insulator, the normal state of  $\text{Sr}_2\text{RuO}_4$  is metallic without the need for any chemical doping. Moreover,  $\text{Sr}_2\text{RuO}_4$  exhibits a well characterized Fermi liquid state below 20 K, displaying a  $T^2$  resistivity dependence and significant quasiparticle mass enhancement on each of its Fermi surface sheets, indicating strong electron correlations [5]. Its relatively low  $T_c$  in comparison to the onset of its Fermi liquid state indicates that superconductivity is taking place in the weak-coupling régime, and so the main BCS results discussed in Section 3.1 are applicable to it. This is in contrast with the cuprates which have complicated doping phase diagrams, where many regions display non-Fermi liquid behaviour, in particular directly above the peak of the superconducting dome [73]. Indeed, understanding the normal state of the cuprates

from which superconductivity condenses is a huge challenge, with all of the competing phases to take into account. The apparent simplicity of  $\text{Sr}_2\text{RuO}_4$ 's normal state makes it an ideal candidate for the study of unconventional superconductivity.

### 3.5.1 Electronic structure

The Fermi surface of  $\text{Sr}_2\text{RuO}_4$  consists of three sheets:  $\beta$  and  $\gamma$  which are electron-like, and  $\alpha$  which is hole-like. The shape of these sheets can be calculated from a simple two-dimensional tight-binding model, as described by Oguchi [75] and by Bergemann et al. [74], and of which we give an overview here.

Conduction in the  $ab$ -plane results from the  $\text{Ru}^{4+}$  electrons which are in a  $4d^4$  configuration, oxygen and strontium having the valencies  $\text{O}^{2-}$  and  $\text{Sr}^{2+}$ . The Ru  $4d$  energy levels are split in the octahedral crystal field into the low-lying  $t_{2g}$  states ( $d_{xy}, d_{xz}, d_{yz}$ ) and the excited  $e_g$  states ( $d_{x^2-y^2}, d_{r^2-3z^2}$ ). The  $t_{2g}$  states, which can accommodate up to six electrons, are therefore partially filled by the Ru  $4d^4$  electrons. Hence, from a tight-binding picture, the Fermi surface sheets are formed by the  $d_{xy}, d_{xz}$  and  $d_{yz}$  orbitals of the ruthenium atoms.

As the  $d_{xz}$  orbital extends mostly in the  $xz$ -plane, we expect nearest-neighbour electron hopping to occur primarily along the  $x$ -direction, with hopping along the  $z$ -direction being negligible due to the quasi-two-dimensional nature of  $\text{Sr}_2\text{RuO}_4$ . This gives a band energy which depends only on  $k_x$ , leading to an open Fermi surface sheet which runs perpendicular to the  $x$ -direction. Similarly, the  $d_{yz}$  orbital produces an open sheet perpendicular to the  $y$ -direction. The  $d_{xy}$  orbitals allow hopping along both in-plane directions, as well as next-nearest-neighbour hopping diagonally along the orbital lobes. This enables electrons to perform closed orbits in the  $xy$ -plane giving rise to the closed cylindrical sheet  $\gamma$  running along the  $z$ -direction. The  $d_{xz}$  and  $d_{yz}$  sheets hybridize, thus forming the  $\alpha$  pocket at the zone corners, and the  $\beta$  pocket at the zone centre, as illustrated in the sketch of the Fermi surface in Figure 3.4a.

The general shape of the Fermi surface thus obtained was confirmed by high resolution angle-resolved photo-emission (ARPES) measurements [76]. A further study of the Fermi surface was performed by analysing the angular dependence of de Haas-van Alphen (dHvA) oscillations. This resulted in a detailed map of  $\text{Sr}_2\text{RuO}_4$ 's Fermi surface, including the warping of the Fermi sheets which is responsible for conduction along the  $c$ -axis [77].

Also important to note about  $\text{Sr}_2\text{RuO}_4$ 's band structure is the proximity of the  $\gamma$ -sheet to a van Hove singularity at the M-point of the Brillouin zone. A van Hove singularity corresponds to a peak in the density of states, which results from a local minimum, maximum or saddle point in the electronic dispersion. The existence of the van Hove point can be shown by performing a tight-binding fit to dHvA data [74], and was directly observed to lie 14 meV above the Fermi level by ARPES [78].

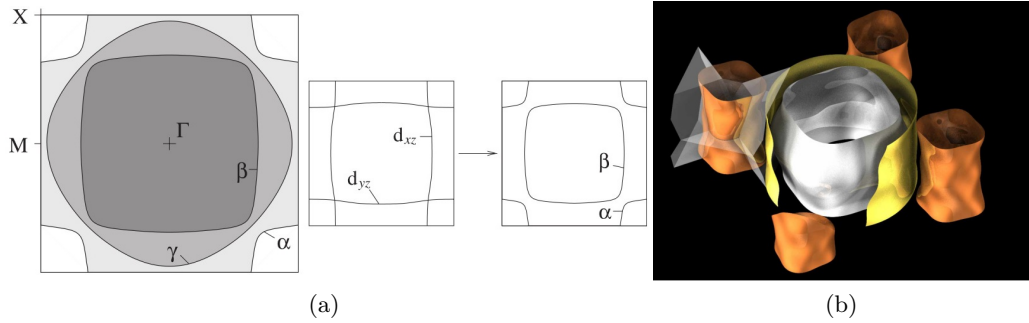


Figure 3.4: (a) Sketch of the Fermi surface of  $\text{Sr}_2\text{RuO}_4$  as calculated from a two-dimensional tight-binding model. The formation of the  $\alpha$  and  $\beta$  sheets from the hybridization of the  $d_{xz}$  and  $d_{yz}$  orbitals is shown in the smaller sketches. (b) Visualization of  $\text{Sr}_2\text{RuO}_4$ 's Fermi surface, with the  $c$ -axis warping exaggerated by a factor of 15. Both images are taken from [74].

### 3.5.2 Evidence for spin-triplet superconductivity in $\text{Sr}_2\text{RuO}_4$

The unconventional nature of  $\text{Sr}_2\text{RuO}_4$ 's superconductivity was demonstrated by the sensitivity of its  $T_c$  to the presence of non-magnetic impurities. As we have seen,  $s$ -wave superconductors have a gap whose phase is  $\mathbf{k}$ -independent, whereas for an unconventional superconductor the gap sums to zero over the whole Fermi surface (equation (3.2.2)). Impurities in the crystal lattice cause elastic scattering which mixes all of the  $\mathbf{k}$ -states, effectively averaging the gap over the Fermi surface. This does not affect isotropic  $s$ -wave superconductors, however it can completely destroy the superconductivity in an unconventional superconductor, as its order parameter is averaged to zero by strong scattering. It was found that superconductivity in  $\text{Sr}_2\text{RuO}_4$  is strongly suppressed with increasing presence of non-magnetic impurities, and that it is completely destroyed in samples with a residual resistivity above  $1 \mu\Omega\text{cm}$  [79], clearly showing it to be unconventional.

Further interest in  $\text{Sr}_2\text{RuO}_4$  was sparked when it was found that its Landau parameters were very similar to those of  $^3\text{He}$ , leading to the first proposals of spin-triplet superconductivity in this material [6]. In addition,  $\text{Sr}_2\text{RuO}_4$  is believed to be close to a ferromagnetic state, which also suggests that Cooper pairing should occur in the triplet channel. This is evidenced both by the  $\gamma$ -sheet's proximity to a van Hove point and the presence of ferromagnetism in  $\text{Sr}_2\text{RuO}_4$ 's three-dimensional analogue  $\text{SrRuO}_3$ .

Strong experimental evidence for spin-triplet superconductivity in  $\text{Sr}_2\text{RuO}_4$  is provided by studies of its spin-susceptibility  $\chi_s$  via measurements of the Knight shift. The spin susceptibility of a metal results from the Zeeman splitting of its Fermi surface in a magnetic field into two spin-polarized Fermi surfaces. In the case of a spin-singlet superconductor, where the Cooper pairs are formed by electrons whose spins are anti-aligned (total spin  $S = 0$ ), the splitting of the Fermi surface

in a magnetic field competes with the formation of Cooper pairs. Indeed, to form a Cooper pair, electrons with states  $(\mathbf{k}, \uparrow)$  and  $(-\mathbf{k}, \downarrow)$  must exist at the Fermi surface. At low magnetic fields, the superconducting condensation energy is greater than the lowering of the free energy  $\frac{1}{2}\chi_s H^2$  due to Zeeman splitting, and so  $\chi_s$  is suppressed below  $T_c$ . However, in the case of a spin-triplet superconductor in which the Cooper pairs are equal-spin paired ( $S = 1$ ), there is no such competition between electron pairing and Zeeman effect, so there is no change in  $\chi_s$  across the superconducting transition.

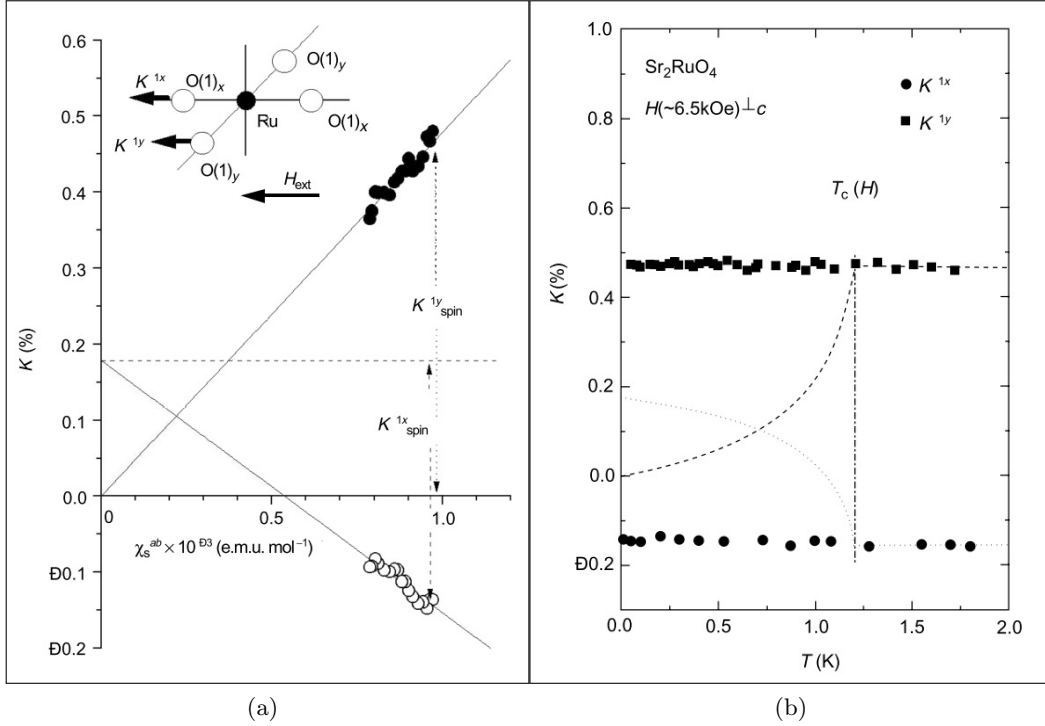


Figure 3.5: (a) Plot of the Knight shift against spin susceptibility  $\chi_s$  for the two oxygen sites shown in the inset, temperature being an implicit parameter. The values of  $K_{orb}$  are found to be 0.18% and 0% for O(1) $_x$  and O(1) $_y$  respectively. (b) Evolution of the Knight shift measured at the two oxygen sites across  $\text{Sr}_2\text{RuO}_4$ 's transition temperature, with the field applied in-plane. The dashed lines show a calculation of the evolution of  $K$  for a spin-singlet  $d_{x^2-y^2}$  state, such as that which occurs in the high- $T_c$  cuprates.

In a superconductor one cannot probe the spin susceptibility directly, due to the Meissner effect. However, by measuring the Knight shift in the nuclear magnetic resonance (NMR) frequency, one can probe  $\chi_s$  indirectly. The Knight shift corresponds to the shift in NMR frequency of the nucleus due to the presence of conduction electrons, as compared to when it is in an insulator. The NMR frequency  $\omega$  can be

written  $\omega = \gamma_{gyr} B_{int}(1 + K_{orb} + K_{spin})$ , with  $\gamma_{gyr}$  the gyromagnetic ratio,  $B_{int}$  the magnetic field in the sample, and  $K_{orb}$  and  $K_{spin}$  the orbital and spin parts of the Knight shift respectively [5].

Ishida et al. measured the Knight shift in  $\text{Sr}_2\text{RuO}_4$  with the magnetic field applied perpendicular to the  $c$ -axis [8], and found that it remained constant across  $T_c$  (Figure 3.5b). In a narrow band system such as  $\text{Sr}_2\text{RuO}_4$ ,  $K_{spin}$  is directly related to  $\chi_s$  by the hyperfine coupling constant  $A$  so that the total Knight shift is  $K = A\chi_s + K_{orb}$ . The measurements were performed on the two inequivalent oxygen sites labelled  $\text{O}(1)_x$  and  $\text{O}(1)_y$ , and the contribution of  $K_{orb}$  to the total Knight shift was found by measuring  $K(\chi_s)$  (Figure 3.5a). The constant nature of the Knight shift observed strongly contrasts with the behaviour expected for a spin-singlet superconductor, where  $K$  is strongly suppressed below  $T_c$  as shown by the dashed lines in Figure 3.5b. This result is therefore consistent with Cooper pairs in equal-spin pairing states  $|\uparrow\uparrow\rangle$  and  $|\downarrow\downarrow\rangle$  where the spins are lying in the  $ab$ -plane. Such a state therefore has a  $d$ -vector which points along the  $c$ -axis. Since Ishida's initial experiment, this measurement has been repeated several times at different fields as well as on the Ru sites [69], giving multiple confirmations of the constant Knight shift across  $T_c$ .

Nevertheless there are still some unresolved questions surrounding the spin configuration of the Cooper pairs. If the spins lie in the plane in an equal-spin pairing state, then one would expect to see a decrease in the Knight shift below  $T_c$  for measurements with the magnetic field applied along the  $c$ -axis. This experiment was successfully carried out by Murakawa et al. in a testing field of 0.02 T, who observed no change of the Knight shift across  $T_c$  within experimental error [80]. This result suggests a state where the  $d$ -vector lies within the  $ab$ -plane, in conflict with the initial NMR result. A possible scenario put forward by the authors to resolve this issue is that the  $d$ -vector is extremely weakly pinned to the  $c$ -axis by spin-orbit interaction in zero applied field, but with fields as low as 0.02 T can be made to re-orient itself along the  $ab$ -plane. There is however some controversy surrounding this interpretation of the data, as Zutic and Mazin [81] point out that for the above scenario to be true, the spin-orbit interaction which keeps the paired spins in the  $ab$ -plane must be weaker than the applied 0.02 T. This field corresponds to an energy scale of  $1.1 \mu\text{eV}$ , which is much smaller than that of spin-orbit coupling in  $\text{Sr}_2\text{RuO}_4$ .

### 3.5.3 Evidence for chiral $p$ -wave superconductivity

Having established that  $\text{Sr}_2\text{RuO}_4$  is most likely a spin-triplet superconductor, the orbital part of its order parameter must be odd to preserve the overall anti-symmetry of the pair wavefunction. The most likely state is therefore  $p$ -wave, as higher angular momentum states such as  $f$ -wave generally have higher energy (although this can depend on the details of the interaction). A list of the  $p$ -wave states allowed for a tetragonal crystal with a cylindrical Fermi surface is given in [5]. Among these are both unitary and non-unitary states. As we discussed in Section 3.3, non-unitary states lead to a double superconducting transition and in general have a lower

condensation energy than their unitary counterparts. Because there is no evidence for a double transition or a residual electronic specific heat in clean  $\text{Sr}_2\text{RuO}_4$ , the search for its order parameter is focused on unitary states.

As we will see below, there is experimental evidence that  $\text{Sr}_2\text{RuO}_4$ 's order parameter breaks time-reversal symmetry (TRS). The only allowed unitary  $p$ -wave order parameter which breaks TRS is  $\mathbf{d}(\mathbf{k}) = \Delta_0 \hat{z}(k_x \pm ik_y)$ , which we described in Section 3.4. One of the key features of this state is that it results in topologically protected edge currents. The edge current flows within a width of approximately the coherence length from the edge, which is  $\xi = 66$  nm in  $\text{Sr}_2\text{RuO}_4$ . The screening current which flows to cancel out the field in the bulk of the sample will itself be distributed within the penetration depth  $\lambda = 152$  nm of the edge. Hence, due to the difference between  $\xi$  and  $\lambda$ , there should be a non-zero magnetic field which arises at domain edges and impurities, which has been estimated to be of the order of 10 G [82].

The first experiment which indicated the appearance of spontaneous magnetic fields in  $\text{Sr}_2\text{RuO}_4$  below  $T_c$  was muon spin-relaxation ( $\mu\text{SR}$ ) performed by Luke et al. in 1998 [83]. In a  $\mu\text{SR}$  measurement, spin-polarized muons are injected into the sample where they come to rest at a typical depth of 0.1 nm. The muon then interacts with the local magnetic environment before decaying and emitting a positron preferentially in the direction of its spin at the time of decay. By measuring many such decays (of the order of  $10^7$ ), the decay rate can be determined and a histogram of the muon polarization after implantation deduced. In a sample with zero magnetization, the muon spin relaxes via interactions with the randomly orientated nuclear dipole moments. In the presence of magnetic order or a distribution of local fields, the relaxation rate is expected to increase. As can be seen from Luke et al.'s data in Figure 3.6, an increase of the muon spin-relaxation rate is observed at the onset of superconductivity. They checked that the increased relaxation rate was a consequence of the superconductivity and not a magnetic state which happened to appear near  $T_c$  by measuring samples with different  $T_c$ 's. They found that the increased relaxation always occurred at the  $T_c$  of the sample, and concluded that the onset of superconductivity in  $\text{Sr}_2\text{RuO}_4$  is accompanied by the spontaneous appearance of magnetic fields within the sample. Further, they argued that the exponential nature of the increase in the relaxation rate reveals a broad distribution of fields within the sample. This is consistent with the model described above where local magnetic fields are expected to occur at impurities or domain edges.

Another experiment which shows strong evidence of broken TRS is the measurement of the magneto-optic Kerr effect. In this technique, linearly polarized light is shone on the sample surface, and the angle of polarization  $\theta_k$  (known as the Kerr angle) of the reflected light is measured. The rotation of the direction of polarization is a consequence of broken TRS at the sample surface, and  $\theta_k$  is directly related to the Hall conductivity  $\sigma_{xy}$ . For example Kerr rotation occurs in the case where the sample is magnetic, and the direction and magnitude of the rotation depend on the magnetization perpendicular to the surface. A common application of this technique

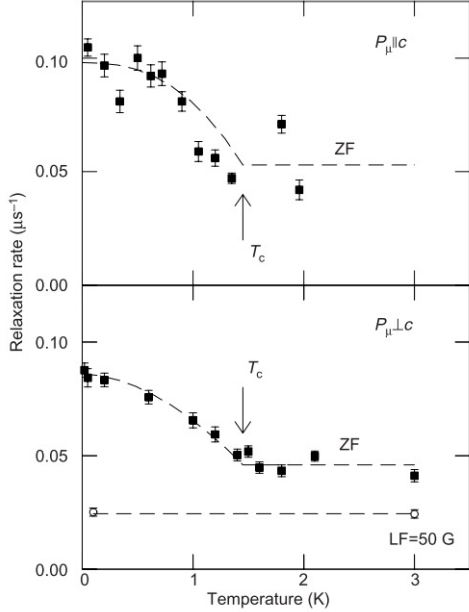


Figure 3.6: The muon spin-relaxation rate is shown as a function of temperature for  $\text{Sr}_2\text{RuO}_4$ . The relaxation rate is seen to increase at the onset of superconductivity, for measurements with the muon spin polarization  $P_\mu$  parallel and perpendicular to the  $c$ -axis. This is believed to be a signature of broken TRS in the superconducting state. From ref. [83].

is therefore the imaging of domains in a ferromagnet.

To measure the Kerr effect in  $\text{Sr}_2\text{RuO}_4$ , J. Xia et al. used a high-precision Sagnac interferometer [7]. They found a non-zero Kerr angle appearing below  $T_c$  with a maximum magnitude of approximately 65 nrad (Figure 3.7a). They performed a series of measurements where the sample was cooled in zero field, and found that the magnitude and sign of  $\theta_k$  were not always the same. They assigned the sign change of  $\theta_k$  to the incident beam falling on domains of different chirality over the many runs, as the chirality should determine the direction of the Kerr rotation. The reduction of  $\theta_k$ 's magnitude could therefore result from the beam falling on a domain wall, which would give a reduced average signal. The beam size used was 25  $\mu\text{m}$ , which led J. Xia et al. to hypothesize that the domains should be of the order of 50-100  $\mu\text{m}$ , as they measured an unreduced  $\theta_k$  roughly half of the time.

A TRS breaking field such as a magnetic field couples to the order parameter  $\mathbf{d}(\mathbf{k}) = \Delta_0 \hat{z}(k_x \pm ik_y)$ , and lifts the degeneracy between the two chiralities by favoring one over the other. Hence by cooling the sample in a magnetic field, one should obtain a single large superconducting domain with a specific chirality. J. Xia et al. tested this effect in  $\text{Sr}_2\text{RuO}_4$ , and found that they could “select” the sign of  $\theta_k$  with the direction in which the magnetic field was applied during cooling (Figure 3.7b). Moreover the magnitude of the signal matched the maximum value obtained in the zero field cooling measurements, which is consistent with the presence of a large single domain in the sample.

Taken together the results from the  $\mu\text{SR}$  [83] and Kerr effect measurements [7] strongly indicate that  $\text{Sr}_2\text{RuO}_4$ 's superconducting state breaks time-reversal symmetry. The corresponding order is therefore proposed to be  $\mathbf{d}(\mathbf{k}) = \Delta_0 \hat{z}(k_x \pm ik_y)$ ,

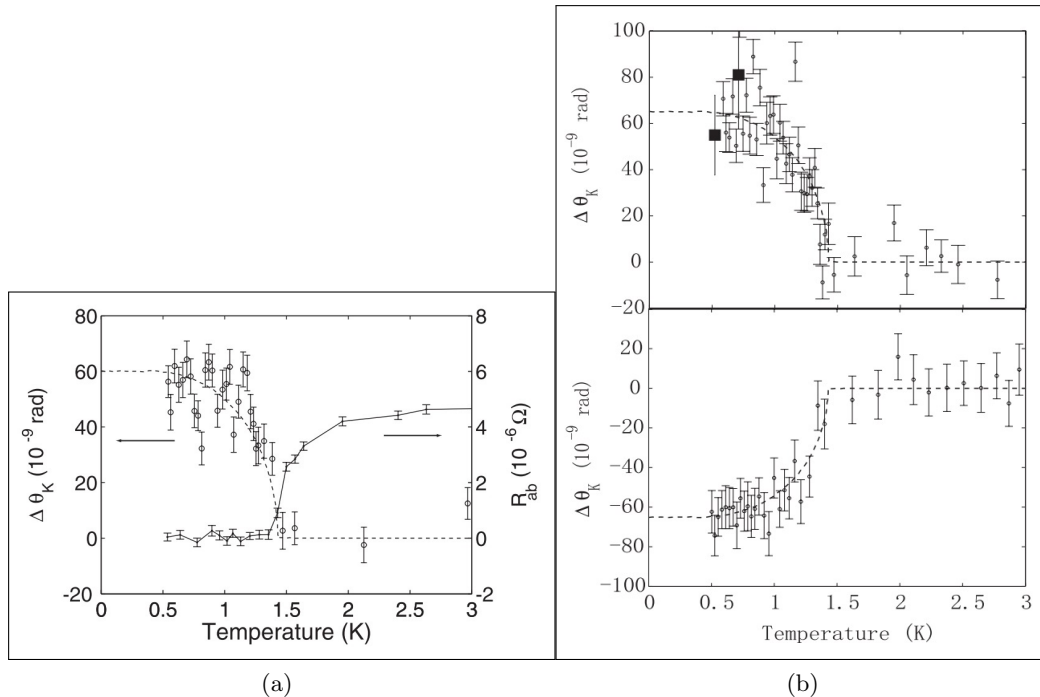


Figure 3.7: (a) Kerr rotation angle measured against temperature for a sample cooled in zero field. The resistance of the sample is plotted on the same graph, showing that the non-zero Kerr rotation occurs at the superconducting transition. Each Kerr angle data point was taken on warming up the sample, and corresponds to an averaging time of 1600 s. (b) Kerr rotation angle for a sample cooled in a magnetic field of +93 Oe (upper panel) and -47 Oe (lower panel). Graphs from ref. [7].

as this is the only one which has odd parity, is unitary, satisfies the tetragonal lattice symmetry and breaks TRS. Evidence of domains with different chirality within the sample further supports this order parameter. It should be pointed out however that spin-orbit coupling, which is often overlooked despite being neither weak nor constant across the Brillouin zone, could have a significant effect on the superconductivity. For example Scaffidi et al. [84] found that, by including spin-orbit coupling and multiband effects in their calculations, they obtained *pseudospin*-triplet<sup>5</sup> order parameters, the details of which strongly depend on the relative magnitudes of the gaps on the different Fermi sheets.

One of the more striking features of the chiral *p*-wave state is the presence of edge currents, which we discussed in Section 3.4. The  $\mu$ SR data are believed to provide indirect evidence of the edge currents, as the increased relaxation rate is assigned to

<sup>5</sup>In the presence of spin-orbit coupling spin is no longer a good quantum number, and pseudospin is used as a quantum degree of freedom which is analogous to spin.

a distribution of local magnetic fields associated with the presence of edge currents. The direct measurement of these edge currents would therefore provide conclusive evidence of the superconducting state's broken TRS and confirm it as an analogue to the  $^3\text{He}$  A-phase.

However to date no search for these edge currents has been successful. One such search was carried out by Hicks et al. using a SQUID magnetometer which could be scanned along the sample edge [85]. In this experiment no magnetic signal of the expected magnitude was detected, meaning that an upper limit on the existing edge currents could be estimated. Hicks et al. determined that for their measurement to be consistent with the presence of edge currents, these would have to be less than  $\sim 0.2\%$  of the magnitude of those predicted, or alternatively that the domains are of the order of 30 nm in size assuming they were randomly distributed. Such a small domain size would however be incompatible with the interpretation of the Kerr effect measurement. Additionally the formation of such small domains appears energetically unfavourable due to the loss of condensation energy which occurs at domain walls.

The apparent lack of edge currents remains an unsolved puzzle, and casts doubt on the nature of  $\text{Sr}_2\text{RuO}_4$ 's order parameter. Several explanations have been put forward to account for the lack of edge currents, many relating to the superconducting gap structure. As we saw in Section 3.4, the gap of the state  $\mathbf{d}(\mathbf{k}) = \Delta_0 \hat{z}(k_x \pm ik_y)$  on a cylindrical Fermi surface is isotropic with no nodes. Nevertheless compelling evidence for line nodes or near-nodes has been found in experiment, indicating that  $\text{Sr}_2\text{RuO}_4$ 's superconducting state is not isotropic. A typical method of looking for nodes is by measuring the specific heat. In a nodeless weak-coupling superconductor, the specific heat decreases exponentially at low temperatures according to BCS theory [54]. However in the presence of nodes, quasiparticle excitations are still possible down to low temperatures, which leads to a power-law dependence of the specific heat. Although  $\text{Sr}_2\text{RuO}_4$ 's specific heat displays a power-law temperature dependence below  $T_c$ , indicating the presence of nodes, there is some controversy about their location and orientation. Indeed there are claims that they are either horizontal [86], or run vertically along the  $\gamma$  sheet in the (100) directions [87, 88]. Regardless of the location of the nodes, it has been argued that the presence of line nodes could significantly alter the predictions for edge currents, by mixing the chiral edge states with low-lying modes in the presence of defects [89].

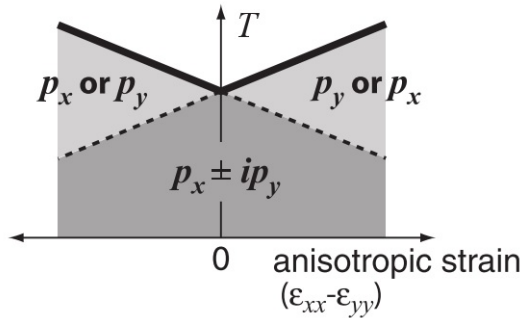
Models where the superconductivity occurs mainly on the quasi-one-dimensional  $\alpha$  and  $\beta$  bands have also been used to explain the absence of edge currents. For example in a renormalization group calculation, S. Raghu and collaborators found that superconducting gaps with a chiral  $p$ -wave nature open up on the  $\alpha$  and  $\beta$  bands [90]. The so-called *Chern number*, which describes the topological properties of the chiral  $p$ -wave state, depends on the chirality of the condensate and the sign of the charge carriers. As the  $\alpha$  and  $\beta$  bands are hole- and electron-like respectively, their respective Chern numbers are of opposite sign, so that the total Chern number of the system is zero. This results in the overall superconducting state being topologically

trivial, meaning that even though edge states may exist, they are not topologically protected. This calculation was further extended to include spin-orbit coupling and multi-band effects, which lead to gaps of similar magnitude opening up on all three bands. The superconducting state which is predicted in this case is chiral and breaks time-reversal symmetry, however has a large Chern number resulting in a strong reduction of the edge currents [91].

### 3.5.4 Uni-axial strain as a probe of the superconducting order parameter

We have seen in the previous section that even though there is significant experimental evidence in favor of chiral  $p$ -wave, the order parameter for  $\text{Sr}_2\text{RuO}_4$ 's superconducting state has not yet been unambiguously established. Many open questions remain regarding superconductivity in  $\text{Sr}_2\text{RuO}_4$ , such as why no edge currents have been detected or what the gap structure is and whether there are nodes. To shed more light on this issue, we propose here to use uni-axial strain as a new means of probing the order parameter.

Figure 3.8: Sketch of the phase diagram expected for a  $p_x \pm ip_y$  superconductor. In-plane anisotropic strain lifts the degeneracy between  $p_x$  and  $p_y$  and splits their transition temperatures. If  $T_c$  is measured with a probe which is mainly sensitive to the upper transition, the observed  $T_c$  versus strain will be the thick black line. From [92].



By straining a tetragonal lattice along one of its in-plane crystal axes, the tetragonal symmetry will be broken. If the superconducting order parameter is of the form  $p_x \pm ip_y$ , the components  $p_x$  and  $p_y$  are degenerate at zero strain and have the same  $T_c$ . However when the tetragonal symmetry is lifted by anisotropic in-plane strain, the degeneracy between both components is also lifted and their transition temperatures split. Based solely on arguments of symmetry, this leads to a phase diagram as shown in Figure 3.8. If one were to measure  $T_c$  with probes such as resistivity or AC magnetic susceptibility, which are only sensitive to the upper transition where the sample first goes superconducting, the  $T_c$  versus strain curve which would be obtained is expected to follow the thick black line in Figure 3.8. The sharp change in the slope of  $T_c$  versus strain at zero strain would be a clear signature of a two-component order parameter.

The phase diagram from Figure 3.8 can be derived by considering the Landau free energy for a two-component order parameter. Let us first recall the case of a single component order parameter, where, in the absence of fields and gradients the

Landau free energy can be written:

$$F = a(T - T_c)|\Delta|^2 + \beta|\Delta|^4. \quad (3.5.1)$$

This expansion of the free energy in powers of the order parameter  $\Delta$  is valid when  $\Delta$  is small, in other words close to the transition temperature. If  $\alpha \equiv a(T - T_c)$  is positive, the minimum of the free energy is at  $\Delta = 0$  and the system is in the normal state. If  $\alpha$  is negative,  $F$  has a minimum for  $|\Delta|^2 = -\alpha/2\beta$ , corresponding to the superconducting state.  $T_c$  is thus given by the temperature at which  $\alpha$  changes sign. Extending (3.5.1) to a system with two degenerate order parameters on an unstrained lattice, we can write the free energy as [10]:

$$F = a(T - T_{c,0})(|\Delta_x|^2 + |\Delta_y|^2) + \beta_1(|\Delta_x|^4 + |\Delta_y|^4) + \frac{\beta_2}{2}(\Delta_x^{*2}\Delta_y^2 + \Delta_x^2\Delta_y^{*2}) + \beta_3|\Delta_x|^2|\Delta_y|^2 \quad (3.5.2)$$

where  $T_{c,0}$  is the transition temperature at zero strain. By inspection we see that parameter  $\beta_2$  determines the relative phase of  $\Delta_x$  and  $\Delta_y$ , depending on its sign. If  $\beta_2 > 0$ , the free energy is lowest for a state with broken time-reversal symmetry such as  $(\Delta_x, \Delta_y) = (1, \pm i)$ . On the other hand if  $\beta_2 < 0$ , a state with no phase difference between the two components is favored, such as  $p_x \pm p_y$ . As we wish to consider the state where TRS is broken, let us set  $\beta_2 > 0$ . We then have  $(\Delta_x^{*2}\Delta_y^2 + \Delta_x^2\Delta_y^{*2}) = -2|\Delta_x|^2|\Delta_y|^2$ , so that we can simplify the fourth order terms in equation (3.5.2) to:

$$\beta_1(|\Delta_x|^4 + |\Delta_y|^4) + \beta_I|\Delta_x|^2|\Delta_y|^2 \quad (3.5.3)$$

with  $\beta_I = \beta_3 - |\beta_2|$ .  $\beta_I$  then describes the interaction between the two order parameters. If  $\beta_I < 0$ , there is a cooperative interaction between the two. In other words the free energy is minimized by both  $\Delta_x$  and  $\Delta_y$  being large, so there is no competition between them. However if  $\beta_I > 0$ , the two order parameters compete meaning that, for example, a large  $\Delta_x$  results in a small  $\Delta_y$ . If we now wish to include the effects of strain along [100] in the free energy, (3.5.2) must be modified in the following manner [10]:

$$F \rightarrow F + \alpha_x\varepsilon_{100}|\Delta_x|^2 + \alpha_y\varepsilon_{100}|\Delta_y|^2 \quad (3.5.4)$$

The constants  $\alpha_x$  and  $\alpha_y$  couple the strain  $\varepsilon_{100}$  along [100] with the  $x$  and  $y$  order parameters. The strain along the  $x$ -direction is given by  $\varepsilon_{xx} = \varepsilon_{100}$ , along the transverse direction by  $\varepsilon_{yy} = -0.4\varepsilon_{100}$  and along the  $z$ -direction by  $\varepsilon_{zz} = -0.2\varepsilon_{100}$ , as the in-plane and out-of-plane Poisson's ratios for  $\text{Sr}_2\text{RuO}_4$  are  $\sim 0.4$  and  $\sim 0.2$  respectively [93]. We assume that there is no shear within the sample:  $\varepsilon_{xy} = 0$ . A more detailed discussion of the strain tensor is given in Section 4.1.2. Using the strain dependent Landau free energy from (3.5.4), we can now calculate the transition temperature for each order parameter by finding where the coefficients of the quadratic terms  $|\Delta_x|^2$  and  $|\Delta_y|^2$  each change sign. Let us start with the case where

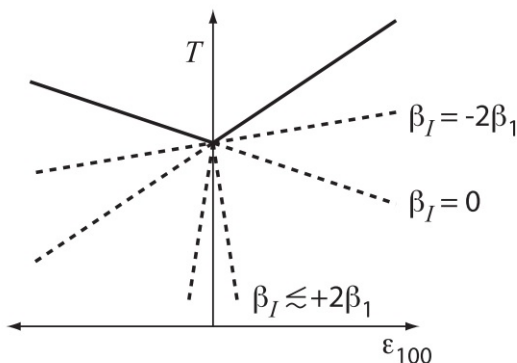
$\beta_I = 0$  so that there are no interactions between the order parameters. This yields  $T_{c,x} = T_{c,0} - \alpha_x \varepsilon_{100}/a$  and  $T_{c,y} = T_{c,0} - \alpha_y \varepsilon_{100}/a$  for the two transition temperatures. Hence  $T_{c,x}$  and  $T_{c,y}$  will be different when  $\varepsilon_{100} \neq 0$ , and if in experiment only the higher transition is observed,  $T_c(\varepsilon_{100})$  will vary linearly, with a sharp discontinuity in its slope at zero strain when the system switches between  $T_{c,x}$  and  $T_{c,y}$ .

The upper transition is not affected by the value of  $\beta_I$ , as when the system first goes superconducting only one of the order parameters is non-zero, and so  $\beta_I |\Delta_x|^2 |\Delta_y|^2 = 0$  (except at  $\varepsilon_{100} = 0$ ). If  $\beta_I = 0$ , there is no interaction between the order parameters and the slopes of  $T_{c,x}$  and  $T_{c,y}$  do not change below the upper transition. On the other hand if  $\beta_I \neq 0$ , the lower transition is affected by the presence of the other order. For example, if we consider the case where  $T_{c,x}$  is the highest transition, we can write  $|\Delta_x|^2 = -a(T - T_{c,x})/2\beta_1$  for  $T_{c,y} < T < T_{c,x}$ . Substituting this into the Landau free energy (3.5.4) and setting the coefficient of  $|\Delta_y|^2$  to zero, we find:

$$T_{c,y} = \frac{T_{c,y0} - bT_{c,x}}{1 - b} \quad (3.5.5)$$

where  $b = \beta_I/2\beta_1$  and  $T_{c,y0}$  is the  $T_{c,y}$  found above for  $\beta_I = 0$ . Equivalently we can calculate the modified  $T_{c,x}$  by reversing  $x$  and  $y$  in the derivation and considering the other half of the phase diagram. From (3.5.5) we can see that if  $b \geq 1$  (i.e. competition between the two orders is strong),  $T_{c,y}$  is never positive and  $p_y$  superconductivity is completely suppressed by the presence of  $p_x$ . The phase diagram from Figure 3.8 is illustrated in Figure 3.9 for different values of  $\beta_I$ .

Figure 3.9: Phase diagram from Figure 3.8 showing how the lower transition is modified depending on the strength of the interaction  $\beta_I$  between the two order parameters. A slight asymmetry between positive and negative strain  $\varepsilon_{100}$  results from the in-plane Poisson's ratio of  $\sim 0.4$  for  $\text{Sr}_2\text{RuO}_4$ . Taken from [92].



One might wonder whether a cusp at zero strain would also occur in the case of two nearly degenerate order parameters, or whether this feature is specific to the degenerate case. As an example, one could consider two non-degenerate order parameters  $\Delta_s$  and  $\Delta_d$  corresponding to  $s$ - and  $d$ -wave states. The Landau free energy is then the sum of the free energies for each order parameter plus an interaction term:

$$F = a_s(T - T_{c,s0})|\Delta_s|^2 + \beta_s|\Delta_s|^4 + a_d(T - T_{c,d0})|\Delta_d|^2 + \beta_d|\Delta_d|^4 + \beta_I|\Delta_s|^2|\Delta_d|^2. \quad (3.5.6)$$

By performing an analysis similar to that described above, it can be shown that whilst the terms containing a single order parameter give a linear dependence of  $T_{c,s}$  and  $T_{c,d}$  on strain, the interaction term leads to a quadratic dependence [92]:

$$T_{c,s} = T_{c,s0} + \frac{2\alpha^2\varepsilon_{100}^2}{a_s a_d (T_{c,s0} - T_{c,d0})}. \quad (3.5.7)$$

Therefore although there is a change of slope in  $T_c(\varepsilon_{100})$  at zero strain due to the switching of the linear term between  $T_{c,s0}$  and  $T_{c,d0}$ , it varies quadratically for small strains on either side of zero strain. This is in contrast with the case with degenerate order parameters, where  $T_c(\varepsilon_{100})$  varies linearly and has a sharp cusp at zero strain.

To summarize, we have shown that in-plane anisotropic strain can be an effective way of probing the superconducting order parameter. In the case of a  $p_x \pm ip_y$  superconductor, we can tune continuously between states where TRS is not broken ( $p_x$  or  $p_y$ ) and one where it is ( $p_x \pm ip_y$ ). A clear signature of a  $p_x \pm ip_y$  superconductor should then be a linear variation of  $T_c$  with strain for small strains, and a cusp at zero strain. A superconducting state which is a mixture of two non-degenerate order parameters would on the other hand give a quadratic dependence on strain. We therefore propose to test the prediction shown in Figure 3.8 for  $\text{Sr}_2\text{RuO}_4$ , by measuring its  $T_c$  as a function of applied strain. The details of the experimental set-up used are described in Chapter 4, and the results of the measurement are shown in Chapter 5.

### 3.6 Summary

In this chapter we have described the building blocks of BCS theory and some of its main predictions, such as the quasiparticle excitation spectrum (3.1.4). As the details of the pairing interaction do not enter the derivation of BCS theory, its main results can also be applied to unconventional (i.e. non- $s$ -wave) superconductors within the weak-coupling régime. We showed how different spin and orbital wavefunctions can be combined to form the Cooper pair wavefunction, as long as the condition for overall antisymmetry of the wavefunction is satisfied. In particular we focused on the possibility of spin-triplet pairing, and how such a state could be described in terms of the  $d$ -vector, which is a useful order parameter of the state. It turns out that the perovskite  $\text{Sr}_2\text{RuO}_4$ , which is isostructural to the parent compound of the La-Ba-Cu-O family of high- $T_c$  cuprates, is a leading candidate for spin-triplet superconductivity. Convincing evidence of this comes from measurements of the Knight shift by NMR. Additionally,  $\mu\text{SR}$  and Kerr effect measurements indicate that its superconducting state breaks TRS. Spin-triplet pairing has led to suggestions that the orbital state is  $p$ -wave. The only unitary  $p$ -wave order parameter which breaks TRS and which is allowed for a tetragonal lattice with a cylindrical Fermi surface is of the form  $\mathbf{d}(\mathbf{k}) = \Delta_0 \hat{z}(k_x \pm ik_y)$ , a so-called chiral state. We described this state in some detail, and showed that one of its most striking features is that it hosts

topologically protected edge currents. Despite these edge currents having been extensively searched for in  $\text{Sr}_2\text{RuO}_4$ , they have not been directly measured to date. This null result casts a doubt on the identification of  $\text{Sr}_2\text{RuO}_4$ 's order parameter as chiral  $p$ -wave. In the last section of this chapter, we proposed an experiment to further probe  $\text{Sr}_2\text{RuO}_4$ 's order parameter, using in-plane uni-axial strain. The prediction is that strain applied along  $[100]$  will lift the degeneracy between the  $x$  and  $y$  components of the order parameter, leading to a linear dependence of  $T_c$  on strain for small strains, with a sharp discontinuity in the slope at zero strain.

## Chapter 4

# Experimental Techniques

In Chapters 2 and 3 we argued that  $\text{Sr}_3\text{Ru}_2\text{O}_7$  and  $\text{Sr}_2\text{RuO}_4$  were strong candidates for investigations using uni-axial strain, as their properties are expected to be sensitive to anisotropic distortions of the crystal lattice. Such a study of the properties of  $\text{Sr}_2\text{RuO}_4$ 's superconducting state or  $\text{Sr}_3\text{Ru}_2\text{O}_7$ 's novel phase presents many experimental challenges, as one must perform high precision AC susceptibility or resistivity measurements, whilst applying strain and magnetic field to the sample and maintaining it at cryogenic temperatures. In this chapter we will give details of the experimental set-up used, starting with an introduction to the uni-axial strain technique, followed by a description of how the samples were prepared and the methods used for resistivity and AC magnetic susceptibility measurements. To conclude the chapter, we will discuss the main cryogenic system used for experiments, namely our adiabatic demagnetization refrigerator.

### 4.1 Uni-axial strain

#### 4.1.1 Introduction

Many experiments on strongly correlated systems are performed under high applied pressures, as a means of studying how the electronic states are affected by deformations of the crystal lattice. For example in the case of  $\text{CePd}_2\text{Si}_2$ , hydrostatic pressure causes the suppression of its antiferromagnetic transition, and the emergence of an unconventional superconducting state at  $\sim 20$  kbar, leading to the suggestion of magnetically mediated Cooper pairing [23, 94]. In the case of the iron pnictide superconductor  $\text{BaFe}_2\text{As}_2$ , it was shown that pressure and chemical doping have similar effects on the electronic structure, indicating that structural distortions rather than charge doping of the layers affect superconductivity in this material [95]. The high- $T_c$  cuprates have also been extensively studied under pressure. For example in the case of  $\text{La}_{1.48}\text{Nd}_{0.4}\text{Sr}_{0.12}\text{CuO}_4$ , it was found that for a hydrostatic pressure of  $\sim 0.1$  GPa, there is an abrupt increase of  $T_c$  accompanied by a sudden change in the Hall coefficient [96]. This was interpreted as a transition between one-

and two-dimensional transport, and a sign of competition between static stripes and superconductivity.

Uni-axial pressure is also a widely employed technique, the difference to hydrostatic pressure being that it is directional and allows the effect of different lattice distortions to be probed. In the case of  $\text{YBa}_2\text{Cu}_3\text{O}_7$ , it was shown that  $T_c$  decreases with pressure applied along  $b$ , increases with pressure along  $a$  and only weakly decreases with pressure along  $c$  [97]. When hydrostatic pressure is applied, the in-plane effects cancel each other out, so that  $T_c$  only has a very weak dependence on pressure. The  $T_c$  of  $\text{La}_{1.64}\text{Eu}_{0.2}\text{Sr}_{0.16}\text{CuO}_4$  can be almost doubled for 3 kbar along [110], whilst it has a much weaker dependence on pressures along [100] and [001] [98]. Static stripe order is believed to compete with superconductivity in this compound, and it is argued that because the principal axes of the strain induced by the [110] pressure are different from those of the stripes, the stripes are suppressed and superconductivity enhanced.

Uni-axial pressure can therefore be an excellent tool for studying the sensitivity of a system's electronic properties to the symmetries of the lattice and different anisotropic distortions. For our measurements of  $\text{Sr}_2\text{RuO}_4$  and  $\text{Sr}_3\text{Ru}_2\text{O}_7$ , we developed a piezoelectric-based apparatus where the control parameter is uni-axial strain rather than pressure, a difference which we will emphasize in Section 4.1.4. With it we are able to apply both tensile and compressive strain, which can be tuned continuously whilst the sample is at cryogenic temperatures. Before describing the apparatus itself however, let us first introduce a framework for describing the stress and strain of a sample.

#### 4.1.2 Strain and stress tensors

Strain is a measure of the deformation of an object, defined as  $\Delta L/L$  for an object of length  $L$ . Let us start by considering the simple one-dimensional case of a long thin rod, illustrated by the sketch in Figure 4.1.

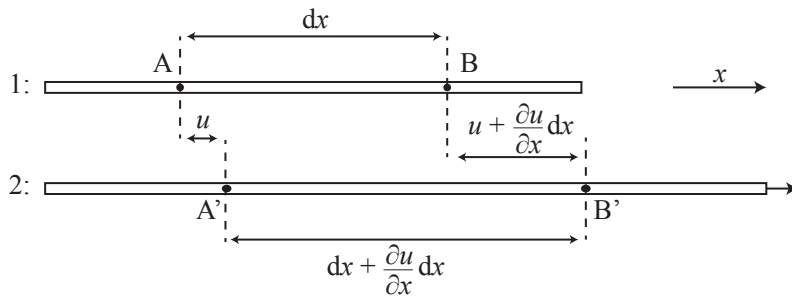


Figure 4.1: A long thin rod is unstrained at time 1. At time 2 a force is acting on one of its ends, causing it to stretch. The length  $AB$  changes to  $A'B'$ , resulting in the sample being strained.

At time 1 there are no forces acting on the rod and it is in a state of equilibrium.

Two points marked A and B are separated by a distance  $dx$ , which can be made infinitesimally small. At time 2 a force is being applied at one end of the rod, whilst the other is held fixed, causing it to be stretched. We do not concern ourselves with what happens between times 1 and 2, or how fast the change occurs, and assume that the system is in equilibrium. We define the displacement of point A as  $u = A' - A$ . Using the various distances shown in Figure 4.1, we can write the resulting strain on element  $dx$  as:

$$\varepsilon = \frac{\Delta L}{L} = \frac{A'B' - AB}{AB} = \frac{dx + \frac{\partial u}{\partial x} dx - dx}{dx} = \frac{\partial u}{\partial x}. \quad (4.1.1)$$

If we wish to generalize this result to three dimensions, we consider a point  $(x, y, z)$  in an unstrained object, whose coordinates become  $(x + u, y + v, z + w)$  when the object is strained. Then, following the derivation shown for example in ref. [99], the full strain tensor is given by:

$$\varepsilon_{ij} = \frac{1}{2} \left( \frac{\partial u_i}{\partial x_j} + \frac{\partial u_j}{\partial x_i} + \frac{\partial u_k}{\partial x_i} \frac{\partial u_k}{\partial x_j} \right), \quad (4.1.2)$$

where  $i, j$  and  $k$  can be any of  $x, y$  and  $z$ , and  $(u_x, u_y, u_z) = (u, v, w)$ . The displacement vector is given by  $(u_i, u_j, u_k)$ . If a body's strain tensor is known, the deformation of the body is completely determined. As can be seen from the structure of the strain tensor it is symmetrical:  $\varepsilon_{ij} = \varepsilon_{ji}$ . Assuming that we are working in the limit of small strains, the last term of equation (4.1.2), being of second order, can be neglected. This enables us to write the more commonly used strain tensor:

$$\varepsilon_{ij} = \begin{pmatrix} \varepsilon_{xx} & \varepsilon_{xy} & \varepsilon_{xz} \\ \varepsilon_{yx} & \varepsilon_{yy} & \varepsilon_{yz} \\ \varepsilon_{zx} & \varepsilon_{zy} & \varepsilon_{zz} \end{pmatrix} = \begin{pmatrix} \frac{\partial u}{\partial x} & \frac{1}{2} \left( \frac{\partial u}{\partial y} + \frac{\partial v}{\partial x} \right) & \frac{1}{2} \left( \frac{\partial u}{\partial z} + \frac{\partial w}{\partial x} \right) \\ \frac{1}{2} \left( \frac{\partial u}{\partial y} + \frac{\partial v}{\partial x} \right) & \frac{\partial v}{\partial y} & \frac{1}{2} \left( \frac{\partial v}{\partial z} + \frac{\partial w}{\partial y} \right) \\ \frac{1}{2} \left( \frac{\partial u}{\partial z} + \frac{\partial w}{\partial x} \right) & \frac{1}{2} \left( \frac{\partial v}{\partial z} + \frac{\partial w}{\partial y} \right) & \frac{\partial w}{\partial z} \end{pmatrix} \quad (4.1.3)$$

The diagonal terms correspond to tensile strains if they are positive, and compressive if they are negative. The off-diagonal terms give a measure of the shear strains. When a body is strained, internal forces arise which tend to restore it to its original state. This results in a *stress*  $\sigma$  of the sample, defined as  $\sigma = F/A_0$  where  $F$  is the restoring force, and  $A_0$  the area on which it is acting. Stress is generally described by considering a volume element within the body. If the volume element is a cube with its principal axes along  $x, y$  and  $z$ ,  $\sigma_{xx}, \sigma_{yy}$  and  $\sigma_{zz}$  are the normal components, and  $\sigma_{xy}, \sigma_{xz}, \sigma_{yz}$ , etc. are the shear components of the stress, in analogy to the strain tensor.  $\sigma_{ij} ds_j$  corresponds to the force along the  $i$ -th direction acting on the face normal to the  $j$ -th direction, where  $ds_j$  is the area of one of the volume element's faces.

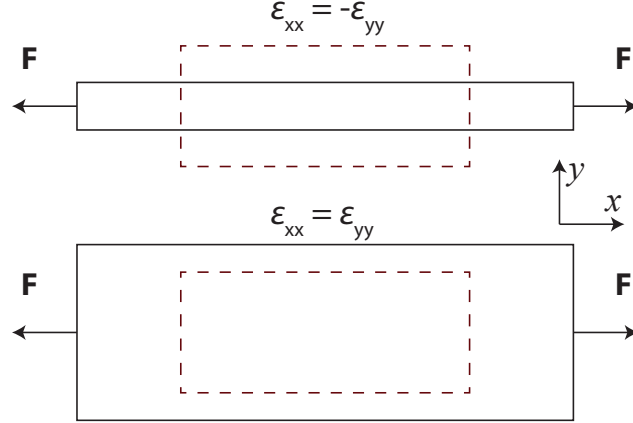


Figure 4.2: The deformation of a bar under tension can be resolved into two types of distortion: one which is anisotropic (top sketch), and one which is an isotropic dilatation (bottom sketch). If strain along  $z$  is neglected, the anisotropic distortion is volume preserving. The dashed box illustrates the original sample shape, and the full line the distorted sample.

Experimentally, we will be working with bar-shaped samples which we tension or compress along their length, so let us focus on this case for now. Consider a simple bar which we tension along  $x$  by applying forces which act uniformly on each of its ends, so that the deformation of the bar is homogeneous, in other words the strain tensor is constant throughout the sample's volume. The deformation of the sample can be resolved into two types of distortions, as illustrated in Figure 4.2: an anisotropic distortion of the form  $\epsilon_{xx} = -\epsilon_{yy} = -\epsilon_{zz}$ , and isotropic dilatation of the form  $\epsilon_{xx} = \epsilon_{yy} = \epsilon_{zz}$ . Note if we neglect strain along  $z$ , the anisotropic distortion is volume preserving. The relative strength of these different distortions is strongly material dependent, and is given by the material's Poisson's ratio  $\nu = -\epsilon_{yy}/\epsilon_{xx} = -\epsilon_{zz}/\epsilon_{xx}$  for an isotropic material. At low strains, stress and strain are related by a proportionality constant  $E$ , which is the material's Young's modulus:  $\sigma = E\epsilon$ . Using Poisson's ratio, we can write out all of the strain tensor components in terms of the stress for an isotropic material:

$$\left. \begin{aligned}
 \epsilon_{xx} &= \frac{1}{E}[\sigma_{xx} - \nu(\sigma_{yy} + \sigma_{zz})] \\
 \epsilon_{yy} &= \frac{1}{E}[\sigma_{yy} - \nu(\sigma_{xx} + \sigma_{zz})] \\
 \epsilon_{zz} &= \frac{1}{E}[\sigma_{zz} - \nu(\sigma_{xx} + \sigma_{yy})]
 \end{aligned} \right\} \quad (4.1.4)$$

$$\epsilon_{xy} = \frac{1 + \nu}{E}\sigma_{xy}, \quad \epsilon_{xz} = \frac{1 + \nu}{E}\sigma_{xz}, \quad \epsilon_{yz} = \frac{1 + \nu}{E}\sigma_{yz}$$

It is interesting to note that it is possible to have non-zero strain along a direction that has no stress.

If we now move to the case of an anisotropic material,  $\nu$  and  $E$  have different values along different directions. To relate stress along direction  $ij$  and strain along direction  $kl$  to each other<sup>1</sup>, one must then use the stiffness tensor  $c_{ijkl}$  (also known as the elastic tensor) or the compliance tensor  $s_{ijkl}$ :

$$\sigma_{ij} = c_{ijkl}\varepsilon_{kl}, \quad (4.1.5)$$

$$\varepsilon_{ij} = s_{ijkl}\sigma_{kl}. \quad (4.1.6)$$

$c_{ijkl}$  and  $s_{ijkl}$  are fourth-rank tensors, and  $s_{ijkl} = (c_{ijkl})^{-1}$ . Because of the symmetry of the stress and strain tensors, we can use the more convenient matrix notation  $\sigma_m = c_{mn}\varepsilon_n$  and  $\varepsilon_m = s_{mn}\sigma_n$ , where  $m$  and  $n$  number the pairs of suffixes  $ij$  from 1 to 6:

Tensor notation ( $ij$ )	11	22	33	23, 32	31, 13	12, 21
Matrix notation ( $m$ or $n$ )	1	2	3	4	5	6

The stiffness and compliance matrices are therefore both  $6 \times 6$  matrices. For a full review of the tensor properties of crystals the reader is pointed to the treatments given in references [100] and [101]. Here we will content ourselves with quoting the main results for a tetragonal crystal with the  $I4/mmm$  space group symmetry of  $\text{Sr}_2\text{RuO}_4$ . In such a crystal there are six independent elastic constants:  $c_{11}, c_{33}, c_{23}, c_{12}, c_{44}$  and  $c_{66}$ , so the full stiffness matrix is:

$$c_{mn} = \begin{pmatrix} c_{11} & c_{12} & c_{13} & 0 & 0 & 0 \\ c_{12} & c_{11} & c_{13} & 0 & 0 & 0 \\ c_{13} & c_{13} & c_{33} & 0 & 0 & 0 \\ 0 & 0 & 0 & c_{44} & 0 & 0 \\ 0 & 0 & 0 & 0 & c_{44} & 0 \\ 0 & 0 & 0 & 0 & 0 & c_{66} \end{pmatrix}. \quad (4.1.7)$$

The elastic constants of  $\text{Sr}_2\text{RuO}_4$  were measured experimentally by resonant ultrasound spectroscopy [93]. For our experiments, we will be applying in-plane strain along a particular crystal direction, and are interested in knowing what transverse strain will result from the applied longitudinal strain. This is given by the Poisson's ratio mentioned above, which is defined as the ratio of the transverse to the longitudinal strain.

For the  $\text{Sr}_2\text{RuO}_4$  measurement, we applied strain along the [100] and [110] directions. When we apply a strain along [100], there is a net stress  $\sigma_{xx}$  which tends

---

<sup>1</sup>Here  $i, j, k, l$  are numbers from 1 to 3 referring to the principle axes  $x, y, z$ . We use the convention that  $ij$  refers to the direction of the specified principle axis when  $i = j$ . When  $i \neq j$ , the direction is given by the sum of the unit vectors along  $i$  and  $j$ ; for example  $12 \equiv xy$  refers to direction [110] in crystallographic notation.

to restore the crystal to its unstrained state, but all other stress components  $\sigma_{ij}$  are zero. Therefore the in-plane Poisson's ratio is given by  $\nu_{in} = -\varepsilon_2/\varepsilon_1 = -s_{12}/s_{11}$  and the out-of plane one by  $\nu_{out} = -\varepsilon_3/\varepsilon_1 = -s_{13}/s_{11}$ , from  $\varepsilon_m = s_{mn}\sigma_n$ . To obtain the compliance tensor, we invert the stiffness tensor measured by Paglione et al. [93], and obtain  $s_{11} = 0.570$ ,  $s_{12} = -0.224$ ,  $s_{13} = -0.118$ ,  $s_{33} = 0.561$ ,  $s_{44} = 1.522$  and  $s_{66} = 1.634$ , each in units of  $10^{-2} \text{ GPa}^{-1}$ , giving  $\nu_{in} = 0.394$  and  $\nu_{out} = 0.207$ .

For strain applied along [110],  $\sigma_{xx} = \sigma_{yy} = \sigma_{xy}$  and  $\sigma_{zz} = 0$ . Additionally, because the strain is applied at  $45^\circ$  to the in-plane axes,  $\varepsilon_{xx} = \varepsilon_{yy}$  by symmetry. It can be shown that the in-plane Poisson's ratio in this case is given by  $\nu_{in} = (\varepsilon_{xy} - \varepsilon_{xx})/(\varepsilon_{xy} + \varepsilon_{xx}) = -(4s_{12} - s_1)/(4s_{11} + s_1) = 0.405$ , where  $s_1 = (s_{66} + 2s_{12} - 2s_{11})$ , by considering the transformation of the axes of the compliance tensor when the longitudinal strain is specified to lie along the [110] direction (see ref. [102]). The out-of-plane Poisson's ratio for [110] strain is  $\nu_{out} = \varepsilon_{zz}/(\varepsilon_{xy} + \varepsilon_{xx}) = -4s_{13}/(4s_{11} + s_1) = 0.203$ . The full stiffness tensor has not been measured for  $\text{Sr}_3\text{Ru}_2\text{O}_7$ , so we are unable to calculate its relevant Poisson's ratios. It is likely that they will be similar to those of  $\text{Sr}_2\text{RuO}_4$ , as the crystal structures of both compounds are similar, although the rotation of the octahedra in  $\text{Sr}_3\text{Ru}_2\text{O}_7$  could modify their value.

### 4.1.3 Uni-axial techniques

Before describing the uni-axial strain probe which we developed, let us give a brief review of other uni-axial techniques, to motivate why a new technique was necessary for our experiments. A common method involves compressing the sample along a particular direction by exerting a force normal to one of its faces, resulting in a uni-axial stress. In this case the controlled quantity is stress rather than strain, as the force is the parameter which is tuned. Pressure is often applied by compressing a spring which pushes on an anvil which in turn compresses the sample. In such a pressure cell, the pressure is often set at room temperature by adjusting a bolt, meaning that the sample must be repeatedly thermally cycled to perform measurements at different pressures. Examples of pressure cell designs are given in references [103] and [104]. In [104], a set-up which enables the continuous tuning of uniaxial pressure whilst maintaining the sample at low temperatures is described, where control is achieved using bellows filled with high pressure helium.

Uni-axial pressure cells present several experimental challenges, the foremost being that of strain homogeneity within the sample. In a typical uni-axial pressure experiment, the sample strain achieved is of the order of  $\sim 0.1\%$ , corresponding to a compression of  $\sim 1 \mu\text{m}$  for a 1 mm long sample. If the anvils are directly in contact with the sample, both the anvil and sample faces must be flat on a scale smaller than  $\sim 1 \mu\text{m}$  in order to obtain high strain homogeneity within the sample. If this is not the case, the force will not be transmitted to the sample evenly across its face, with high strains becoming concentrated around any sharp features. To reduce strain inhomogeneity it is therefore important to polish the sample and anvil faces to a high level of smoothness, which is often challenging due to the mechanical properties and small sizes of the samples. A further source

of inhomogeneity is the frictional locking of the sample faces to the anvils. As the sample is compressed, its faces become locked to the anvils and cannot expand, whilst its centre will expand according to its Poisson's ratio, causing strain gradients within the sample [105]. Strain inhomogeneity within the sample makes determining to high accuracy sample properties as a function of applied pressure difficult. For example, if one wishes to measure the pressure dependence of a superconducting transition, strain inhomogeneities will lead to different parts of the sample having different  $T_c$ 's. Then when the  $T_c$  of the whole sample is measured, the superconducting transition will broaden at high pressures due to the distribution of  $T_c$ 's within the sample. This effect is illustrated in Figure 4.3, where the superconducting transition of  $\text{La}_{1.64}\text{Eu}_{0.2}\text{Sr}_{0.16}\text{CuO}_4$  goes from a sharp one at zero pressure, to one which is spread over  $\sim 5$  K at 3.0 kbar [98]. Strain homogeneity can be improved in pressure cell experiments by increasing the sample's aspect ratio (length/width), thus relaxing the constraint on face smoothness, as well as placing foils between the sample and anvils to reduce frictional locking [106].

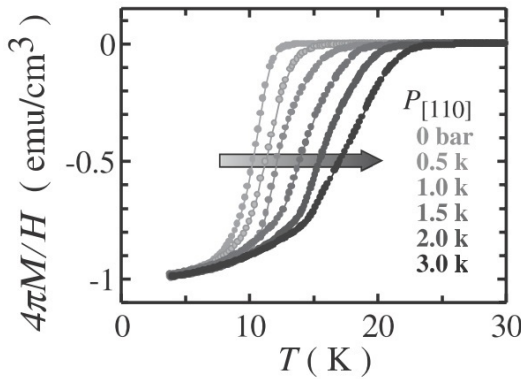


Figure 4.3: Magnetization divided by field of  $\text{La}_{1.64}\text{Eu}_{0.2}\text{Sr}_{0.16}\text{CuO}_4$  as a function of temperature showing its superconducting transition for a series of different pressures applied along [110]. Two effects are observed: the superconducting transition moves up in temperature with pressure, and broadens with pressure. The second is due to strain inhomogeneity within the sample, and introduces uncertainty in the determination of  $T_c$  against pressure. Taken from [98].

A method for applying uni-axial strain which offers higher strain homogeneity and *in situ* strain tunability is glueing the sample directly to a piezoelectric stack, as described in ref. [107]. Applying a voltage to the piezoelectric stack causes its length to change and results in a strain being transmitted to the sample through the glue. The faces of the sample and the piezoelectric stack do not need to be perfectly smooth for high strain homogeneity, as imperfections will be taken up by the glue. However, this method also presents some drawbacks. Piezoelectric stacks lengthen by  $\sim 0.1\%$  along their poling direction as they are cooled down from room temperature to 4 K (see for example [108]), whilst most materials contract by  $0.2\% - 0.3\%$ . Therefore when the sample-on-stack system is cooled down, there will be a large differential thermal contraction resulting in the sample being highly strained. The range of motion of the stacks decreases as temperature is lowered. For the stacks used in our experiments, we found that the range of motion at 4 K is  $\sim 0.06\%$  (discussed in Section 4.1.4), meaning that the sample strain at low temperature is much greater

than the range of motion of the stacks, and it is impossible to tune back to isotropic strain.

Our experimental requirements were the following: (1) high strain homogeneity as, in the case of  $\text{Sr}_2\text{RuO}_4$  for example, we need to be able to resolve  $T_c$  to a high accuracy; (2) the ability to apply both positive and negative strains, as was motivated in Section 3.5.4; (3) the ability to tune the strain continuously *in situ*. In an effort to fulfil these, Clifford Hicks designed a new uni-axial strain probe based on the use of piezoelectric stacks, which we will now describe. The parts for the probes were made by the in-house mechanical workshops in St Andrews and Dresden, and the probes themselves assembled and wired by Clifford and myself.

#### 4.1.4 Uni-axial strain probe

A schematic of the uni-axial strain probe used for our experiments is shown in Figure 4.4a, and described in detail in ref. [109]. A bar-shaped sample is secured across the gap between the two sample plates, using epoxy to fix it at either end. One of the sample plates is held fixed relative to the probe's body, whilst the other can be moved using the three piezoelectric stacks to change the length of the gap and thus apply a strain to the sample. The three stacks are arranged in parallel, and are joined by a bridge at one end, so that to zeroth order their thermal contraction does not cause the sample to be strained. The piezoelectric stacks lengthen along their polling direction when a positive voltage is applied to them (a negative voltage causes them to contract), so in this configuration a positive voltage to the central stack causes the sample to become compressed, whereas a positive voltage to the outer stacks causes it to become tensioned. As the stacks are longer than the sample, higher strains are achievable than if the sample were simply glued to a stack. Approximating the strain to be homogeneous within the sample (we will discuss strain homogeneity further on), the sample strain is given by:

$$\frac{\Delta L_s}{L_s} = \frac{(\Delta L_{outer} - \Delta L_{inner})}{L_s} = \frac{L_p}{L_s}(\varepsilon_{outer} - \varepsilon_{inner}), \quad (4.1.8)$$

where  $L_s$  is the strained length of the sample,  $L_p$  the length of the stacks, and  $\varepsilon_{inner} = \Delta L_{inner}/L_p$  and  $\varepsilon_{outer} = \Delta L_{outer}/L_p$  the strains on the inner and outer stacks respectively. Hence, even with a strain range of  $\sim 0.06\%$  on the stacks at low temperature, with  $L_p = 4$  mm and  $L_s = 1$  mm we are able to achieve a strain range of  $\sim 0.5\%$  on the sample, centred on zero strain. A picture of the first generation strain probe used for the experiments on  $\text{Sr}_2\text{RuO}_4$  is shown in Figure 4.4b, where two 2 mm stacks were glued together to give  $L_p = 4$  mm. The inner and outer stacks can be used in conjunction to ramp the strain smoothly across zero strain. For example, if we wish to go from high compression to high tension we can ramp the voltages on the (inner, outer) stacks from (300 V, 0 V) to (0 V, 300 V), which avoids any discontinuity across zero strain.

It is worth noting that the probe described here is best approximated as an applied strain rather than an applied stress apparatus. The elastic constant of the

apparatus being high compared to that of the sample, the sample must deform in response to any displacement applied by the stacks, if it does not break<sup>2</sup>. Due to the sample's Poisson's ratios, an applied longitudinal strain will result in induced transverse strains, so the total strain is not strictly speaking uni-axial. The fact however that we are directly controlling strain along a single axis, and that the stress within the sample is uni-axial, justifies the description of the present device as a uni-axial strain probe.

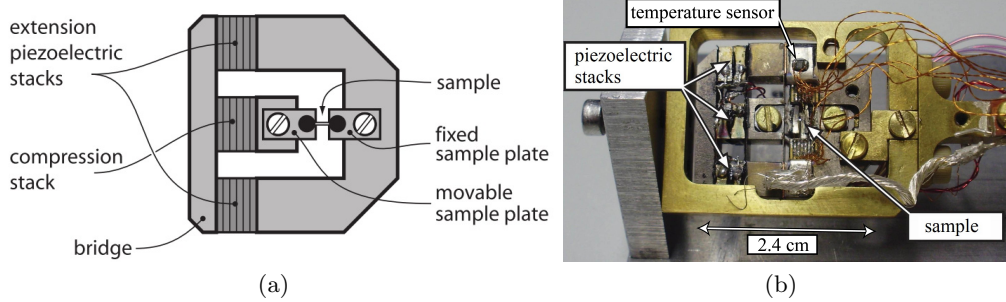


Figure 4.4: (a) Schematic of the uni-axial strain probe. The inner and outer piezoelectric stacks can be actuated independently to either compress or tension the sample. Taken from [109]. (b) Picture of the first generation strain probe used for the measurements on  $\text{Sr}_2\text{RuO}_4$ . The stacks are 4 mm long, and the sample gap  $\sim 1$  mm, giving a strain range of  $\sim 0.5\%$ . The probe is mounted in a brass frame, which can itself be mounted in a cryogenic system.

Let us now turn to the details of the construction of the strain probe. We used lead zirconium titanate (PZT) stacks from Piezomechanik GmbH<sup>3</sup> which, according to the catalog, can be operated between  $-30$  and  $+150$  V at room temperature. We found in practice that the stacks could be safely operated between at least  $-280$  and  $+420$  V at  $\sim 1$  K, giving a  $\sim 0.06\%$  movement range. The device is made out of titanium, whose thermal contraction is similar to that of the piezoelectric stacks along their transverse direction<sup>4</sup>. As titanium's thermal contraction is relatively small, the differential thermal contraction between the sample and the probe can cause the sample to become significantly strained at low temperatures. Several approaches can be taken to avoid this problem. In the first generation strain probe, this was solved by including copper “thermal contraction foils”, which are shown in Figure 4.5a. The idea here is that copper has a much higher thermal contraction than titanium, so by making the foils of the right thickness, one can cancel out the

<sup>2</sup>In the case of an applied stress device, the apparatus has a lower elastic constant than the sample, for example when a spring is used to apply the force; the applied force is then constant and the sample allowed to deform.

<sup>3</sup>The model of stacks used is Pch 150/5 $\times$ 5/2.

<sup>4</sup>Between room temperature and 4 K, titanium contracts by 0.151% [110], whilst the stacks contract by  $\sim 0.12\%$  perpendicular to their poling direction [108].

differential thermal contraction between the sample and the body. In the case of  $\text{Sr}_2\text{RuO}_4$ , which has an in-plane thermal contraction of 0.23% [72], we estimated that 200  $\mu\text{m}$  thick copper foil would keep the sample at approximately zero strain, for a distance of  $\sim 800 \mu\text{m}$  between the sample plates.

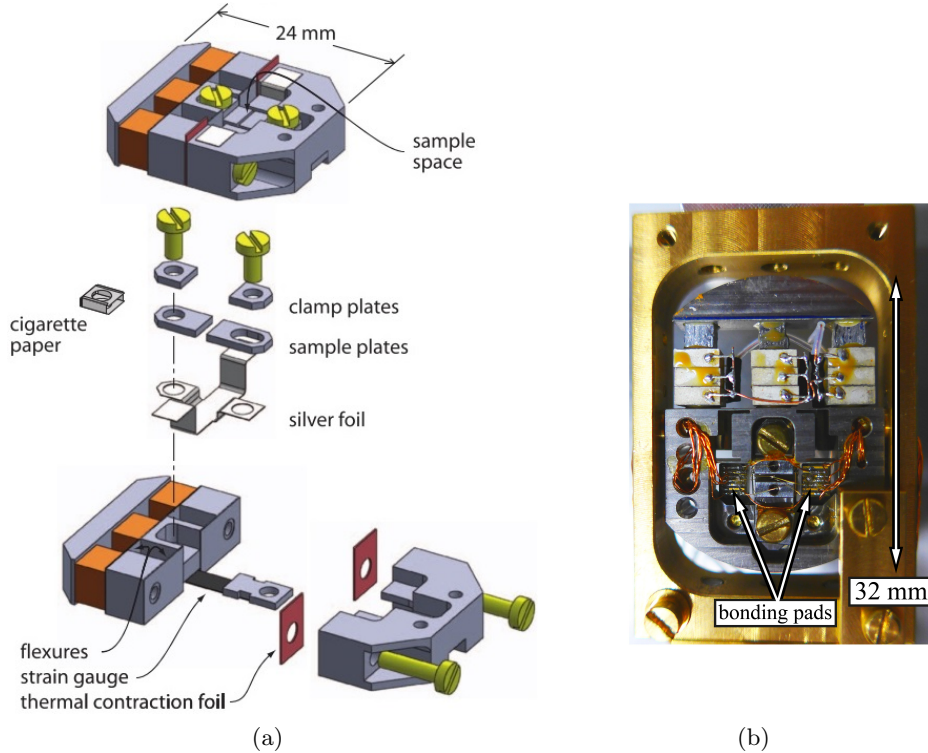


Figure 4.5: (a) Diagram showing the components of the first generation strain probe. From [109]. (b) Photograph of the second generation strain probe with 6 mm long stacks, indicating the positions of the bonding pads.

The different elements of the first generation strain probe are illustrated in Figure 4.5a. The copper foils go in between the two titanium blocks which make up the main part of the probe's body. The blocks are secured together with brass screws, which have a larger thermal expansion than the titanium, so they are held together more tightly as the apparatus is cooled down. The sample plates are also made out of titanium, and are fixed in place with brass screws on top of a silver foil, which serves to increase the thermal link between the sample and the temperature sensor. The temperature sensor is a ruthenium oxide chip, and is epoxied to one of the silver foil's free tabs, as shown in Figure 4.4b. A thick silver wire is attached to another of the silver foil's tabs, linking it to the fridge's cooling stage (the details of which are given in Section 4.5). The sample plates can be electrically isolated from the body, which may be necessary for transport measurements for example, by wrapping them in cigarette paper. Flexures were included in the design to protect

the stacks and sample from any unwanted transverse forces, which may occur during sample mounting or when the probe is mounted on a fridge. The flexures being much thinner along the direction of applied strain than perpendicular to it, they have a much higher spring constant for transverse or twisting motions than for longitudinal motion.

The stacks were found to be hysteretic, especially at higher voltages, so it was necessary to include an independent means of determining the sample strain. In the first generation probe, this took the form of a strain gauge which was mounted across the gap directly under the sample. The gauge factor  $GF$  is the proportionality constant between the strain gauge's resistance and the strain it is under:  $GF = (\Delta R/R) \cdot 1/\varepsilon$ . For the strain gauge we used,  $GF = 2$  and we approximate it to be temperature independent<sup>5</sup>. To accurately measure the strain gauge's change in resistance, it is placed in a bridge circuit. The current required to measure changes in resistance in a bridge circuit is small (we used  $10 \mu\text{A}$ ), which ensures that very little heat is generated.

The second generation strain probe, which was used to measure two  $\text{Sr}_3\text{Ru}_2\text{O}_7$  samples, is pictured in Figure 4.5b. It is similar to the first generation strain probe except for three main features. The first is that it has 6 mm long stacks, resulting in higher achievable strains. The second is that it contains no thermal contraction foils. Instead, the body is made from a single piece of titanium, so as to reduce the possibility of strains across the sample due to differences in thermal contraction of the different parts. We found that this yielded a significant improvement in strain homogeneity within the sample, as will be discussed in Section 6.2.5. To prevent the sample breaking due to differential thermal contractions, it is necessary to bias it towards compression. Indeed, if the sample is already under sufficient compression when it is cooled down it will not be pulled apart due to the differential thermal contractions. The biasing is achieved by applying a positive voltage to the outer stacks when the epoxy in the sample mounts is curing, resulting in the sample being compressed when the epoxy is hard and the voltage released. The third difference is that, instead of a strain gauge, a parallel plate capacitor was used to measure the displacement of the sample plates. The reason for this was to avoid the temperature and magnetic field dependence exhibited by the strain gauge, to enable accurate control of the strain at different fields and temperatures as well as simplify data analysis. The capacitor is made of two rectangular titanium plates of area  $A$  which are spaced by approximately  $35 \mu\text{m}$ . The displacement which is applied by the stacks is directly transmitted to one of the plates, changing their separation. We use the parallel plate approximation  $C = \varepsilon_0 A/d$  to estimate the plate separation  $d$  from the measured capacitance  $C$ , and estimate the applied strain.

To perform measurements on the sample, bonding pads are installed on the

---

<sup>5</sup>The strain gauge used is a Vishay Micro-Measurements EK-06-250PD-10C/DP. In Tech Note TN-504-1 by Vishay Micro-Measurements, it is stated that the gauge factor changes linearly by 1.0% between  $24^\circ \text{C}$  and  $-73^\circ \text{C}$ , which would give by extrapolation a  $\sim 3\%$  larger  $GF$  at 0 K than at room temperature.

probe on either side of the sample, as shown in Figure 4.5b. Insulated copper wires, which are twisted in pairs to reduce pick-up noise [110], are soldered to the ends of the bonding pads and join up at a 24-pin connector which serves as an interface between the probe and whichever cryogenic platform it is mounted on. Wiring from the sample, or whichever probe is used to measure it, can then be attached to the bonding pads, providing a direct connection between the sample at low temperature and room-temperature electronics. As the probe is often used for experiments in magnetic fields, we ensure that wherever possible the wiring is tightly secured to the frame, to prevent vibrations of the wires, which can give rise to induced voltages and become a large source of noise.

#### 4.1.5 Sample mounting

The way in which the sample is mounted in the probe has a large influence on how homogeneous the strain within the sample is. To secure the sample onto the sample plates, we used Stycast 2850FT epoxy which we cured at 60°C for 4-5 hours. The advantage of using an epoxy rather than mechanically clamping the sample is that the sample's faces and sample plates do not need to be polished to a high level of smoothness, and it avoids the concentration of high strain gradients in the sample at the edges of the sample plates. For early samples, we simply placed a droplet of epoxy at the ends of the sample, as illustrated in Figures 4.6a and c. Although this provides an easy way to apply strain to the sample, the asymmetry in the mounting conditions can lead to large strain inhomogeneities in the middle of the sample. The reason for this is that the sample is held more firmly on its lower face than its upper face, so that when the sample is strained it is made to bend (upwards when compressed and downwards when tensioned), as shown in Figure 4.6e.

To prevent this issue, we mounted later samples such that they were also held on their top face by a rigid titanium cap foil, to try and achieve symmetrical mounting conditions (Figures 4.6b and d). In the case of  $\text{Sr}_2\text{RuO}_4$  where we performed measurements using both mounting techniques, we found that the superconducting transitions broadened less with strain when a cap foil was used, indicating a higher strain homogeneity within the sample. According to finite element analysis calculations carried out by Mark Barber and described in [109], if the sample is mounted perfectly symmetrically, strain inhomogeneity decays exponentially towards the sample centre. Therefore any measurement on the strained sample should preferably take place towards its centre, to ensure that a region with homogeneous strain is being probed. In the calculations it was shown, for example, that for a sample mounted as shown in Figure 4.6d, the strain is homogeneous within 1% as soon as one moves 0.4 times the sample width away from the sample plate edge.

#### 4.1.6 Strain calculation

To calculate the strain on the sample, we need to know its strained length ( $L_s$  in equation (4.1.8)) to high accuracy. In general however, the strained length is not

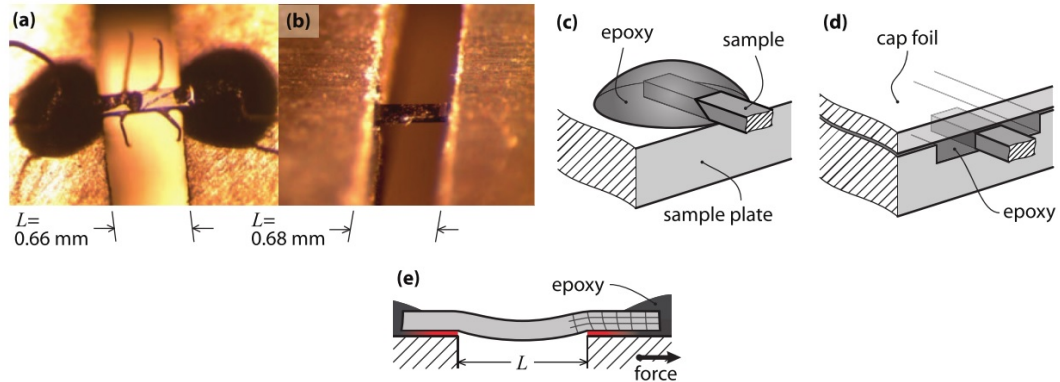


Figure 4.6: Different sample mounting techniques. (a) A picture of a sample secured with drops of epoxy at either end, the sketch of which is shown in (c). The asymmetrical mounting conditions lead to a bending of the sample when strain is applied, as illustrated in (e). The regions in red represent where the force is predominantly being transmitted to the sample. (b) and (d): picture and sketch of a sample mounted with a cap foil, to try and achieve symmetrical mounting conditions. Taken from [109].

the same as the gap between the sample plates, as the epoxy in the sample mount deforms and takes up some of the applied displacement. A force applied to one of the sample plates is transmitted to the sample via the epoxy over a length  $\lambda$ , so the total displacement applied by the stacks and measured by the strain gauge is distributed over a length  $L_s = L + 2\lambda$  in the sample ( $L$  is the separation of the plates).

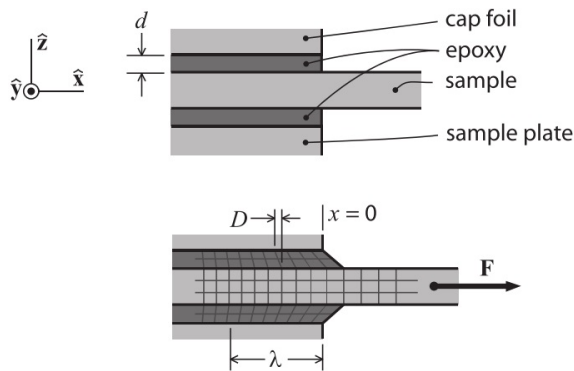


Figure 4.7: Illustration of the model used to calculate  $\lambda$  in equation (4.1.10). When  $n = 2$  the sample is held by epoxy on its top and bottom faces. A force  $\mathbf{F}$  on the sample is transmitted to the sample plate and cap foil via the epoxy over a length-scale  $\lambda$ , causing the sample displacement  $D(x)$  to decay exponentially within the mount. From [109].

$\lambda$  can be estimated using a simple model with some basic assumptions: the sample's width  $w$  is much larger than its thickness  $t$ , so we only consider bonding of the epoxy on its upper and lower faces; the sample plates and cap foils are perfectly rigid; we neglect any shears within the sample, and assume that the strain is constant across the sample's width and thickness. This model is illustrated in Figure 4.7. If

the displacement is applied along the  $x$ -direction, the sample experiences a force at position  $x$  given by  $F(x) = Ewt\varepsilon_{xx}$  ( $E$  is the sample's Young's modulus). Then, if  $S$  is the shear stress at the interface between the sample and the epoxy, we have:

$$\frac{dF}{dx} = nwS(x) \approx nwC_{66,e} \frac{D(x)}{d}, \quad (4.1.9)$$

where  $C_{66,e}$  is the epoxy's shear elastic constant,  $D(x)$  the displacement at position  $x$ ,  $n = 1$  if the sample is secured only through its bottom face and  $n = 2$  if it is secured through its top and bottom faces, and  $d$  is the epoxy thickness [109]. As  $\varepsilon_{xx} = dD(x)/dx$ , we obtain a second order differential equation for  $D$ . We find that the displacement decays exponentially within the sample mount over the length-scale:

$$\lambda = \sqrt{\frac{Etd}{nC_{66,e}}}. \quad (4.1.10)$$

Taking  $C_{66,e} = 15$  GPa for Stycast 2850FT, a Young's modulus  $E = 1/s_{11} = 176$  GPa for longitudinal deformations in  $\text{Sr}_2\text{RuO}_4$  [93], typical sample dimensions ( $t = 50 \mu\text{m}$ ,  $d = 30 \mu\text{m}$ ) and  $n = 2$ , we obtain  $\lambda \approx 100 \mu\text{m}$ . Equation (4.1.10) is particularly useful for estimating what length of the sample to embed in epoxy when mounting it. However, due to the many assumptions which went into its derivation, to obtain a more accurate estimate of the strain at the middle of the sample, it is necessary to perform a full finite element analysis calculation modelling the deformations of the sample and epoxy. These calculations were carried out for both the  $\text{Sr}_2\text{RuO}_4$  and  $\text{Sr}_3\text{Ru}_2\text{O}_7$  experiments by Mark Barber, and his results are used in Chapters 5 and 6 to estimate the sample strain during our measurements.

## 4.2 Sample preparation

All of the samples used were cut from single crystals grown by the floating-zone method. The  $\text{Sr}_3\text{Ru}_2\text{O}_7$  crystals were all grown by Robin Perry, whilst two batches of  $\text{Sr}_2\text{RuO}_4$  crystals were used: one grown by Alex S. Gibbs and the other by Keigo Nishimura in Prof. Y. Maeno's group. Crystals are produced by mixing powders of  $\text{SrCO}_3$  and  $\text{RuO}_2$  and pressing them into a rod which is sintered and then placed in an image furnace. The section of the rod which sits at the focal point of the furnace's two infra-red lamps becomes molten. As the rod is moved vertically through the focal point, impurities gather in the melt leaving a high purity single crystal at one end. The optimization of the growth process for  $\text{Sr}_3\text{Ru}_2\text{O}_7$  is presented in detail in ref. [37]. Sample quality can vary significantly from growth to growth, and so to select the best  $\text{Sr}_3\text{Ru}_2\text{O}_7$  crystals we referred to the extensive sample characterisation work carried out by J.-F. Mercure and Robin Perry [111]. All of the  $\text{Sr}_3\text{Ru}_2\text{O}_7$  experiments described in Chapter 6 were performed on samples cut from crystal C697B, as labelled in [111], which has a residual resistivity of  $\rho_0 \approx 0.25 \mu\Omega\text{cm}$ . For  $\text{Sr}_2\text{RuO}_4$ , the first batch of crystals has a  $T_c$  of 1.35 K, whilst for the second  $T_c = 1.45$  K.

Before mounting samples in the strain probe, they must be cut into bars with accurately known dimensions and aligned along a specific direction with respect to the crystal axes. Both  $\text{Sr}_2\text{RuO}_4$  and  $\text{Sr}_3\text{Ru}_2\text{O}_7$  cleave easily along the  $ab$ -plane, resulting in a highly reflective surface and thus making it straightforward to identify the the direction of the  $c$ -axis. Smooth cleaves were achieved by gently pressing on the sample with a sharp scalpel blade. To determine the alignment of the in-plane axes, we performed X-ray Laue diffraction measurements using the Laue set-up at the Centre for Science at Extreme Conditions at the University of Edinburgh. The X-ray beam was incident on the crystal normal to the  $ab$ -plane, this alignment being achieved using a laser which was reflected off of the sample's cleaved surface. The reflected X-ray beam was recorded on an image plate, resulting in an observed diffraction pattern, an example of which is shown in Figure 4.8a. The spots of high intensity correspond to where the Bragg condition for constructive interference of the reflected beam is fulfilled, thus enabling one to deduce the orientation of the crystal axes, as the diffraction pattern has the same symmetry as the crystal structure. Figure 4.8a shows the diffraction pattern of a  $\text{Sr}_2\text{RuO}_4$  crystal, and Figure 4.8b the corresponding simulated diffraction pattern. The axes of four-fold in-plane symmetry are easily identifiable in the diffraction pattern, allowing us to determine the directions of the in-plane axes with respect to the sample to high accuracy<sup>6</sup>. The diffraction patterns of the  $\text{Sr}_3\text{Ru}_2\text{O}_7$  crystals were also measured. These are not affected in a measurable way by the crystal structure's slight orthorhombicity, and look qualitatively the same as those of  $\text{Sr}_2\text{RuO}_4$ .

After aligning the sample, it was mounted on a goniometer and cut with a wire saw<sup>7</sup> along the desired direction. To obtain the necessary fine cuts we used a 30  $\mu\text{m}$  diameter wire and a cutting slurry made from a mixture of glycerine and silicon carbide powder. With this set-up we were able to reliably produce bar-shaped samples with lengths ranging between 0.5 – 2.5 mm and widths between 100 – 300  $\mu\text{m}$ . The cuts were made along the  $[100]$  direction, with the upper face of the bar being the  $ab$ -plane. In the case of  $\text{Sr}_2\text{RuO}_4$  we also cut samples along  $[110]$ . Accurately controlling the thickness of the bars is difficult, as they tended to cleave during the cutting process resulting in a distribution of thicknesses between 30–100  $\mu\text{m}$ . Cleaves could also be performed manually with a scalpel blade, however this is not a precise enough technique to accurately set the thickness of the bar. In practice we would identify the sample with the highest quality cleave and the desired dimensions among a large selection by studying them under a microscope. Typical sample dimensions used were  $\sim 1.5 \times 0.2 \times 0.04$  mm, so that if a gap of  $\sim 1$  mm between the sample plates was used, there would be a sufficient length of the sample embedded in epoxy at either end to ensure that the strain was properly transmitted.

---

<sup>6</sup>We estimate that the alignment of the  $a$ - and  $b$ -axes with respect to the sample is known within an accuracy of  $\sim 2^\circ$ , the error arising from uncertainty in the precise alignment between the sample and the image plate.

<sup>7</sup>The wire saw used was a KD Unipress WS22.

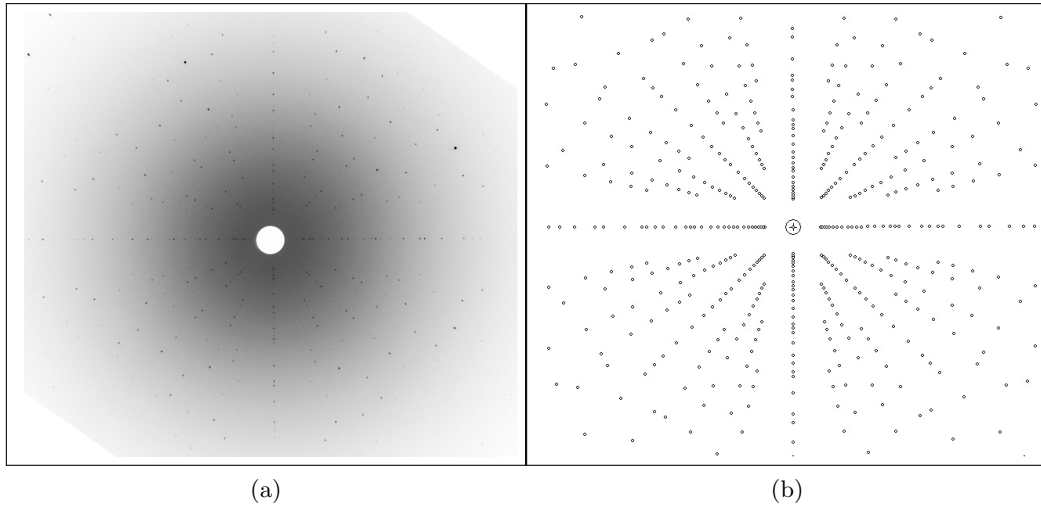


Figure 4.8: (a) Laue diffraction pattern of a  $\text{Sr}_2\text{RuO}_4$  crystal, measured with an incident beam normal to its  $ab$ -plane. (b) Simulated diffraction pattern of a  $\text{Sr}_2\text{RuO}_4$  crystal for an incident beam normal to its  $ab$ -plane, produced with Orient Express. In both cases the  $a$ - and  $b$ -axes run respectively vertically and horizontally.

### 4.3 Resistivity measurements

For the  $\text{Sr}_3\text{Ru}_2\text{O}_7$  experiment, we measured resistivity as a function of strain and magnetic field. To do this, we ran a known current through the bar-shaped sample and measured the voltage drop along its middle section. A picture of a sample with electrical contacts mounted on a quartz plate is shown in Figure 4.9a. The current contacts are attached to the ends of the bar, such that the current flows predominantly along the  $ab$ -plane, and two pairs of voltage contacts are on opposite sides of the bar. All of the contacts are made using gold wires ( $50\ \mu\text{m}$  for the current contacts,  $25\ \mu\text{m}$  for the voltage ones), which are attached to the sample using DuPont 6838 silver epoxy. To achieve sub- $1\ \Omega$  contact resistances, it is necessary to anneal the contacts at  $450^\circ\text{C}$  for five minutes. Once the contacts have been prepared, the wires are cut to remove the sample from the quartz plate and it is mounted in the strain probe, as illustrated in Figure 4.9b. As can be seen, it is necessary to make a hole in the cap foil to be able to access the current wires. As long as the hole is placed far enough back from the edge of the sample plate, this will not affect how strain is transmitted to the sample, as this occurs within the leading  $\sim 100\ \mu\text{m}$  from the edge. Connections from the floating gold wires on the sample are made to bonding pads on the strain probe using  $50\ \mu\text{m}$  gold wires and room-temperature curing DuPont 4929 silver epoxy.

In the set-up shown in Figure 4.9b, the resistivity of the sample is determined by sourcing a current through wires 1 and 2, and then measuring the voltage drop between 3 and 4 and between 5 and 6; the two pairs are measured simultaneously

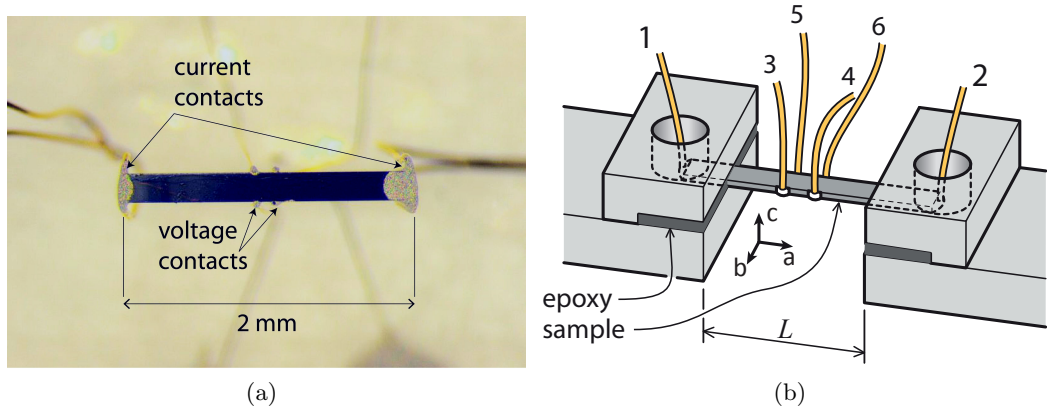


Figure 4.9: (a) Photograph of a Sr<sub>3</sub>Ru<sub>2</sub>O<sub>7</sub> sample. The sample is held above a quartz plate by gold wires, which are attached to it with silver epoxy. (b) Sketch of how a sample is mounted in the strain probe for transport measurements. The directions of the crystal axes are indicated.

as a consistency check. For a perfectly shaped bar, the longitudinal resistivity  $\rho_{xx}$  is related to the measured voltage by  $V = I\rho_{xx}l/A$ , for a separation  $l$  between the voltage contacts, and a cross-section  $A$  of the bar. If we run a current  $I = 1$  mA through the sample, and take a typical value  $l/A = 20000$  m<sup>-1</sup>, the resulting voltage drop will be  $V \approx 40$  nV for a sample with a residual resistivity of  $0.2$   $\mu\Omega$ cm at temperatures close to 0 K. Therefore to accurately measure the resistance of Sr<sub>3</sub>Ru<sub>2</sub>O<sub>7</sub> at low temperature, it is necessary to employ noise-reduction and signal amplification techniques.

We used lock-in amplifiers (LIA) to perform phase sensitive measurements of AC voltages<sup>8</sup>. To generate an AC current, we connect the LIA's voltage output to a battery powered voltage source<sup>9</sup>; this voltage is placed across a resistance in series with the sample. The resistance is chosen to set the desired current running through the sample. The LIA consists of an amplifier followed by a phase sensitive detector, enabling the detection of a signal at a given frequency within a very narrow bandwidth, resulting in a high signal-to-noise ratio. The LIAs used have a low input noise of  $6$  nV/ $\sqrt{\text{Hz}}$  at  $1$  kHz, however we found further amplification was necessary to reduce the noise levels further. To achieve optimum noise levels, we used a transformer<sup>10</sup>, whose output was fed into a preamplifier<sup>11</sup>, giving us noise levels of  $\sim 0.1$  nV/ $\sqrt{\text{Hz}}$  at  $100$  Hz. Measurements were performed at frequencies between  $80$  and  $200$  Hz, which corresponds to the DC limit for a typical metal, where relaxation times are of the order of  $\sim 10^{-14}$  s [15].

<sup>8</sup>The model used is SR830 from Stanford Research Instruments.

<sup>9</sup>This serves to avoid ground loops in the circuit.

<sup>10</sup>SR554 transformer/preamplifier from Stanford Research Instruments.

<sup>11</sup>SR550 preamplifier from Stanford Research Instruments.

## 4.4 AC magnetic susceptibility measurements

For the  $\text{Sr}_2\text{RuO}_4$  experiment, we wished to track the superconducting  $T_c$  as a function of strain. A convenient way of determining  $T_c$  is to measure the sample's AC magnetic susceptibility, as this changes abruptly at  $T_c$ . This technique probes a finite volume of the sample, providing the average over that volume of the sample's magnetic response; this is in contrast to resistivity, where a single least-resistance percolative path is measured, making it much more sensitive to strain inhomogeneity. The AC magnetic susceptibility is defined as  $\chi = dM/dH_{ac}$ , where  $M$  is the magnetization and  $H_{ac}$  an applied oscillating field. The real part of the AC susceptibility  $\chi'$  drops from its normal state value to -1 in the Meissner state, whilst the imaginary part  $\chi''$  has a peak in the mixed superconducting state, corresponding to AC losses, and is zero in the Meissner state [112]. A photograph and sketch of the experimental set-up are shown in Figures 4.10a and 4.10b, where there is a large excitation coil mounted above the sample, and a smaller pick-up coil on the surface of the sample. The superconducting transition is found by running an AC current through the excitation coil, and measuring the change in induced voltage in the pick-up coil which occurs when the sample goes superconducting, due to the change in magnetic flux through the pick-up coil.

Approximating the excitation coil as a series of  $N_1$  current loops of radius  $a$ , the field produced at the centre of the coil is:

$$H_{exc} = \frac{\mu_0 I_{exc}}{2a} N_1, \quad (4.4.1)$$

when a current  $I_{exc}$  is run through it. If the pick-up coil is sitting in the centre of the excitation coil, has  $N_2$  turns, and a radius  $b$ , the induced voltage in the pick-up coil due to an AC current  $I_{exc} = I_0 \cos(\omega t)$  in the absence of a sample is:

$$V_{emf} = -\frac{d\Phi}{dt} = -\pi b^2 N_2 \frac{dH_{exc}}{dt} = -\frac{\mu_0 \pi b^2}{2a} N_1 N_2 \frac{dI_{exc}}{dt} = -L_m \frac{dI_{exc}}{dt}, \quad (4.4.2)$$

where  $\Phi$  is the magnetic flux threading the pick-up coil, and  $L_m = \mu \pi b^2 N_1 N_2 / 2a$  is the mutual inductance between the coils. Now considering the sample, the measured voltage across the pick-up coil will be shifted due to the sample's magnetization  $M$  which contributes to the flux through the pick-up coil:

$$\Delta V_{emf} \propto -\frac{dM}{dt} \pi b^2 N_2. \quad (4.4.3)$$

In the case of an excitation field of the form  $H_{exc} = H_0 \cos(\omega t)$ , the sample's magnetization is given by the real and imaginary parts of its susceptibility [112]<sup>12</sup>:

$$M(t) = H_0 (\chi' \cos(\omega t) + \chi'' \sin(\omega t)), \quad (4.4.4)$$

---

<sup>12</sup> $H_0 = \frac{\mu_0 N_1}{2a} I_0$ , for an applied oscillating current  $I_{exc} = I_0 \cos(\omega t)$ , from equation (4.4.1).

if we are in the linear régime<sup>13</sup>. Plugging the expression for  $M(t)$  into (4.4.3), we obtain:

$$\Delta V_{emf} = L_m \omega I_0 (\chi' \sin(\omega t) - \chi'' \cos(\omega t)). \quad (4.4.5)$$

Hence the real part of  $\Delta V_{emf}$  is proportional to the imaginary part of the susceptibility, and vice-versa, enabling the detection of the onset of superconductivity.

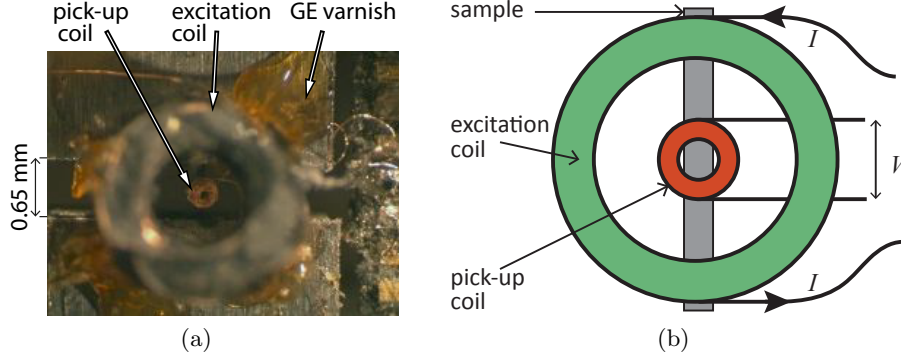


Figure 4.10: (a) Photograph of the susceptibility coils mounted above a Sr<sub>2</sub>RuO<sub>4</sub> sample in the strain probe. The sample is mounted across a gap of 0.65 mm, and the pick-up coil placed directly on top of it, in its middle section. (b) Sketch of the susceptibility set-up, illustrating how the coils are placed in relation to the sample. A current  $I$  is run through the excitation coil, giving rise to an induced voltage  $V$  which is measured.

However it is important to note that  $\Delta V_{emf}$ , the shift in inductance between the excitation and pick-up coils due to the sample, takes place on top of a large background  $V_{emf}$  arising from the excitation field. With our simple two coil set-up, it is not possible to distinguish the sample's contribution from the background, and so no absolute value of  $\chi$  can be given. This is because the geometry of the coils and their relative positions are not known to high enough precision to calculate the background. Equation (4.4.4) is technically only accurate if the sample is in the centre of the coil; experimentally this is not the situation as the sample is just below the coil, meaning that the field felt by the sample will be somewhat reduced compared to  $H_0$ . We should also note that demagnetization is likely to be important for a sample of this shape, and will affect the magnitude of the measured signal. None of the above are an issue for our experiment however, as we only require a qualitative measure of  $\chi$  to determine the temperature where it changes, so as to find  $T_c$ .

Experimentally we measure the AC voltage  $V$  across the pick-up coil, which is the sum of  $V_{emf}$  and  $\Delta V_{emf}$ . The background  $V_{emf}$  is approximately constant in the

<sup>13</sup>In the mixed superconducting state for example, non-linear effects can take place such that  $M$  cannot be expressed as a sinusoidal function of a single frequency, and a full Fourier expansion is necessary. However, for all of our measurements we are using lock-in amplifiers, and so are only measuring at the fundamental frequency.

small temperature range studied around  $\text{Sr}_2\text{RuO}_4$ 's  $T_c$  (changes in  $V_{emf}$  can arise because of the temperature dependence of the coils' resistance). The susceptibility of  $\text{Sr}_2\text{RuO}_4$  in the normal state close to  $T_c$  is also constant; therefore any observed change in  $V$  is assigned to the change in the sample's susceptibility as it goes superconducting. We can define the quantity  $m$ , the mutual inductance between the coils in the presence of the sample, where  $m' = V''/(2\pi I_0)$  is related to  $\chi'$  and  $m'' = V'/(2\pi I_0)$  is related to  $\chi''$ .

We now turn to the details of our experimental set-up. The excitation and pick-up coils were each wound by hand:  $\sim 100$  turns with a  $\sim 1$  mm radius out of  $50 \mu\text{m}$  diameter copper wire for the excitation coil;  $\sim 30$  turns with a  $\sim 0.15$  mm radius out of  $14 \mu\text{m}$  diameter copper wire for the pick-up coil. This gives a mutual inductance  $L_m \approx 13 \times 10^{-8}$  H. The excitation coil was coated with Stycast 2850FT to fix the loops of wire rigidly together and facilitate its manipulation. The wire used for the pick-up coil has a self-bonding coating, which when immersed in ethanol causes the windings to adhere to one another and form a rigid coil<sup>14</sup>. Both coils were placed above the sample, with the pick-up coil directly in contact with the sample, and stuck in place using GE varnish. The pick-up coil was positioned in the middle of the sample, so as to probe the region with the highest strain homogeneity. An AC current was run through the excitation coil by putting the output voltage of a LIA across the excitation coil which was in series with a variable resistor, the latter enabling tuning of the current. The induced voltage in the pick-up coil was passed through a transformer and preamplifier to improve the signal to noise ratio, as described in Section 4.3, and then measured by the LIA. In this case however the transformer used was a low-temperature, lead-shielded transformer<sup>15</sup> fixed to the 1 K-plate on the fridge (see Section 4.5), the advantage being that noise on the wires between the 1 K-plate and room temperature does not get amplified. The LIA records both the in-phase and out-of-phase parts of the induced voltage, giving us a qualitative measure of the sample's susceptibility. A discussion of the excitation currents and frequencies used is given in Chapter 5.

## 4.5 Adiabatic demagnetization refrigerator

The low-temperature environment for our experiments was produced using an adiabatic demagnetization refrigerator (ADR). Cooling by adiabatic demagnetization is achieved by putting the experimental probe in thermal contact with a pill of some paramagnetic salt, the entropy of which strongly depends on the applied magnetic field [113]. By magnetizing the salt pill isothermally, its entropy decreases as its electron spins order. If the pill is then adiabatically demagnetized, the sample temperature is lowered as entropy is transferred from the sample to the pill. This cycle is illustrated in Figure 4.11, where the temperature dependence of the entropy of a paramagnetic salt is plotted for different fields. The structure made up of the

<sup>14</sup>The wire used is AB15 Butybond from Elektrisola.

<sup>15</sup>Model LTT/m from CMR-Direct.

salt pill, sample probe and metallic structure connecting them is called the low-temperature stage (LTS), and is shown in the right-hand diagram of Figure 4.12. During the adiabatic demagnetization process (from B to C in Figure 4.11), the LTS is thermally isolated from the environment, and conservation of energy dictates that its total change in internal energy should remain zero, so:

$$-TdS = C_B^{LTS}(T)dT, \quad (4.5.1)$$

where  $C_B^{LTS}(T)$  is the heat capacity of the LTS in constant field, and  $dS$  the change in entropy. The change in entropy will be dominated by the salt pill, as the other components of the LTS are non-magnetic materials. From equation (4.5.1) we can see that cooling by adiabatic demagnetization is most effective when the heat capacity of the LTS is small, in other words when the system is already at a low temperature. The system is therefore initially cooled to  $\sim 1.5$  K using the 1 K stage, which is shown in the left-hand diagram of Figure 4.12.

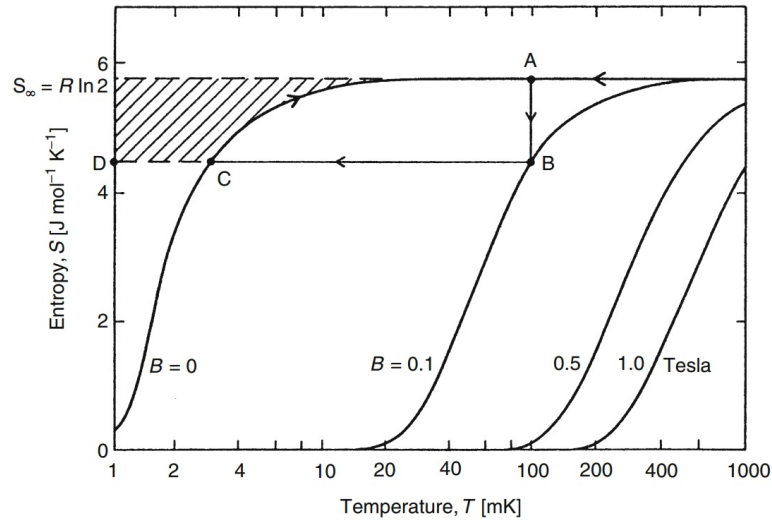


Figure 4.11: Entropy of the paramagnetic salt CMN as a function of temperature and magnetic field. Starting at point A on the zero-field curve, the system is magnetized by turning on the magnetic field, causing a decrease in the entropy. The system is maintained in thermal contact with a heat bath so that the process from A to B is isothermal. The link to the thermal bath is then severed and the system is adiabatically demagnetized (B to C), causing a reduction of the temperature. The system is then allowed to warm up, and follows the zero-field line. This cycle can be repeated indefinitely to repeatedly cool and warm the system. Taken from [113].

The 1 K stage is made of a copper plate to which a 1 K pot is fixed. The pot is filled with liquid  $^4\text{He}$  from the main bath via a fill line, and pumped on to reduce the vapour pressure of the  $^4\text{He}$  and lower its temperature. By reducing the pressure above the liquid to 0.1 mbar, the boiling point of  $^4\text{He}$  is reduced to  $\sim 1$  K [113]. With

the pump used in our set-up, we are able to achieve a 1 K pot temperature of  $\sim 1.5$  K. The low-temperature transformers are fixed on top of the 1 K stage, to maintain their temperature constant and ensure that they provide a constant gain. The 1 K stage is connected to the LTS via a heat-switch, which can be opened or closed by turning a knob at room temperature. The heat switch is closed to initially cool the whole system to  $\sim 1.5$  K, and subsequently while the pill is being magnetized (A to B in Figure 4.11) to evacuate the heat generated by the pill and maintain its temperature constant. When the heat switch is opened, the LTS hangs off of the 1 K stage by thin Kevlar wires, which have an extremely low thermal conductivity. To prevent the LTS from swinging on the wires, a centring mechanism is installed below the probe. Both the 1 K stage and LTS are enclosed in a vacuum chamber which is evacuated, such that when the heat switch is open the LTS is essentially thermally isolated from the environment. The isolation is not perfect however, as heat-leaks take place through the measurement wires which must run between the 1 K stage and the LTS. Therefore to maintain the sample at low temperature, it is necessary to constantly demagnetize the pill at a low rate, to cancel out the heat-leaks. This limits the hold-time at low temperature, as once the pill has been completely demagnetized there is no longer any cooling power available, which is why adiabatic demagnetization is called a “one-shot” technique.

The pill is magnetized using a superconducting magnet with a maximum field of 6 T. A second superconducting magnet centred on the sample space is used to apply fields to the sample. On the LTS below the pill there is a small platform in a field-compensated region where the thermometers and heaters are located. Two thermometers are installed: a Cernox sensor which is used to monitor the temperature between 300 K and 1.5 K, and a Ge sensor which is calibrated between 100 mK and 40 K. The heater provides access to temperatures higher than that of the 1 K pot, and enables continuous operation between base temperature and  $\sim 25$  K. The measurement probe is attached to a platform below the thermometry, such that the sample lies in the field centre. A thick silver wire runs between the thermometry platform and the probe, to reduce the thermal time-constant between the two.

For the  $\text{Sr}_2\text{RuO}_4$  experiment, we performed temperature ramps between 1 – 2.5 K at different applied strains. To do this, we would fully magnetize the pill and, with the heat switch closed, wait for the sample to cool to the desired upper limit of the temperature ramp. The heat switch would then be opened, and the current in the demagnetization magnet ramped down to cool the LTS. Once the lower limit of the ramp was reached, the magnet would be ramped back up, so that data from both ramp directions could be compared to take into account temperature lag between the temperature sensor and the sample when performing data analysis. To obtain the desired temperature ramp-rate (typically 20 – 40 mK/min), software with a feedback loop using the Ge sensor as the input was used to set the correct ramp-rate of the current through the pill magnet. We found that as many as twenty runs at different strains could be performed before a full re-magnetization of the pill magnet was necessary.

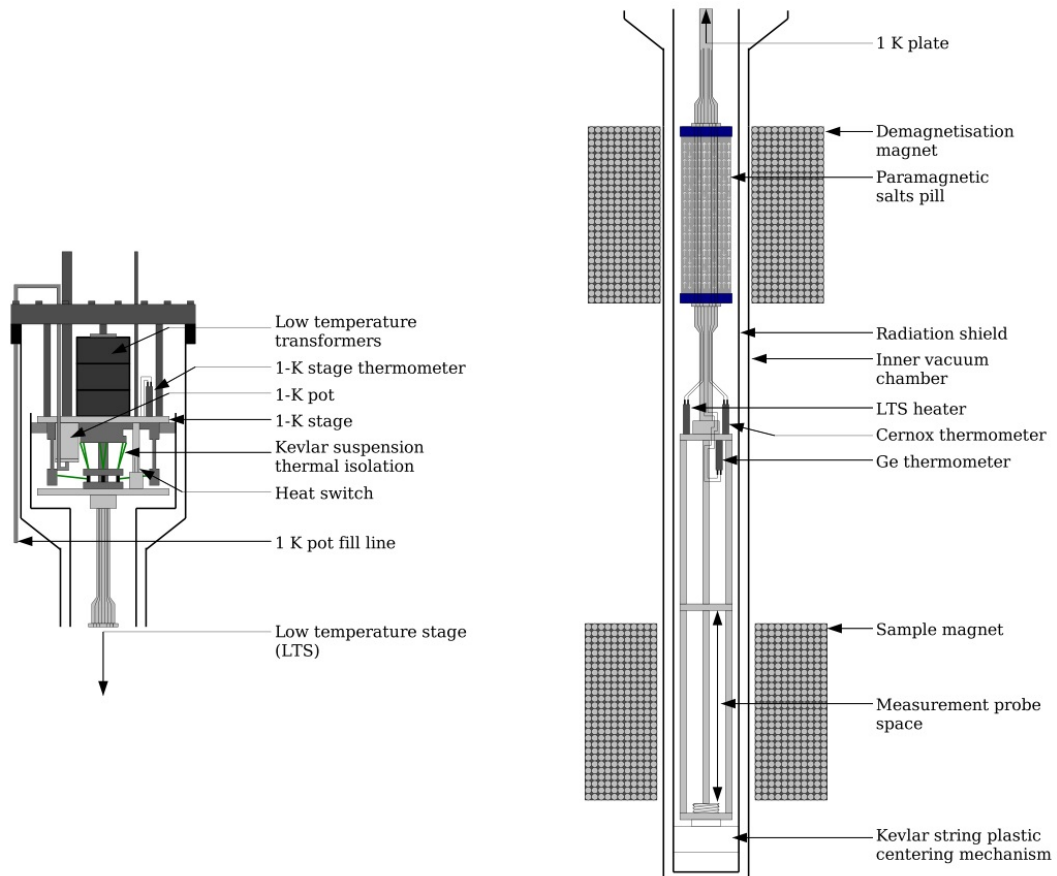


Figure 4.12: Diagram of the ADR's 1 K stage (*left*) and LTS (*right*). The thermal link between the two stages is controlled by a heat switch, which can be opened or closed. Both stages are enclosed in a vacuum chamber, which along with the demagnetization and sample magnets is immersed in a bath of liquid  $^4\text{He}$ . Taken from [111].

In the case of the  $\text{Sr}_3\text{Ru}_2\text{O}_7$  experiment, we wished to maintain the sample at a low temperature, and perform field ramps at different strains. This was achieved by opening the heat switch and demagnetizing the pill magnet after the system had cooled to  $\sim 1.7$  K. Once the desired temperature was reached (typically 300 mK), we used the software with a feedback loop to stabilize the temperature by slowly demagnetizing the salt pill. At a hold temperature of 300 mK, the hold time was typically around 7 hours before the pill became completely demagnetized. The hold time decreases rapidly at lower temperatures, with the hold time at 100 mK being between 1 – 2 hours.

#### 4.5.1 Stray field cancellation (for $\text{Sr}_2\text{RuO}_4$ experiment)

We found that there were stray fields of the order of  $\sim 5$  G at the sample, arising from the demagnetization magnet. This is a very small field, and does not affect the  $\text{Sr}_3\text{Ru}_2\text{O}_7$  measurement where we are applying high fields up to 10 T to the sample with the sample magnet. For the  $\text{Sr}_2\text{RuO}_4$  experiment however we wanted to obtain an accurate estimate of  $T_c$ , which can be affected by such small fields. We therefore cancelled out the stray field from the pill magnet by applying a small field in the opposite direction with the sample magnet. The correct cancellation field was found by keeping the current through the demagnetization magnet constant, and setting the current through the main magnet such that the sample's  $T_c$  was maximized. In this way we obtained the ratio  $I_{\text{sample}}/I_{\text{pill}} = 4.7 \times 10^{-4}$  of the current through the sample magnet to the current through the pill magnet to cancel out the stray field at the sample. While performing temperature ramps during the  $\text{Sr}_2\text{RuO}_4$  experiment,  $I_{\text{pill}}$  was used as an input to calculate the correct  $I_{\text{sample}}$  and minimize the stray field.

#### 4.5.2 Sample temperature (for $\text{Sr}_2\text{RuO}_4$ experiment)

Although temperature control was performed using the Ge sensor on the ADR, the sample temperature itself was monitored with the  $\text{RuO}_x$  chip mounted directly on the probe, and thermally linked to the sample via a piece of silver foil. The proximity of the  $\text{RuO}_x$  chip enabled us to accurately determine the sample's temperature, which is crucial for measuring its  $T_c$  to high accuracy. The  $\text{RuO}_x$  sensor was calibrated against the Ge sensor by performing a 40 mK/min temperature ramp. To measure the chip's resistance, we ran a 10  $\mu\text{A}$  current through it and measured the voltage drop across it with a lock-in amplifier. To increase the sensitivity of our measurement, a current at the same frequency was run through a high-precision variable resistor at room temperature, and the voltage across it was subtracted from that across the  $\text{RuO}_x$  chip; the variable resistor was set such that at  $\sim 1.5$  K the reading at the lock-in would be 0 V. The subtracted voltage corresponds to a resistance of  $\sim 1520 \Omega$ . The raw data from a calibration run, along with the resulting calibration curve, are shown in Figure 4.13. The calibration of the  $\text{RuO}_x$  chip was checked after each cool-down to ensure that there was no drift in our temperature

measurement over time.

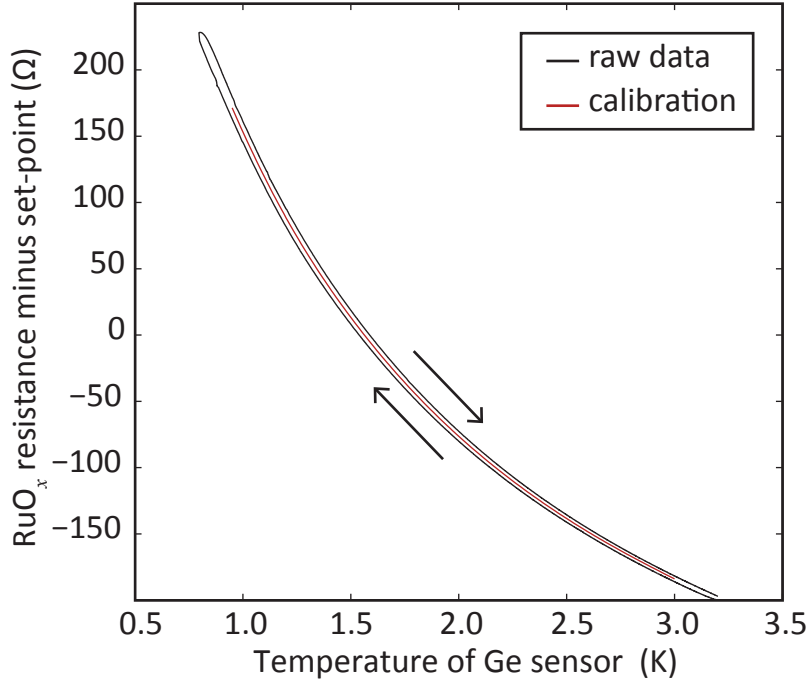


Figure 4.13: Raw data used to calibrate the  $\text{RuO}_x$  sensor, and the resulting calibration curve. A set-point was chosen such that the measured resistance would be zero for  $T \approx 1.5$  K, as described in the text. The black arrows indicate the direction of the temperature ramp.

### 4.5.3 Note on temperature for the $\text{Sr}_3\text{Ru}_2\text{O}_7$ experiment

For the  $\text{Sr}_3\text{Ru}_2\text{O}_7$  experiment, we were performing field- rather than temperature-ramps, and so it was not crucial to have the temperature sensor right next to the sample. We therefore used the Ge sensor on the ADR to estimate the sample's temperature. The ADR, which was manufactured by Cambridge Magnetic Refrigeration, was used with a 15 T sample magnet manufactured by Oxford Instruments to give access to a larger field range for the  $\text{Sr}_3\text{Ru}_2\text{O}_7$  experiment. At the time of the experiment, it was believed that the Ge and Cernox temperature sensors were situated in the field-compensated region of the Oxford magnet, and so temperature control was performed using the Ge sensor. However it was later realized that due to an error in the position of the Oxford magnet relative to the ADR, the temperature sensors lie outside of the field-compensated region, giving rise to an error in our temperature estimate due to the Ge sensor's magnetoresistance. As the magnetic field is ramped, the temperature is therefore not held constant at 300 mK (the temperature at which we wished to stabilize), as the reading of the temperature sensor

changes with field. We estimate that there was a systematic increase of  $\sim 80$  mK between 0 and 12 T, the total field range studied. In the region of particular interest between 7 and 10 T, we estimate an increase of  $\sim 20$  mK. As we note in Chapter 6, our conclusions from the data are not affected by this effect, as the temperature dependence of the resistivity in the phase is very small at  $\sim 300$  mK [39]. The  $\text{Sr}_2\text{RuO}_4$  measurements are not affected by this, as they were performed in the 8 T magnet from Cambridge Magnetic Refrigeration, for which the temperature sensors were measured to be in the middle of the field-compensated region so that the temperature was accurately known.

## Chapter 5

# Effect of Uni-axial Strain on $T_c$ of $\text{Sr}_2\text{RuO}_4$ : Results and Discussion

The key question which we wished to address by straining  $\text{Sr}_2\text{RuO}_4$  is whether the strain dependence of  $T_c$  is consistent with a two-component order parameter of the form  $p_x \pm ip_y$ . As argued in Section 3.5.4, a signature of such a state would be a cusp at zero strain, where there is an abrupt change in the slope  $dT_c/d\varepsilon$ . To test this hypothesis, we measured  $T_c(\varepsilon)$  using AC magnetic susceptibility for a total of six samples: three aligned along [100] and three along [110]. The dimensions of the samples are given in the following table, where  $L$  is the length of the gap between the sample plates,  $w$  and  $t$  the sample width and thickness, and  $d_l$  and  $d_u$  the thickness of the epoxy layer below and above the sample:

sample	$L$ ( $\mu\text{m}$ )	$w$ ( $\mu\text{m}$ )	$t$ ( $\mu\text{m}$ )	$d_l, d_u$ ( $\mu\text{m}$ )	$\varepsilon L/\Delta L$ (%)
[100] #1	750	110	30	20, 20	80
[100] #2	660	170	60	10	63
[100] #3	700	160	50	10	—
[110] #1	680	150	45	10, 40	74
[110] #2	840	250	60	15, 15	78
[110] #3	660	190	60	10, 30	71

Table 5.1:  $\text{Sr}_2\text{RuO}_4$  sample dimensions.

All of the dimensions given were measured using a microscope. The final column gives an estimate of the actual sample strain  $\varepsilon$  as a percentage of  $\Delta L/L$ , where  $\Delta L$  is the change in gap length caused by the motion of the piezoelectric stacks. These numbers were obtained by Mark Barber who performed finite element calculations for each sample, using the dimensions from the above table and modelling the de-

formation of the epoxy in the sample mounts. To calculate the sample strain, we applied this factor to the displacement of the sample plates measured by the strain gauge. All of the  $\text{Sr}_2\text{RuO}_4$  samples were measured with the first generation strain probe, pictured in Figure 4.4b. Samples [100] #1 and [110] #1 were cut from the crystal batch WD03 which has  $T_c = 1.35$  K, while samples [100] #2, [100] #3, [110] #2 and [110] #3 came from crystal batch c362c2b which has  $T_c = 1.45$  K. All of the samples were cut and mounted using the protocols described in Sections 4.1.5, 4.2 and 4.4. To improve strain homogeneity in the centre of the samples, we used cap foils so that the samples were fixed on their top and bottom faces, with the exception of samples [100] #2 and #3 which were only secured on their lower faces.

## 5.1 Strong dependence of $T_c$ of $\text{Sr}_2\text{RuO}_4$ on uni-axial strain

We will now present our main experimental results, which consist of a series of temperature ramps performed at different applied strains, and which we first published in ref. [92]. Figure 5.1 shows the superconducting transition of sample [100] #2 for several compressive and tensile strains. The measurement was performed with a 1 mA AC current with a frequency of  $f = 63.13$  Hz running through the excitation coil, corresponding to a field of  $\sim 0.25$  G at the sample<sup>1</sup>. This is much smaller than the sample's upper critical field, which is 750 G at  $T = 0$  K [5]. We have plotted the in-phase and out-of-phase parts of the mutual inductance  $m$  between the coils, which were defined in Section 4.4, and which are directly related to the in-phase and out-of-phase parts of the sample's susceptibility respectively.

The onset of superconductivity is clearly seen in each case where a drop in  $m'$  is accompanied by a peak in  $m''$  as the sample becomes diamagnetic. A clear trend is observed: the superconducting transition is pushed upwards in temperature for both compression and tension along [100]. We also note that the transitions broaden as strain is increased, signalling the presence of strain inhomogeneity. As noted for this sample, the mounting conditions are not symmetric as no cap foil was used, and it is possible that the sample becomes bent at high strains. A consequence of the pick-up coil diameter being roughly the same size as the sample width is that local variations in  $T_c$  across the sample will cause a broadening of the observed transition.

The data were obtained by ramping the temperature at 40 mK/min, and averaging the up- and down-ramps to cancel out any hysteresis. The sample temperature was measured using the  $\text{RuO}_x$  sensor on the strain probe, as detailed in Section 4.5.2. A new strain was set at the beginning of each ramp by changing the voltages applied to the piezoelectric stacks, and then holding the voltages constant during the ramp. To go from compression to tension, we incrementally changed the voltages on the inner and outer stacks from  $(V_{inner}, V_{outer}) = (400 \text{ V}, 0 \text{ V})$  to  $(0 \text{ V}, 400 \text{ V})$  in 20 V steps, giving strain steps of  $\sim 0.01\%$ . To further extend the range on the

<sup>1</sup>The excitation coil has 100 turns, a  $\sim 2$  mm diameter and is  $\sim 1$  mm above the sample.

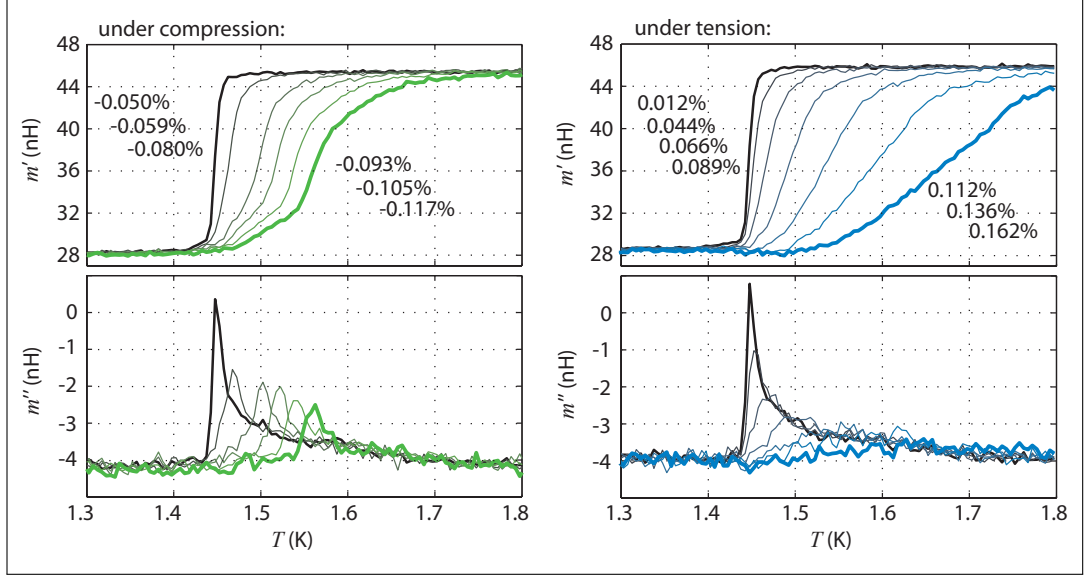


Figure 5.1: Superconducting transitions of  $\text{Sr}_2\text{RuO}_4$  sample [100] #2 under compression and tension. The onset of superconductivity is signalled by a drop in  $m'$  and a peak in  $m''$ . The estimated strains for each curve are labelled. Reproduced from [92].

compression side, we applied negative bias voltages to the outer stacks, going up to (137.5 V, -412.5 V). This gave a total strain range on the sample from  $\sim -0.12\%$  to  $\sim +0.16\%$ .

To test the reproducibility of these results, we repeated the above experiment on sample [100] #1 which comes from a different batch of crystals. The transitions of this sample were measured at 369 Hz and are shown in Figure 5.2, along with a picture of the sample and pick-up coil. The same ramp-rate and voltage steps as before were used, however this time the strain range was extended on both the tension and compression sides. To achieve higher tension the inner stacks were reverse biased up to (-342 V, 138 V), and for higher compression we went up to (169 V, -421 V); this gave a strain range on the sample from  $\sim -0.23\%$  to  $\sim +0.22\%$ . We observe again the strong increase of  $T_c$  when the sample is either compressed or tensioned, with broadening and extra structure in the transition likely due to strain inhomogeneity. This time we have labelled the  $y$ -axis as the susceptibility in arbitrary units (as we do not extract an absolute value from our data), normalized to the height of the drop in  $\chi'$  at  $T_c$ . We define the  $T_c$  of the sample as the 50% level of the drop in  $\chi'$ , as illustrated by the dashed line. Extracting  $T_c$  in this way for both [100] samples, we plot  $T_c$  versus strain (Figure 5.3A). The two sets of points correspond to the  $T_c$ 's of each sample, and the black lines to the 20% and 80% levels of the drop in  $\chi'$ . These are there to illustrate how much the transition broadens at high strains. We note that the transitions of sample [100] #1 remain narrower than

those of [100] #2, reflecting the fact that the former was mounted with a cap foil and the latter without.

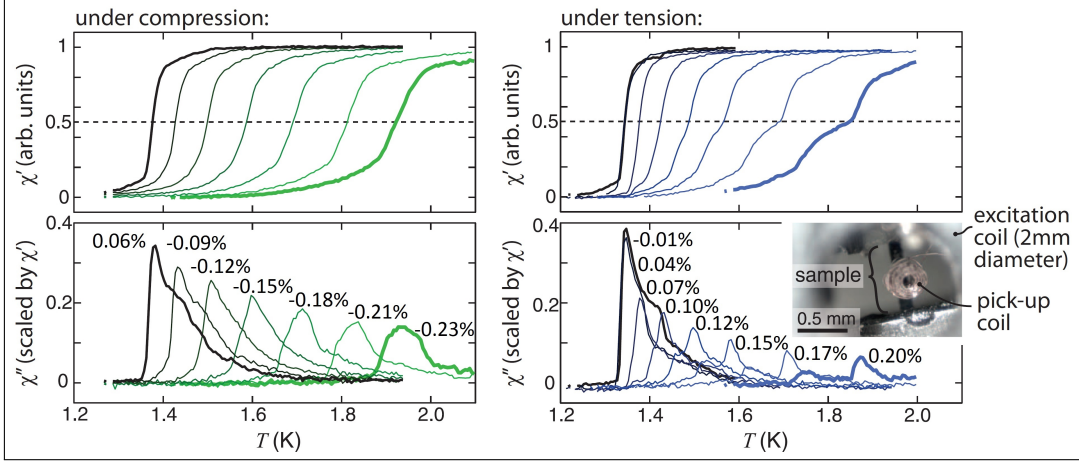


Figure 5.2: Superconducting transitions of sample [100] #1 under compression and tension. The 50% level of the drop in  $\chi'$  is used to define  $T_c(\varepsilon_{100})$ , which is plotted in Figure 5.3. A photograph of the sample and the pick-up coil is shown in the lower right panel. Reproduced from [92].

The results shown in Figure 5.3A are striking: superconductivity in  $\text{Sr}_2\text{RuO}_4$  is highly sensitive to strain  $\varepsilon_{100}$  applied along [100], with the  $T_c$  of sample [100] #1 being enhanced from 1.35 K at zero strain to  $\sim 1.9$  K at  $\sim 0.2\%$  compression. We are able to increase  $T_c$  by more than 40% for a  $\sim 0.2\%$  strain. Moreover we note that there is a large component of the response which is symmetric about zero strain, and that the increase in strain is not linear. Figure 5.3C shows the derivative  $dT_c/d\varepsilon_{100}$  for both samples: for  $|\varepsilon_{100}| < 0.03\%$ ,  $T_c(\varepsilon_{100})$  and  $dT_c/d\varepsilon_{100}$  are essentially flat, whilst beyond  $\sim 0.03\%$  strain  $dT_c/d\varepsilon_{100}$  increases linearly meaning that  $T_c(\varepsilon_{100})$  behaves quadratically. The flat region around zero strain may be affected by strain inhomogeneity, however the large increase of  $T_c$  is unambiguous in both samples, and was reproduced using several different excitation currents and frequencies (see Section 5.2). Another striking observation is that there appears to be no discontinuity in the slope at zero strain, contrary to what was predicted for the  $p_x \pm ip_y$  order parameter.

To further investigate the effect of strain on superconductivity in  $\text{Sr}_2\text{RuO}_4$ , we mounted samples which were cut along [110] to apply  $\varepsilon_{110}$ . The raw data for sample [110] #2, measured with an excitation current of 2 mA at 68.38 Hz, are shown in Figure 5.4;  $T_c(\varepsilon_{110})$  of samples [110] #1 and #2 is plotted in Figure 5.3B. The temperature scales in Figures 5.3A and B are the same to highlight the large difference in magnitude between the responses to both types of strain.  $T_c(\varepsilon_{110})$  appears quantitatively and qualitatively very different to  $T_c(\varepsilon_{100})$ : its strain dependence is far weaker, and appears to be roughly linear. The width of the transitions remains ap-

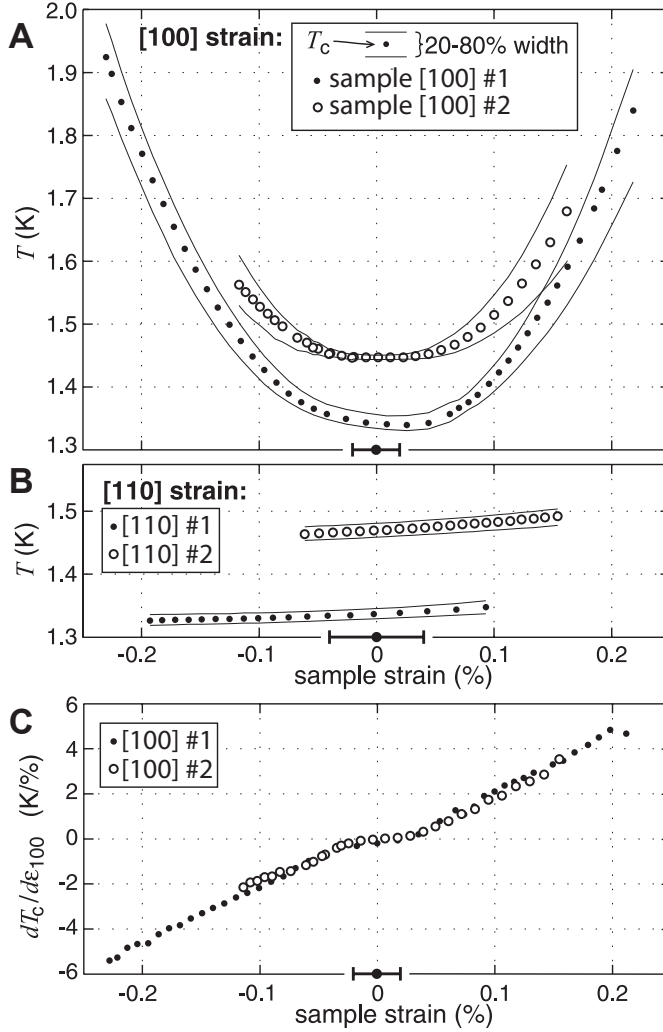


Figure 5.3: **A:**  $T_c$  versus strain for both samples aligned along [100]. The points represent the 50% level of the drop in  $\chi'$  at the transition, extracted from the raw data. The width of the transitions is illustrated by the solid lines, which mark the 20% and 80% levels of  $\chi'$ . Negative strain corresponds to compression. **B:** Strain dependence of  $T_c$  for the samples aligned along [110]. Samples [110] #1 and [110] #2 were cut from the same crystals as [100] #1 and [100] #2 respectively. **C:** Derivative  $dT_c/d\varepsilon_{100}$  of the data shown in **A**. The error bars on the strain axis show the estimated error in locating zero strain. Reproduced from [92].

proximately constant for all strains, indicating that there is not a broad distribution of  $T_c$ 's throughout the sample. This is a consequence of  $T_c$  not being very sensitive to [110] strain: one only expects the transitions to broaden with strain if  $T_c$  depends strongly on the local strain. Again, the discontinuity in slope at zero strain which is predicted for a chiral superconductor is not observed. One fact which is emphasized by Figure 5.3 is the strong dependence of  $T_c$  on the direction of applied strain. Whereas  $p_x \pm ip_y$  superconductivity is often modelled for an isotropic Fermi surface, our data highlight that the tetragonal crystal symmetry is greatly influential.

### 5.1.1 Effect of cut-angle on $T_c(\varepsilon)$

Although  $T_c(\varepsilon)$  of both [110] samples plotted in Figure 5.3B appears to be roughly linear, the data possess a slight curvature. One hypothesis is that a slight misalign-

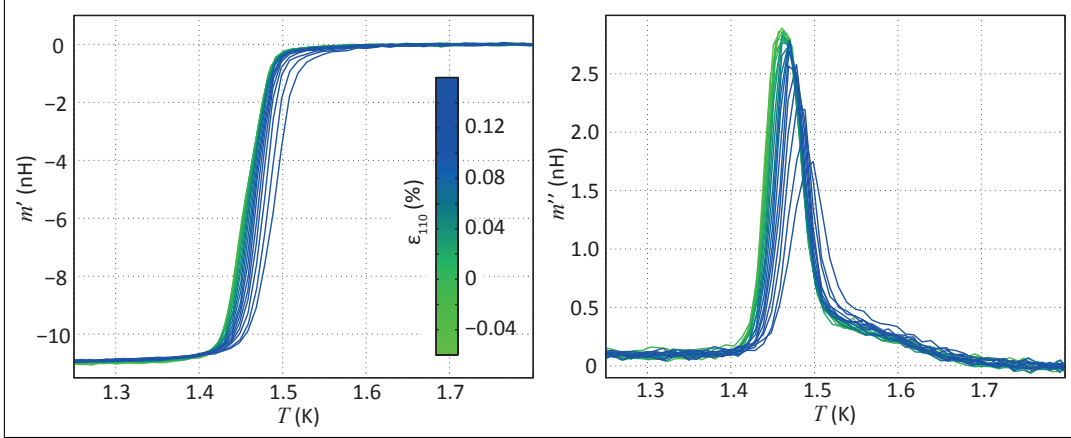


Figure 5.4: Superconducting transitions of sample [110] #2 at different applied strains.

ment of the sample with respect to [110] could lead to the response developing a symmetric component due to a small  $\epsilon_{100}$  component being mixed into the strain. To test this hypothesis, we cut sample [110] #3 from the same crystal as [110] #2, with the cut rotated by  $2.5^\circ$  in-plane relative to the original [110] cut. A picture and sketch illustrating how the samples were cut relative to each other are shown in Figures 5.5a and 5.5b. The alignment of the cuts for sample [110] #2 was performed using X-Ray Laue diffraction as described in Section 4.2. The cuts for sample [110] #3 were aligned by setting the angle between the cutting wire and the original [110] cut under a microscope.

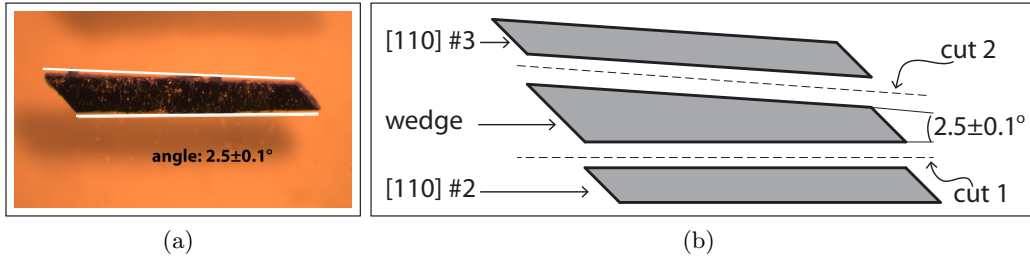


Figure 5.5: (a) Photograph of the wedge of  $\text{Sr}_2\text{RuO}_4$  which was cut between samples [110] #2 and [110] #3, sketched in (b). (b) Diagram showing how the two samples were cut relative to each other. Cut 1 was aligned by X-ray Laue diffraction, and cut 2 was aligned under a microscope relative to cut 1.

The results of the measurements on sample [110] #3 are compared to those of the previous two samples in Figure 5.6A. A larger symmetric response is clearly seen for [110] #3 compared to the other two. The magnitude of the additional symmetric response seems consistent with the additional  $\epsilon_{100}$  that would result from an extra

2.5° misalignment with [110]. For a sample perfectly aligned along [110], the applied strain  $\varepsilon$  can be written as  $\varepsilon = \varepsilon_{xy}$ , with  $\varepsilon_{xx} = \varepsilon_{yy}$ . For a 2.5° misalignment  $\varepsilon \neq \varepsilon_{xy}$  and  $|\varepsilon_{xx} - \varepsilon_{yy}| = (\cos(42.5^\circ) - \sin(42.5^\circ))\varepsilon \approx 0.06\varepsilon$ . So for a strain  $\varepsilon = 0.013\%$  applied along the sample's length, there will be a component of anisotropic strain  $|\varepsilon_{xx} - \varepsilon_{yy}| \approx 0.08\%$ , which causes a small additional increase in  $T_c$ , as this is beyond the flat region in  $T_c(\varepsilon_{100})$ .<sup>2</sup>

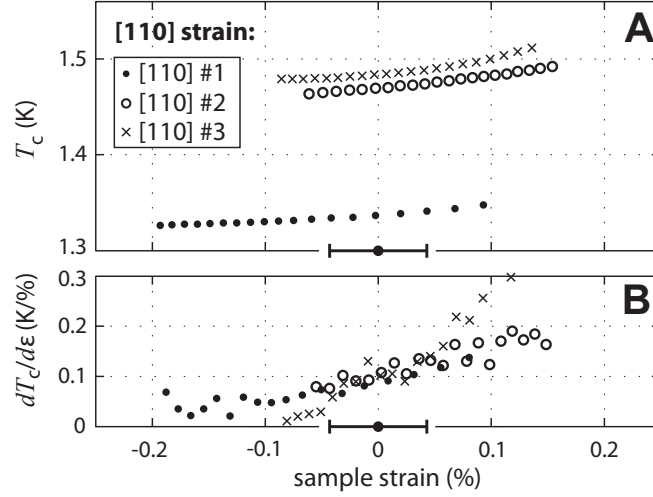


Figure 5.6: **A**:  $T_c$  versus strain for the three [110] samples. Sample [110] #3 is cut at an angle of 2.5° relative to sample [110] #2. **B**: Derivatives of the data shown in **A**. Reproduced from [92].

Figure 5.6B shows the derivatives of the data in panel **A**. All three data-sets indicate that the slope of  $T_c$  against  $\varepsilon_{110}$  is approximately +0.1 K/% at zero strain. The above results show that the response of  $T_c$  to in-plane strain is extremely sensitive to the precise direction along which strain is applied. It appears very likely that the response for a sample perfectly aligned along [110] would be completely linear in strain. Any curvature we observe would then be due to a slight misalignment which mixes in a symmetric component from [100] strain.

Two important questions are raised by our data: (1) why does the response depend so strongly on the direction of applied strain, and (2), why is no cusp at zero strain observed? These questions are discussed in detail in Section 5.3, where various models are explored to try and account for our experimental observations.

## 5.2 Experimental details

We now give an in-depth account of several experimental details which are crucial in demonstrating the reproducibility and reliability of our data.

<sup>2</sup>The flat region in  $T_c(\varepsilon_{100})$  extends up to  $\varepsilon_{100} \sim 0.03\%$ , which corresponds to an anisotropic strain of  $|\varepsilon_{xx} - \varepsilon_{yy}| \approx 0.02\%$ , assuming a Poisson's ratio of 0.4 and that  $\varepsilon_{100} = \varepsilon_{xx}$ .

### 5.2.1 Strain measurement and determination of zero strain

To accurately determine  $T_c(\varepsilon)$  it is necessary to know both the sample temperature and strain to high accuracy. The sample temperature is known to high accuracy thanks to its proximity to the  $\text{RuO}_x$  sensor, as discussed in Section 4.5.2. In this section we will focus on how the strain was determined, beginning with a description of how the displacement of the plates was measured with the strain gauge before showing how zero strain was estimated.

As described in Section 4.1.4, a strain gauge is mounted on the strain probe under the sample, such that the displacement which is applied by the stacks causes the strain gauge to become strained. We assume that the change in length of the strain gauge is the same as the change in length of the gap between the sample plates  $\Delta L$ . Using the gauge factor of 2 for our strain gauge we calculate  $\Delta L$  from its change in resistance, and estimate the strain on the sample by multiplying  $\Delta L/L$  by the correction factor  $\varepsilon L/\Delta L$  of Table 5.1.

The active strain gauge is measured in a bridge circuit with three other strain gauges, as sketched in Figure 5.7a. The three unstrained gauges are mounted on copper plates which are thermalized to the probe. For all of our measurements, a 10  $\mu\text{A}$  AC current was run between terminal 1 and ground, and the voltage between terminals 2 and 3 measured with a lock-in amplifier. A strain applied to the active strain gauge will cause its resistance to change and the bridge circuit to become unbalanced, giving rise to a voltage  $V_{23} = V_2 - V_3$ . An example of the measured voltage  $V_{23}$  is shown in Figure 5.7b for a series of voltages applied to the piezoelectric stacks. Both the up- and down-ramps are shown. As can be seen, the strain gauge resistance has a small temperature dependence, which is the same at all strains.

We also note that the voltages measured at the beginning and end of each ramp are not exactly the same. This is caused by a drift in the length of the stacks over time, as they relax after a new voltage has been applied to them. To prevent large changes in sample strain at the beginning of the ramp, we would typically wait 1 minute after setting the voltages on the stacks to allow them to relax, before starting the temperature ramp. The drift in strain gauge voltage between the beginning and end of a ramp corresponds to a strain variation of  $\sim 0.001\%$  throughout the ramp, or roughly 10% of the step in strain between ramps.

To estimate the sample plate displacement from  $V_{23}$ , we first subtracted the temperature dependence, which was obtained by measuring  $V_{23}$  with no voltage applied to the stacks. We then took the average value of  $V_{23}$  over a given strain run  $\bar{V}_{23}$ , and plugged it in to the strain gauge equation:

$$\frac{\Delta L}{L_g} = \frac{\Delta R}{2R} \approx \frac{2(\bar{V}_{23} - V_{23}(0))}{IR}, \quad (5.2.1)$$

which is valid for  $\Delta R \ll R$ .<sup>3</sup>  $L_g$  is the length of the strain gauge,  $V_{23}(0)$  the voltage at zero strain,  $R$  the resistance of the strain gauge and  $I$  the current through the

---

<sup>3</sup>This is indeed the régime we are working in, as  $R = 1000 \Omega$  and  $\Delta R < 1 \Omega$ .

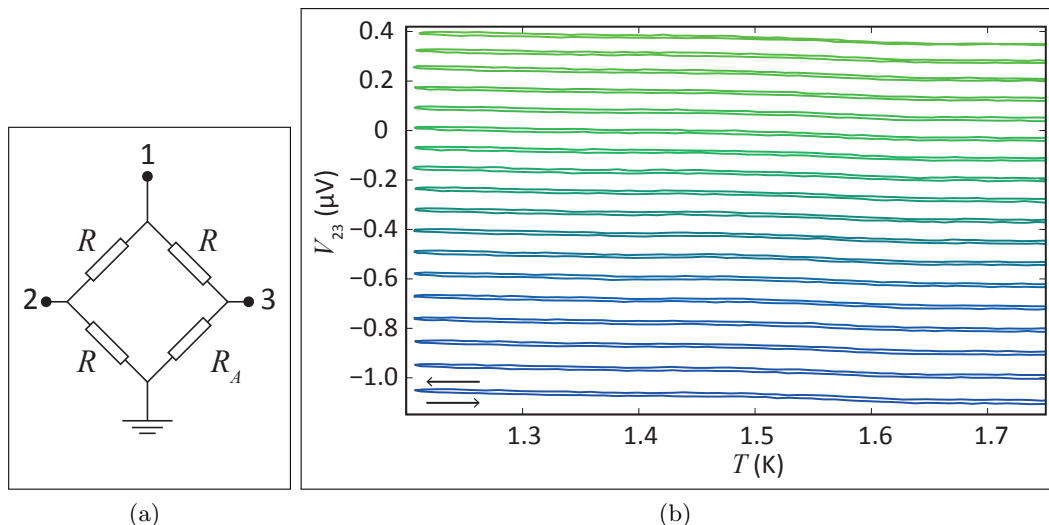


Figure 5.7: (a) Diagram of the bridge circuit in which the strain gauge on the probe is measured. The four resistances shown correspond to strain gauges (all of the same model), with  $R = 1000 \Omega$ .  $R_A$  denotes the active strain gauge, whose change in resistance due to an applied strain from the piezoelectric stacks causes a change in  $V_{23}$ . (b) Plot of  $V_{23}$  as a function of temperature for a series of voltages applied to the stacks. The direction of the temperature ramp is indicated by the black arrows. A lower value of  $V_{23}$  corresponds to greater tension. The voltages on the stacks go from  $(V_{inner}, V_{outer}) = (400 \text{ V}, 0 \text{ V})$  for the uppermost curve to  $(76 \text{ V}, 324 \text{ V})$  for the lowest curve, in 18 V steps.

bridge circuit. The calculated displacement  $\Delta L$  is the average displacement over the entire temperature run. We found that within each cool-down the strain gauge produced a reliable and reproducible measure of the displacement. However, we observed that there were  $\sim 0.1 \Omega$  shifts in the bridge circuit balance each time the system was thermal-cycled between room and low temperature.

It is important to note that the strain gauge measurement only gives us an estimate of the displacement relative to a chosen origin at which  $\bar{V}_{23} = V_{23}(0)$ , and not the absolute displacement. It is therefore essential to have an accurate estimate for where zero strain is located, so as to scale all of the measured displacements relative to it. However, as noted in Section 4.1.4, differential thermal contractions between the strain probe and the sample can lead to the sample becoming highly strained at low temperatures. To minimize this effect, we used copper thermal contraction foils, whose thickness was calculated to try and match the thermal expansion of the probe to  $\text{Sr}_2\text{RuO}_4$ . However we did not have accurate enough control over the foil thickness to perfectly cancel out differential thermal contractions. A consequence of this is that the sample is most likely in a strained state at low temperature even with no voltage applied to the stacks, and so the exact location of zero strain is

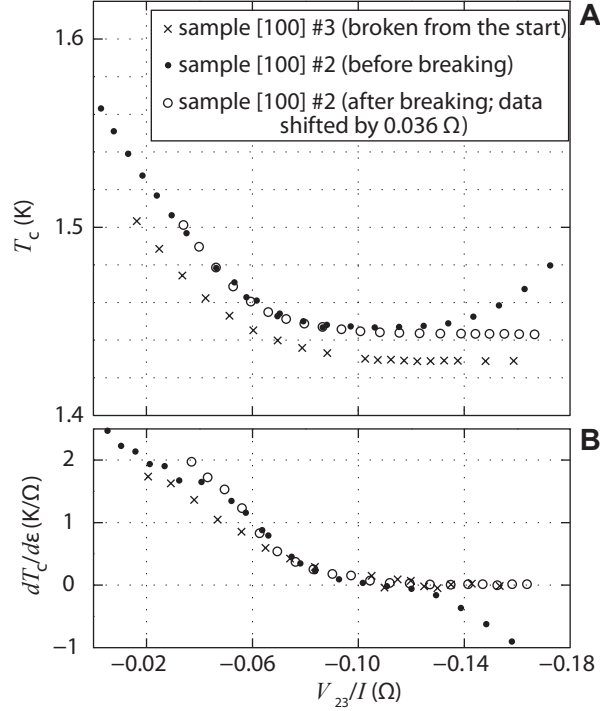


Figure 5.8: **A**:  $T_c$  of broken samples versus strain gauge response. A more negative response corresponds to stronger tension, the  $x$ -axis being flipped so that tension is on the right side of the plot. Sample [100] #2 was thermal-cycled between the pre- and post-break measurements, so that a shift of  $0.036 \Omega$  to the strain gauge reading is needed to align the data on the compression side. **B**: Derivatives of the data shown in **A**. Reproduced from [92].

unknown.

The first method used for estimating the location of zero strain was directly calculating the differential thermal contraction using the sample and foil dimensions. In this way we found that zero strain always lay within 0.04% of the centre of the flat section of  $T_c(\varepsilon_{100})$ , there being no clear bias towards one side or the other. The second method was to measure broken samples.

We found that sample [100] #3 was broken when we cooled it down, meaning that it could only be compressed. Additionally, after finishing the main measurement on sample [100] #2, we snapped it intentionally by applying a high tensile strain. To snap the sample we brought the probe back up to room temperature where the stacks have a larger range of motion. In both cases, observation under the microscope revealed that the breaks had occurred in the centre of the sample. The results from the measurements of the broken samples are shown in Figure 5.8**A**. Starting on the tension side and gradually compressing the sample,  $T_c$  does not change with strain until a given separation of the plates is reached and  $T_c$  increases

quadratically. By comparing the data from the broken and unbroken samples, we can estimate at which strain both ends of the broken sample first touch to determine the location of zero strain. Due to the mentioned shift in the strain gauge resistance with thermal-cycling, it was necessary to shift the post-break data by  $0.036 \Omega$  to line up the curves on the compression side. Having done this, the pre- and post-break data from sample [100] #2 match extremely well. We note that  $T_c$  on the tension side of the post-break sample (where no force is being applied to it) almost exactly matches that of the flat region of  $T_c(\varepsilon_{100})$  of the unbroken sample, indicating the zero strain lies within this region. Additionally, the behaviour of  $dT_c/d\varepsilon$  of both broken samples (Figure 5.8B) also indicates that zero strain is located somewhere in the flat region:  $dT_c/d\varepsilon$  rises smoothly from zero as the sample is compressed. If instead zero strain were at a point with a large slope, we would expect a jump in  $dT_c/d\varepsilon$  as the sample initially becomes compressed.

For the samples cut along [100], we estimate that zero strain is located within 0.02% of the centre of the flat region, which we have illustrated with the error bars in Figures 5.3A and C. In the case of the [110]-oriented samples, there is no clear feature near zero strain, so we rely solely on our calculation of the differential thermal contraction, and assign a  $\pm 0.04\%$  error on zero strain. We also assign a 10% error to the stated strains, arising from the slow drift of the stack length over the temperature runs.

As a final note, we should mention that these strain calculations do not take into account any possible bending of the strain gauge due to motions of the stacks and differential thermal contractions which may affect our strain calculation. At the time of measurement we did not have the capability of performing an independent check of the strain measurement, however for future experiments it would be useful to carry out a low-temperature calibration of the mounted strain gauge. This could be done using an interferometer for example.

### 5.2.2 Excitation current and frequency

As noted in Section 5.1, one of our main observations is the lack of a cusp in  $T_c(\varepsilon)$  at zero strain, and the large increase of  $T_c$  at higher strains. It is therefore important to establish that these observations are intrinsic behaviours of the sample, rather than an artefact of the measurement itself. In particular, the cusp at zero strain may be small, so it should be checked whether the excitation field used to measure the AC susceptibility could affect the shape of  $T_c(\varepsilon)$  at low strains.

For samples [100] #1 and #2 we measured  $T_c(\varepsilon_{100})$  by running a series of currents between 0.05 mA and 2 mA through the excitation coil, corresponding to fields at the sample between  $\sim 0.01$  G and  $\sim 0.5$  G. Measurements were also performed with 0.02 mA and 0.01 mA, however in these cases the data were too noisy to reliably extract  $T_c$ . Raw data from sample [100] #2 taken at different excitation currents are shown in Figure 5.9, and the transition temperatures of both samples are plotted in Figure 5.10A. The shapes of the transitions do not change much with current, and we are able to reliably define a  $T_c$  for excitation currents as low 0.05 mA, by

taking the 50% level of the drop in  $\chi'$ . The shape of  $T_c(\varepsilon_{100})$  appears identical at all the currents used, and its low-strain behaviour does not seem to be affected by the magnitude of  $I_{exc}$ . As  $I_{exc}$  is increased from 0.05 mA to 2 mA, the measured  $T_c$  falls by  $\sim 20$  mK.

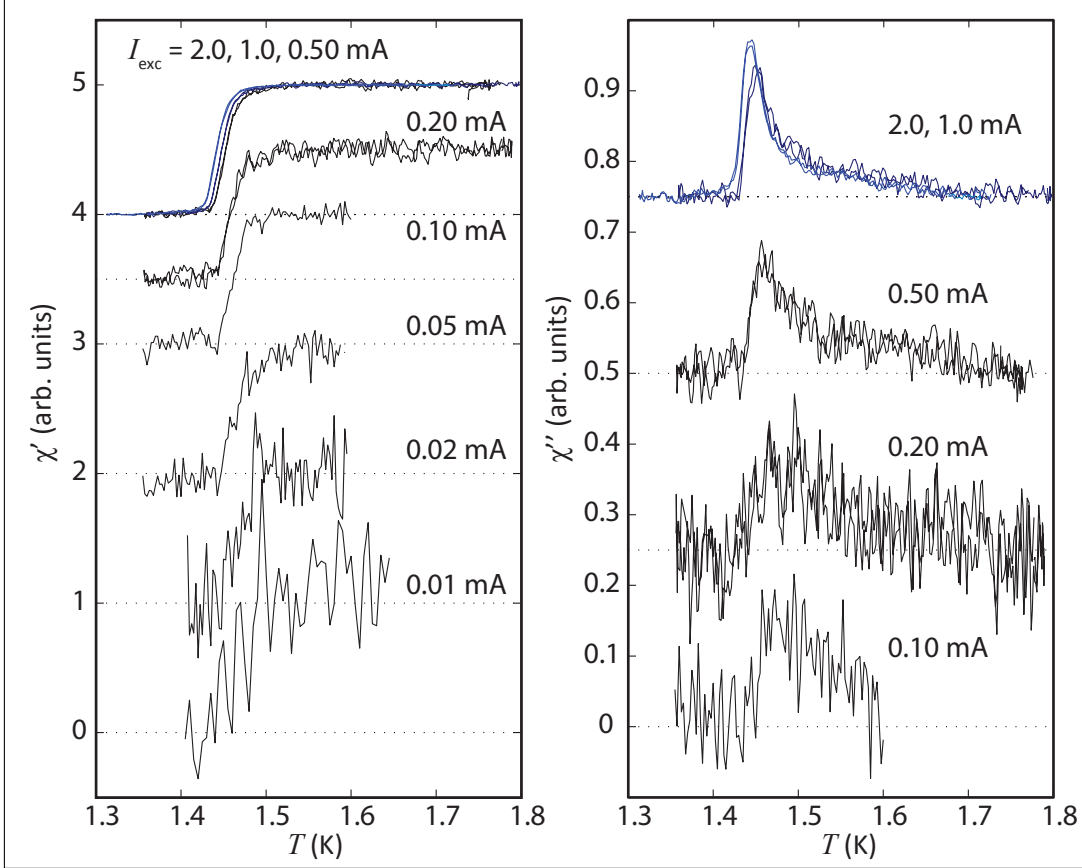


Figure 5.9: Real and imaginary parts of  $\text{Sr}_2\text{RuO}_4$ 's AC susceptibility measured with the excitation current  $I_{exc}$  ranging from 0.01 mA to 2.0 mA, corresponding to fields from  $\sim 2.5$  mG to  $\sim 0.5$  G. All measurements are at the same strain. A well defined transition is observed for currents between 2.0 mA and 0.05 mA, whilst for lower currents the noise levels are too high. No peak in the imaginary part can be distinguished below 0.1 mA.

We performed the same test on sample [110] #2 to see if the magnitude of  $I_{exc}$  has any effect on the shape of  $T_c(\varepsilon_{110})$ . The results, shown in Figure 5.10B, indicate that as in the case of the [100] samples, the observed behaviour does not depend on  $I_{exc}$ ; indeed the curves at higher current appear simply to be rigidly shifted downwards in temperature, with no significant effect on the shape of the curve.

Through this study of the effect of  $I_{exc}$  on  $T_c$  of both [100] and [110] samples, we have shown that our results are reproducible over a wide range of magnitudes for

$I_{exc}$ , and conclude that the shape of  $T_c(\varepsilon)$  measured does not have a large dependence on  $I_{exc}$ . We should note that the flattening of  $T_c(\varepsilon_{100})$  around zero strain occurs within  $\sim 20$  mK, similar to the shift in  $T_c$  caused by the probing field. It is therefore possible that the observed behaviour close to zero strain is affected to some extent by the probing field.

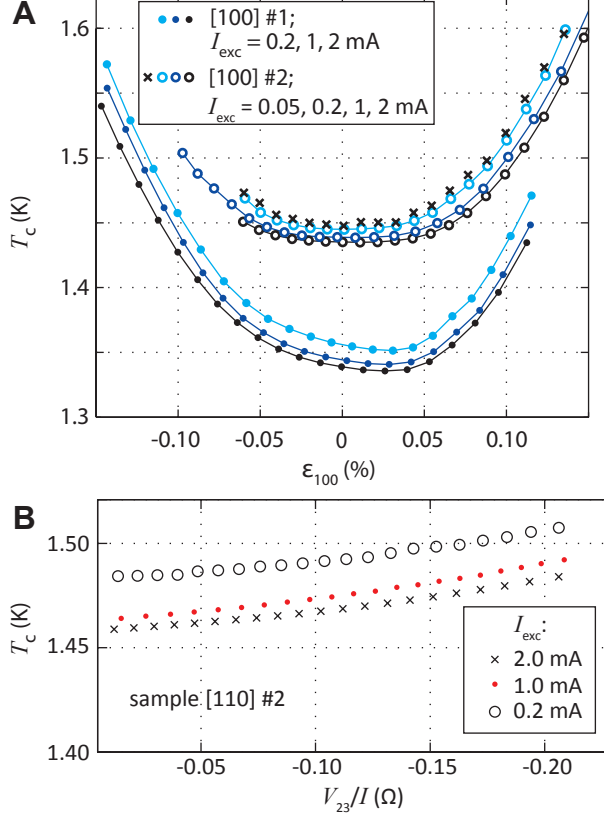


Figure 5.10: **A:**  $T_c(\varepsilon_{100})$  of two [100] samples, plotted for different excitation currents. There is a shift of 20 mK between the curves taken at 0.05 mA and 2 mA. Reproduced from [92]. **B:**  $T_c$  of sample [110] #2 against the strain gauge reading at three different excitation currents. In both **A** and **B**, the curves appear to be rigidly shifted in temperature with respect to one another, and no significant effect of  $I_{exc}$  on the shapes of the curves is seen. Samples [100] #1 and [110] #2 were measured at 68.38 Hz, whilst sample [100] #2 was measured at 63.13 Hz.

Let us now turn to the frequency of the probing current used. All of the measurements were performed with excitation currents between 60 Hz and 370 Hz. Over this range, we observed no qualitative change in the shapes of the transitions, and only a very slight shift in the measured  $T_c$ . Plotted in Figure 5.11 is  $T_c(\varepsilon_{100})$  of sample [100] #1 measured at 68.38 Hz and 368.7 Hz. The  $T_c$  of the 68.38 Hz curve is lower by  $\sim 7$  mK, with the shape of both curves being almost identical. It seems likely that the frequency range in which we are operating is much too low to have any significant effect on the outcome of the measurement.

To summarize, in this section we have shown that the phenomena we report are not dependent on the magnitude or frequency of the excitation current, and appear intrinsic to the sample. This brings us to the discussion section, where we will explore how our results can be accounted for, and what their implications are.

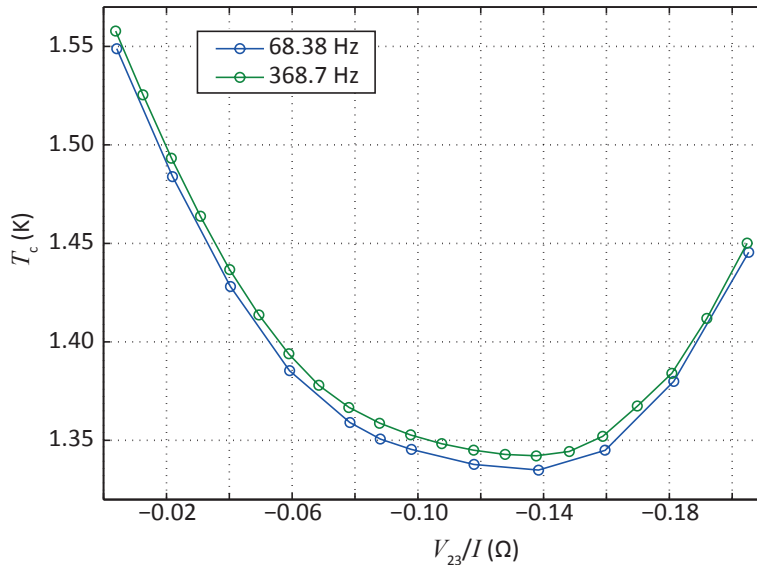


Figure 5.11:  $T_c$  of sample [100] #1 measured at two different frequencies. The curve at 68.38 Hz is shifted down by  $\sim 7$  mK with respect to the one at 368.7 Hz.

### 5.3 Discussion

We have seen that superconductivity in  $\text{Sr}_2\text{RuO}_4$  is strongly affected by uni-axial strain, and that  $T_c(\varepsilon)$  is highly dependent on the direction of applied strain. Our results look qualitatively very different from those predicted for a  $p_x \pm ip_y$  order parameter, where a cusp in  $T_c(\varepsilon)$  at zero strain accompanied by a linear strain-dependence at low strains is expected (see Figure 3.8).

Uni-axial pressure measurements are often analyzed in the context of the Ehrenfest relation

$$\frac{dT_c}{dP_i} = VT_c \frac{\Delta\alpha_i}{\Delta C}, \quad (5.3.1)$$

which is valid in the elastic limit. It relates the change in  $T_c$  with pressure  $P_i$  along direction  $i$  to the changes in thermal expansion  $\alpha_i$  and heat capacity  $\Delta C$  at a second order phase transition.  $V$  is the sample volume. This was done for example in  $\text{YBa}_2\text{Cu}_3\text{O}_7$  [97], where  $T_c$  was measured as a function of stress along  $a$ ,  $b$  and  $c$ . The measured values of  $dT_c/dP_i$  were found to be in good agreement with those calculated using the Ehrenfest relation (5.3.1) with previous thermal expansion measurements. In fact, the Ehrenfest relation (5.3.1) agrees with experiment for a number of other cuprate superconductors, including  $\text{YBa}_2\text{Cu}_4\text{O}_8$  [114] and  $\text{HgBa}_2\text{CuO}_{4+\delta}$  [115], leading to the suggestion of a “universal trend” in the cuprates [115].

The case appears to be very different for  $\text{Sr}_2\text{RuO}_4$  however, where this equation does not capture our experimental observations. Using ultrasound measurements, N. Okuda et al. calculated  $dT_c/dP_i$  from (5.3.1) for the different crystal directions

and found  $(1/T_c)dT_c/dP_{\parallel a} = -0.85 \text{ GPa}^{-1}$ , and  $(1/T_c)dT_c/dP_{\parallel c} = 0.7 \text{ GPa}^{-1}$  [116]. In contrast, in our measurements we found that  $dT_c/dP_{\parallel a}$  (ie. for strain applied along [100]) is large in magnitude and changes sign across zero strain. Additionally, a uni-axial pressure measurement along the  $c$ -axis, previously carried out by S. Kittaka et al., was found to disagree with the Ehrenfest relation, the enhancement of  $T_c$  being much larger than that calculated from the ultrasound data: they found  $(1/T_c)dT_c/dP_{\parallel c} \approx 5$  [117]. A different approach must therefore be taken to understand the changes of  $T_c$  with strain in  $\text{Sr}_2\text{RuO}_4$ .

In this section we will investigate the differences between prediction and experiment, and assess to what extent our data are compatible with different  $p_x \pm ip_y$  scenarios. We will conclude the section with a brief discussion of future work which could be undertaken to explore superconductivity in  $\text{Sr}_2\text{RuO}_4$  further.

### 5.3.1 Strain inhomogeneity

Let us first focus on the low-strain region, to see if the absence of a cusp in our data can be explained by inhomogeneity effects. We have noted that the transitions become broader with strain, with the narrowest transitions being observed for sample [100] #2 near zero strain. This indicates that the broadening is due to strain inhomogeneity and is not intrinsic. Strain inhomogeneity in the sample could arise for a variety of reasons, for example the presence of defects in the lattice such as dislocations or inclusions. As described in Section 4.2, the samples were cut with a wire saw, so it is likely that there will be a high density of dislocations along the sample edges. Additionally, if the sample is bent this will give rise to strain gradients across it. This could occur if there were some asymmetry in how the sample is mounted, such as a difference in the epoxy thickness above and below it. The broadening of the transition will increase at higher strains, even if the level of strain inhomogeneity remains constant, as  $dT_c/d\varepsilon$  increases with  $\varepsilon$ .

If there is a broad distribution of  $T_c$ 's across the sample due to strain inhomogeneity, the observed transition can become strongly dependent on the excitation field used. This is caused by isolated islands of superconductivity forming in the sample which interact via the proximity effect and form a Josephson network, the shielding fraction of which falls off rapidly at high excitation fields. This phenomenon was observed for example in  $\text{Sr}_2\text{RuO}_4$  samples with high densities of Ru inclusions, where higher- $T_c$  superconductivity occurs at the interface between the Ru inclusions and the bulk crystal [117]. As we showed in Section 5.2.2 however, the shapes of the transitions are not affected by the magnitude of the excitation current. It therefore seems unlikely that this effect alone is obscuring a feature near zero strain. Nevertheless the transitions are suppressed by  $\sim 20 \text{ mK}$  as the excitation field is increased from  $\sim 0.01 \text{ G}$  to  $\sim 0.5 \text{ G}$ , giving  $dT_c/dH_{exc} \approx -40 \text{ mK/G}$ . This is quite large: by applying DC fields up to  $180 \text{ G}$  along the  $c$ -axis with the main sample magnet, we measured  $dT_c/dH = -2.7 \text{ mK/G}$ . The observed  $\sim 20 \text{ mK}$  shift may therefore be a consequence of inhomogeneity.

Additionally, strain inhomogeneity will round out features at low strain as the

measured transition consists of a distribution of local  $T_c$ 's. Broadening of the transitions would however not cause the quadratic increase in  $T_c(\varepsilon)$  observed at higher strains, as the transitions at all strains are far narrower than the amount by which  $T_c$  increases. In Figure 5.12 we illustrate the effect of strain inhomogeneity on two scenarios: one where  $T_c(\varepsilon)$  is V-shaped, and the other where it is a parabola. The solid curves represent the intrinsic forms of  $T_c(\varepsilon)$ , and the dashed lines show how inhomogeneity affects the measured curve. Strain inhomogeneity within the sample is modelled by a Gaussian distribution with a full width at half-maximum of 0.04%, and the applied strain is added homogeneously to the distribution. When  $T_c$  varies non-monotonically within the distribution of local  $T_c$ 's, the median  $T_c$  is affected causing the rounding out of the curve around zero strain.

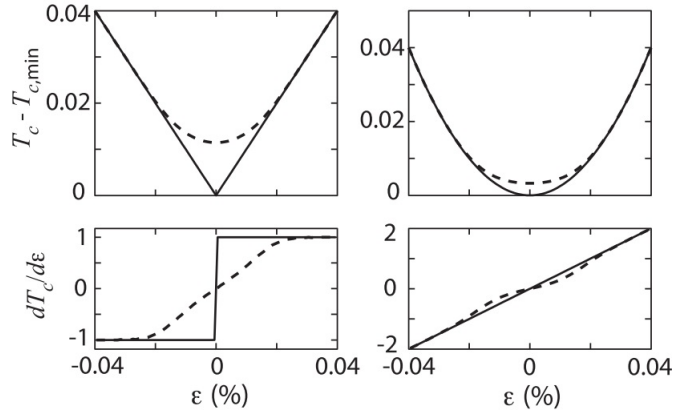


Figure 5.12: Simulation of the effect of strain inhomogeneity for two different scenarios. The solid lines represent the intrinsic forms of  $T_c(\varepsilon)$  and  $dT_c/d\varepsilon$ :  $T_c(\varepsilon)$  is V-shaped in the left panel, and  $\propto \varepsilon^2$  in the right one. The dashed lines are given by the medians of the distribution of local  $T_c$ 's, illustrating the effect of strain inhomogeneity on the measurement. Reproduced from [92].

In the case of the V-shaped curve, instead of a sharp discontinuity in  $dT_c/d\varepsilon$  at zero strain,  $T_c(\varepsilon)$  behaves approximately quadratically near zero strain. This scenario appears incompatible with our data, as the response away from zero strain is far from quadratic, and there is no flat region around zero strain. For the quadratic curve, there is a noticeable flattening of the parabola around zero strain. The flatter section is compensated for by adjacent sections with higher  $dT_c/d\varepsilon$ , so that the dashed line joins up the solid line at higher strains. Although a flat region is seen in our data, we do not observe the sections with higher  $dT_c/d\varepsilon$ .

From this brief analysis it seems likely that the measured shape of  $T_c(\varepsilon)$  is affected by strain inhomogeneity, and it is plausible that a sharp feature at zero strain was rounded out. The flat section around zero strain may be an effect of inhomogeneity, but the difference between our data and the right panel of Figure 5.12 suggests that this is in fact an intrinsic effect. The large quadratic increase of  $T_c$  at higher strains is however unambiguous and can not be explained by inhomogeneity effects.

A possible future experiment would be to explore the low strain section of  $T_c(\varepsilon_{100})$  using a susceptibility probe with a much higher spatial resolution. This would allow one to overcome the problem of strain inhomogeneity by probing smaller regions of the sample.

### 5.3.2 $T_c(\varepsilon)$ and chiral $p$ -wave superconductivity in $\text{Sr}_2\text{RuO}_4$

For strain applied along [100], the response is large and mainly symmetric about zero strain, whilst for [110] strain the response is weak and predominantly linear. As discussed in Section 4.1.2, the sample distortion under applied strain can be resolved into two components: one which corresponds to an anisotropic distortion ( $\varepsilon_{xx} = -\varepsilon_{yy}$ ) and the other to dilatation ( $\varepsilon_{xx} = \varepsilon_{yy}$ ). Under the tetragonal symmetry of  $\text{Sr}_2\text{RuO}_4$ , the anisotropic distortion must give a symmetric response, as the in-plane axes are equivalent; dilatation on the other hand is expected to give a linear response. The response along [100] is therefore dominated by the anisotropic distortion, and that along [110] by dilatation. The results from a sample cut  $2.5^\circ$  from [110] (Section 5.1.1) suggest that by rotating the direction of applied strain, one can tune the effect of the two kinds of distortion on  $T_c$ . This strong directional dependence indicates that the superconductivity in  $\text{Sr}_2\text{RuO}_4$  is highly anisotropic, and that the tetragonal crystal symmetry and details of its Fermi surface play an important role. In this section we will consider several scenarios to see if they could explain the observed strain dependence of  $T_c$ , and assess whether our data can be compatible with some form of  $p_x \pm ip_y$  superconductivity.

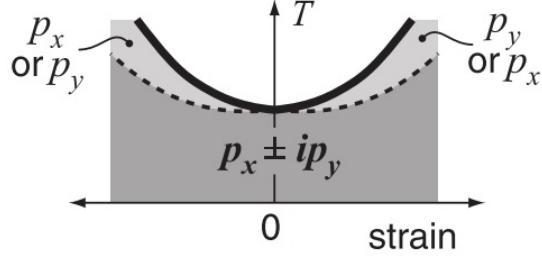
As previously noted, the most striking and unambiguous aspect of our data is the quadratic form of  $T_c(\varepsilon_{100})$  beyond  $\sim 0.03\%$  strain. A quadratic dependence can generally be explained by a strain-induced mixture of nearly degenerate order parameters, as discussed in Section 3.5.4. This is caused by the interaction term between the two order parameters in the Ginzburg-Landau free energy expansion which results in  $T_c \propto \varepsilon^2$  for small strains. Given the tetragonal crystal symmetry and strong response to strain along [100], obvious candidates would be  $d_{(x^2-y^2)}$ - and  $s$ -wave order parameters, as these will give a symmetric response to anisotropic distortions of the lattice. These order parameters are however in conflict with both the proposed spin-triplet pairing and broken time-reversal symmetry in  $\text{Sr}_2\text{RuO}_4$ .

A second possibility is that there are in fact two degenerate order parameters at zero strain, which couple to the lattice in a way such that the cusp at zero strain occurs on top of a strong underlying strain response. Figure 5.13 shows an illustration of such a scenario. It would therefore be useful to estimate the size of the change in slope at zero strain for such a model, to determine whether we should have been able to detect it experimentally.

#### 5.3.2.1 Electronic structure calculations

Electronic structure calculations were carried out by E. A. Yelland and C. W. Hicks using the Wien2k package [118] to gain insight into the effect of strain on  $\text{Sr}_2\text{RuO}_4$ 's

Figure 5.13: Possible phase diagram for two degenerate order parameters  $p_x$  and  $p_y$ , where the cusp at zero strain is obscured by a strong underlying strain response. Reproduced from [92].



Fermi surface [92]. The calculations were converged on a mesh of  $20 \times 20 \times 20$  points in  $k$ -space in the full Brillouin zone, and spin-orbit coupling was included. Strain was modelled by setting the lattice parameters to obtain the desired longitudinal strain, with the transverse strains being given by the in-plane and out-of-plane Poisson's ratios. The calculated Fermi surfaces for  $\varepsilon_{100}$  and  $\varepsilon_{110} = \pm 0.5\%$  are shown in Figure 5.14.

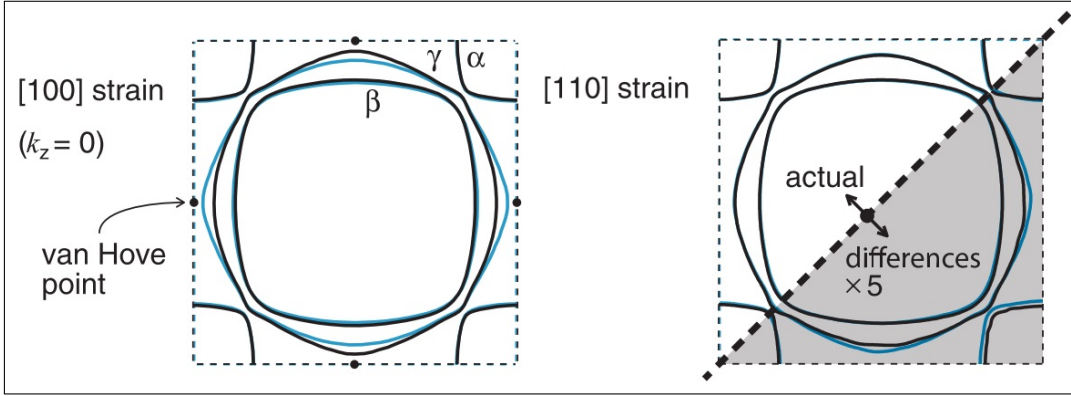


Figure 5.14: Calculated Fermi surfaces of  $\text{Sr}_2\text{RuO}_4$  under applied strain. The left panel corresponds to strain applied along  $[100]$ , and the right panel along  $[110]$ . The blue sheets correspond to 0.5% compression, and the black ones to 0.5% tension. The dashed lines represent the two-dimensional Brillouin zone boundaries of the  $\text{RuO}_2$  planes. In the shaded portion of the right-hand panel, the differences between the Fermi surfaces for compression and tension were exaggerated by a factor of five to make them visible. The Fermi surfaces in this portion were slightly distorted to make the zone boundaries match. Reproduced from [92].

$\text{Sr}_2\text{RuO}_4$ 's Fermi surface changes more dramatically when it is strained along  $[100]$  than along  $[110]$ . In particular, the  $\{100\}$  sections of the  $\gamma$  sheet are the most strongly affected, with the response along  $[100]$  and  $[010]$  being large and opposite: as the system is compressed along  $[100]$ , the  $\gamma$  sheet extends towards the van Hove point at  $(\pi, 0)$  and shrinks away from that at  $(0, \pi)$ ; tension along  $[100]$  has the exact opposite effect. The  $\alpha$  and  $\beta$  sheets are not noticeably altered by  $[100]$  strain. In contrast, strain along  $[110]$  is seen to have almost no effect on any of the sheets,

the changes only being distinguishable when they are exaggerated, as shown in the shaded section of the right panel in Figure 5.14.

The very different response of the various parts of the Fermi surface to strain suggests that the magnitude of the cusp in  $T_c(\varepsilon)$  that one would expect will depend strongly on which sections of the Fermi surface are gapped out by superconductivity. We have already argued that our data are consistent with a highly anisotropic superconducting state in  $\text{Sr}_2\text{RuO}_4$ , and by combining our data with the electronic structure calculations, we can make some predictions regarding the structure of the gap. In Section 3.5 we discussed the controversy surrounding the structure of the superconducting gap. Angular dependent specific heat measurements indicate that the superconducting gap may be largest on the  $\{110\}$  sections of the  $\gamma$  sheet [87,88], whereas other authors have suggested that superconductivity lives predominantly on the  $\alpha$  and  $\beta$  sheets [90].

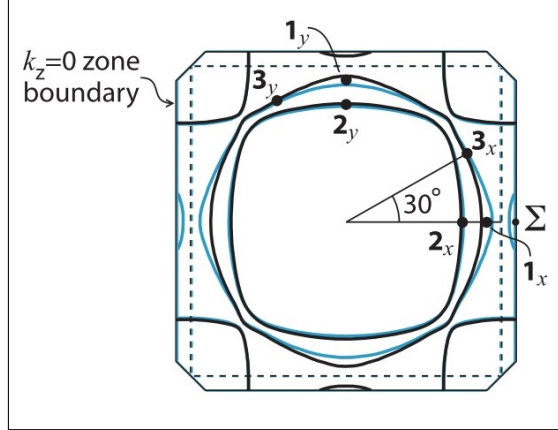
By changing the shape of the Fermi surface with strain, we are also modifying  $N_0$ , the density of states at the Fermi surface. For  $[100]$  strain in particular we can expect a strong increase of  $N_0$  as the  $\gamma$  sheet approaches the van Hove point. This will in turn affect  $T_c$ , which we can estimate using the BCS expression  $T_c \propto \exp(-1/\lambda N_0)$ , where  $\lambda$  is the strength of the pairing interaction. Assuming that  $\lambda$  remains constant with strain, the derivative is given by:

$$\frac{dT_c}{d\varepsilon} = \frac{T_c}{\lambda N_0} \left( \frac{1}{N_0} \frac{dN_0}{d\varepsilon} \right). \quad (5.3.2)$$

The magnitude of the cusp for a  $p_x \pm ip_y$  state corresponds to the change in  $dT_c/d\varepsilon$  across zero strain, where the order parameter switches from longitudinally- to transversely-oriented order ( $p_x$  to  $p_y$  in the case of  $[100]$  strain). The cusp is expected to be strongest when the longitudinal and transverse responses to strain are very different. As illustrated in Figure 5.14, this is most clearly the case on the  $\{100\}$  sections of the Fermi surface, where the density of states along  $[100]$  and  $[010]$  change rapidly and oppositely.

The magnitude of the cusp was calculated for three different models: where the superconducting gap is largest (1) on the  $\{100\}$  sections of the  $\gamma$  sheet, (2) on the  $\{100\}$  sections of the  $\beta$  sheet, and (3) on the  $\{110\}$  sections of the  $\gamma$  sheet.  $\lambda N_0$  was set to a typical weak-coupling value of 0.3, and  $N_0$  was taken to be proportional to the inverse Fermi velocity  $v_F^{-1}$ . The inverse Fermi velocity was determined at two points for each model, shown in Figure 5.15, to compare the response along the  $x$ - and  $y$ -directions. For model (3), a point just outside the region with the avoided band crossings was chosen for simplicity. The band structure was calculated for a series of small strains, to obtain an estimate of  $dv_F^{-1}/d\varepsilon$  at zero strain and thus obtain an estimate of  $dT_c/d\varepsilon$  from equation (5.3.2). The results of the calculation are displayed in Table 5.2, where  $v_F^{-1}(0)$  is the inverse Fermi velocity at zero strain in  $10^{-6}$  s/m. As  $dT_{c,x}/d\varepsilon$  is greater than  $dT_{c,y}/d\varepsilon$  in all cases,  $dT_{c,x}/d\varepsilon$  is expected to be the slope for tension and  $dT_{c,y}/d\varepsilon$  that for compression, by comparison with our data.

Figure 5.15: Fermi surfaces of  $\text{Sr}_2\text{RuO}_4$  at the same strains as those in Figure 5.14. The labelled points are those at which the values of  $v_F^{-1}$  were calculated at different strains, to obtain the results displayed in Table 5.2. The dashed lines show the 2D zone boundaries of the  $\text{RuO}_2$  planes, and the full zone shown corresponds to the  $k_z = 0$  cut of the Brillouin zone of the tetragonal lattice. From [92].



Model	Gap	Strain dir.	$v_F^{-1}(0)$	$dT_{c,x}/d\varepsilon$ (K/%)	$dT_{c,y}/d\varepsilon$ (K/%)
1	$\{100\}$ $\gamma$	[100]	6.2	+4.0	-3.1
2	$\beta$	[100]	2.6	+0.6	-0.3
3	$\{110\}$ $\gamma$	[110]	2.6	+0.115	+0.104

Table 5.2: Results from electronic structure calculations for models with the superconducting gap on different sections of the Fermi surface.

The magnitude of the cusp for a given model corresponds to  $dT_{c,x}/d\varepsilon - dT_{c,y}/d\varepsilon$  evaluated at zero strain. As expected, the cusp for the model with the gap on the  $\{100\}$  sections of the  $\gamma$  sheet is the largest, with the jump in  $dT_c/d\varepsilon$  being  $\sim 7$  K/%. This is a large jump which should have been easily observable within our experimental resolution, however no trace of it is seen in  $T_c(\varepsilon)$ . Perhaps this is not surprising, as by symmetry one would not expect a large gap on the  $\{100\}$  sections of the Fermi surface for a  $p$ -wave order parameter. Indeed, the gap must vanish at the van Hove points themselves, due to the opposite phase of the gaps in adjacent Brillouin zones.

For model 2 with the gap on the  $\beta$  sheet the cusp is much smaller, with the jump being  $\sim 0.9$  K/%. Such a jump may have been observable with our experimental set-up. The calculation described is however approximate, so it is possible that the actual jump is slightly smaller than the one calculated, such that it would be obscured by the strong underlying response to [100] strain.

If, as in model 3, superconductivity lives on the  $\{110\}$  sections of the Fermi surface, a larger cusp for [110] rather than [100] strains is expected. But as we have observed, [110] strain barely affects the shape of the Fermi surface, with the response of the  $\{110\}$  and  $\{1\bar{1}0\}$  sections being nearly identical. The predicted cusp for this model is therefore very weak, of the order of  $\sim 0.01$  K/%. This jump is well below the resolution of our measurement, and we would have not detected such a small change in slope at zero strain.

Our data, combined with the estimates given in Table 5.2, still permit certain models of  $p_x \pm ip_y$  superconductivity, placing however a number of constraints on them. The case of an isotropic gap is clearly ruled out by the dependence on direction of applied strain of our data. We also rule out the case described by model 1, where the superconducting gap is dominant on the  $\{100\}$  sections of the  $\gamma$  sheet, as no large jump in  $dT_c/d\varepsilon$  is observed at zero strain, and it is disfavoured for symmetry reasons. However, both models 2 and 3 could be consistent with the lack of observed cusp, as the jump in  $dT_c/d\varepsilon$  may have been too small compared to our resolution.

That said, models 2 and 3 do not give a natural explanation for the strong increase of  $T_c$  with  $[100]$  strain. This increase is most naturally explained by the changes in the density of states of the  $\gamma$  sheet, which evolves oppositely along the  $\{100\}$  and  $\{010\}$  sections of the Fermi surface with  $[100]$  strain. A natural hypothesis then, would be that even though the gap may be largest elsewhere on the Fermi surface, superconductivity is strongly linked to the  $\{100\}$  and  $\{010\}$  sections of the  $\gamma$  sheet and its proximity to the van Hove point; a possibility being that the pairing interaction is related to ferromagnetic fluctuations about the van Hove point. Exploring such models further would be of great interest, as they could yield great insight into the structure of  $\text{Sr}_2\text{RuO}_4$ 's superconducting state, as well as its pairing mechanism.

## 5.4 Summary and outlook

In this chapter we described the experimental results obtained on  $\text{Sr}_2\text{RuO}_4$  under uni-axial strain. We found that  $T_c(\varepsilon)$  depends very strongly on the direction in which strain is applied. For strain applied along the  $[100]$  direction, there is a large symmetric response about zero strain, with  $T_c$  being increased by more than 40% for  $\sim 0.2\%$  applied strain. The region within  $\sim 0.03\%$  of zero strain is approximately flat, whilst beyond that  $T_c(\varepsilon_{100})$  behaves roughly quadratically. The response to  $[110]$  strain is on the other hand very weak and linear. In neither case was a discontinuity in  $dT_c/d\varepsilon$  observed at zero strain, contrary to the predictions made for a simple  $p_x \pm ip_y$  model. We discussed effects of strain inhomogeneity, and argued that although the shape of the low-strain data may be affected by inhomogeneity, the quadratic increase of  $T_c(\varepsilon_{100})$  could not be explained by such effects and must be intrinsic.

Electronic structure calculations indicate that the strong increase of  $T_c(\varepsilon_{100})$  is linked to the density of states of the  $\gamma$  sheet and its proximity to the van Hove points. Estimates from the electronic structure calculations show that certain models of  $p_x \pm ip_y$  superconductivity could still be consistent with our data, as the cusp would have been too small to detect within our experimental resolution. Nevertheless any model for chiral  $p$ -wave superconductivity must be able to account for both the directional dependence of the strain response and the apparent weakness of the cusp.

Interestingly, several aspects of our data-set can be explained by considering a strain-induced mixture of  $d_{(x^2-y^2)}$ - and  $s$ -wave order parameters, as this would pro-

duce the quadratic form of  $T_c(\varepsilon_{100})$ . As already mentioned however, such a state is not compatible with the observation of spin-triplet superconductivity or broken time-reversal symmetry. That said, there have been suggestions that experiments which are believed to show spin-triplet superconductivity in  $\text{Sr}_2\text{RuO}_4$  may be interpreted in alternative ways. Zutic and Mazin [81] argue that the phase-sensitive measurement performed by K. D. Nelson et al. using a Josephson junction between  $\text{Sr}_2\text{RuO}_4$  and a conventional superconductor [119] is also in fact compatible with a  $d$ -wave state. As previously mentioned in Section 3.5.2, they also note there is some ambiguity regarding the NMR result, as the Knight shift is found to remain constant across  $T_c$  when the magnetic field is in the plane as well as when it is along  $c$ .

Many open questions remain concerning the superconducting state of  $\text{Sr}_2\text{RuO}_4$ , several of which can be addressed using the uni-axial strain probe. Perhaps the key question is whether the superconducting state at zero strain is comprised of two degenerate order parameters and breaks time-reversal symmetry. For the experiment described in this chapter, we measured  $T_c$  using AC magnetic susceptibility and so were only sensitive to the upper transition. If a splitting of the transitions is actually occurring, one could prove this by measuring both transitions, and thus track the transition between the one-component and two-component order parameter states to map out the full phase diagram. To do this one would need to use a probe which is sensitive to the lower transition, such as specific heat. Measuring specific heat under strain is however highly challenging, as the sample is firmly anchored at both ends to titanium plates, and so cannot be thermally isolated from the probe. Thermal expansion under strain could also yield information about the splitting of the transitions, as it is related to the change in heat capacity at the transitions, as shown by (5.3.1).

An advantage of the uni-axial strain probe compared to other pressure measurements is that the upper face of the sample is exposed, making spectroscopic measurements possible. Another experiment which one could envisage is studying the Kerr effect under strain. In this way, one could determine the strain dependence of the Kerr effect, which is a signature of broken time-reversal symmetry. If the chiral  $p$ -wave scenario is correct, one should then be able to tune as a function of strain between states where time-reversal symmetry is preserved and broken. This would provide an independent measure of  $\text{Sr}_2\text{RuO}_4$ 's phase diagram.

## Chapter 6

# Sr<sub>3</sub>Ru<sub>2</sub>O<sub>7</sub> Under Uni-axial Strain: Results and Discussion

Sr<sub>3</sub>Ru<sub>2</sub>O<sub>7</sub> offers the rare opportunity of exploring a phase diagram in the vicinity of quantum criticality in the clean limit and without introduction of point defects. While the recent discovery that Sr<sub>3</sub>Ru<sub>2</sub>O<sub>7</sub>'s novel phase is linked to SDW formation provided vital new insight, many questions about the phase's properties were left unanswered, with several new ones being raised. For instance, what is the link between quantum criticality and phase formation? As discussed in Section 2.5.4, several models which only consider Sr<sub>3</sub>Ru<sub>2</sub>O<sub>7</sub>'s band structure can account for many of the experimental observations, suggesting that phase formation could be taking place on a background of quantum criticality, rather than being driven by it. Another question relates to the resistivity inside the phase, and how SDW formation could lead to such a drastic increase in the resistivity. In their neutron experiment, Lester et al. [44] find elastic scattering peaks corresponding to SDWs running along *a* and *b*, however are not able to resolve whether these arise from domains of [100]- and [010]-oriented order, or from microscopically coexisting density waves. Domains would provide a natural explanation for the enhanced resistivity, however to date no evidence of domains has been found.

Given the sensitivity of Sr<sub>3</sub>Ru<sub>2</sub>O<sub>7</sub>'s phase to in-plane symmetry-breaking magnetic fields, we decided to investigate it with another-symmetry breaking field: in-plane strain. We measured the resistivity of three samples under strain, all of which were cut along [100]. The samples were all cut from the same crystal<sup>1</sup> with a residual resistivity of  $\rho_0 \approx 0.25 \mu\Omega\text{cm}$ . The dimensions of the samples are given in Table 6.1. As before, *L* is the length of the gap between the sample plates, *w* and *t* the sample width and thickness, and *d<sub>l</sub>* and *d<sub>u</sub>* the epoxy thickness below and above the sample. The last column gives an estimate of the strain at the middle of the sample as a percentage of the strain applied by the piezoelectric stacks, as calculated by finite element analysis by Mark Barber.

---

<sup>1</sup>Crystal C697B, grown by Robin Perry and characterised by J.-F. Mercure and Robin Perry [111].

sample	$L$ ( $\mu\text{m}$ )	$w$ ( $\mu\text{m}$ )	$t$ ( $\mu\text{m}$ )	$d_l, d_u$ ( $\mu\text{m}$ )	$\varepsilon L/\Delta L$ (%)
#1	670	170	45	80, 80	52
#2	1050	212	45	50, 100	69
#3	820	820	43	20, 20	78

Table 6.1:  $\text{Sr}_3\text{Ru}_2\text{O}_7$  sample dimensions.

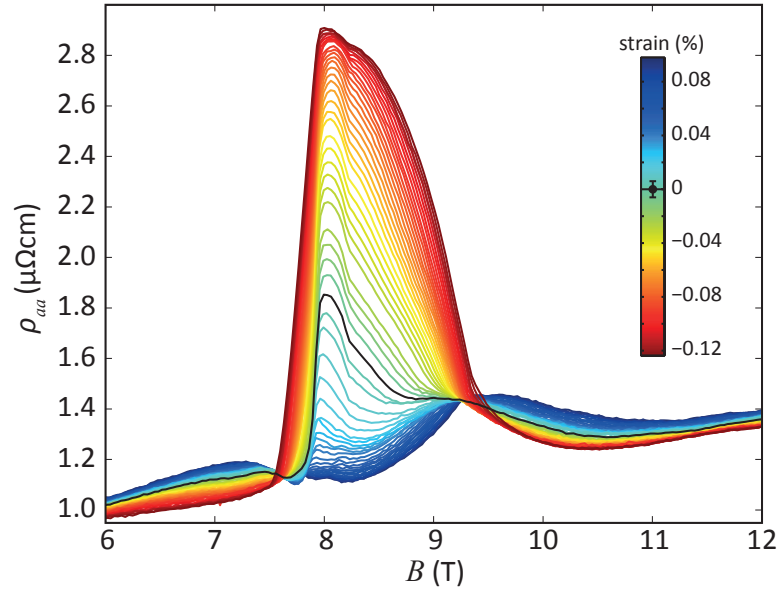
## 6.1 Effect of uni-axial strain on novel phase of $\text{Sr}_3\text{Ru}_2\text{O}_7$

In this section we will present the main experimental results obtained on  $\text{Sr}_3\text{Ru}_2\text{O}_7$  under uni-axial strain. The resistivity of the three samples was measured for a series of magnetic field sweeps, each performed at a different sample strain. The sample temperature was held at approximately 300 mK for the whole measurement<sup>2</sup>. Sample #1 was measured with the first generation strain probe, whilst samples #2 and #3 were measured with the second generation probe. The magnetic field was always applied parallel to the  $c$ -axis, with an estimated  $\pm 2^\circ$  error in the alignment of the sample's  $c$ -axis with the field direction. The samples were mounted for measurement as described in Section 4.3, with the contact configuration shown again for reference in Figure 6.1b.

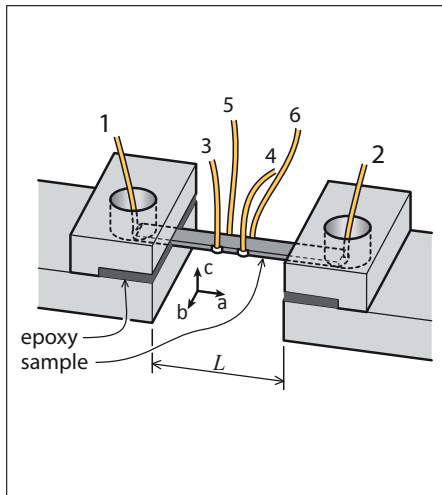
Figure 6.1a shows  $\rho_{aa}$ , the resistivity parallel to the direction of applied strain, of sample #1 as a function of field between 6 T and 12 T at different applied strains. The measurement was performed by running an AC current  $I = 1$  mA at 76 Hz between contacts 1 and 2, and measuring the voltage drops  $V_{34}$  and  $V_{56}$  across the voltage pairs with a lock-in amplifier. The resistivity was calculated using the formula  $\rho_{aa} = (V/I)(A/l)$ , where  $V$  is one of the measured voltages,  $A = wt$ , and  $l$  is the separation between the voltage contacts. The data displayed in Figures 6.1a and 6.1c correspond to the measurement across contacts 3 and 4; the measurement across 5 and 6 yields very similar results, and we compare the measurements from both sides of the sample in Section 6.2.5. The sample dimensions and contact separation were measured under a microscope, meaning that there is some error in our calculation of the resistivity due to uncertainty in the measured lengths. We estimate that the error linked to this geometrical uncertainty is  $\sim 8\%$ . We should also note that we are not taking into account the change in sample size due to the applied strain in our calculation, as the change in length of the sample (of the order of 1  $\mu\text{m}$ ) is much smaller than the uncertainty previously mentioned. Moreover, the in-plane Poisson's ratio of  $\text{Sr}_3\text{Ru}_2\text{O}_7$  is not known, so that the change in the sample cross-section cannot be accurately calculated.

The magnetic field was ramped at 0.2 T/min, and the data from the up- and

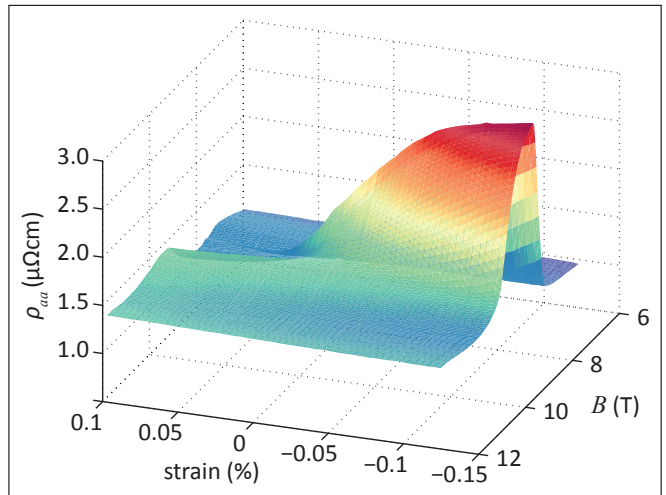
<sup>2</sup>As discussed in Section 4.5.3, due to the magnetoresistance of the temperature sensor, there is a systematic increase of the sample temperature of  $\sim 80$  mK between 0 and 12 T. This however does not affect our main results, as the resistivity of  $\text{Sr}_3\text{Ru}_2\text{O}_7$  has a very small temperature dependence at  $\sim 300$  mK.



(a)



(b)



(c)

Figure 6.1: (a) Resistivity of sample #1 as a function of magnetic field at different applied strains, shown by the colour bar. The black curve is that where the sample is nearest to zero strain. The error on the colour bar indicates the error in locating zero strain. The temperature is  $T \approx 300$  mK. (b) Sample configuration in the strain probe for measuring resistivity, as described in Section 4.3. (c) Surface plot of the data shown in (a).

down-ramps were averaged to cancel out effects from any magnet hysteresis. As for the  $\text{Sr}_2\text{RuO}_4$  experiment, the strain was set at the beginning of each ramp by

applying a voltage to the stacks and waiting until the length of the stacks had stabilized. Starting with voltages on the inner and outer stacks of  $(V_{inner}, V_{outer}) = (0 \text{ V}, 400 \text{ V})$ , we went up to  $(400 \text{ V}, 0 \text{ V})$  in 10 V steps, corresponding to strain steps of  $\sim 0.005\%$ . The black curve in Figure 6.1a corresponds to the run which is closest to zero strain, the location of which was estimated by comparing the data with a reference sample cut from the same crystal, as discussed in Section 6.2.3. The sample mounted in the strain probe nicely reproduces the main features of the zero-strain resistivity reported in the literature, namely the fields at which the transitions into and out of the phase occur, as well as the magnitude of the increase in resistivity inside the phase (compare with, for example, Figure 2.11a). We can also clearly distinguish the B-phase, or “shoulder” region.

The data displayed in Figure 6.1a show that  $\rho_{aa}$  changes dramatically with sample strain within the phase. As the sample is compressed along [100],  $\rho_{aa}$  increases sharply until roughly 0.05% strain where it appears to start saturating. Conversely, if the sample is tensioned,  $\rho_{aa}$  decreases until the resistive signature of the phase has all but disappeared. Whereas at zero strain the resistivity jumps by a factor of  $\sim 1.6$  upon entering the phase, under 0.12% compression the jump is of a factor of  $\sim 2.6$ . Another striking aspect of this data-set is the extent to which the B-phase is affected by strain. At zero strain the B-phase is a narrow region between approximately 8.1 T and 8.5 T, with a smaller enhanced resistivity than the A-phase. Under strong compression however, the B-phase develops a resistivity nearly as high as that of the A-phase, and spills out up to  $\sim 9.4$  T. This “spilling out” of the B-phase is in contrast to the metamagnetic transitions themselves, which appear to only be weakly strain dependent. If under strain the metamagnetic transitions remain associated with the same signatures in resistivity as at zero strain, then the lower transition, which is at  $\sim 7.8$  T at zero strain, shifts to  $\sim 7.6$  T at 0.12% compression; the upper transition, associated with the kink in resistivity near 8.1 T, appears more or less constant in strain. A surface plot of the resistivity against magnetic field and strain is shown in Figure 6.1c, illustrating the rapid increase of  $\rho_{aa}$  with compression inside the phase, followed by its saturation.

Another unusual aspect of the data in Figure 6.1a is that the vertical ordering of the curves inside the phase is opposite to that outside: whereas the curves under compression have the lowest resistivity outside the phase, they have by far the highest resistivity inside the phase. For a weakly correlated metal, where the dominant effect is the change in size of the unit cell, one would typically expect the measured resistance to decrease under compression and increase under tension. In general one can write the change in measured resistance as [120]:

$$\frac{\Delta R}{R} = \frac{\Delta \rho}{\rho} + \frac{\Delta L}{L} - \frac{\Delta A}{A}. \quad (6.1.1)$$

The last two terms correspond to the geometric changes associated with the applied strain, and give the linear change in resistance expected for a typical metal. For our measurement however, the change in measured resistance is dominated by the

resistivity term, both inside and outside the phase. Indeed, the geometric term is of the order of  $\varepsilon \sim 0.1\%$ , whilst  $|\Delta R|/R$  is  $\sim 1\%$  outside the phase and goes up to nearly 60% inside the phase. This justifies the approximation of neglecting the geometric effect which we made in calculating  $\rho_{aa}$ .

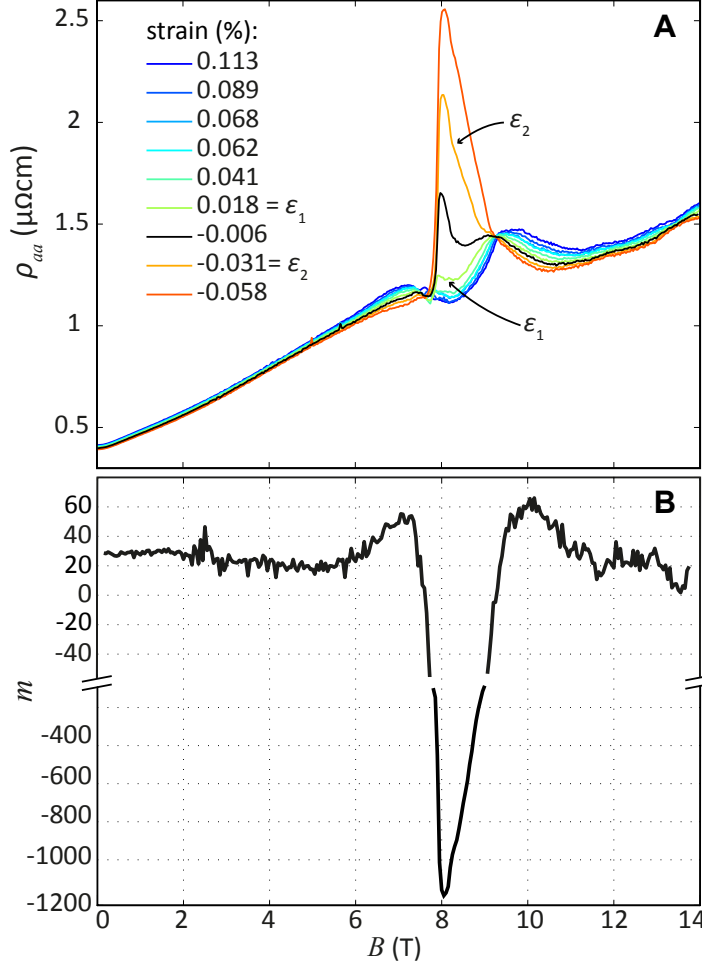


Figure 6.2: **A**: Full range magnetic field sweeps at different applied strains. The black curve corresponds to the run during which the sample was closest to zero strain. **B**: Elasto-resistive coupling  $m$  of the sample, calculated using the curves on either side of zero strain which are indicated in panel **A**.

These numbers in themselves indicate that electron correlations must play an important role in  $\text{Sr}_3\text{Ru}_2\text{O}_7$ , in particular inside the phase where the electronic behaviour is very strongly affected by small distortions of the lattice. To compare the effect of strain on  $\text{Sr}_3\text{Ru}_2\text{O}_7$  inside and outside of the phase, we measured  $\rho_{aa}$  between 0 T and 14 T (Figure 6.2A). From this data-set we can calculate the elasto-resistive coupling  $m \equiv (1/R)(dR/d\varepsilon)$ , which gives a measure of how strongly the measured resistance is affected by the applied strain  $\varepsilon$  (Figure 6.2B). In the region near zero strain  $\rho_{aa}(\varepsilon)$  of  $\text{Sr}_3\text{Ru}_2\text{O}_7$  is approximately linear, so we can calculate  $m$  using:

$$m \approx \frac{\rho_{aa}(\varepsilon_1) - \rho_{aa}(\varepsilon_2)}{|\varepsilon_1 - \varepsilon_2| \rho_{aa}(0)}, \quad (6.1.2)$$

where  $\varepsilon_1$  and  $\varepsilon_2$  are the strains on either side of zero strain labelled in Figure 6.2A.  $\rho_{aa}(0)$  is the value of  $\rho_{aa}$  interpolated at zero strain.

As can be seen in Figure 6.2A, outside of the phase strain causes the value of the resistivity to shift, but does not significantly change the overall shape of  $\rho_{aa}(B)$ . The inversion of the ordering of the curves inside the phase mentioned above means that all of the curves must cross each other. Interestingly all of the curves cross at relatively well defined points near 7.6 T and 9.2 T. We will return to the question of how sharp these crossing points really are at the end of the section. Despite strain not altering the shape of  $\rho_{aa}(B)$  outside of the phase, the elasto-resistive coupling is very high:  $m \approx 30$  for low values of magnetic field, compared to weakly correlated metals where the geometric contribution is  $(1 + 2\nu) \approx 2$  for typical values of the Poisson's ratio  $\nu$ . This again emphasizes that electron correlations are strong well outside the phase, where we find the system to be highly sensitive to lattice distortions. As the phase is approached from both the high- and low-field sides,  $m$  increases to above 50, perhaps signalling an increase in the strength of interactions in the vicinity of the phase, before rapidly becoming very large and negative. The magnitude of the elasto-resistive coupling inside the phase is impressive, with the largest value of  $\sim -1180$  being reached near 8 T. The change of sign of  $m$  inside the phase implies that there are two points where  $m = 0$ , and where, for small strains,  $\rho_{aa}$  is strain independent. These points correspond to the observed crossing points mentioned previously.

### 6.1.1 Longitudinal and transverse measurements

The data from sample #1 are reminiscent of the tuning between the easy and hard responses with in-plane magnetic field. Borzi et al. showed that increasing the component of in-plane field along  $a$  caused the resistivity inside the phase to decrease along  $b$  whilst remaining more or less constant along  $a$  [4] (see Figure 2.11a). Therefore to check whether strain acts on the phase in a similar way to in-plane field, we must also measure the response in the direction perpendicular to that of the applied strain. To obtain a qualitative measure of the transverse resistivity  $\rho_{bb}$ , samples #2 and #3 were wired as shown in Figure 6.3.

The numbered points in the diagram correspond to the bonding pads on the strain probe. The longitudinal resistivity  $\rho_{aa}$  is measured as before: by running a current between contacts 1 and 2, and measuring  $V_{34}$  or  $V_{56}$ . To measure the transverse response, we ran a current between contacts 7 and 8, and measured the voltage drop between contacts 9 and 10. The wires to the bonding pads were twisted in pairs to reduce pick-up noise: 3 and 4, 5 and 6, 9 and 10 for the voltage pairs; 1 and 2, 7 and 8 for the current pairs. The requirement of using twisted pairs meant that it was necessary to use pairs of adjacent bonding pads on the probe, so that wires had to be run across the sample to be able to perform the transverse measurement. These wires, which join pads 7 to 3 and 6 to 10 as illustrated in Figure 6.3, were made from 50  $\mu\text{m}$  diameter copper wire which was soldered to the bonding pads.

The high aspect-ratio (length/width) of the sample is ideal for obtaining an ac-

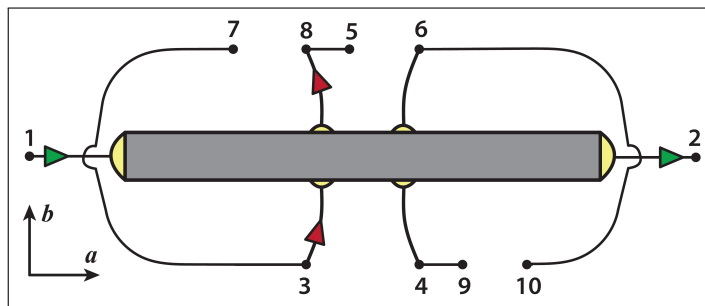


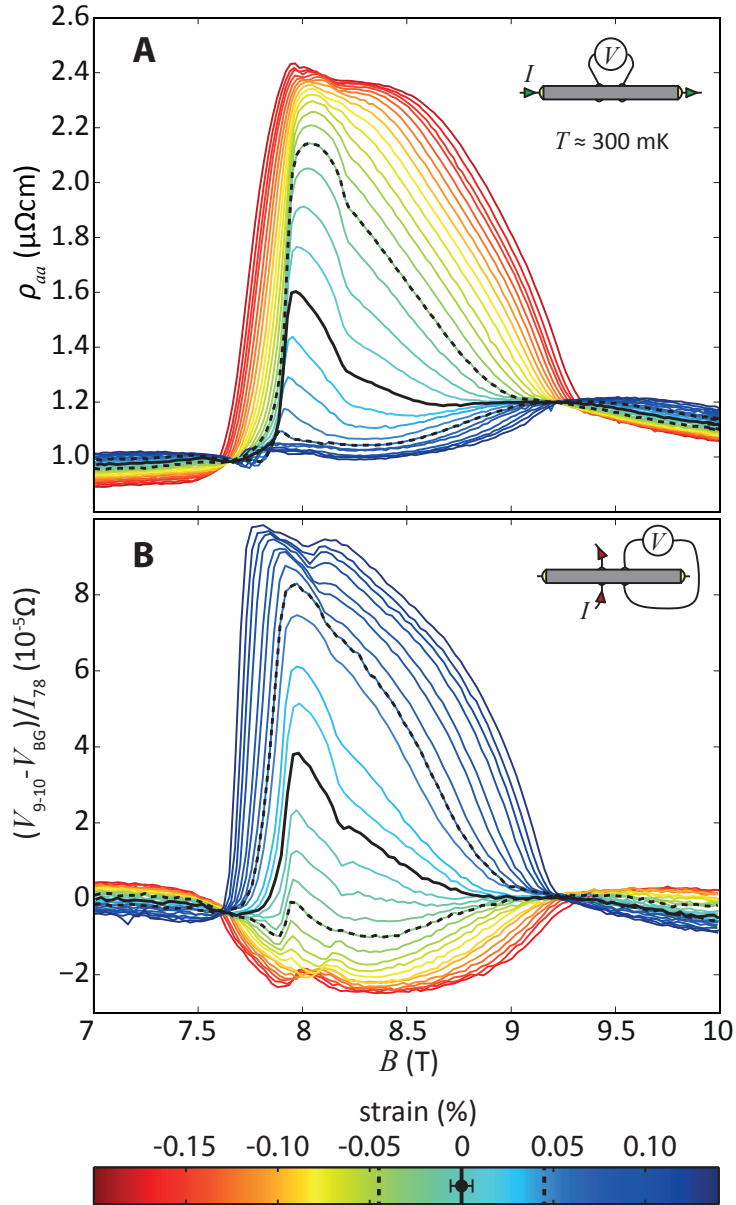
Figure 6.3: Wiring configuration for samples #2 and #3, enabling measurement of the response in the directions parallel and perpendicular to the applied strain. The green and red arrows show the current paths for the longitudinal and transverse measurements respectively. The directions of the in-plane crystal axes are indicated.

curate measurement of  $\rho_{aa}$ , as the current flow through the sample will be highly homogeneous across its width in the middle section where the voltage drop is measured. On the other hand, the high aspect-ratio, which is also necessary for obtaining high strain homogeneity at the centre of the sample, is far from ideal for measuring  $\rho_{bb}$ . Indeed, the current flow between contacts 7 and 8 is not homogeneous across the sample, as the current will spread out in the  $a$  direction. This means that the voltage measured between 9 and 10, although dominated by  $\rho_{bb}$ , will be affected by the magnitude of  $\rho_{aa}$ . Therefore  $V_{9-10}$  gives a qualitative rather than a quantitative measure of  $\rho_{bb}$ . We return to the question of the extent to which  $V_{9-10}$  is affected by  $\rho_{aa}$  in Section 6.2.6.

The data from the longitudinal and transverse measurements on sample #3 are shown one above the other in Figure 6.4. As for sample #1, the data were collected at  $T \approx 300$  mK, with the field being swept at 0.2 T/min. All of the longitudinal runs were carried out, followed by the transverse ones, applying the same sets of voltages to the piezoelectric stacks in each case: 20 V steps from  $(V_{inner}, V_{outer}) = (220 \text{ V}, 0 \text{ V})$  to  $(0 \text{ V}, 0 \text{ V})$  for the compression runs, and  $(0 \text{ V}, 0 \text{ V})$  to  $(0 \text{ V}, 260 \text{ V})$  for the tension runs. This gave strain steps of  $\sim 0.012\%$  and a total strain range of roughly  $-0.19\%$  to  $+0.12\%$ . The measurements were performed with a 1 mA excitation current at 119.3 Hz for both the longitudinal and transverse runs. We found that the signal from the transverse measurement occurred on top of a strong field-dependent but strain-independent background,  $V_{BG}$ , which is subtracted from the data in Figure 6.4B. The origin of this background and its subtraction are discussed in detail in Section 6.2.1, however it does not affect the qualitative observations which we make about the transverse response here.

The longitudinal data from sample #3 (Figure 6.4A) are qualitatively very similar to those of sample #1 (Figure 6.1a), with compression along [100] strongly enhancing  $\rho_{aa}$  inside the phase, and tension suppressing the enhancement. The transverse response shown in Figure 6.4B exhibits the opposite behaviour: tension along [100] causes a strong increase of the measured signal, whilst compression sup-

Figure 6.4: Longitudinal (A) and transverse (B) data from sample #3. The transverse data are shown after subtraction of the background  $V_{BG}$ . The measurement configurations are sketched in the top right corner of each panel, showing the current path and voltage pair used. The black curve is that where the sample is nearest to zero strain. The strains of the dashed curves, which are marked on the colour bar, are approximately  $\pm 0.048\%$ . The error in locating zero strain is also shown on the colour bar.



presses it. Under high tension  $\rho_{aa}$  is nearly constant within the phase, so the large transverse signal must be the result of a strong increase in  $\rho_{bb}$ . Conversely, the large value of  $\rho_{aa}$  under compression causes the dip in the transverse signal upon entering the phase, as the current flow for the transverse measurement becomes more restricted along  $a$  thus reducing the voltage measured between 9 and 10. Therefore although we are unable to extract an absolute value of  $\rho_{bb}$  from the raw data due to  $V_{BG}$ , this data-set reveals the basic phenomenology within the phase: compression along [100] enhances  $\rho_{aa}$  and suppresses  $\rho_{bb}$ , whilst tension along [100] has the

opposite effect.

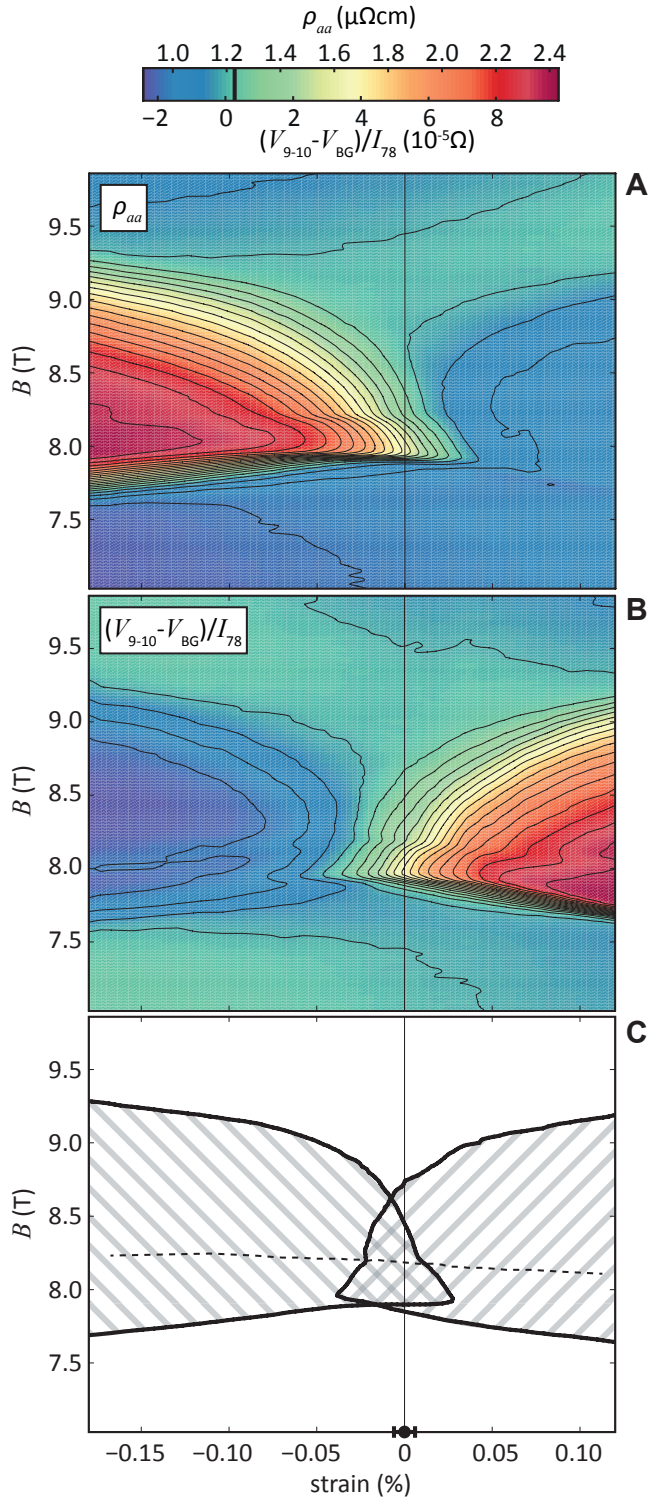


Figure 6.5: **A** and **B**: Contour plots of the longitudinal and transverse response respectively, overlaid on top of colour plots illustrating the magnitude of the response. **C**: Contours enclosing regions of high  $\rho_{aa}$  and high  $\rho_{bb}$ . The levels at which the contours are taken are shown by the thick black line in the colour bar:  $1.23 \mu\Omega\text{cm}$  for  $\rho_{aa}$  and  $0.3 \times 10^{-5}\Omega$  for the transverse signal. The overlap of the two regions around zero strain is marked by the cross-hatch pattern. The dashed line marks the approximate location of the upper metamagnetic transition, extracted from the raw data. The vertical line in the three panels is to emphasize the mirroring of the longitudinal and transverse data about zero strain, with the error in zero strain shown by the error bar in panel **C**.

The dashed curves in Figures 6.4**A** and **B** were taken at strains of approximately  $\pm 0.048\%$ . We observe that within this strain range, both the longitudinal and transverse signals appear to be enhanced within the phase. In other words, there is a region with a finite width in strain over which both  $\rho_{aa}$  and  $\rho_{bb}$  display signatures of the phase. To better illustrate this overlap region, contour plots of the longitudinal and transverse signals are shown in Figures 6.5**A** and **B**. The two responses appear to mirror each other: the region of enhanced  $\rho_{aa}$  extends out on the compression side, whilst that of enhanced  $\rho_{bb}$  extends out on the tension side. In panel **C**, contours which denote the approximate boundaries of these regions are shown, with the level at which the contours are taken shown by the thick black line in the colour bar. The overlap region, shown by the cross-hatched section in panel **C**, has a field dependent width, with a maximum width of  $\sim 0.08\%$  near 8 T.

We note that the borders of two regions of enhanced resistivity do not cross at exactly zero strain, whereas by symmetry one would expect them to cross at zero strain. Indeed, at zero strain and in the absence of an in-plane field  $\rho_{aa}$  and  $\rho_{bb}$  are identical [4]. There are several sources of error which could contribute to the boundaries not crossing at zero strain. First, as discussed previously, the transverse measurement itself does not give a proper measure of  $\rho_{bb}$ , which could be a significant contribution. Another source is the determination of zero strain, which is described in Section 6.2.3. An error in the alignment between the sample's  $c$ -axis and the magnetic field would also cause a shift in the crossing points, due to the effect of the in-plane field component. Finally, we should emphasize that the boundaries shown in Figure 6.5**C** correspond to contours which were chosen to illustrate the extent of the phase, and are not strictly speaking phase boundaries.

The approximate location of the second metamagnetic transition, marked by the dashed line in Figure 6.5**C**, was determined from the resistive anomaly associated with the transition. As noted for sample #1, this transition has a very weak dependence on strain. The fact that the dashed line has a small slope at zero strain suggests that the transition may be more sensitive to the dilatation rather than anisotropic distortion of the sample under strain. The large and symmetric response of the longitudinal and transverse responses displayed in Figures 6.5**A** and **B** indicates on the other hand that the anisotropic distortion is the dominant effect on the resistivity enhancement.

In Figures 6.6a and 6.6b the longitudinal and transverse strain responses are shown at a series of different fields, the curves being interpolated from the data shown in Figure 6.4. These illustrate the strong contrast between the behaviour of  $\rho_{aa}(\varepsilon)$  and  $\rho_{bb}(\varepsilon)$  inside and outside the phase<sup>3</sup>. On the low- and high-field sides (curves at 7.1 T and 9.8 T) the response is roughly linear, whilst inside the phase (curves at 8.0 T, 8.5 T and 9.0 T) there is a rapid increase of the signal which onsets at a particular strain. This occurs most dramatically for the 8 T curve of  $\rho_{aa}$ , which is weakly strain dependent above  $\sim 0.04\%$  strain, and below which there is a rapid

---

<sup>3</sup>As noted previously, the transverse data only serve to make qualitative observations about  $\rho_{bb}$ , and the magnitudes of the two signals cannot be compared directly.

onset of the high  $\rho_{aa}$  state, with  $\rho_{aa}$  saturating at high compression. The slopes of the curves above and below the phase are nearly identical, with the ones from the transverse data-set lying on top of each other due to the subtracted background.

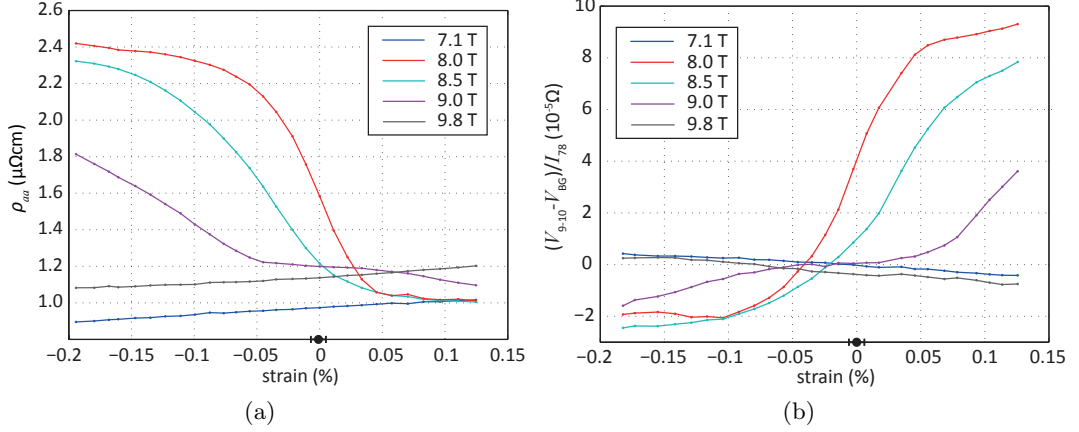


Figure 6.6: (a) and (b) Longitudinal and transverse response against strain at different applied fields.

We conclude this section by returning to the question of the crossing points mentioned earlier. As seen in Figures 6.1a and 6.4, there appear to be relatively well defined points where the curves at different strains cross each other at 7.6 T and 9.2 T. To determine the sharpness of these crossing points, we have plotted the strain dependence of the longitudinal and transverse signals at these fields in Figures 6.7a and 6.7b. For comparison, the longitudinal data from samples #1 and #3 are shown, the difference in magnitude between the two most likely due to geometric errors in the resistivity calculation. We observe that  $\rho_{aa}$  is almost completely strain independent around zero strain for both samples, indicating sharp crossing points. At around -0.08% for sample #1 and -0.10% for sample #3,  $\rho_{aa}$  begins to rise with compression. On the tension side it looks like the signal may take a down-turn around 0.10% strain, however we do not have enough data to confirm this. The transverse data, although noisier, appear approximately flat around zero strain, with sharp up- and down-turns at  $\pm 0.10\%$  strain. We do not expect the transverse signal to be strongly affected by  $\rho_{aa}$ , as we have shown that  $\rho_{aa}$  does not have much of a strain dependence at low strains at 7.6 T and 9.2 T. This suggests that  $\rho_{bb}$  also possesses these sharp crossing points.

The up- and down-turns at  $\pm 0.10\%$  correspond to the region of enhanced resistivity spreading outwards in field, in other words the high-strain curves cross the low-strain curves at a lower field on the low-field side and at a higher field on the high-field side. The difference in the strains at which the up-turn occurs for samples #1 and #3 could be a result of the higher strain inhomogeneity observed in sample #1, which is discussed further on in Section 6.2.5. The data in Figures 6.7a and

6.7b indicate that there are crossing points in  $\rho_{aa}$  and  $\rho_{bb}$  which remain sharp over a wide range of strain, between approximately -0.10% and +0.10%.

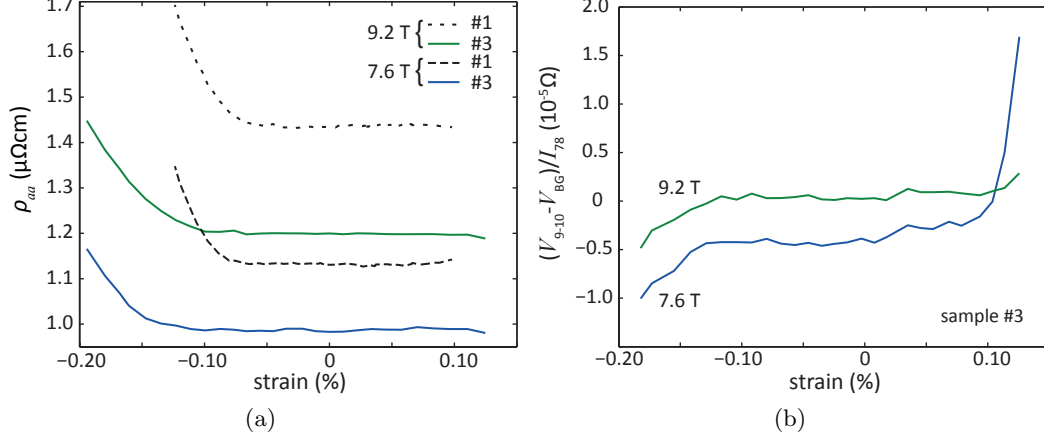


Figure 6.7: (a) Strain dependence of  $\rho_{aa}$  of samples #1 and #3 at 7.6 T and 9.2 T, corresponding to the crossing points. (b) Transverse response of sample #3 at the crossing points.

## 6.2 Experimental details

Having presented the main results from the strain measurements on  $\text{Sr}_3\text{Ru}_2\text{O}_7$  in the previous section, we now explore in greater depth several of the experimental details before moving on to a discussion of the data.

### 6.2.1 Frequency dependence and subtraction of background for samples #2 and #3

As shown in Figure 6.3, to be able to measure both the longitudinal and transverse response on the same sample during the same cool-down, it is necessary to run two wires across the sample. We found that for samples #2 and #3 which were wired up in this configuration, the transverse signal occurred on top of a large field-dependent, but strain-independent, background. We also found that this background depended on the frequency of the current used for the measurement. Raw data from sample #3 are plotted in Figure 6.8, showing the unusual background of the transverse signal. These data were measured at  $T \approx 300$  mK with the usual ramp rate of 0.2 T/min and a current of 1 mA. No voltages were applied to the stacks for these measurements, so that the sample was under a slight compression of  $\sim 0.07\%$ . We can clearly see the signatures of the phase, with the onset of both the A- and B-phases being easily distinguishable above the noise. These are superimposed onto a background which we found is well-fitted by a third order polynomial. As the

background is negative of sign and increases in magnitude with field, the measured voltage  $V_{9-10}$  in the vicinity of the phase is negative.

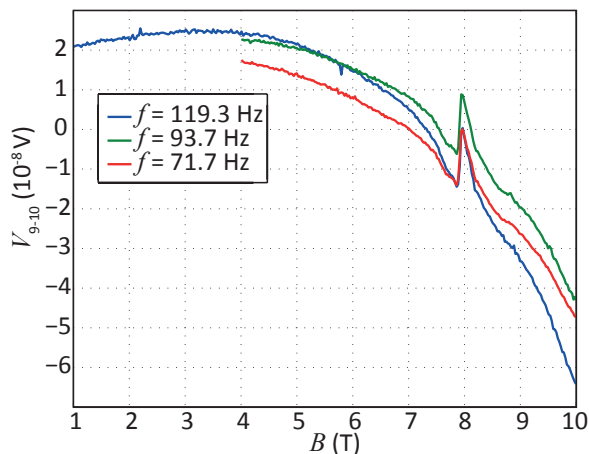


Figure 6.8: Raw data from the transverse measurement on sample #3, measured at three different frequencies.

To further investigate the nature of this background, we performed frequency sweeps whilst holding the temperature at  $T \approx 0.6$  K and the field at  $B = 8$  T, and measured the longitudinal and transverse signals with a 1 mA current (Figures 6.9a and 6.9b). The frequency was ramped from 60 to 2000 Hz in 1 Hz steps, with the signal being averaged over 5 s at each step.

The longitudinal signal appears to be roughly frequency independent between 80 Hz and 140 Hz and between 400 Hz and 690 Hz. The peaks at multiples of 50 Hz correspond to oscillations in the measurement circuitry induced by the mains power supply. We observe broad peaks in the in-phase component of the signal centred at 280 Hz and 812 Hz, with the out-of-phase signal resembling the derivative of these peaks. The transverse signal exhibits a large out-of-phase component which grows with frequency. For frequencies greater than 300 Hz, the magnitude of both the in- and out-of-phase components of the transverse signal increased beyond the measurement range to which the lock-in amplifier was set. Despite the signal being overloaded at high frequencies, we note that both components change sign several times, consistent with the presence of broad peaks like in the longitudinal measurement. This behaviour of the longitudinal and transverse signals is suggestive of a mechanical oscillation in the measurement wires, which is driven by the application of an AC current in a high magnetic field. As the transverse measurement is affected to a much greater extent than the longitudinal one, it is likely that the oscillation is taking place in the wires which run across the sample, mentioned previously. These are relatively long (4-5 mm) and flexible, and are not fixed to the probe except at their ends. The current leads for the longitudinal measurement are on the other hand much stiffer, being directly fixed to the ends of the sample where they are embedded in epoxy, and their length to the bonding pads is shorter

(1-2 mm). Hence the elastic constant of the transverse measurement wires will be smaller than that of the longitudinal ones, making the transverse measurement more sensitive to oscillations.

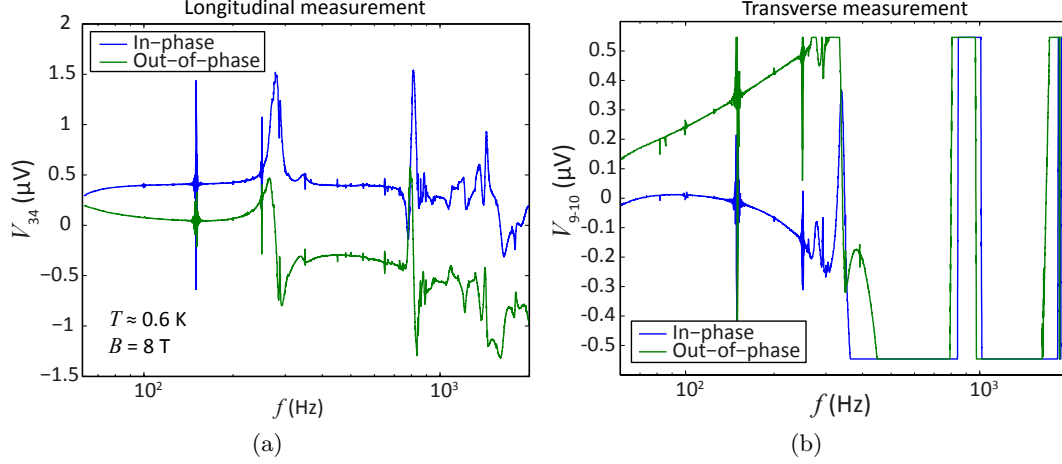


Figure 6.9: (a) and (b): longitudinal and transverse response of sample #3 measured against frequency at fixed field and temperature.

We attempted to eliminate the oscillations in the measurement wires by fixing them to the probe where possible, however were unable to completely suppress the frequency dependence of the signal. For sample #3, we therefore chose to operate at 119.3 Hz where the longitudinal signal did not display any significant frequency dependence, and no unusual background in  $\rho_{aa}$  was observed. This is illustrated by Figure 6.10, where  $\rho_{aa}$  is plotted over a wide field range. All of the data from sample #3 shown in Section 6.1 were taken at 119.3 Hz. For the transverse data we subtracted the background by fitting a third order polynomial to the 119.3 Hz curve shown in Figure 6.8. The same background was subtracted from each of the transverse measurements, to produce Figure 6.4B. In this way the relative change in magnitude of the signal across the data-set is not affected. Therefore although we cannot make quantitative arguments about the transverse data, qualitative arguments are not affected by the background as the signal shown in Figure 6.4B is dominated by the response of  $\text{Sr}_3\text{Ru}_2\text{O}_7$ .

Sample #2 (the data from which are shown in Section 6.2.4), showed a very similar behaviour to that of sample #3. We found that the optimal frequency at which to measure sample #2 was around 317 Hz. In the case of sample #1, which was not wired up for the transverse measurement, no unusual field-dependent background was observed, as illustrated by the full-range field ramps of Figure 6.2A, and all measurements were performed at 76 Hz.

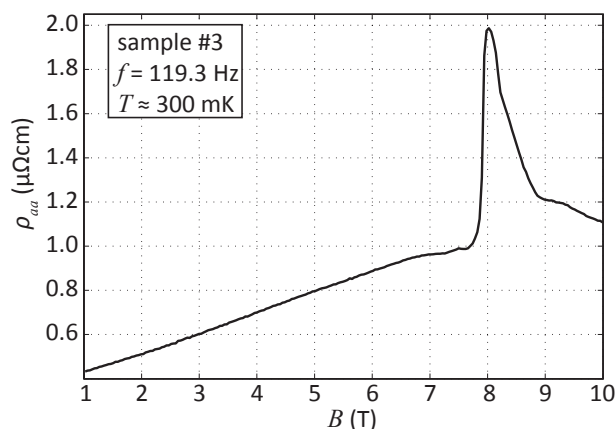


Figure 6.10:  $\rho_{aa}$  of sample #3 measured over a wide field range, showing the absence of any unusual background to the data, which are similar to those from a large body of previous work on samples mounted for conventional transport studies at zero strain. The measurement was performed with a 1 mA current, and no voltage applied to the stacks, so that the sample was under a slight compression of  $\sim 0.07\%$ .

### 6.2.2 Measurement current

Aside from the frequency of the measurement current, its amplitude could also have an effect on the observed signal. Indeed, at low temperatures the contact resistances are typically much larger than that of the sample, and can be a source of heating when a current is run through the sample. This could cause the temperature of the sample to be higher than that of the temperature sensor. We therefore check that the current we run through the sample is not affecting the shapes the measured curves, which would be a sign that the sample temperature is changing. One of these tests for sample #1 is displayed in Figure 6.11a, where the longitudinal signal was measured with no voltage applied to the piezoelectric stacks for three different measurement currents: 100  $\mu\text{A}$ , 0.5 mA and 1.0 mA. The measured voltage divided by the current is plotted, so that the three curves can be shown on the same scale, with the curves at 0.5 mA and 1.0 mA being offset by 50  $\mu\Omega$  and 100  $\mu\Omega$  respectively for ease of comparison. The three curves appear to be identical, aside from the signal-to-noise ratio which is highest for the 1 mA data: the height of the jump of the signal is the same for all three curves, as are fields at which the different transitions are observed.

Given the similarity in the response for the three measurement currents used, we decided to use a current of 1 mA for all three samples to obtain a high signal-to-noise ratio. We found no evidence that the temperature of the sample was being affected at this current level. To further illustrate this point, we plot a series of curves at different strains measured with a 100  $\mu\text{A}$  current on sample #1. Despite the higher noise levels, the results are qualitatively and quantitatively very similar to those shown in Figure 6.1a, which were measured with a 1 mA current.

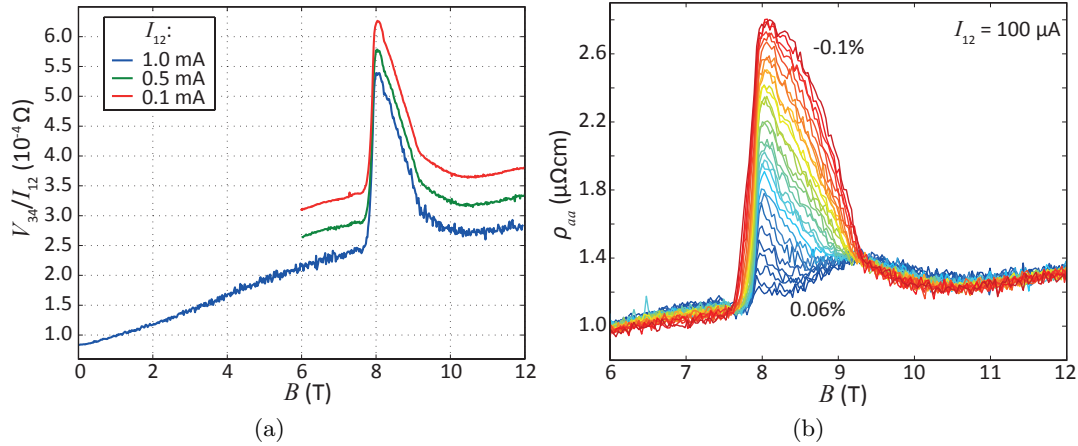


Figure 6.11: (a) Longitudinal signal of sample #1 measured with three different currents. The curves at 0.5 mA and 1.0 mA are offset by  $50 \mu\Omega$  and  $100 \mu\Omega$  respectively. No voltages were applied to the stacks during these runs, with the sample being at approximately 0.04% strain. (b) Series of field ramps at different strains measured with a current of  $100 \mu\text{A}$  on sample #1. The approximate strains of the highest compression and highest tension curves are labelled.

### 6.2.3 Strain measurement and determination of zero strain

Sample #1 was measured in the first generation strain probe, so the strain was monitored using the strain gauge, as described in Section 5.2.1 for the  $\text{Sr}_2\text{RuO}_4$  experiment. Samples #2 and #3 were measured in the second generation strain probe, where the strain is measured using a parallel plate capacitor. The capacitance was recorded continuously during the field sweeps using a capacitance bridge<sup>4</sup>. As the length of the piezoelectric stacks drifts slightly over time, we use the average capacitance over an entire run to estimate the strain. The strain is calculated using the parallel plate approximation  $C = \epsilon_0 A/d$ , where  $A$  is the area of the plates, and  $d$  their separation. In this way, we can calculate the change in plate separation and, using the correction factor  $\epsilon L/\Delta L$  in Table 6.1, estimate the sample strain. Here  $\Delta L$ , the change in sample plate separation, is equivalent to  $\Delta d$  as the motion of the stacks is rigidly transmitted to the movable capacitor plate.

Both the strain gauge and capacitor measurements only give the relative displacement of the sample plates, and as was the case for the  $\text{Sr}_2\text{RuO}_4$  experiment, we therefore need a separate method for determining the location of zero strain. As the height of the jump in resistivity in the phase is strongly dependent on strain near zero strain, we use it to determine zero strain. This is done by matching the height of the jump of the sample mounted in the strain probe to that of an unstrained reference sample. We cut our reference sample from the same crystal as the other

<sup>4</sup>Andeen Hagerling 2500 A.

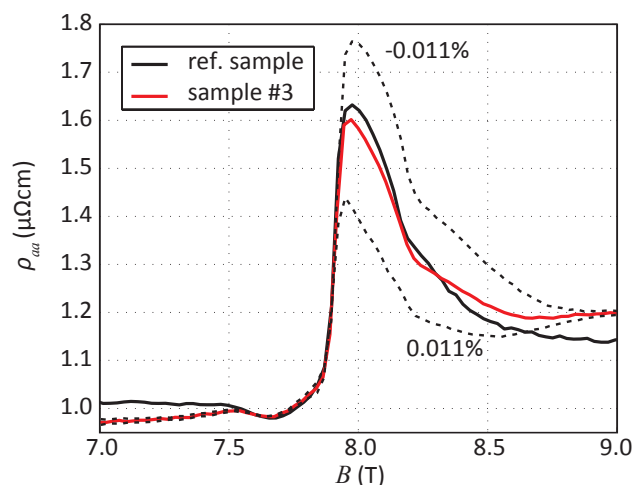


Figure 6.12: Comparison between sample #3 mounted on the strain probe and an unstrained reference sample. The red curve, which was measured at  $(V_{inner}, V_{outer}) = (0 \text{ V}, 60 \text{ V})$ , matches the reference sample most closely. All of the strains for sample #3 were calculated relative to the red curve. The dashed curves, the approximate strains of which are labelled, show the data from the strain steps directly above and below the red curve.

three samples, and mounted it such that it was suspended from its measurement wires (like the sample shown in Figure 4.9a). The wires being made out of gold and highly flexible, the sample remains unstrained as it is cooled down from room temperature, with any thermal contraction being taken up by the wires.

The comparison between the reference sample and the curve from sample #3 which most closely matches it is shown in Figure 6.12. For reference, we also show the curves which were taken one step higher and one step lower in strain. The height of the jump in resistivity of sample #3 is very close to that of the reference sample, although not exactly the same. Zero strain of sample #3 clearly lies somewhere between the two dashed curves, and we choose the red curve as the zero strain reference. Taking the capacitance reading from this run, we calculate all of the other strains relative to it. We assign an error of  $\sim 0.012\%$  to our estimate of the location of zero strain, which corresponds to a 20 V step on the piezoelectric stacks (the step between the red and dashed curves in Figure 6.12). As for the  $\text{Sr}_2\text{RuO}_4$  experiment, we additionally assign an error of  $\sim 10\%$  to the stated strains, to take into account the drift of the stacks over a given run. A similar comparison to the reference sample was also carried for samples #1 and #2 to locate zero strain.

#### 6.2.4 Sample comparison

Transport in three samples of  $\text{Sr}_3\text{Ru}_2\text{O}_7$  was measured under strain, with sample #1 being measured only in the longitudinal direction, and samples #2 and #3 wired

so that both the longitudinal and transverse responses could be measured. In this section we compare the data from all three samples to show that the data reported Section 6.1 was reproducible and consistent across the our sample set.

We have already discussed the similarity of  $\rho_{aa}$  measured on samples #1 and #3, with all of the main features reported being reproduced across both data-sets. The longitudinal and transverse data of sample #2 are plotted in Figure 6.13, which were measured under the same conditions as sample #3. Although we did not measure a large field-dependent background on the transverse signal of sample #2, it displays a strong frequency dependence as discussed in Section 6.2.1 and the data are overall much noisier than for sample #3. Nevertheless, the main qualitative features from sample #3 are reproduced, as can be seen by comparing Figures 6.5 and 6.13: compression and tension along [100] enhance the longitudinal and transverse signals respectively. There is also a clear area of overlap around zero strain between the region of enhanced  $\rho_{aa}$  and enhanced  $\rho_{bb}$ .

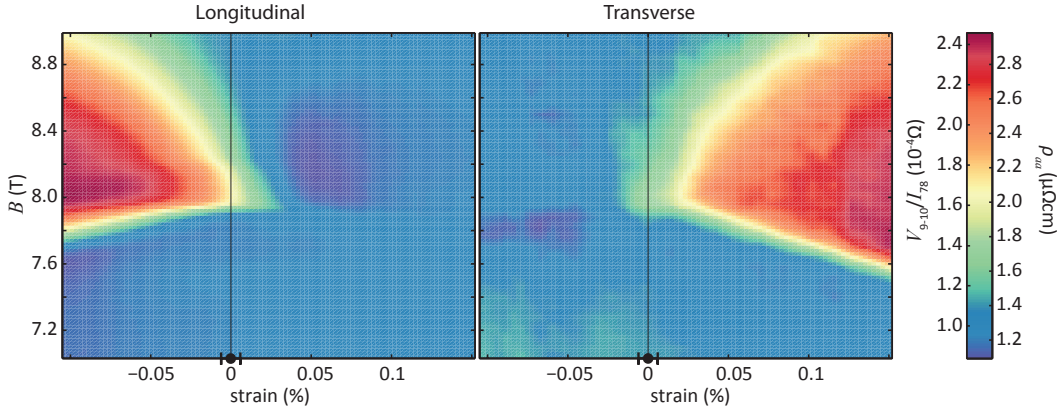


Figure 6.13: Longitudinal and transverse data of sample #2.

The strain response of the three samples is directly compared in Figure 6.14, where the longitudinal resistivity is plotted against strain for a field of 8 T (where the resistivity enhancement is at its highest). The resistivities are each normalized to their value at zero strain, to cancel out any geometric uncertainty in the resistivity calculation and facilitate comparison between the samples. We observe that the enhancement of  $\rho_{aa}$  for each sample onsets between  $\sim 0.03\%$  and  $0.05\%$  strain, with the response at higher tension being approximately flat. The height of the increase in resistivity, although not identical across all three samples, is very similar. We note that there is a difference in slope at zero strain between the three curves. This is likely due to slight differences in the mounting conditions of the three samples, such as the thickness of the epoxy above and below the sample and the length of sample embedded in epoxy. These variations will affect the efficiency with which the strain is transmitted from the sample plates to the sample. These effects are taken into account by the finite element calculations performed to estimate the strain, however the models used are only an approximation of the actual experimental set-up.

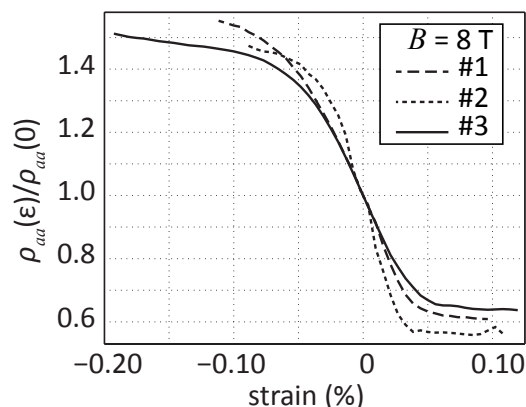


Figure 6.14: Comparison of the strain dependence of the longitudinal resistivity of the three samples at 8 T. The signal of each sample is normalized to its value at zero strain.

We conclude that although there are some quantitative differences between the data-sets from the three samples, the main qualitative behaviours reported were observed for each sample. The differences most likely stem from slight variations in the experimental set-up, such as the sample mounting conditions or quality of the electrical contacts.

### 6.2.5 Strain inhomogeneity

Achieving high strain homogeneity within the sample is one of the major challenges of performing uni-axial strain experiments. One advantage of the uni-axial strain probes used here is the high-aspect ratio of the sample, which allows strain inhomogeneity to decay away from the sample mounts, as discussed in Section 4.1.5. However, if the sample is not mounted perfectly symmetrically, for instance if there is more epoxy above than below it or if it is not exactly aligned with the direction of motion of the stacks, the sample can become bent as strain is applied which results in strain gradients across it. Strain inhomogeneity, which tends to be highest at the edges of sample, will affect our resistivity data as the voltage drop is measured along the sides of the sample. To determine whether the sample is being bent and the strain gradients across its width, we compare the signals measured with the voltage contacts on either side of the sample.

The longitudinal resistance measurements from both sides of samples #1 and #3 are shown in Figures 6.15A and B respectively. The strain scale for both panels was calculated using the height of the resistive jump measured with the voltage pair 3-4. The curves measured with both voltage pairs appear qualitatively very similar for both samples. Differences in the magnitude of the resistance measured on either side of the sample are most likely due to differences in contact separation.

One immediately noticeable difference between the two samples is that the two

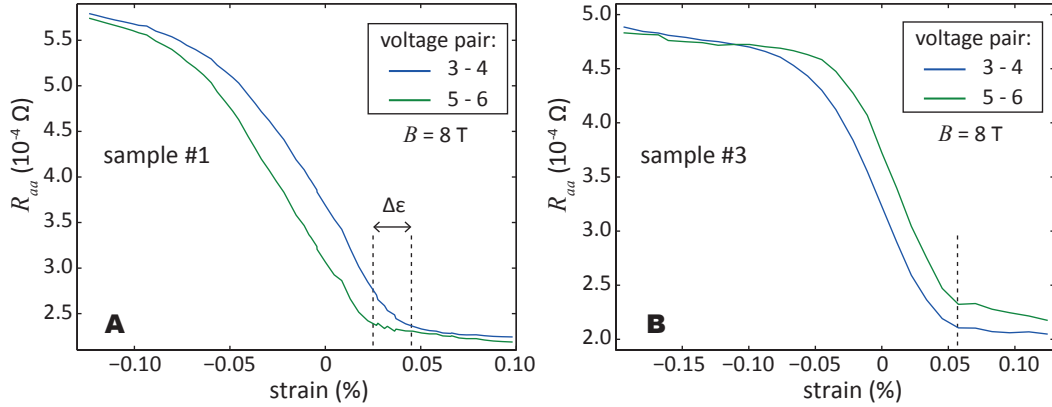


Figure 6.15: **A** and **B**: Comparison between the two voltage pairs of samples #1 and #3. The strain dependence of the measured resistance is plotted for a field of 8 T. The measurements from the pairs of sample #1 appear shifted by  $\Delta\epsilon \sim 0.02\%$  strain. The dashed line in **B** indicates the onset of the high resistivity state for both pairs of sample #3. The data from pair 3-4 of sample #1 were offset by  $0.5 \times 10^{-4} \Omega$  for ease of comparison.

curves from sample #1 are shifted in strain relative to each other, by an amount  $\Delta\epsilon \sim 0.02\%$  labelled in Figure 6.15A. For sample #3, the strain below which  $R_{aa}$  is enhanced is the same within less than  $0.01\%$  with both voltage pairs. A similarly good agreement in strain was also found between both sides of sample #2. The shift in strain between the two sides of sample #1 indicates that it is bent in the  $ab$ -plane. The difference in bending between the samples is most likely due to the strain probe which was used: sample #1 was measured on the first generation probe, whilst samples #2 and #3 were measured on the second generation probe. As detailed in Section 4.1.3 the first generation strain probe is constructed out of several blocks of titanium and incorporates thermal contraction foils, whilst the second generation probe is made out of a single piece of titanium. This was done in a effort to reduce strain inhomogeneity in the sample, by making the body of the probe more rigid and avoiding differential thermal contraction between different parts. It seems likely that such differential thermal contractions imposed a slight bending to the sample as the probe was cooled down. Given these results, it appears that a good strategy for reducing bending in the sample is to minimize the number of parts used to construct the strain probe.

For sample #1 we therefore estimate that there is  $\sim 0.02\%$  strain inhomogeneity across the sample, with side 3-4 being under higher tension than 5-6. The strain variation across the width of samples #2 and #3 is less than  $0.01\%$ . Sample bending causes the data-sets collected on either side of a given sample to be shifted relative to each other in strain, and so zero should be determined separately for each side of the sample. This inhomogeneity places a limit on the accuracy with which we can state the sample strain, however is small enough that it does not affect any of the

qualitative observations made so far.

### 6.2.6 Transverse signal and $\rho_{bb}$

In Section 6.1 we argued that the transverse response  $(V_{9-10} - V_{BG})/I_{78}$  gives a qualitative measure of the behaviour of  $\rho_{bb}$ . The measure is only qualitative for two reasons: (i) the field-dependent background described in Section 6.2.1 prevents us from obtaining an absolute value of the transverse voltage and (ii), the current flow is not homogeneous across the sample in the transverse configuration, so the signal has some dependence on  $\rho_{aa}$ . The background  $V_{BG}$  being strain-independent, as it is a result of an oscillation in the measurement wires, does not affect the evolution of the transverse signal with strain. The question is then to what extent the transverse signal is affected by  $\rho_{aa}$ , and how well it represents the behaviour of  $\rho_{bb}$ .

We previously discussed how the strong increase in the transverse signal at high tension must be a consequence of a large change in  $\rho_{bb}$ , as  $\rho_{aa}$  is low and roughly constant in this region. Conversely, at high compression where  $\rho_{aa}$  is large and changes rapidly with strain, a dip in the transverse signal is observed upon entering the phase due to the restriction of the current paths in the  $a$  direction. Although these arguments are sufficient to interpret the transverse data qualitatively, using a simple model we estimate here the extent to which the transverse signal is affected by the resistive anisotropy.

The sample is modelled by a  $100 \times 15$  grid to mimic the aspect ratio of the measured samples. Current flow is modelled by holding one point at a voltage  $V$  and another at ground, and then solving Kirchoff's law at each point of the grid iteratively until a solution is converged upon. The voltage can be set at collections of points instead of at a single point to better model the geometry of an actual contact. We performed the calculation using a contact configuration which mimicked that of the transverse measurement, for a series of resistive anisotropies from  $r = \rho_{aa}/\rho_{yy} = 0.1$  to 3. A colour plot of the potential within the sample calculated for  $r = 3$  is shown in Figure 6.16a, where the locations of the contacts are indicated. The calculation of the transverse voltage  $V_{9-10}$  as a function of resistive anisotropy is plotted in Figure 6.16b.

This calculation clearly shows that the transverse signal is affected by the magnitude of  $\rho_{aa}$ . Assuming that the magnitudes of  $\rho_{aa}$  and  $\rho_{bb}$  are similar and that they change by similar amounts with strain, we can estimate the range of  $r$  from the longitudinal measurement. For sample #3  $\rho_{aa}$  goes from  $\sim 2.4 \mu\Omega\text{cm}$  under compression to  $\sim 1.0 \mu\Omega\text{cm}$  under tension, so  $r$  should go from  $\sim 2.4$  to  $\sim 1/2.4 = 0.4$ . At zero strain,  $r = 1$  and the measured signal is  $\sim 8\%$  that of the voltage applied across the current contacts. When  $r \approx 2.5$  (corresponding to strong compression),  $V_{9-10}/V_{78} \approx 2\%$ , whilst when  $r \approx 0.4$  (high tension) we find  $V_{9-10}/V_{78} \approx 17\%$ . Relative to zero strain, the magnitude of the signal therefore varies by less than  $\pm 10\%$  due to the resistive anisotropy over the strain range studied. This indicates that the qualitative statements which we have made in relation to  $\rho_{bb}$  are not affected by the changes in  $\rho_{aa}$ .

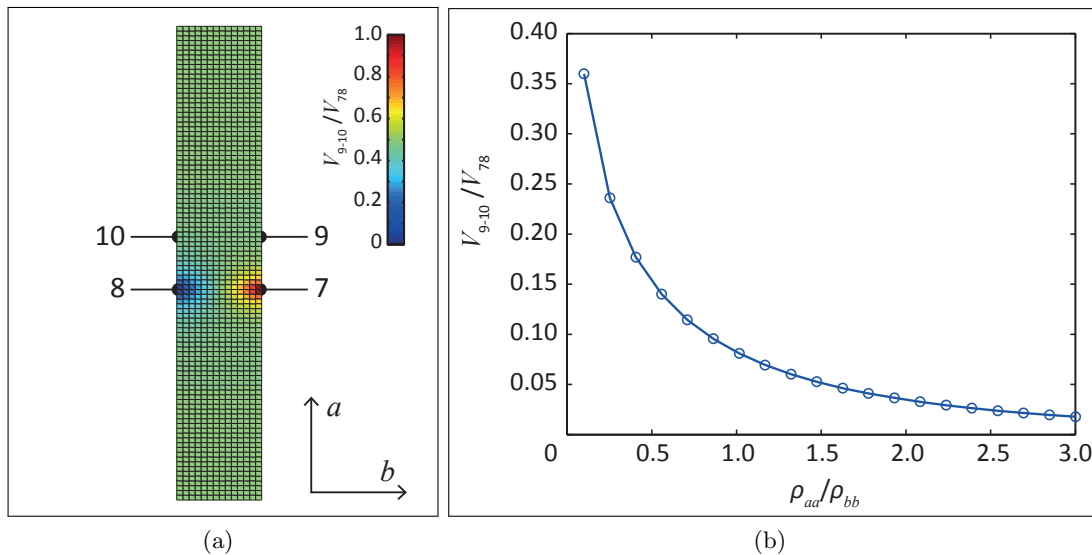


Figure 6.16: (a) Colour plot of the potential for a resistive anisotropy of  $r = 3$ . A voltage is held at contact 7, with contact 8 being held at ground. The voltage is then measured between 9 and 10. (b) Transverse voltage  $V_{9-10}$  normalized by the applied voltage  $V_{78}$  as a function of  $r$ .

### 6.3 Discussion

Let us briefly summarize our main experimental findings on  $\text{Sr}_3\text{Ru}_2\text{O}_7$  under uniaxial strain. We have shown that resistivity inside the phase is strongly affected by strain, with compression along  $[100]$  enhancing  $\rho_{aa}$  and tension along  $[100]$  enhancing  $\rho_{bb}$ . Whereas for an unstrained sample the resistivity jumps by a factor of  $\sim 1.6$  upon entering the phase, under compression the jump can be increased to a factor of  $\sim 2.5$ . The responses of  $\rho_{aa}$  and  $\rho_{bb}$  appear to approximately mirror each other about zero strain, with an overlap at zero strain of the regions of enhanced  $\rho_{aa}$  and  $\rho_{bb}$ . The width in strain of this region is field-dependent, reaching a maximum of  $\sim 0.08\%$  near 8 T. Another noteworthy observation is the high value of the elastoresistive coupling  $m$  outside the phase, indicating the presence of strong correlations and a high susceptibility to lattice distortions. We also found that at low strains there are two points where both the longitudinal and transverse responses appear to be strain independent, near 7.6 T and 9.2 T.

Despite the imperfection of the transverse measurement, our data show that  $\rho_{aa}$  and  $\rho_{bb}$  evolve oppositely with strain along  $[100]$ , indicating that the anisotropic distortion of the sample is the dominant effect. The responses of  $\rho_{aa}$  and  $\rho_{bb}$  are however not expected to be symmetric about zero strain, as the unit cell volume is not the same between tension and compression due to sample dilatation. Not knowing  $\text{Sr}_3\text{Ru}_2\text{O}_7$ 's in plane Poisson's ratios, we are unable to separate the effects

from both kinds of distortion.

### 6.3.1 Symmetry of the phase

One question which previous experiments have been unable to answer is whether  $\text{Sr}_3\text{Ru}_2\text{O}_7$ 's phase, in the absence of any symmetry-breaking fields, breaks the four-fold rotational symmetry of the crystal lattice or not. Indeed, the state with reduced symmetry, seen for instance by a large in-plane resistive anisotropy [4], has only been observed with an applied in-plane magnetic field. With our experiment we have shown that in-plane strain can also induce a strong in-plane anisotropy. It is therefore possible that the underlying state is  $C_4$  symmetric with a strong susceptibility to symmetry-breaking fields, rather than  $C_2$  symmetric. Understanding the symmetry of the phase is vital in terms of determining its order parameter. Let us briefly explore the expected behaviour for a  $C_2$  and  $C_4$  symmetric phase respectively.

If we associate an enhanced resistivity in the phase along  $a$  and  $b$  with an order parameter  $\Delta_a$  and  $\Delta_b$  respectively, two scenarios can be put forward. In the first, the phase is locally  $C_2$  symmetric. The degeneracy of  $\Delta_a$  and  $\Delta_b$  implies the formation of domains in the absence of any symmetry-breaking fields, where the order parameter is rotated by  $90^\circ$  between domains. Under zero strain and with no in-plane field the measured response would be isotropic, as the signal would be averaged over a large number of domains. The effect of a symmetry-breaking field would be lift the degeneracy between the two order parameters. In the second scenario, the phase is locally  $C_4$  symmetric, meaning that the components along  $a$  and  $b$  do not compete strongly and can coexist locally. In this case a symmetry-breaking field would continuously suppress one order parameter whilst enhancing the other, with the two orders coexisting over a finite range. Both of these scenarios correspond to particular limits of the Ginzburg Landau model for a two component order parameter discussed in relation to  $\text{Sr}_2\text{RuO}_4$  in Section 3.5.4. For the first scenario, the interaction term  $\beta_I$  between the order parameters is very large and prevents coexistence of the two orders, whilst for the second,  $\beta_I$  is much smaller. The phase diagrams for the two scenarios are sketched in Figure 6.17.

In these phase diagrams we have neglected the first order metamagnetic transitions and drawn the phase boundaries as second order transitions. Evidence of symmetry-breaking inside the phase was found by Lester et al. [44], who showed that it was host to a SDW. Only the transition at  $f = 0$  in the left-hand panel is first order, as it takes place when the  $C_4$  symmetry is already broken. In  $\text{Sr}_3\text{Ru}_2\text{O}_7$  some coupling must occur between the second order transitions and the metamagnetism to make some of the observed transitions first order: those bounding the A-phase for instance are distinctly first order [33].

Our data appear qualitatively much closer to the second scenario, where both types of order coexist microscopically in the region around zero strain. This can be seen by comparing the right-hand panel of Figure 6.17 with Figure 6.5C, where the outlines of the regions of enhanced  $\rho_{aa}$  and  $\rho_{bb}$  are plotted. As noted previously, the region of overlap which we measured is approximately centred on zero strain

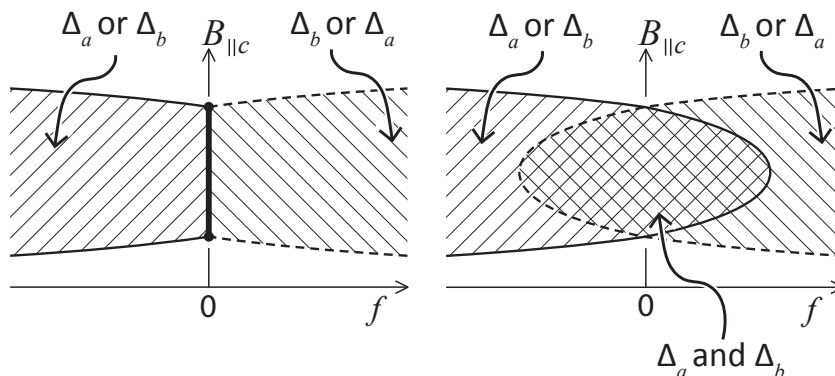


Figure 6.17: Phase diagrams for two different scenarios in  $\text{Sr}_3\text{Ru}_2\text{O}_7$ .  $f$  is a symmetry-breaking field, either magnetic field or strain. *Left*: Strong competition between the order parameters causes domain formation at  $f = 0$  where they are degenerate, with the degeneracy being lifted by non-zero  $f$ . The thick black line denotes a first order transition, whilst all of the other boundaries denote second order transitions. *Right*: Order along  $a$  and  $b$  do not compete strongly and coexist over a range of  $f$ .

and has a field dependent width in strain. These observations are consistent with the qualitative predictions made for the second scenario. Is it possible however that domains of locally  $C_2$  symmetric order could be stabilized over a finite region in strain, giving the appearance of coexistence and  $C_4$  symmetry?

It is plausible for instance that domains could be stable over a finite strain range if there is an inhomogeneous strain field within the sample. Strain inhomogeneity could be due to a random distribution of defects within the sample, or dislocations along the edge caused by the wire saw. The main source of inhomogeneity in our experiment is most likely due to bending of the sample, which as discussed in Section 6.2.5 gave rise to  $\sim 0.02\%$  inhomogeneity for sample #1 and less than  $0.01\%$  for samples #2 and #3. The width of the coexistence region is however  $\sim 0.08\%$ , larger than the inhomogeneity in any of the samples. Moreover, if this region were being broadened by strain inhomogeneity, one would not expect its width in strain to be field-dependent, as was observed. We therefore argue that the coexistence region measured in our samples is not a consequence of strain inhomogeneity. Additionally, we should emphasize that the data were collected by repeatedly ramping  $B \parallel c$  through the phase at a series of steps in strain. Hence the overlap region is not a result of latency across the first order line shown in the left-hand panel of Figure 6.17.

Long-range elastic or ferromagnetic interactions between domains could in theory cause them to become stabilized over a finite strain range. A lattice deformation of the order of  $10^{-6}$  was measured upon entering the phase under an applied in-plane field [41]. This is much smaller than the  $0.08\%$  strain width of the coexistence region, so it does not seem plausible that long-range elastic interactions are causing

a domain structure to stabilize. Domain stabilization via ferromagnetic interactions also appears unlikely, as the coexistence region extends over a field range of  $\sim 1$  T. The metamagnetic jump at 7.85 T, which is the larger of the two, is by comparison only  $\mu_0\Delta M = 0.008$  T [36], indicating that internal fields in the sample are likely much smaller than the width of the coexistence region.

A signature of domains in the sample would be the observation of hysteresis. Indeed, domains tend to become pinned around local defects in the lattice, so that a finite amount of energy is required to change their size and alignment. In the case of a ferromagnet, hysteresis is observed by measuring magnetization as a function of field which produces a hysteresis loop as the field is ramped up and then back down again. A similar effect was previously searched for in  $\text{Sr}_3\text{Ru}_2\text{O}_7$  during a series of experiments performed with a vector-magnetic field [121]. In these the magnetic field parallel to  $a$  was slowly swept up and then back down, whilst controlling the field along  $c$  to always remain within the phase. No sign of hysteresis was observed between the up- and down-ramps, indicating that if domains do exist they must be extremely weakly pinned.

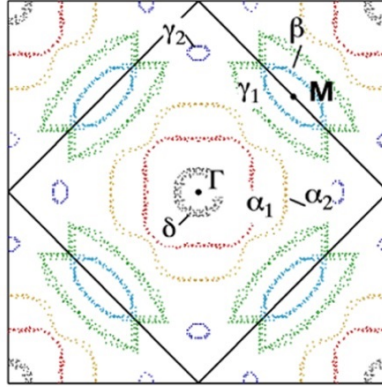
Our data, combined with the lack of evidence for domains, strongly suggest that the phase is  $C_4$  symmetric with a high susceptibility to in-plane fields. The question of how to explain the magnitude of the enhancement in resistivity in the phase however remains. Indeed, one of the primary explanations for the increase in resistivity has been domain wall scattering. Locally  $C_2$  symmetric order aligned along  $a$  or  $b$  would tend to favour domain formation along the  $\langle 110 \rangle$  directions, similar to twin boundaries [47]. The resistive anisotropy is however aligned along the in-plane axes, which also indicates that domains do not play a role in the resistivity enhancement.

### 6.3.2 Resistivity enhancement and the SDW

The discovery of an SDW in the phase could provide an explanation for an increase in resistivity, namely through the gapping-out of charge carriers.  $\text{Sr}_3\text{Ru}_2\text{O}_7$ 's Fermi surface, which was described in Section 2.5.1 and shown again for reference in Figure 6.18, is complex with many different pockets. The measured wavevectors at  $(\pm 0.233, 0, 0)$  and  $(0, \pm 0.233, 0)$  approximately match the distance between the flat faces of the  $\alpha_1$  pocket and the distance between  $\gamma_2$  pockets in adjacent zones. A halving of the conductivity in the phase would result from losing approximately half of the charge carriers. By inspection however it appears unlikely that a full gapping of the  $\alpha_1$  and/or  $\gamma_2$  pockets would cause a large enough loss of carriers, as these contribute much less than half of the total number of charge carriers in the Brillouin zone [29]. For comparison in chromium, which is also host to an incommensurate SDW, the resistivity  $\rho_{\parallel}$  parallel to the direction of the SDW grows to be  $\sim 8\%$  greater than  $\rho_{\perp}$ , that perpendicular to it. This is much smaller than the resistive anisotropy measured in  $\text{Sr}_3\text{Ru}_2\text{O}_7$ , where  $\rho_{\parallel}/\rho_{\perp} \approx 1.6$  in a small in-plane field [4].

Nevertheless, as pointed out in Section 2.5.3, the striking similarity between the profiles of the Bragg peak intensity and the resistivity against magnetic field

Figure 6.18: Fermi surface of  $\text{Sr}_3\text{Ru}_2\text{O}_7$ , as measured by ARPES. Taken from [28].



indicates that there must be an intimate connection between the SDW and the anomalous behaviour of the resistivity. A hint may be provided by the large value of the elasto-resistive coupling, which indicates that due to correlation effects small changes to the electronic structure could have an unusually large effect on the conductivity. The enhancement of the resistivity in the phase is a problem which merits further investigation, as any SDW model for the phase must be able to account for the unusually large magnitude of this effect.

If we extend the analogy between the strength of the SDW and the resistivity to our strain data, we can identify the regions of enhanced  $\rho_{aa}$  and  $\rho_{bb}$  with a SDW oriented along  $[100]$  and  $[010]$  respectively. In-plane strain would then act to tune the relative intensities of the two SDWs, perhaps by affecting the quality of the nesting between different sections of the Fermi surface. This would be one of the first examples of tuning through the phase diagram of a SDW with uni-axial strain, with the ability to tune between single- and double- $\mathbf{q}$  states.

### 6.3.3 Resistivity enhancement and metamagnetism

We remarked during our presentation of the data in Section 6.1 that while the magnitude of the resistivity enhancement varies greatly with strain, the metamagnetic transitions themselves do not seem to move significantly. The resistive signature of the upper metamagnetic transition at  $\sim 8.1$  T does not appear to change much with strain, and can be easily followed by eye across most of the strain range in Figures 6.1a and 6.4A. We therefore identify the kink in the resistivity near 8.1 T with this metamagnetic transition at all strains, and its location is plotted as the dashed line in Figure 6.5C.

The situation is slightly more ambiguous for the lower metamagnetic transition. Here the sharp vertical jump in resistivity which is associated with the metamagnetism at zero strain becomes broader and moves to slightly lower fields at high compression. The broadening in  $\rho_{aa}$  seems to appear beyond roughly -0.05% strain (see for example Figure 6.4A), suggesting that the primary source of broadening may not be strain inhomogeneity. A possibility is that at low strains the jump in

resistivity tracks the metamagnetic transition, and at some threshold strain becomes “unstuck” from it and begins moving to lower fields. Overall, the phase becomes stabilized over a much wider field range at high strains, with the phase on the high-field side extending far beyond the second metamagnetic jump.

In previous studies, the phase was found to be mostly contained within the two metamagnetic transitions, suggesting that phase formation occurs as a result of fluctuations about the QCEP [38]. In a previous vector magnet experiment it was however shown that the resistive anisotropy spills out beyond the second metamagnetic transition [42], whilst we have shown that strain can cause the phase to extend far beyond it. These observations seem to suggest that phase formation in  $\text{Sr}_3\text{Ru}_2\text{O}_7$  is not driven by the metamagnetic quantum criticality, but rather occurs on a background of metamagnetic quantum criticality. Coupling between the lower metamagnetic transition and the phase could cause the two to onset at the same field at low strains, whilst at higher strains the phase is stable at lower fields and the transitions split. It would be useful to measure the magnetization of the sample under strain, to check if such a splitting between the onset of high resistivity and the metamagnetic jump occurs. The lack of evidence for a metamagnetic transition bounding the high-field side of the phase equally supports this scenario.

This is all speculation however, and further experimental and theoretical investigations are necessary to determine the nature of the relationship between the quantum criticality and phase formation.

## 6.4 Summary and outlook

Through a series of measurements on  $\text{Sr}_3\text{Ru}_2\text{O}_7$ , we have shown that the transport properties of the novel phase are sensitive to in-plane strain. The behaviour of  $\rho_{aa}$  and  $\rho_{bb}$  approximately mirror each other about zero strain, with compression along  $a$  increasing the enhancement of  $\rho_{aa}$  and suppressing that of  $\rho_{bb}$  in the phase, and tension having the opposite effect<sup>5</sup>. There is a small but definite overlap between the regions of enhanced  $\rho_{aa}$  and  $\rho_{bb}$  centred on zero strain, which suggests that the phase is  $C_4$  rather than  $C_2$  symmetric at zero strain. The magnitude of the resistivity enhancement within the phase remains an unresolved question. A hint could come from the very large value of the elasto-resistive coupling both inside and outside of the phase, which indicates that strong electronic correlations may enhance the effect of lattice distortions on the transport. Another open question is the link between quantum criticality and phase formation. Our data led us to the speculation that although there is some coupling between the two phenomena, they may not be as intimately connected as previously thought. This issue however requires further experimental and theoretical investigation.

This initial experiment on  $\text{Sr}_3\text{Ru}_2\text{O}_7$  under uni-axial strain shows that strain is an effective probe for the study of its novel phase, and opens up many possibil-

---

<sup>5</sup>Note that given the near-tetragonal symmetry of the lattice, we treat the  $a$  and  $b$  directions as equivalent.

ities for future experiments. In particular, strain can be combined with different measurement techniques to gain new insight into the properties of the phase. One particularly interesting experiment would be to measure sample magnetization and susceptibility under strain. This would allow one to track the metamagnetic transitions as a function of strain, to see if the metamagnetism and resistivity enhancement always occur at the same field, or if there is a splitting of the transitions. Such a measurement would be important in determining the link between phase formation on the one hand and quantum criticality and metamagnetism on the other. Tracking the height of the jumps in magnetization as a function of strain could also reveal a connection between the two: do the jumps change with the resistivity, or remain constant with strain? Combining strain with neutron scattering measurements would be a powerful but challenging experiment. One could explicitly trace out the phase boundaries of the [100]- and [010]-oriented SDWs, and combine these with the resistivity data to make a strong argument about the nature of the phase's order parameter. The drawback of neutron scattering measurements is that they typically require much larger samples than can be mounted in our strain probe, so a different probe would need to be used

Exploring the phase diagram at higher temperatures would allow one to study how the signatures of quantum criticality, such as linear resistivity, evolve with strain, and could reveal further information about the character of the quantum critical fluctuations. Higher temperature measurements would also yield more clues about the phase's order parameter: if the phase has a two component order parameter, one would expect to observe a splitting of the transitions of the two components at non-zero strain, in analogy to the scenario presented in Section 3.5.4 for  $\text{Sr}_2\text{RuO}_4$ .

## Chapter 7

# Conclusions and Outlook

In this thesis I have presented results from experiments on  $\text{Sr}_3\text{Ru}_2\text{O}_7$  and  $\text{Sr}_2\text{RuO}_4$  under uni-axial strain. The measurements were performed using a novel uni-axial strain probe, which was designed and built specifically for these experiments. The uni-axial strain probe, which is based on the use of piezo-electric stacks, enables continuous control of the sample strain whilst maintaining the sample at cryogenic temperatures. An important feature of the probe is that it can apply both positive and negative strains, thus allowing one to study the symmetry of the response about zero strain. Due to the arrangement of the stacks, their thermal contraction does not cause the sample to become strained, meaning that a wide strain range on the sample is achievable even at low temperatures. In our experiments the maximum strain range achieved was  $-0.23\%$  to  $+0.22\%$  on a sample of  $\text{Sr}_2\text{RuO}_4$ .

The main aim of the experiment on  $\text{Sr}_2\text{RuO}_4$  was to test the predictions which were made for the chiral  $p$ -wave order parameter  $p_x \pm ip_y$ . A signature of such a superconducting state would be a sharp discontinuity in the slope of  $T_c(\varepsilon)$  at zero strain, where  $\varepsilon$  is an in-plane anisotropic strain, caused by the splitting of the transition temperatures of the order parameter's two components with strain. The response to strain along the  $[100]$  direction is highly symmetric about zero strain, with  $T_c(\varepsilon_{100})$  evolving quadratically at strains beyond roughly  $\pm 0.03\%$ . The magnitude of the response is very large:  $T_c$  is enhanced by  $\sim 40\%$  for  $\pm 0.2\%$  strain. We observed a small flat region at zero strain in  $T_c(\varepsilon_{100})$ , which extends out to approximately  $\pm 0.03\%$ , with no distinguishable cusp at zero strain. The response to strain along  $[110]$  is on the other hand much weaker and mostly anti-symmetric about zero strain. No cusp was observed at zero strain along this direction either.

The strong directional dependence of  $T_c$ 's response to strain indicates that superconductivity in  $\text{Sr}_2\text{RuO}_4$  is highly anisotropic in the plane, and that the tetragonal symmetry is hugely influential. At first glance the lack of cusp appears to be inconsistent with a  $p_x \pm ip_y$  order parameter. Using results from electronic structure calculations performed by E. A. Yelland and C. W. Hicks, we argued that certain scenarios of chiral  $p$ -wave superconductivity could be consistent with our data, as the resulting cusp would be below our experimental resolution. In particular, these

calculations suggest that the strong response to  $\varepsilon_{100}$  is closely linked to the density of states of the  $\gamma$  sheet and its proximity to the van Hove points. Overall our experiment places new constraints on models for superconductivity in  $\text{Sr}_2\text{RuO}_4$ , as they must be able to account for the strong directional dependence of the response as well as the apparent weakness of the cusp.

In the case of  $\text{Sr}_3\text{Ru}_2\text{O}_7$ , its novel phase had already been found to be sensitive to symmetry-breaking magnetic fields [4], and strain offers another means for studying the effects of symmetry breaking. Strain was applied along the [100] direction, and in-plane transport measured both parallel and perpendicular to the direction of applied strain to observe the behaviours of  $\rho_{\parallel}$  and  $\rho_{\perp}$  respectively. We found that the behaviour of  $\rho_{\parallel}$  and  $\rho_{\perp}$  approximately mirror each other about zero strain, with compression increasing the enhancement of  $\rho_{\parallel}$  and suppressing that of  $\rho_{\perp}$  inside the phase, and tension having the opposite effect. The increase of the enhancement is large, with  $\rho_{\parallel}$  jumping by a factor of  $\sim 2.5$  under 0.12% compression, compared to a factor of  $\sim 1.6$  at zero strain. In addition to the changes in resistivity, the phase is made to extend out far beyond its zero strain boundaries: from approximately 7.6 T to 9.4 T for 0.12% strain, compared to 7.85 T to 8.5 T at zero strain. In contrast, the metamagnetic transitions move around very little with strain.

This last observation led to the speculation that metamagnetic quantum criticality may in fact not be driving the phase formation, as the phase appears to be much more strongly affected by strain than the metamagnetism. Another key observation which we made was the overlap at zero strain between the regions of enhanced  $\rho_{\parallel}$  and  $\rho_{\perp}$ . The width in strain of the overlap region is field-dependent, with a maximum width of  $\sim 0.08\%$  at 8 T. We argued that our data were most easily explained by associating the regions of enhanced  $\rho_{\parallel}$  and  $\rho_{\perp}$  with an order parameter  $\Delta_{\parallel}$  and  $\Delta_{\perp}$  respectively, the order parameters not competing strongly such that they can microscopically coexist at zero strain. This implies that within the finite region about zero strain the phase would be  $C_4$  symmetric, with strain acting to enhance the order along one direction and suppress it along the other. An open question is that of the magnitude of the resistivity enhancement within the phase. A previously suggested explanation for this is domain wall scattering [4], however our data appear inconsistent with the formation of locally  $C_2$  symmetric domains.

At the end of Chapters 5 and 6, we proposed several ways in which the work presented here on  $\text{Sr}_2\text{RuO}_4$  and  $\text{Sr}_3\text{Ru}_2\text{O}_7$  could be expanded upon. Both compounds show a strong response to strain, and there remain many open questions which can be addressed by going to higher strains or coupling the strain probe with a different measurement, such as magnetization of specific heat. The uni-axial strain technique discussed in this thesis is also relevant to a wide range of materials beyond the ruthenates, and opens up the way to many new experiments. Indeed, through this work we have demonstrated that the uni-axial strain probe can be used to sensitively tune the electronic properties of a material with good directional resolution. Moreover this is done without introduction of defects into the sample allowing us to study systems in the clean limit. High strain homogeneity within the sample

is achievable through careful mounting, enabling the accurate measurement of the strain dependence of various physical properties.

Materials with a Fermi surface close to a van Hove point are likely to display a large response to strain, as indicated by the case of  $\text{Sr}_2\text{RuO}_4$ . If strain acts to move the Fermi surface closer to or further away from the van Hove point, the density of states will change rapidly with strain, which would cause dramatic effects on the transport and magnetization of the system. A large family of systems possessing a Fermi surface near a van Hove point is that of the overdoped high- $T_c$  cuprates [122], which are likely to be good candidates for strain experiments. Uni-axial strain is a powerful probe for studying the effect of lattice symmetry on the electronic states, and can be used to study competition between degenerate or nearly-degenerate states. A good example of this is the competition between stripe order and superconductivity in the cuprates [98]. Finally, we should emphasize that as the sample's surface is left exposed when it is mounted in the strain probe, the uni-axial strain technique can in principle be combined with spectroscopic probes such as angle-resolved photo-emission or scanning probe microscopy. This would enable a host of exciting new experiments where the electronic structure of a material can be directly observed under different lattice distortions.



# Bibliography

- [1] R. B. Laughlin, D. Pines. The Theory of Everything. *PNAS*, **97**, 28-31 (2000).
- [2] A. P. Mackenzie, J. A. N. Bruin, R. A. Borzi, A. W. Rost and S. A. Grigera. Quantum criticality and the formation of a putative electronic liquid crystal in  $\text{Sr}_3\text{Ru}_2\text{O}_7$ . *Physica C*, **481**, 207-214 (2012).
- [3] A. J. Schofield. Non-Fermi liquids. *Contemporary Physics*, **40**, 95-115 (1999).
- [4] R. A. Borzi, S. A. Grigera, J. Farrell, R. S. Perry, S. J. S. Lister, S. L. Lee, D. A. Tennant, Y. Maeno and A. P. Mackenzie. Formation of a Nematic Fluid at High Fields in  $\text{Sr}_3\text{Ru}_2\text{O}_7$ . *Science*, **315**, 214-217 (2007).
- [5] A. P. Mackenzie and Y. Maeno. Superconductivity of  $\text{Sr}_2\text{RuO}_4$  and the physics of spin-triplet pairing. *Rev. Mod. Phys.*, **75**, 657-712 (2003).
- [6] T. M. Rice and M. Sigrist.  $\text{Sr}_2\text{RuO}_4$ : an electronic analogue of  $^3\text{He}$ ?. *J. Phys. Condens. Matter*, **7**, L643-L648 (1995).
- [7] J. Xia, Y. Maeno, P. Beyersdorf, M. Fejer and A. Kapitulnik. High Resolution Polar Kerr Effect Measurements of  $\text{Sr}_2\text{RuO}_4$ : Evidence for Broken Time-Reversal Symmetry in the Superconducting State. *PRL*, **97**, 167002 (2006).
- [8] K. Ishida, H. Mukuda, Y. Kitaoka, K. Asayama, Z. Q. Mao, Y. Mori and Y. Maeno. Spin-triplet superconductivity in  $\text{Sr}_2\text{RuO}_4$  identified by  $^{17}\text{O}$  Knight shift. *Nature*, **396**, 658-660 (1998).
- [9] C. Nayak, S. H. Simon, A. S. Stern, M. Freedman and S. D. Sarma. Non-Abelian anyons and topological quantum computation. *Rev. Mod. Phys.*, **80**, 1083-1159 (2008).
- [10] M. B. Walker and P. Contreras. Theory of elastic properties of  $\text{Sr}_2\text{RuO}_4$  at the superconducting transition temperature. *PRB*, **66**, 214508 (2002).
- [11] L. D. Landau. The theory of a Fermi liquid. *JETP*, **30**, 1058-1064 (1956).
- [12] L. D. Landau. Oscillations in a Fermi liquid. *JETP*, **32**, 59-66 (1957).
- [13] L. D. Landau. On the theory of a Fermi liquid. *JETP*, **35**, 97-104 (1958).

- [14] P. Drude. Zur Elektronentheorie der Metalle. *Annalen der Physik*, **1**, 566-613 (1900).
- [15] N. Ashcroft and N. Mermin. Solid State Physics. *Brooks/Cole Cengage Learning* (1976).
- [16] R. Joynt and L. Taillefer. The superconducting phases of UPt<sub>3</sub>. *Rev. Mod. Phys.*, **74**, 235-294 (2002).
- [17] N. Majlis. The Quantum Theory of Magnetism. *World Scientific Publishing* (2000).
- [18] R. Levitin and A. Markosyan. Itinerant metamagnetism. *Sov. Phys. Usp.*, **31**, 730-749 (1989).
- [19] A. W. Overhauser. Spin Density Waves in an Electron Gas. *Phys. Rev.*, **128**, 1437-1452 (1962).
- [20] E. Fawcett. Spin-density-wave antiferromagnetism in chromium. *Rev. Mod. Phys.*, **60**, 1, 209-283 (1988).
- [21] S. A. Grigera, A. P. Mackenzie, A. J. Schofield, S. R. Julian and G. G. Lonzarich. A Metamagnetic Quantum Critical Endpoint in Sr<sub>3</sub>Ru<sub>2</sub>O<sub>7</sub>. *International Journal of Modern Physics B*, **16**, 20-22 (2002).
- [22] J. Custers, P. Gegenwart, H. Wilhelm, K. Neumaier, Y. Tokiwa, O. Trovarelli, C. Geibel, F. Steglich, C. Pépin and P. Coleman. The break-up of heavy electrons at a quantum critical point. *Nature*, **424**, 524-527 (2003).
- [23] F. M. Grosche, P. Agarwal, S. R. Julian, N. J. Wilson, R. K. Haselwimmer, S. J. S. Lister, N. D. Mathur, F. V. Carter, S. S. Saxena and G. G. Lonzarich. Anomalous low temperature states in CeNi<sub>2</sub>Ge<sub>2</sub> and CePd<sub>2</sub>Si<sub>2</sub>. *J. Phys.: Condens. Matt.*, **12**, 553-540 (2000).
- [24] D. Belitz, T. R. Kirkpatrick and J. Rollbühler. Tricritical Behavior in Itinerant Quantum Ferromagnets. *PRL*, **94**, 247205 (2005).
- [25] S.-I. Ikeda, Y. Maeno, S. Nakatsuji, M. Kosaka and Y. Uwatoko. Ground state in Sr<sub>3</sub>Ru<sub>2</sub>O<sub>7</sub>: Fermi liquid close to a ferromagnetic instability. *PRB*, **62**, 10, 6089-6092 (2000).
- [26] R. Kiyonagi, K. Tsuda, N. Aso, H. Kimura, Y. Noda, Y. Yoshida, S.-I. Ikeda and Y. Uwatoko. Investigation of the Structure of Single Crystal Sr<sub>3</sub>Ru<sub>2</sub>O<sub>7</sub> by Neutron and Convergent Beam Electron Diffractions. *JPSJ*, **73**, 3, 639-642 (2004).
- [27] H. Shaked, J. D. Jorgensen, O. Chmaissem, S. Ikeda and Y. Maeno. Neutron Diffraction Study of the Structural Distortions in Sr<sub>3</sub>Ru<sub>2</sub>O<sub>7</sub>. *Journal of Solid State Chemistry*, **154**, 361-367 (2000).

- [28] A. Tamai, M. P. Allan, J. F. Mercure, W. Meevasana, R. Dunkel, D. H. Lu, R. S. Perry, A. P. Mackenzie, D. J. Singh, Z.-X. Shen and F. Baumberger. Fermi Surface and van Hove Singularities in the Itinerant Metamagnet  $\text{Sr}_3\text{Ru}_2\text{O}_7$ . *PRL*, **101**, 026407 (2008).
- [29] J.-F. Mercure, A. W. Rost, E. O’Farrell, S. K. Goh, R. S. Perry, M. L. Sutherland, S. A. Grigera, R. A. Borzi, P. Gegenwart, A. S. Gibbs, and A. P. Mackenzie. Quantum Oscillations near the metamagnetic transition in  $\text{Sr}_3\text{Ru}_2\text{O}_7$ . *PRB*, **81**, 235103 (2010).
- [30] J.-F. Mercure, S. K. Goh, E. O’Farrell, R. S. Perry, M. L. Sutherland, A. W. Rost, S. A. Grigera, R. A. Borzi, P. Gegenwart and A. P. Mackenzie. Quantum Oscillations in the Anomalous Phase in  $\text{Sr}_3\text{Ru}_2\text{O}_7$ . *PRL*, **103**, 176401 (2009).
- [31] R. S. Perry, L. M. Galvin, S. A. Grigera, L. Capogna, A. J. Schofield, A. P. Mackenzie, M. Chiao, S. R. Julian, S. I. Ikeda, S. Nakatsuji, Y. Maeno and C. Pfleiderer. Metamagnetism and Critical Fluctuations in High Quality Single Crystals of the Bilayer Ruthenate  $\text{Sr}_3\text{Ru}_2\text{O}_7$ . *PRL*, **86**, 12, 2661-2664 (2001).
- [32] R. S. Perry, T. Tayama, K. Kitagawa, T. Sakakibara, K. Ishida and Y. Maeno. Investigation into the Itinerant Metamagnetism of  $\text{Sr}_3\text{Ru}_2\text{O}_7$  for the Field Parallel to the Ruthenium Oxygen Planes. *JPSJ*, **74**, 4, 1270-1274 (2005).
- [33] S. A. Grigera, R. A. Borzi, A. P. Mackenzie, S. R. Julian, R. S. Perry and Y. Maeno. Angular dependence of the magnetic susceptibility in the itinerant metamagnet  $\text{Sr}_3\text{Ru}_2\text{O}_7$ . *PRB*, **67**, 214427 (2003).
- [34] S. A. Grigera, R. S. Perry, A. J. Schofield, M. Chiao, S. R. Julian, G. G. Lonzarich, S. I. Ikeda, Y. Maeno, A. J. Millis and A. P. Mackenzie. Magnetic Field-Tuned Quantum Criticality in the Metallic Ruthenate  $\text{Sr}_3\text{Ru}_2\text{O}_7$ . *Science*, **294**, 329-332 (2001).
- [35] A. W. Rost, S. A. Grigera, J. A. N. Bruin, R. S. Perry, D. Tian, S. Raghu, S. A. Kivelson and A. P. Mackenzie. Thermodynamics of phase formation in the quantum critical metal  $\text{Sr}_3\text{Ru}_2\text{O}_7$ . *PNAS*, **108**, 40, 16549-16553 (2011).
- [36] A. W. Rost, R. S. Perry, J.-F. Mercure, A. P. Mackenzie and S. A. Grigera. Entropy Landscape of Phase Formation Associated with Quantum Criticality in  $\text{Sr}_3\text{Ru}_2\text{O}_7$ . *Science*, **325**, 1360-1363 (2009).
- [37] R. S. Perry and Y. Maeno. Systematic approach to the growth of high-quality single crystals of  $\text{Sr}_3\text{Ru}_2\text{O}_7$ . *J. Cryst. Growth*, **271**, 134-141 (2004).
- [38] A. G. Green, S. A. Grigera, R. A. Borzi, A. P. Mackenzie, R. S. Perry and B. D. Simons. Phase Bifurcation and Quantum Fluctuations in  $\text{Sr}_3\text{Ru}_2\text{O}_7$ . *PRL*, **95**, 086402 (2005).

- [39] S. A. Grigera, P. Gegenwart, R. A. Borzi, F. Weickert, A. J. Schofield, R. S. Perry, T. Tayama, T. Sakakibara, Y. Maeno, A. G. Green and A. P. Mackenzie. Disorder-Sensitive Phase Formation Linked to Metamagnetic Quantum Criticality. *Science*, **306**, 1154-1157 (2004).
- [40] A. M. Berridge, A. G. Green, S. A. Grigera and B. D. Simons. Inhomogeneous Magnetic Phases: A Fulde-Ferrell-Larkin-Ovchinnikov-Like Phase in  $\text{Sr}_3\text{Ru}_2\text{O}_7$ . *PRL*, **102**, 136404 (2009).
- [41] C. Stingl, R. S. Perry, Y. Maeno and P. Gegenwart. Symmetry-Breaking Lattice Distortion in  $\text{Sr}_3\text{Ru}_2\text{O}_7$ . *PRL*, **107**, 026404 (2011).
- [42] J. A. N. Bruin, R. A. Borzi, S. A. Grigera, A. W. Rost, R. S. Perry and A. P. Mackenzie. Study of the electronic nematic phase of  $\text{Sr}_3\text{Ru}_2\text{O}_7$  with precise control of the applied magnetic field vector. *PRB*, **87**, 161106 (2013).
- [43] E. Fradkin, S. A. Kivelson, M. J. Lawler, J. P. Eisenstein and A. P. Mackenzie. Nematic Fermi Fluids in Condensed Matter Physics. *Annu. Rev. Condens. Matter Phys.*, **1**, 153-178 (2010).
- [44] C. Lester, S. Ramos, R. S. Perry, T. P. Croft, R. I. Bewley, T. Guidi, P. Manuel, D. D. Khalyavin, E. M. Forgan and S. M. Hayden. Field-tunable spin-density-wave phases in  $\text{Sr}_3\text{Ru}_2\text{O}_7$ . *Nature Materials*, **14**, 373-378 (2015).
- [45] C. M. Puetter, J. G. Rau and H.-Y. Kee. Microscopic route to nematicity in  $\text{Sr}_3\text{Ru}_2\text{O}_7$ . *PRB*, **81**, 081105 (2010).
- [46] H. Yamase and A. A. Katanin. Van Hove Singularity and Spontaneous Fermi Surface Symmetry Breaking in  $\text{Sr}_3\text{Ru}_2\text{O}_7$ . *JPSJ*, **76**, 7, 073706 (2007).
- [47] H. Doh, Y. B. Kim and K. H. Ahn. Nematic Domains and Resistivity in an Itinerant Metamagnet Coupled to a Lattice. *PRL*, **98**, 126407 (2007).
- [48] W.-C. Lee and C. Wu. Theory of unconventional metamagnetic electron states in orbital band systems. *PRB*, **80**, 104438 (2009).
- [49] S. Raghu, A. Paramakanti, E. A. Kim, R. A. Borzi, S. A. Grigera, A. P. Mackenzie and S. A. Kivelson. Microscopic theory of the nematic phase in  $\text{Sr}_3\text{Ru}_2\text{O}_7$ . *PRB*, **79**, 214402 (2009).
- [50] U. Karahasanovic, F. Krüger and A. G. Green. Quantum order-by-disorder driven phase reconstruction in the vicinity of ferromagnetic quantum critical points. *PRB*, **85**, 165111 (2012).
- [51] Y. B. Kim and A. J. Millis. Residual resistivity near a two-dimensional metamagnetic quantum critical point. *PRB*, **67**, 085102 (2003).
- [52] E. Rossi and D. K. Morr. Vertex corrections for impurity scattering at a ferromagnetic quantum critical point. *PRB*, **81**, 054443 (2010).

- [53] J. Bardeen, L. N. Cooper, J. R. Schrieffer. Theory of Superconductivity. *PRL*, **108**, 1175-1204 (1957).
- [54] Michael Tinkham. Introduction to Superconductivity, Second Edition. *Dover Publications* (2004).
- [55] F. Steglich, J. Aarts, C. D. Bredl, W. Lieke, D. Meschede, W. Franz and H. Schäfer. Superconductivity in the Presence of Strong Pauli Paramagnetism: CeCu<sub>2</sub>Si<sub>2</sub>. *PRL*, **43**, 1892-1896 (1979).
- [56] J. G. Bednorz and K. A. Müller. Possible High  $T_c$  Superconductivity in the Ba-La-Cu-O System. *Z. Phys. B*, **64**, 189-193 (1986).
- [57] L. N. Cooper. Bound Electron Pairs in a Degenerate Fermi Gas. *PRL*, **104**, 1189-1190 (1956).
- [58] W. Buckel and Reinhold Kleiner. Superconductivity Fundamentals and Applications. *Wiley* (1991).
- [59] C. E. Gough, M. S. Colcough et al. Flux quantization in a high- $T_c$  superconductor. *Nature*, **326**, 855 (1987).
- [60] V. P. Mineev and K. V. Samokhin. Introduction to Unconventional Superconductivity. *Gordon and Breach Science Publishers* (1999).
- [61] W. Kohn and J. M. Luttinger. New Mechanism for Superconductivity. *PRL*, **15**, 524-526 (1965).
- [62] D. J. Scalapino, E. Loh and J. E. Hirsch. d-wave pairing near a spin-density-wave instability. *PRB*, **34**, 8190-8192 (1986).
- [63] R. Balian and N. R. Werthamer. Superconductivity with Pairs in a Relative  $P$  Wave. *PRL*, **131**, 1553-1564 (1963).
- [64] H. K. Pal, V. I. Yudson and D. L. Maslov. Resistivity of non-Galilean-invariant Fermi- and non-Fermi liquids. *arXiv*, 1204.3591v2 (2012).
- [65] D. Vollhardt and P. Wölfle. The Superfluid Phases of Helium 3. *Taylor & Francis* (1990).
- [66] M. Stone and R. Roy. Edge modes, edge currents, and gauge invariance in  $p_x + ip_y$  superfluids and superconductors. *PRB*, **69**, 184511 (2004).
- [67] J. Sauls. Surface states, edge currents, and the angular momentum of chiral  $p$ -wave superfluids. *PRB*, **84**, 214509 (2011).
- [68] A. J. Leggett. Quantum Liquids: Bose Condensation and Cooper Pairing in Condensed-Matter Systems. *Oxford University Press* (2006) .

- [69] Y. Maeno, S. Kittaka, T. Nomura, S. Yonezawa and K. Ishida. Evaluation of Spin-triplet Superconductivity in  $\text{Sr}_2\text{RuO}_4$ . *J. Phys. Soc. Jpn.*, **81**, 011009 (2012).
- [70] Y. Maeno, H. Hashimoto, K. Yoshida, S. Nishizaki, T. Fujita, J. G. Bednorz and F. Lichtenberg. Superconductivity in a layered perovskite without copper. *Nature*, **372**, 532-534 (1994).
- [71] N. E. Hussey, A. P. Mackenzie, J. R. Cooper, Y. Maeno, S. Nishizaki and T. Fujita. Normal-state magnetoresistance of  $\text{Sr}_2\text{RuO}_4$ . *PRB*, **57**, 5505-5511 (1998).
- [72] O. Chmaissem, J. D. Jorgensen, H. Shaked, S. Ikeda and Y. Maeno. Thermal Expansion and Compressibility of  $\text{Sr}_2\text{RuO}_4$ . *PRB*, **57**, 9, 5067-5070 (1998).
- [73] M. Norman. The Challenge of Unconventional Superconductivity. *Science*, **332**, 196-200 (2011).
- [74] C. Bergemann, A. P. Mackenzie, S. R. Julian, D. Forsythe and E. Ohmichi. Quasi-two-dimensional Fermi liquid properties of the unconventional superconductor  $\text{Sr}_2\text{RuO}_4$ . *Advances in Physics*, **52**, 639-725 (2003).
- [75] T. Oguchi. Electronic band structure of the superconductor  $\text{Sr}_2\text{RuO}_4$ . *PRB*, **51**, 2, 1385-1388 (1995).
- [76] A. Damascelli, D. H. Lu, K. M. Shen, N. P. Armitage, F. Ronning, D. L. Feng, C. Kim, Z.-X. Shen, T. Kimura, Y. Tokura, Z. Q. Mao and Y. Maeno. Fermi Surface, Surface States, and Surface Reconstruction in  $\text{Sr}_2\text{RuO}_4$ . *PRL*, **85**, 24, 5194-5197 (2000).
- [77] C. Bergemann, S. R. Julian, A. P. Mackenzie, S. NishiZaki and Y. Maeno. Detailed Topography of the Fermi Surface of  $\text{Sr}_2\text{RuO}_4$ . *PRL*, **84**, 12, 2662-2665 (2000).
- [78] K. M. Shen, N. Kikugawa, C. Bergemann, L. Balicas, F. Baumberger, W. Meevasana, N. J. C. Ingle, Y. Maeno, Z.-X. Shen, and A. P. Mackenzie. Evolution of the Fermi Surface and Quasiparticle Renormalization through a van Hove Singularity in  $\text{Sr}_{2-y}\text{La}_y\text{RuO}_4$ . *PRL*, **99**, 187001 (2007).
- [79] A. P. Mackenzie, R. K. W. Haselwimmer, A. W. Tyler, G. G. Lonzarich, Y. Mori, S. Nishizaki and Y. Maeno. Extremely Strong Dependence of Superconductivity on Disorder in  $\text{Sr}_2\text{RuO}_4$ . *PRL*, **80**, 1, 161-164 (1998).
- [80] H. Murakawa, K. Ishida, K. Kitagawa, Z. Q. Mao and Y. Maeno. Measurement of the  $^{101}\text{Ru}$ -Knight Shift of Superconducting  $\text{Sr}_2\text{RuO}_4$  in a Parallel Magnetic Field. *PRL*, **93**, 16, 167004 (2004).

- [81] I. Zutic and I. Mazin. Phase-Sensitive Tests of the Pairing State Symmetry in  $\text{Sr}_2\text{RuO}_4$ . *PRL*, **95**, 217004 (2005).
- [82] H.-J. Kwon, V. Yakovenko and K. Sengupta. How to detect edge electron states in  $(\text{TMTSF})_2\text{X}$  and  $\text{Sr}_2\text{RuO}_4$  experimentally. *Synthetic Metals*, **133-134**, 27-31 (2003).
- [83] G. Luke, Y. Fudamoto, K. Kojima, M. Larkin, J. Merrin, B. Nachumi, Y. Uemura, Y. Maeno, Z. Mao, Y. Mori, H. Nakamura and M. Sigrist. Time-reversal symmetry-breaking superconductivity in  $\text{Sr}_2\text{RuO}_4$ . *Nature*, **394**, 558-561 (1998).
- [84] T. Scaffidi, J. C. Romers and S. H. Simon. Pairing symmetry and dominant band in  $\text{Sr}_2\text{RuO}_4$ . *PRB*, **89**, 220510 (2014).
- [85] C. Hicks, J. Kirtley, T. Lippman, N. Koshnick, M. Huber, Y. Maeno, W. Yuhasz, M. Brian Maple and K. Moler. Limits on superconductivity-related magnetization in  $\text{Sr}_2\text{RuO}_4$  and  $\text{PrOs}_4\text{Sb}_{12}$  from scanning SQUID microscopy. *PRB*, **81**, 214501 (2010).
- [86] K. Izawa, H. Takahashi, H. Yamaguchi, Y. Matsuda, M. Suzuki, T. Sasaki, T. Fukase, Y. Yoshida, R. Settai and Y. Onuki. Superconducting Gap Structure of Spin-Triplet Superconductor  $\text{Sr}_2\text{RuO}_4$  Studied by Thermal Conductivity. *PRL*, **86**, 12, 2653-2656 (2001).
- [87] K. Deguchi, Z. Q. Mao, H. Yaguchi and Y. Maeno. Gap Structure of the Spin-Triplet Superconductor  $\text{Sr}_2\text{RuO}_4$  Determined from the Field-Orientation Dependence of the Specific Heat. *PRL*, **92**, 4, 047002 (2004).
- [88] K. Deguchi, Z. Q. Mao and Y. Maeno. Determination of the Superconducting Gap Structure in All Bands of the Spin-Triplet Superconductor  $\text{Sr}_2\text{RuO}_4$ . *JPSJ*, **73**, 5, 1313-1321 (2004).
- [89] C. Kallin. Chiral p-wave order in  $\text{Sr}_2\text{RuO}_4$ . *Rep. Prog. Phys.*, **75**, 042501 (2012).
- [90] S. Raghu, A. Kapitulnik and S. A. Kivelson. Hidden Quasi-One-Dimensional Superconductivity in  $\text{Sr}_2\text{RuO}_4$ . *PRL*, **105**, 136401 (2010).
- [91] T. Scaffidi and S. H. Simon. Large Chern Number and Edge Currents in  $\text{Sr}_2\text{RuO}_4$ . *PRL*, **115**, 087003 (2014).
- [92] C. W. Hicks, D. O. Brodsky, E. A. Yelland, A. S. Gibbs, J. A. N. Bruin, M. E. Barber, S. D. Edkins, K. Nishimura, S. Yonezawa, Y. Maeno and A. P. Mackenzie. Strong Increase of  $T_c$  of  $\text{Sr}_2\text{RuO}_4$  Under Both Tensile and Compressive Strain. *Science*, **344**, 283-285 (2014).

- [93] J. Paglione, C. Lupien, W. A. MacFarlane, J. M. Perz and L. Taillefer. Elastic tensor of  $\text{Sr}_2\text{RuO}_4$ . *PRB*, **65**, 220506 (2002).
- [94] N. D. Mathur, F. M. Grosche, S. R. Julian, I. R. Walker, D. M. Freye, R. K. W. Haselwimmer and G. G. Lonzarich. Magnetically mediated superconductivity in heavy fermion compounds. *Nature*, **394**, 39-43 (1998).
- [95] S. Kimber, A. Kreyssig, Y.-Z. Zhang, H. O. Jeschke, R. Valenti, F. Yokaichiya, E. Colombier, J. Yan, T. C. Hansen, T. Chatterji, R. J. McQueeney, P. C. Canfield, A. I. Goldman and D. N. Argyriou. Similarities between structural distortions under pressure and chemical doping in superconducting  $\text{BaFe}_2\text{As}_2$ . *Nature Materials*, **8**, 471-475 (2009).
- [96] S. Arumugam, N. Mori, N. Takeshita, H. Takashima, T. Noda, H. Eisaki and S. Uchida. Competition of Static Stripe and Superconducting Phases in  $\text{La}_{1.48}\text{Nd}_{0.4}\text{Sr}_{0.12}\text{CuO}_4$  Controlled by Pressure. *PRL*, **88**, 24, 247001 (2002).
- [97] U. Welp, M. Grimsditch, S. Fleshler, W. Nessler, J. Downey and G. W. Crabtree. Effect of Uniaxial Stress on the Superconducting Transition in  $\text{YBa}_2\text{Cu}_3\text{O}_7$ . *PRL*, **69**, 14, 2130-2133 (1992).
- [98] N. Takeshita, T. Sasagawa, T. Sugioka, Y. Tokura and H. Takagi. Gigantic Anisotropic Uniaxial Pressure Effect on Superconductivity within the  $\text{CuO}_2$  Plane of  $\text{La}_{1.64}\text{Eu}_{0.2}\text{Sr}_{0.16}\text{CuO}_4$ : Strain Control of Stripe Criticality. *JPSJ*, **73**, 5, 1123-1126 (2004).
- [99] L. D. Landau and E. M. Lifshitz. Theory of Elasticity, Course of Theoretical Physics Volume 7. *Pergamon Press* (1970).
- [100] J. F. Nye. Physical Properties of Crystals. *Oxford University Press* (1985).
- [101] D. R. Lovett. Tensor Properties of Crystals, Second Edition. *IOP Publishing* (1999).
- [102] A. Ballato. Poisson's Ratio for Tetragonal, Hexagonal, and Cubic Crystals. *IEEE Transactions on Ultrasonics, Ferroelectrics, and Frequency Control*, **43**, 1, 56-62 (1996).
- [103] N. Aso, Y. Uwatoko, H. Kimura, Y. Noda, Y. Yoshida, S.-I. Ikeda and S. Katano. A uniaxial pressure cell for neutron diffraction investigation and its use in studying the single-crystalline  $\text{Sr}_3\text{Ru}_2\text{O}_7$  compound. *J. Phys.: Condens. Matter*, **17**, 3025-3028 (2005).
- [104] C. Pfeleiderer, E. Bedin and B. Salce. He activated loading device for low temperature uniaxial and anvil cell pressure experiments. *Rev. Sci. Inst.*, **68**, 3120-3124 (1997).

- [105] X. X. Wei and K. T. Chau. Finite and transversely isotropic elastic cylinders under compression with end constraint induced by friction. *Int. J. Solids Struct.*, **46**, 1953-1965 (2009).
- [106] F. Bourdarot, N. Martin, S. Raymond, L.-P. Regnault, D. Aoki, V. Taufour and J. Flouquet. Magnetic properties of URu<sub>2</sub>Si<sub>2</sub> under uniaxial stress by neutron scattering. *PRB*, **84**, 184430 (2011).
- [107] J.-H. Chu, H.-H. Kuo, J. G. Analytis and I. R. Fisher. Divergent Nematic Susceptibility in an Iron Arsenide Superconductor. *Science*, **337**, 710-712 (2012).
- [108] A. M. Simpson and W. Wolfs. Thermal expansion and piezoelectric response of PZT Channel 5800 for use in low-temperature scanning tunneling microscope designs. *Rev. Sci. Inst.*, **58**, 2193-2195 (1987).
- [109] C. W. Hicks, M. E. Barber, S. D. Edkins, D. O. Brodsky and A. P. Mackenzie. Piezoelectric-based apparatus for strain tuning. *Rev. Sci. Inst.*, **85**, 065003 (2014).
- [110] J. Ekin. Experimental Techniques for Low-Temperature Measurements: Cryostat Design, Material Properties and Superconductor Critical-Current Testing. *Oxford University Press* (2006).
- [111] J.-F. Mercure. The de Haas van Alphen effect near a quantum critical end point in Sr<sub>3</sub>Ru<sub>2</sub>O<sub>7</sub>. PhD Thesis, *University of St Andrews* (2008).
- [112] M. Nikolo. Superconductivity: A guide to alternating current susceptibility and alternating current susceptometer design. *Am. J. Phys.*, **63**, 1, 57-65 (1995).
- [113] F. Pobell. Matter and Methods at Low Temperatures. *Springer* (1992).
- [114] C. Meingast, J. Karpinski and E. Kaldis. Uniaxial pressure dependence of  $T_c$  of single crystalline YBa<sub>2</sub>CuO<sub>4</sub> via thermal expansion. *Physica C*, **209**, 4, 591-596 (1993).
- [115] F. Hardy, N. J. Hillier, C. Meingast, D. Colson, Y. Li, N. Barisic, G. Yu, X. Zhao and J. S. Schilling. Enhancement of the Critical Temperature of HgBa<sub>2</sub>CuO<sub>4+δ</sub> by Applying Uniaxial and Hydrostatic Pressure: Implications for a Universal Trend in Cuprate Superconductors. *PRL*, **105**, 167002 (2010).
- [116] N. Okuda, T. Suzuki, Z. Mao. Y. Maeno and T. Fujita. Unconventional Strain Dependence of Superconductivity in Spin-Triplet Superconductor Sr<sub>2</sub>RuO<sub>4</sub>. *JPSJ*, **71**, 1134-1139 (2002).
- [117] S. Kittaka, H. Taniguchi, S. Yonezawa, H. Yaguchi and Y. Maeno. Higher- $T_c$  superconducting phase in Sr<sub>2</sub>RuO<sub>4</sub> induced by uniaxial pressure. *PRB*, **81**, 180510 (2010).

- [118] P. Blaha, K. Schwarz, G. K. H. Madsen, D. Kvasnicka and J. Luitz. WIEN2k: An Augmented Plane Wave Plus Local Orbitals Program for Calculating Crystal Properties (Karlheinz Schwarz, Techn. Universität Wien, Austria, 2001); ISBN 3-9501031-1-2.
- [119] K. D. Nelson, Z. Q. Mao, Y. Maeno and Y. Liu. Odd-Parity Superconductivity in  $\text{Sr}_2\text{RuO}_4$ . *Science*, **306**, 1151-1154 (2004).
- [120] H.-H. Kuo, M. C. Shapiro, S. C. Riggs and I. R. Fisher. Measurement of the elastoresistivity coefficients of the underdoped iron arsenide  $\text{Ba}(\text{Fe}_{0.975}\text{Co}_{0.025})_2\text{As}_2$ . *PRB*, **88**, 085113 (2013).
- [121] J. A. N. Bruin. Transport Studies of the Itinerant Metamagnet  $\text{Sr}_3\text{Ru}_2\text{O}_7$  Near its Quantum Critical Point. PhD Thesis, *University of St Andrews* (2012).
- [122] J. G. Storey, J. L. Tallon and G. V. M. Williams. Saddle-point van Hove singularity and the phase diagram of high- $T_c$  cuprates. *PRB*, **76**, 174522 (2007).